BEHAVIOR OF SOILS SUBJECTED TO THERMO-HYDRO-MECHANICAL COUPLED ACTIONS

A Dissertation

by

BOHAN ZHOU

Submitted to the Office of Graduate and Professional Studies of
Texas A&M University
in partial fulfillment of the requirements for the degree of

DOCTOR OF PHILOSOPHY

Chair of Committee,	Marcelo Sanchez
Committee Members,	Charles Aubeny
	Bjorn Birgisson
	Frederick M. Chester
Head of Department,	Robin Autenrieth

December 2020

Major Subject: Civil Engineering

ABSTRACT

Coupled Thermo-Hydro-Mechanical (THM) analyses involving soils and rocks are becoming increasingly more popular because of the need to develop infrastructure under every time more challenges ground conditions, as well as, due to the expansion of geochemical engineering to applications involving complex geo-environmental and geo-energy problems. This dissertation focuses on three research topics involving the coupled THM behavior of soils:

1) Experimental and constitutive studies of **frozen soils** subjected to freezing-thawing (F-T) cycles. The behavior of soils is investigated in the lab by under controlled environmental conditions, which are mainly focused on the volume change response of soils subjected cyclic F-T actions. Also, a new and comprehensive constitutive model for soils subjected to F-T cycles is proposed.

2) Constitutive mechanical modeling of **hydrate bearing sediments** (HBS). An advanced elastoplastic model is proposed to capture the complex response of this type of soil when subjected to THM interactions. The proposed approach includes inelastic mechanisms to account for the following effects, amongst others: soil and hydrates structure; temperature; dilatancy; and time-dependent behavior.

3) Experimental study on **gas migration** phenomena through **clay-barrier** systems intended for the safe isolation of **high-level nuclear waste**. The investigation looks at effect of soil suction, and swelling pressure on gas permeability This work also investigates the effect of cracking and self-healing on gas flow characteristics.

The underlain aim of this project is to gain a better understanding of soil behavior under these complex multiphase conditions to progress current knowledge in these three very relevant and timely subjects.

ACKNOWLEDGEMENTS

I would like to thank my committee chair, Dr. Sanchez, and my committee members, Dr. Abeny, Dr. Birgisson, and Dr. Chester, for their guidance and support throughout the course of this research.

Firstly, I want to thank Dr. Romero for his guidance and Muhammad Ali and Yue Chen for their help during my gas permeability and gas breakthrough tests. Also, I need to say thanks to Dr. Ajay for helping me at various stages of my work on frozen soil tests. Besides, I want to thank to Dr. Gai for his help during my modeling work on methane hydrate sediment. Moreover, I would like to extend my gratitude to my friends, the department faculties and staffs for making my time at Texas A&M University a great experience.

Finally, thanks to my father and mother for their encouragement and love, and to my friends and roommates for their patience and companionship.

CONTRIBUTORS AND FUNDING SOURCES

This work was supervised by a dissertation committee consisting of Dr. Marcelo Sanchez, Dr. Charles Aubeny, and Dr. Bjorn Birgisson of the Department of Civil Engineering, and Dr. Frederick M. Chester of the Department of Geology & Geophysics.

The tests and modeling work in Chapter I is guided by Dr. Ajay and the modeling work in Chapter II is helped by Dr. Gary and the experiment introduced in Chapter IV is achieved with the guidance of Dr. Romero and help of Muhammad Ali and Yue Chen.

Graduate study was supported mainly by research assistantship funded by Department of Energy (DOE) of United States with the project titled “Impact of coupled gas migration and thermo-hydro-mechanical process on the performance of repositories for high level nuclear waste”.

Graduate study was also supported by teaching assistantship funded by Zachary Department of Civil and Environmental Engineering of Texas A&M University as well as two fellowships, one by Zachary Department of Civil and Environmental Engineering of Texas A&M University and one by Terracon Consultants, Inc.

TABLE OF CONTENTS

Page

LIST OF FIGURES

Page

LIST OF TABLES

Page

1 INTRODUCTION

1.1 Background

Seasonal frozen soils dominate approximately 55% of the total earth's surface land. This area amounts, approximately, to 55 million km^2 (see Figure 1.1). In those regions, a good understating of the behavior of frozen soils is critical for a safe and economical design of new civil infrastructure and for assessing the condition of existing structures. Furthermore, with the discovery of fossil fuels in recent years, like petroleum and gas hydrates near the Arctic Circle as well as permafrost regions worldwide, frozen soils will become a topic of central interest.

Figure 1.1 Distribution of frozen ground (reprinted from Rekacewicz, 2005)

Although this topic has received an increased attention in past years, the current knowledge is still limited. Previous studies focused on different components of frozen-soil behavior, such as the effect of freezing temperatures on mechanical properties (e.g. strength, pre-consolidation pressure, stiffness or dynamic characteristics), and the impact of freezing-thawing (Fr-Th) cycles on hydraulic and mechanical properties. However, the combined effect of Fr-Th cycles and stress-history on frozen-soil behavior has received almost no attention in the literature. This combined effect is a relevant subjected considering the impact that it can have on, amongst others, volume change, stiffness, and hydraulic conductivity of frozen soils.

As mentioned above, methane hydrate, as a new and promising energy resource, is attracting increasing research interest worldwide. It exists not only in frozen ground, the methane hydrate sediments, which lay on the seabed, should also be paid much attention to. Methane hydrate bearing sediments (MHBS) are typically found in the seabed or permafrost regions where the low temperature and high-pressure conditions (see Figure 1.2) favor the formation of a crystalline structure where it is trapped together with water among its pores. Surveys indicate that this a promising energy resource, with very large reserves of methane worldwide that can satisfy the anticipated global energy demand. However, the production of methane from hydrate bearing sediments is very challenging, amongst other reasons, because of the complex behavior of this type of material.

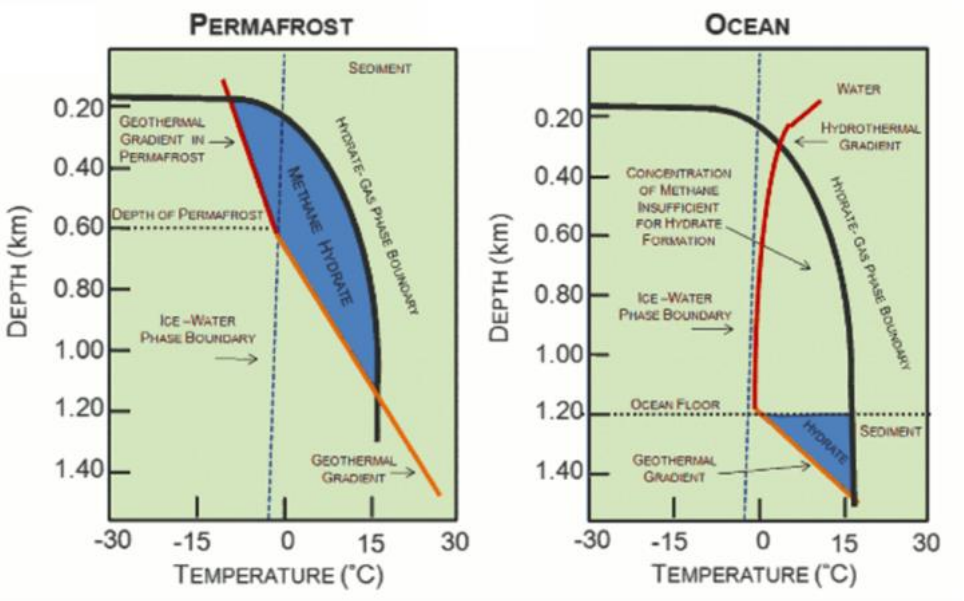

Figure 1.2 MHBS stability zone (reprinted from Sunjay et al., 2014)

The mechanical behavior of MHBS is quite complex. A good understanding and modelling of MHBS is a critical component to address the challenges and opportunities associated with this type of sediment. Several constitutive models have been proposed in the last few years to simulate the mechanical behavior of MHBS (Uchida et al., 2016, Gai et al., 2017, Sanchez et al., 2017). However, these models have limitations when dealing with effect of soil structure and temperature; high dilatancy; and time-dependent behavior of HBS. Besides, in terms of time-dependent behavior of HBS research, triaxial tests published is quite limited and the modeling work on HBS visco-plastic behavior is still almost blank. All of these existing gaps call for the research work on HBS.

Sometimes, hydrate dissociation will happen when temperature and pressure conditions change, and the gas formed due to dissociation will migrate through the porous media, which bring about another timely and hot research topic in coupled THM problems. The third part of my

research is related to this topic and will mainly focus on gas migration, gas breakthrough pressure as well as cracking and self-healing behaviors together with their impacts on gas permeability of high-level nuclear waste barrier material.

The safe isolation of high-level radioactive waste (HLW) is an unavoidable requisite for the use of nuclear power as a resource to meet present and future social energy need. The main safety function of a geological repository for the disposal of HLW is to confine pollute waste, prevent or delay the radionuclides to the host rock. Complex Thermo-Hydro-Mechanical and Chemical (THMC) phenomenon will take place in the repository due to heating and hydration under highly confined conditions. This THMC coupled problems will result in the erosion of steel container, the release of hydrogen gas and the migration of produced gas or penetrate through the surrounding barrier materials (see Figure 1.3).

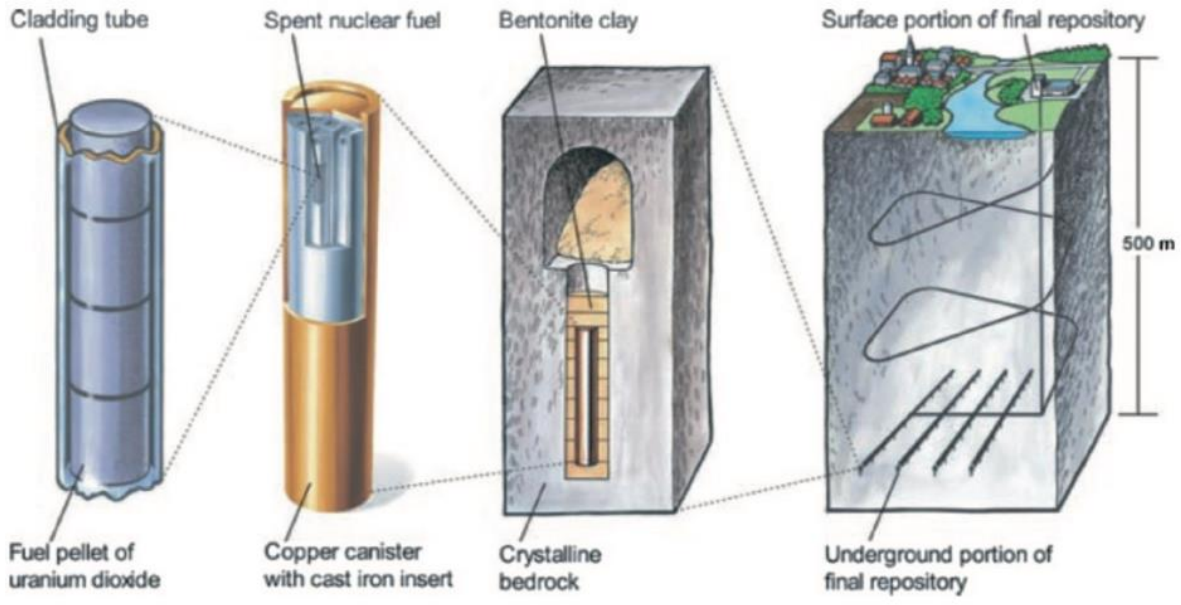

Figure 1.3 Repositories barrier system for HLW (reprinted from Kärnbränslehantering, 2011)

However, how gas migrates under complex surrounding conditions is still unclear particularly the present of interfaces between materials and discontinuities. The gap in the current knowledge on engineered barrier systems (EBS) should be bridged by undertaking fundamental, experimental and numerical investigations. My research in this dissertation is part of the project with Department of Energy (DOE) of U.S. aiming to bridge the gap discussed above and mainly focused on part of the experimental campaign. My research is to study gas migration phenomena in the context of barrier systems intended for the isolation of high-level nuclear waste. The investigation looks at effect of soil suction, and swelling pressure on gas permeability. This work also investigates the effect of cracking and self-healing on gas flow characteristics.

1.2 Objectives and activities

The objectives and activates envisaged for the three main topics investigated in this dissertation are outlined below.

1.2.1 Frozen soil subjected to cyclic freezing-thawing

The underlying goal is to gain a better understanding of the behavior of frozen soils, particularly on the mechanical response of soil subjected to cyclic F-T solicitations. Experimental, fundamental and numerical investigations have been conducted to achieve this objective.

- The goal of the experimental campaign is to produce a new set of high-quality experimental data associated with the volume change of soils subjected to freezing-thawing cycles that would help to understand the behavior of soils under these complex conditions;
- The fundamental studies focus on the effect of unfrozen water on the mechanical behavior of soils and on how to incorporate the three-phase condition of this type of soil (i.e. unfrozen water, solid and ice) in a consistent mathematical framework for frozen soils;

- The modeling activities have been focused on the developing a constitutive model for soils subjected to freezing-thawing cycles and its validation against the experimental data generated in this project and also already published ones.

1.2.2 Mechanical modeling of methane hydrate bearing sediment

The research goal is to model and capture better the complex mechanical behavior of HBS subjected to coupled multiphases conditions. This is achieved by enhancing an existing model to incorporate mechanisms capable of explaining and simulating features of HBS that are still unresolved, as for example, the large dilatancy typically observed in this type of material, the influence of temperature, and time-effects. An already published mechanical model for HBS developed at TAMU (i.e. Gai and Sanchez, 2017) is upgraded by incorporating the three main following components: i) an enhanced hardening law for materials with large dilatancy; ii) a modified evolution law for the pre-consolidation pressure to account for temperature effects; and iii) a visco-plastic law based on Perzyna's concept to simulate time-dependent effects. The model is validated against already test results available in the open literature.

1.2.3 Gas migration in barrier systems for high-level nuclear waste disposals

The goal is to gain a better understanding of gas migration phenomena in barriers for high-level nuclear waste disposals through experimental investigations. The aim of experimental campaign is to investigate effect of soil suction, and swelling pressure on gas permeability. Besides, gas breakthrough pressure measurements are conducted with interface problems evaluations. Moreover, cracking and self-healing behavior of barrier material is studied based on different initial dry densities and heating and drying conditions; gas permeability evolutions due to such cracking and self-healing behavior is also investigated by experiments.

1.3 Methodology

1.3.1 Frozen soil subjected to cyclic freezing-thawing

As for the experimental campaign, the first step is the physical characterization of the soil adopted in this research. A kind of silt from U.S. Silica Company is chosen in this dissertation. Routinely geotechnical tests are conducted to learn about the basic properties of this soil. Proctor and mechanical tests are also conducted to learn about the mechanical properties of this material. Slurry soil sample with a water content of 30% is chosen to perform tests for achieving the goal of fully saturated and evident test results. Cyclic freezing-thawing tests with a given temperature range (i.e. -7℃ to 5℃ and -0.3℃ to 5℃) are conducted in a freezing Chamber, in which temperature values between positive and negative can be set and circulated. Devices with open system are designed and 3D printed for the purpose of allowing water moving in and out freely during freezing-thawing cycles. Normally consolidated loose soil samples with pre-consolidation pressure of 10kpa and 100kpa are tested under same load steps together with over consolidated dense soil samples with pre-consolidation pressure of 500kpa and 1250kpa, so as to obtain ample tests results under different mechanical conditions, also, these results can be compared more effectively and obviously. Test data is measured by LVDT, and values as well as plots are recorded and shown by LabVIEW program on the computer connected. Collapse tests due to thawing as well as a method using electrical conductivity to measure unfrozen water are also introduced in experimental investigation.

As for the modeling campaign, BBM concept, incorporating cryogenic suction and temperature, is extended to developing the preliminary mechanical model for frozen soils subjected to cyclic freezing-thawing back on the experiment data gathered in the experimental campaign as well as on published results. Matlab is selected to help develop and modify the mechanical model.

1.3.2 Mechanical modeling of methane hydrate bearing sediment

The modeling investigation in this part is constructed on an already published mechanical model by Gai and Sanchez, 2017. Three new components are incorporated in the model. The first progress is to incorporate Nova theory which takes shear strain into consideration on hardening law to capture HBS high dilatancy behavior; then, a well-established thermos-plasticity theory is adopted for capturing temperature effects on HBS mechanical behavior; besides, time-dependent behavior of HBS is investigated and simulated by adopting visco-plasticity theory. Models are coded in Matlab and validated against some already published test results by former researchers.

1.3.3 Gas permeability and migration for high-level nuclear waste disposal

As for the experimental investigation, MX-80 bentonite in powder is mainly tested in different dry densities (i.e. 1.3g/cm^3, 1.6g/cm^3), and the corresponding retention curves are obtained by both WP4 and filter paper methods; preference pathway through the soil-metallic ring contact is minimized by a thin glued sand-bentonite mixture layer; different larger suction values (i.e. larger than 4MPa) are controlled by vapor transfer technique in a hydration path (i.e. wetting sample using a series of salt solutions); axis translation technique with high air entry value (HAEV) disk can also be a choice for controlling smaller suctions (i.e. smaller than 1.5MPa); gas nitrogen is injected from the upstream of the soil specimen; gas permeability under different stable suction (i.e. saturation degree) of soil specimen are measured using mass flowmeter and calculated with steady state method; combined with triaxial cell (i.e. no interface problem), more relationships among suction, stress and permeability during swelling are obtained. Cracking and self-healing behavior of barrier material is studied based on different initial dry densities and heating and drying conditions and the cracking patterns can be captured and recorded by both digital camera with time

remote controller and stereomicroscope. How the particles moved during cracking and healing is analyzed with Digit Image Correlation (DIC) technique.

1.4 Contributions to current knowledge

The following contributions to current knowledge have been made:

- The study of volumetric behavior of frozen soil subjected to cyclic freezing-thawing combines fundamental, experimental, and numerical investigations to advance current understanding in this complex and critical subject. High-quality experimental data associated with the frozen-soil behavior subjected to Fr-Th cycles under different stress levels is produced to expand the rather limited current database in this area. A mechanical multiphase coupled model is proposed to tackle engineering problems involving frozen soils subjected to complex loading conditions and Fr-Th cycles.
- The work on HBS conducted in this research can provide a new avenue for simulating high-dilatancy behavior and temperature effects on HBS. Besides, the visco-plastic component incorporated can fill the gap in the current modelling work about time-dependent behavior of HBS.
- The experimental investigation on gas migration through clay barrier material can bridge the gap in the current knowledge on how gas flows affect the performance of repositories for high level nuclear waste. It can help to establish more relationships among suction, swelling pressure and gas permeability at different steps during hydration for clay barrier systems, which is still an open topic of research in this subject. For gas breakthrough in barrier material investigations, potential shortcoming in traditional gas breakthrough pressure measurement device is evaluated and this can help better avoid interface problems in future research. Cracking and self-healing behavior study on nuclear waste barrier material and how such behaviors affect the gas permeability of the material is also a new research topic, which can enlarge the current knowledge

on gas migration in nuclear waste disposal barrier system as well as on safer isolation of nuclides from releasing to our environment.

1.5 Organization of the dissertation

This proposal contains five Sections, the first Section is an introduction of my research work, including the background and current gaps of my research topics, my objectives and activities to achieve them, the methodology adopted for the research work as well as the contributions to current knowledge on corresponding research area.

Section 2 gives details of the study on frozen soil subjected to cyclic freezing-thawing process in both experimental aspects and modeling aspects, this part is an extent of my research work during Master degree.

Section 3 mainly talks about the modeling work performed on methane hydrate bearing sediments by incorporating Nova, thermal plasticity and visco-plasticity theory. A detailed introduction on these three new components is presented and a series of already published triaxial tests cases are adopted for model validations.

Section 4 is mainly focus on the experimental campaign on gas permeability and migration in high-level nuclear waste barriers material. Base on two different initial dry densities (i.e. 1.3g/cm^3 and 1.6g/cm^3), study on cracking and self-healing behavior and how such behavior affect gas permeability of barrier material are presented; gas breakthrough pressure measurements with self-designed steel cell are introduced; gas permeability measurements with different devices and under different conditions for mutual complementation will also be elaborated in this Chapter.

Section 5 is a summary of research works that have been finished in this dissertation as well as some future works that can be conduct in the future.

2 STUDY ON FROZEN SOIL SUBJECTED TO CYCLIC FREEZING-THAWING

2.1 Introduction

Frozen soils are soils subjected to freezing process, in which phase change from water to ice will happen. Frozen ground can be divided into seasonally frozen ground, intermittently frozen ground, and permafrost ground. In seasonally frozen ground, soil is frozen for 15 days or more per year, while in intermittently frozen ground, soil is frozen for fewer than 15 days per year. Permafrost ground occupies about 22.79 million km^2 or 23.9% of the exposed land surface, while on average, the maximum extent of seasonally frozen ground is about 55 million km^2 or 55% of the total land area.

As a result of their wide distribution, frozen soils are closely connected to our life, and problems resulted from frozen soils, especially soils subjected to cyclic freezing-thawing process are becoming more significant constraints in many fields (i.e. engineering construction, waste disposal and energy exploitation). The interest on the mechanical behavior of frozen soils was initially driven (mainly) by problems associated with ground heave, because for a given amount of water, volume will increase when frozen to ice. Afterwards, the noticeable recent changes in climate worldwide have increased the interest in the study of frozen soils, especially in places where freezing-thawing process will accrue, like Canada and Russia. In addition, engineering properties of the soils such as strength, stiffness, coefficient of permeability, and mechanical behavior change drastically with changes in temperature and freezing-thawing cycles. These property changes give rise to many engineering practical problems, such as distress of foundations due to thawing leading to cracking of the super structure; road surface thaw damage; differential movements caused in roads and other infrastructure due to thaw weakening; glacial and periglacial slope failures causing landslides; and railroad distortion due to heaving of the soil. These problems bring about great financial losses and safety problems, and some are shown in Figure 2.1. In order

to well understand the behavior of frozen, and solve problems encountered in practical engineering problems, many researchers have made their attempts, not only in experimental tests but also in modeling work.

a) b) c)

Figure 2.1 Practical engineering problems a) building failure due to thaw settlement (reprinted from Romanovsky) b) road failure (reprinted from Turchetta, 2010) c) surface thaw damage (reprinted from Saarenketo & Aho, 2005)

When the temperature falls below the water freezing point, all the pore-water present in the soil is not converted into ice (Taber. 1930). The presence of unfrozen-water in frozen soils is mainly attributed to capillary phenomena. Figure 2.2a) shows a schematic representation of a frozen soil containing ice and unfrozen-water. Different experimental techniques have been proposed to determine the amount of unfrozen-water in soils, e.g., calorimeter method (William, 1964); time domain reflectometry (Feldler-Feldegg, 1969); dilatometer technique (Pusch, 1979); nuclear magnetic resonance (Tice et al., 1982); electron microscope device (White, 1999); differential scanning calorimetry (Kanitha and Reid, 2004); and electrical conductivity (Mao et al., 2018). Tice et al. (1976) estimated it from the soil liquid limit.

Cryonic suction in frozen soils is defined as the difference between the ice and the liquid pressures (i.e. S=Pi-Pl). Through the Clausius-Clapeyron equation (Clayperon, 1834; Clausius, 1850), a specific (freezing) temperature (T) can be directly associated with the corresponding Pi and Pl and, therefore with the cryonic suction. The unfrozen-water retention curve relates the amount of unfrozen-water retained by a frozen soil with the corresponding freezing temperature (as suggested by Tice et al., 1988), or with the associated cryonic suction (as suggested, e.g., by Nishimura et al., 2009).

Mechanical properties of frozen soils depend on freezing temperature and drastically change upon thawing, leading to several engineering problems in buildings and infrastructure, including foundations distress (triggered by soil-thaw-weakening, Figure 2.1a); road-surface thaw damage, Figure 2.1c); and slope failures. Qi et al. (2010) investigated the behavior of reconstituted frozen samples in a K0 compression apparatus. It was observed that a decrease in the freezing temperature induces an increase in both, the pre-consolidation pressure, and the frozen soil stiffness (Figure 2.2 b)). Chamberlain et al. (1972) reported that the confining pressure has a significant influence on the shear strength of remolded frozen soils. Shear behavior was also studied by Parameswaran & Jones (1981) through unconfined triaxial tests using reconstituted frozen soil samples. It was observed that both, stiffness and maximum deviatoric stress of frozen soils increased with the decrease in freezing temperature. Small-strain stiffness characteristics of frozen clays were measured at different loading rates and temperatures by Wang et al. (2019). Creep behavior of frozen soils has been intensively investigated (e.g. Andersland & Akili, 1967; Ma et al., 1997; Mathew, 2012; Yao et al., 2019).

Viklander (1998) conducted one of the first studies focused on the effect of Fr-Th cycles on soil behavior, with particular emphasis on the impact of Fr-Th cycles on soil permeability.

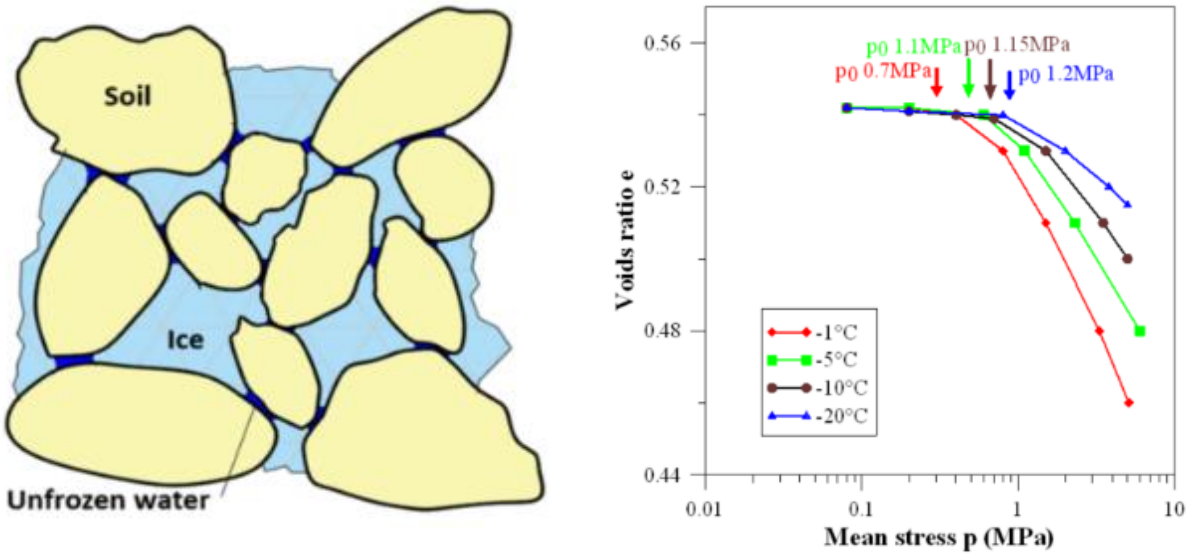

a) b)

Figure 2.2 a) Schematic representation of frozen soils; b) behavior of a reconstituted frozen soil (reprinted from Qi et al., 2010).

Most of the experimental studies related to the effect of Fr-Th cycles on soils have been based on testing specimens previously subjected to Fr-Th cycles (either in the lab or in the field) and comparing their responses against the untreated soils. For example, Graham & Au (1985) studied the effect of Fr-Th cycles on the preconsolidation pressure. Lee et al. (1995) investigated the impacts of Fr-Th cycles on the elastic modulus of cohesive soils gathered from pavement subgrades. Wang et al. (2007) and Qi et al. (2008) conducted similar studies aimed at understanding the effects of Fr-Th on elastic properties and soil strength. It was observed that stress-strain relationship is slightly affected by Fr-Th cycles, while the friction angle tends to increase with the number of cycles. Cui et al. (2014) studied the changes in soil microstructure induced by freeze-thaw by comparing scanning electron microscopy (SEM) images of soils before and after Fr-Th cycles. Han et al. (2018) also used SEM images to study the effect of Fr-Th cycles

and water salinity on soil microstructure. Tang et al. (2018) proposed a multiscale approach to investigate the microstructural and mechanical changes of expansive soils subjected Fr-Th cycles.

The rapidly increasing interest in the (artificial) ground freezing method, as a temporary soil improvement technique during construction (e.g. tunnels), has also promoted the study of Fr-Th effects on soil behavior. For example, Zhang et al. (2018) conducted triaxial tests to analyze the effects of Fr-Th on dynamic characteristics of a K0-consolidated silty-clay. Tang et al. (2018) studied (via stress-controlled cyclic triaxial tests) the behavior of saturated sandy-silt specimens previously subjected to Fr-Th cycles.

Zhou et al. (2018) conducted triaxial compression, creep, and stress relaxation tests at T=−6°C on a frozen loess. Strength, stiffness, and rheological properties of the frozen loess were studied, however no information about the volume change of frozen soils was reported. Lu et al. (2019) studied the mechanical degradation and volume change behavior of a compacted unsaturated expansive soil subjected to Fr-Th cycles. The main emphasis of this research was on the effect of the unsaturated condition and Fr-Th on mechanical properties, while the effects of stress-history on soil behavior were not addressed. Ling et al. (2015) studied the dynamic properties of frozen compacted sands previously subjected to Fr-Th cycles. Lin et al. (2017) investigated the accumulative plastic strain of a thawed saturated clays (subgrade material) under long-term cyclic loading considering the effect of Fr-Th cycles, dynamic stress amplitude, confining pressure and multi-stage cyclic loads. Hazirbaba (2019) investigated the settlement under cyclic loading of fine-grained soils previously subjected to Fr-Th cycles. Tian et al. (2019) conducted a similar research for a granular base course intended for a high-speed train. Zhang et al. (2019) examined the dynamic properties of frozen silts with different coarse-grained contents subjected to cyclic triaxial loading.

As for the constitutive/numerical modeling of frozen soils, different approaches have been proposed. The most recent frameworks incorporate the effect of cryonic suction in the model formulation (e.g. Nishimura et al., 2009; Thomas et al., 2009; Amiri et al. 2016). Yang et al. (2010) proposed an elasto-plastic constitutive model to simulate the non-linear behavior of frozen silts. Zhang & Michalowski (2015) extended the modified Cam Clay model to frozen soils incorporating, as stress state variables, the pore-ice-ratio and the effective stress. The model was implemented in a Thermo-Hydro-Mechanical (THM) framework and applied to solve boundary value problems. Lai et al. (2016) incorporated the effect of salt content into the constitutive modeling of frozen soils. Rotta Loria et al. (2017) introduced an elastoplastic model with an associated flow rule. Xu et al. (2017) proposed elasto-plastic models for frozen soils capable of tackling strain-rate effects; Nassr et al. (2018) adopted data mining technique to modeling frozen soil behaviors.

Based on the brief review discussed above, most of the studies focused on the effect of Fr-Th cycles on soil behavior compare untreated soils with specimens previously subjected to Fr-Th cycles. The combined effect of Fr-Th cycles and stress-history on frozen-soil behavior has received almost no attention in past. Also, no mechanical model was developed to simulate the behavior during this cyclic process. This component of soil behavior is very relevant when designing new civil infrastructure, or when assessing the condition of existing ones, in regions with grounds experiencing temperatures below the freezing point.

In order to gain a better understanding on the mechanical behavior of frozen soils, particularly on the mechanical behavior of soil subjected to cyclic freezing-thawing with different stress-history. Experimental and modelling investigations will be elaborated in the following part.

2.2 Experimental investigations

2.2.1 Material and methods

A low plasticity silt (i.e. SIL-75 from the U.S. Silica Company) with specific gravity around 2.65 was selected. An initial water content around 30% (i.e. ~1.2 times the liquid limit=25.3%) was adopted. A high-quality 3D printer was used to manufacture the one-dimensional cell adopted in this research. It consists of the following main components: a base pedestal; an inner-ring (to house the soil); a plunger (to apply the vertical stress); an outer-ring (to provide a seal all around and to support the plunger); a LVDT (linear variable differential transformer); and a mount (which assembles all the components together). Figure 2.3 shows some of the setup components.

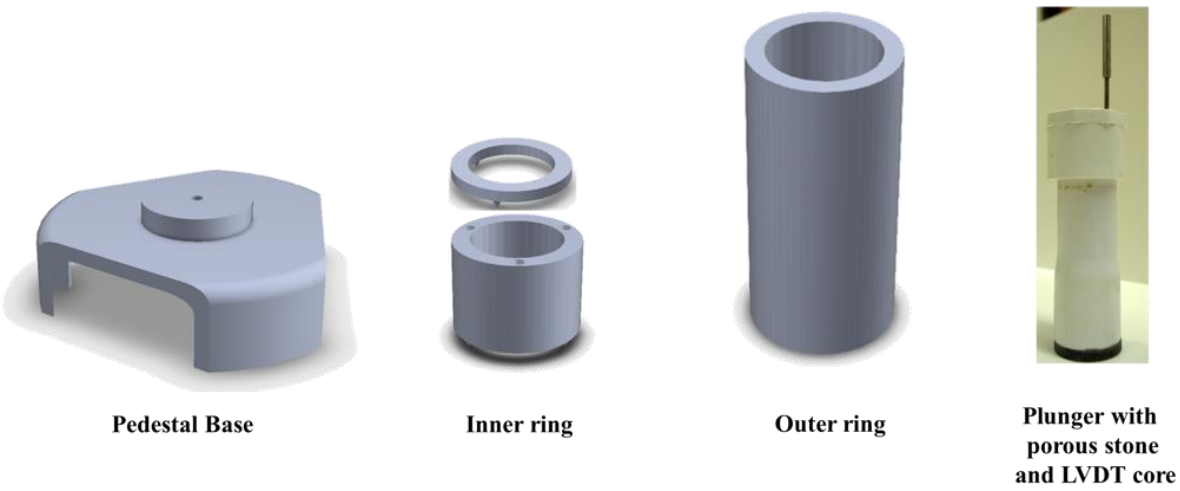

Figure 2.3 Schematic of the various components of experimental setup

O-Ring seals between outer-ring and pedestal were included to ensure a water tight setup. The pedestal was designed with a drainage at the bottom connected to a source of free water to produce an open system and allow free drainage. The inner-ring can host soil specimens 39mm

height and 39mm diameter. Porous stones were placed at the bottom and top of the samples. The vertical load was applied as a dead load through the plunger. The whole setup is shown in Figure 2.4.

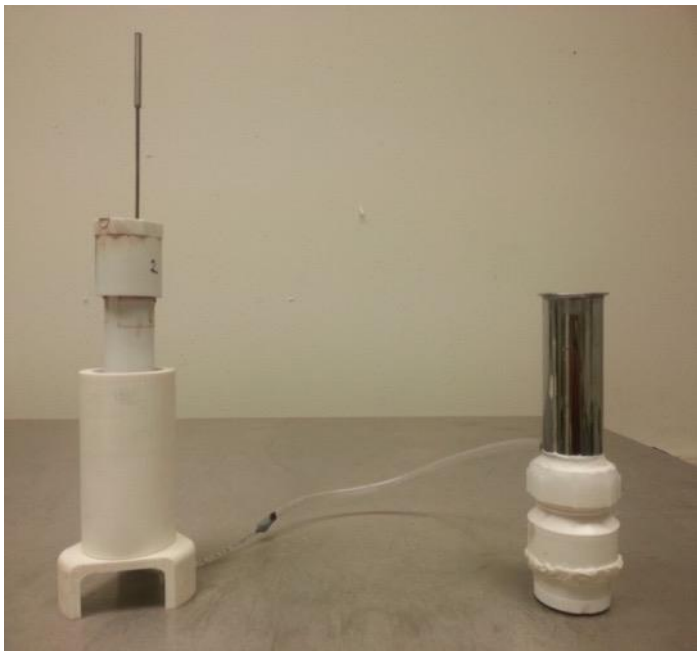

Figure 2.4 Whole setup for the tests

The LVDT (SE-750-500) attached to the top of the plunger tracked the vertical displacements during the test. This LVDT is specially designed to operate under freezing temperature (-20°C to 70°C). The Fr-Th cycles were conducted inside a CSZ 0.45m3 (16ft3) environmental chamber capable of temperature (-40°C to 179°C) and relative humidity (5% to 98%) computer-controlled cycling (Figure 2.5). The temperature inside chamber was also measured using an in-built thermocouple. The set-up was calibrated for the range of temperature contemplated in this research.

Figure 2.5 CSZ environmental chamber

The oven-dried silt was mixed with distilled water at the target water content (i.e. ~w=30%) and the mixtures were left inside hermetic plastic bags for 24 hours to attain homogenized specimens. All the samples were prepared inside the cell in slurry state. A light tapping was applied to remove any possible air-bubble. The samples were then subjected to the (small) contact pressure exerted by the plunge (i.e. $\sim\sigma'_v$=0.2kPa) and allowed to consolidate for 24 hours under room temperature (i.e. ~20°C). The test protocols described below were applied afterwards.

2.2.2 Effect of stress history and Fr-Th cycles on soil behavior

Three cases were designed to investigate the response of the soil to *Fr-Th* cycles subjected to different stress history. After loading and/or unloading the specimens to target stresses at ambient temperature (i.e. T=20°C), eight *Fr-Th* cycles were applied in all the cases with

temperature variations between 5°C and -7°C. A full *Fr-Th* cycle was completed in one day, as in previous works (Cui et al., 2014; Han et al., 2018; and Lu et al., 2019).

Tests in this part can be divided into six cases, and in each case, soil samples were under cyclic freeze-thaw with different loading history. To take case 1 for illustration, soil sample was loaded to 10kPa, after which, the first series of freeze-thaw cycles were conducted at a vertical pressure of around 10 kPa. After these cycles, the sample was loaded at 20°C up to a vertical stress of 100 kPa and, at this stress level, another series freeze- thaw cycles were applied. Then the sample was unloaded (at 20°C) up to 10 kPa and third series of freeze-thaw cycles were applied. The two first series of freeze-thaw cycles were conducted under normally consolidated (NC) conditions and the last one corresponded to an over consolidated (OC) sample. The symbols 'N' and 'O' were used to identify normally consolidated and over consolidated accordingly. 'r' means same loading is added again. '$C1_{N\_10}$' means Case 1, Normally consolidated under loading of 10kPa, the same reasoning is applied to all other cases and steps. The symbols 'A-B' were also used to represent the stages in each case in an easier way (i.e. used in later parts), A means case number, and B means stage number. Therefore, the steps followed for the case 1 are as follows:

Case 1: 10kPa NC ($C1_{N\_10}$ or 1-1) – 100 kPa NC ($C1_{N\_100}$ or 1-2), and 10 kPa OC ($C1_{O\_10}^{r}$ or 1-3).

Similarly, the other five cases can be denoted as:

Case 2: 100kPa NC ($C2_{N\_100}$ or 2-1) – 10 kPa OC ($C2_{O\_10}$ or 2-2), and 100 kPa NC ($C2_{N\_100}^{r}$ or 2-3);

Case 3: 500kPa-10kPa OC ($C3_{O\_10}$ or 3-1) – 100 kPa OC ($C3_{O\_100}$ or 3-2), and 10 kPa OC ($C3_{O\_10}^{r}$ or 3-3);

Case 4: 500kPa-100kPa OC ($C4_{O\_100}$ or 4-1) – 10 kPa OC ($C4_{O\_10}$ or 4-2), and 100 kPa OC ($C4_{O\_100}^{r}$ or 4-3);

Case 5: 1250kPa-100kPa OC ($C5_{O\_100}$ or 5-1) – 10 kPa OC ($C5_{O\_10}$ or 5-2);

Case 6: 1250kPa-10kPa OC ($C6_{O\_10}$ or 6-1).

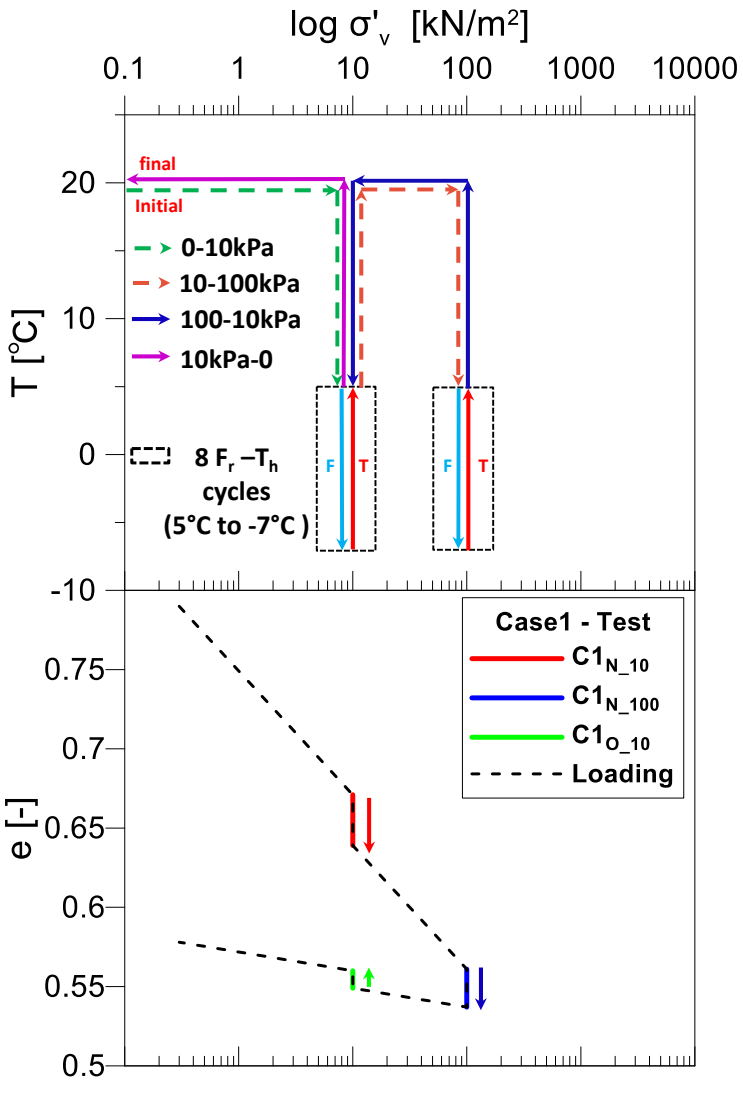

Figure 2.6 Generalized σ'_v -T paths and the associated void ratio changes for Case 1

In Case 1 (Figure 2.6), the sample was loaded until σ'_v=10kPa and the first series of *Fr-Th* cycles were applied maintaining σ'_v constant. The collapse compression behavior observed during these cycles under normally consolidation (*NC*) conditions is identified as $C1_{N\_10}$ (i.e. C1: Case 1; N: *NC;* 10: σ'_v=10kPa; a similar reasoning was followed for other stages/Cases) After the *Fr-Th* cycles, the sample was loaded up to σ'_v=100kPa and subjected to another series of *Fr-Th* cycles, exhibiting a subsequent volume reduction ($C1_{N\_100}$). Then, the sample was unloaded until σ'_v=10kPa and the third series of *Fr-Th* cycles was applied. Under this over consolidated (*OC*) state, the sample experienced a volume expansion ($C1_{O\_10}$).

Similar as Case 1, the adopted generalized effective vertical stress-temperature (σ'_v-*T*) paths together with the tests results in terms σ'_v and void ratio (*e*) for Case 1 to Case 6 are presented from Figure 2.6 to Figure 2.11 accordingly. The temperature range among these Cases are the same but the loading histories and stress states are different in different Cases. Comparisons among them in terms of Over Consolidation Ratio (OCR) are also be presented.

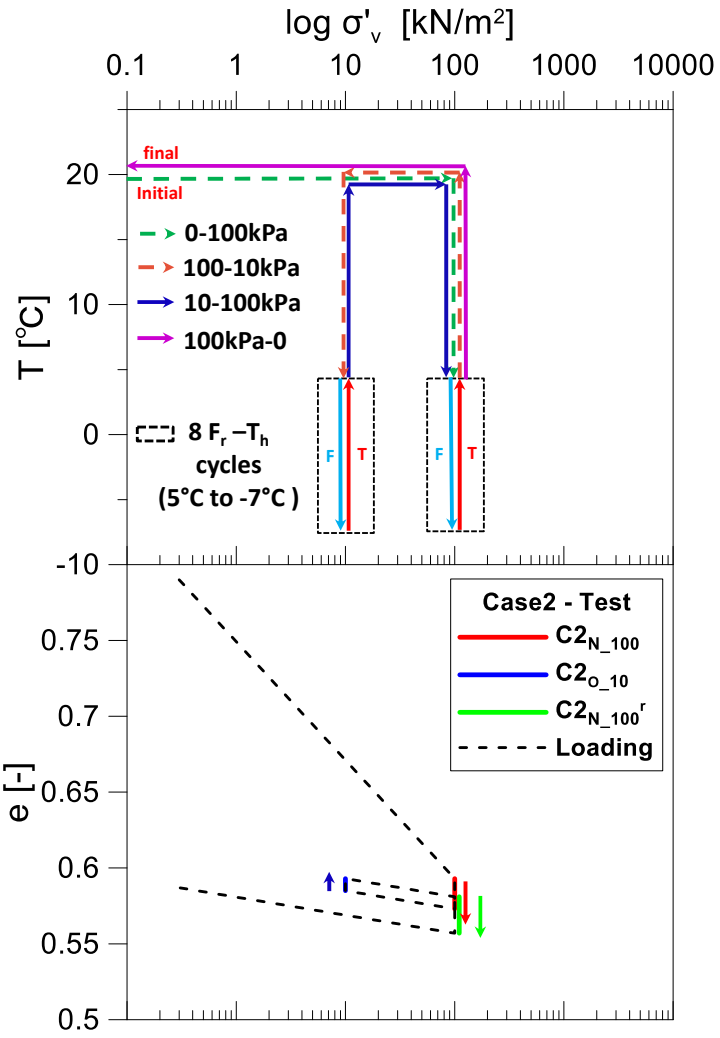

Figure 2.7 Generalized σ'_v -T paths and the associated void ratio changes for Case 2

In Case 2 (Figure 2.7), the initial stage is similar to Case 1, but the first series of *Fr-Th* cycles was conducted at *NC* conditions under a constant σ'_v=100kPa. A net compression ($C2_{N\_100}$) of the material was observed under these conditions. Then, the sample was unloaded and exhibited an expansion ($C2_{O\_10}$) after applying *Fr-Th* cycles at σ'_v=10kPa. Afterwards, the specimen was reloaded and subjected to the last series of *Fr-Th* cycles under σ'_v=100kPa. The soil developed a final net compression ($C2_{N\_100}^{r}$) under this *NC* state achieved after unloading-reloading (^{r}).

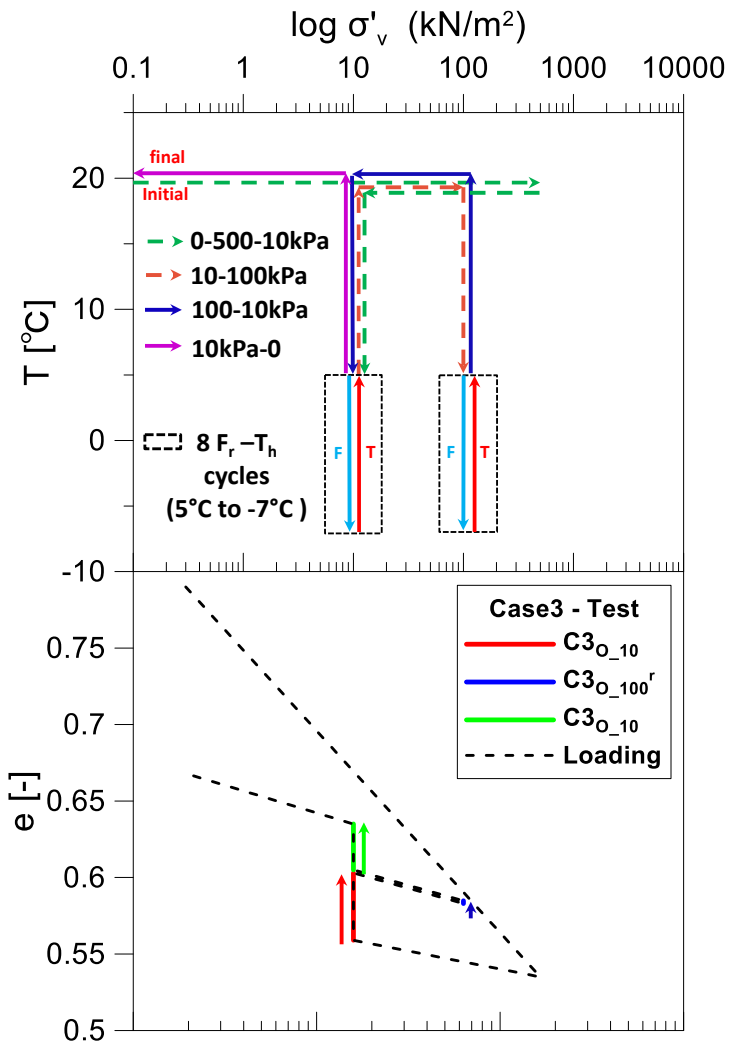

Figure 2.8 Generalized σ'_v -T paths and the associated void ratio changes for Case 3

In Case 3 (Figure 2.8), the first series of *Fr-Th* cycles were applied under *OC* conditions, after loading the sample up to σ'_v=500kPa (in the same cell but in an odometer outside the chamber) and unloading it at σ'_v=10kPa. The sample expanded after this thermal cycle ($C3_{O\_10}$). Then, the sample was reloaded and exhibited a small expansion ($C3_{O\_100}{}^{r}$) after applying *Fr-Th* cycles at σ'_v=100kPa. Afterwards, the specimen was unloaded and subjected to the last series of *Fr-Th* cycles under σ'_v=10kPa. The soil developed another expansion ($C3_{O\_10}$) under this *OC* state.

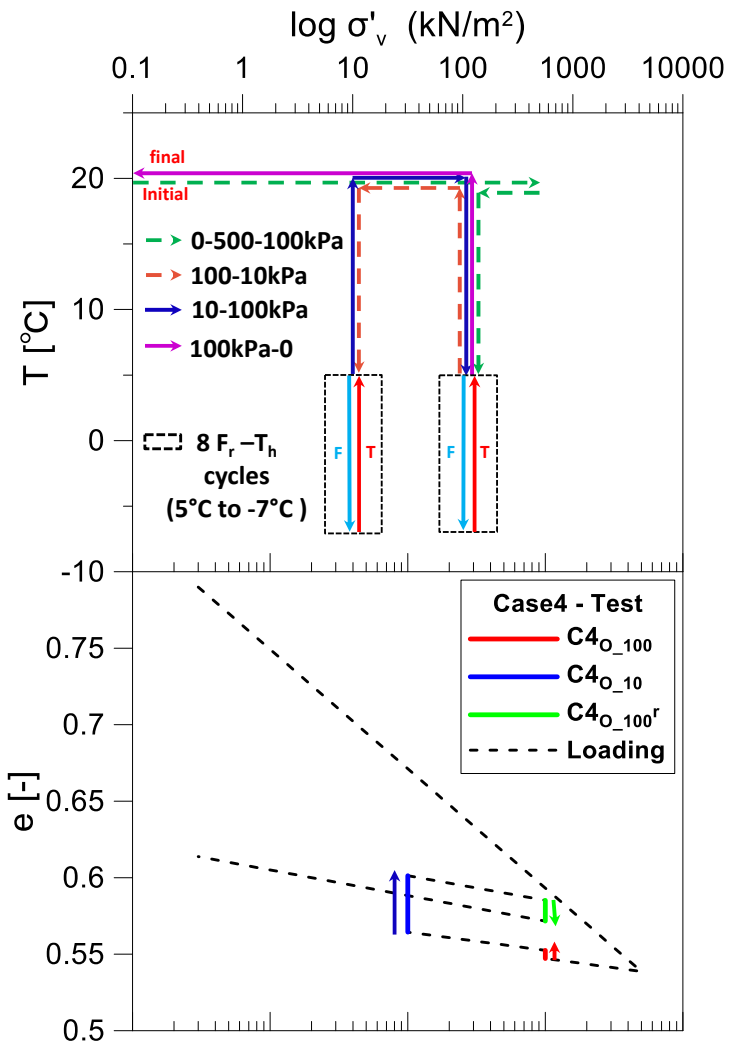

Figure 2.9 Generalized σ'_v -T paths and the associated void ratio changes for Case 4

In Case 4 (Figure 2.9), the first series of *Fr-Th* cycles were applied under *OC* conditions, after loading the sample up to σ'_v=500kPa (in the same cell but in an odometer outside the chamber) and unloading it at σ'_v=100kPa. The sample expanded after this thermal cycle ($C4_{O\_100}$). Then, the sample was unloaded again to 10kPa and exhibited a larger expansion ($C4_{O\_10}$) after applying *Fr-Th* cycles at σ'_v=10kPa. Afterwards, the specimen was reloaded and subjected to the last series of

Fr-Th cycles under σ'_v=100kPa. The soil developed another compression ($C4_{O\_100}^{r}$) under this *OC* state.

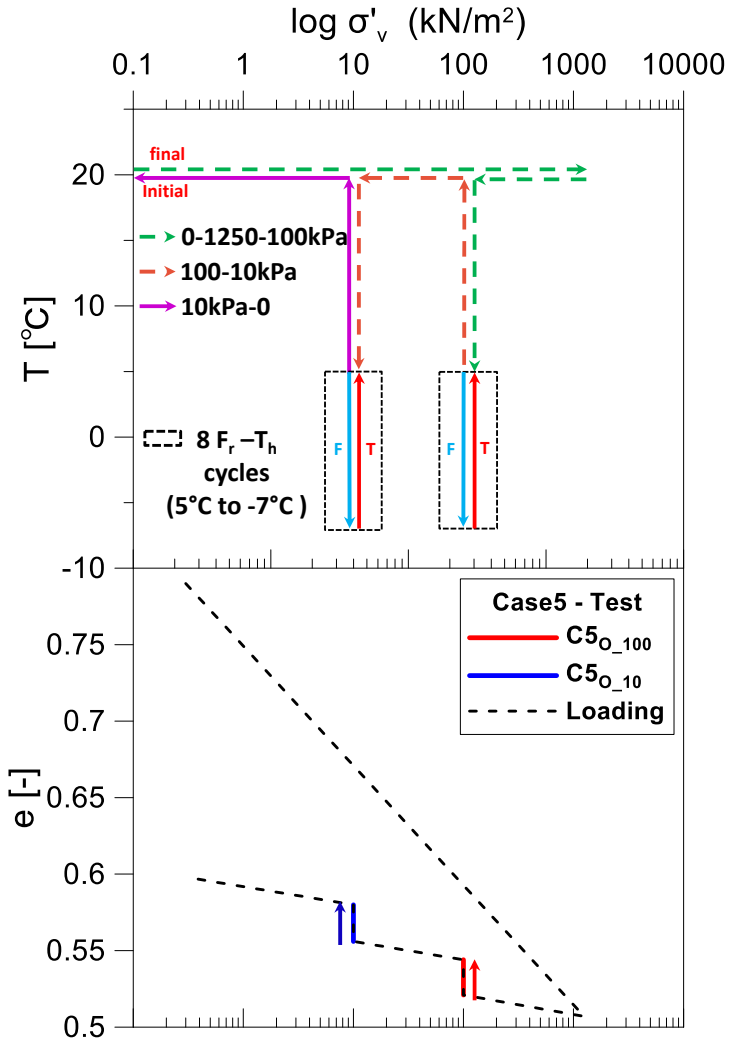

Figure 2.10 Generalized σ'_v -T paths and the associated void ratio changes for Case 5

In Case 5 (Figure 2.10), the first series of *Fr-Th* cycles were applied under *OC* conditions, after loading the sample up to σ'_v=1250kPa (in the same cell but in an odometer outside the chamber) and unloading it at σ'_v=100kPa. The sample expanded after this thermal cycle ($C5_{O\_100}$).

Then sample was unloaded again to lower σ'_v=10kPa, it showed a similar expansion ($C5_{O\_10}$) as expected.

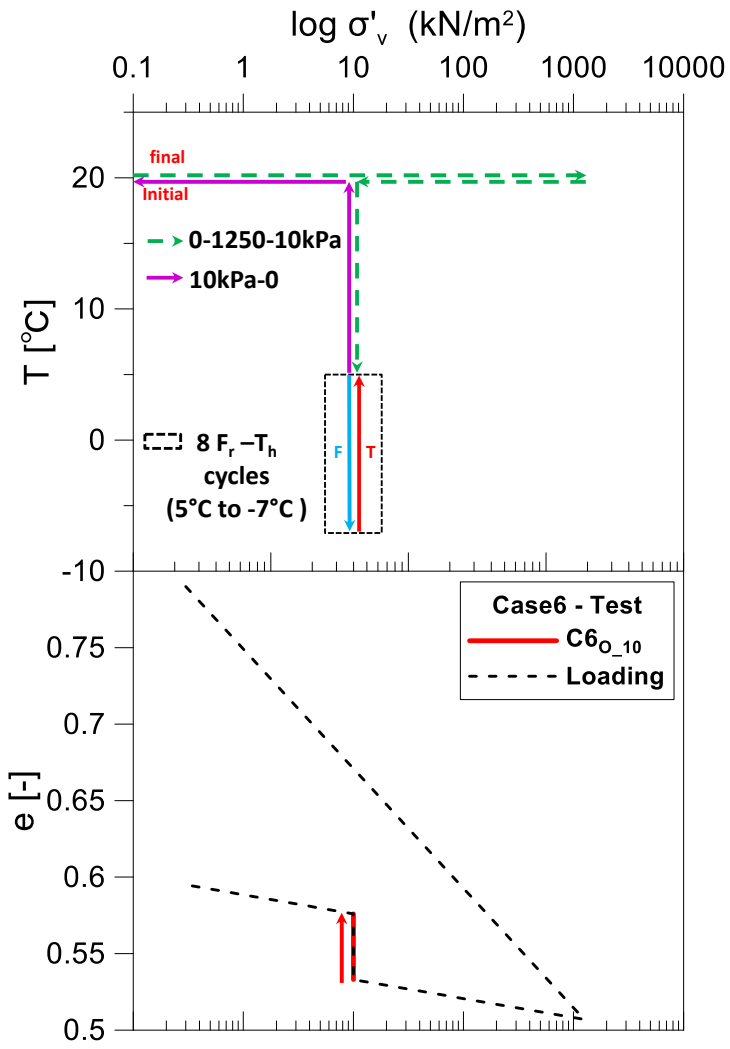

Figure 2.11 Generalized σ'_v -T paths and the associated void ratio changes for Case 6

In Case 6 (Figure 2.11), the first series of *Fr-Th* cycles were applied under *OC* conditions, after loading the sample up to σ'_v=1250kPa (in the same cell but in an odometer outside the

chamber) and unloading it at σ'_v=10kPa. The sample largely expanded after this thermal cycle ($C6_{O\_10}$).

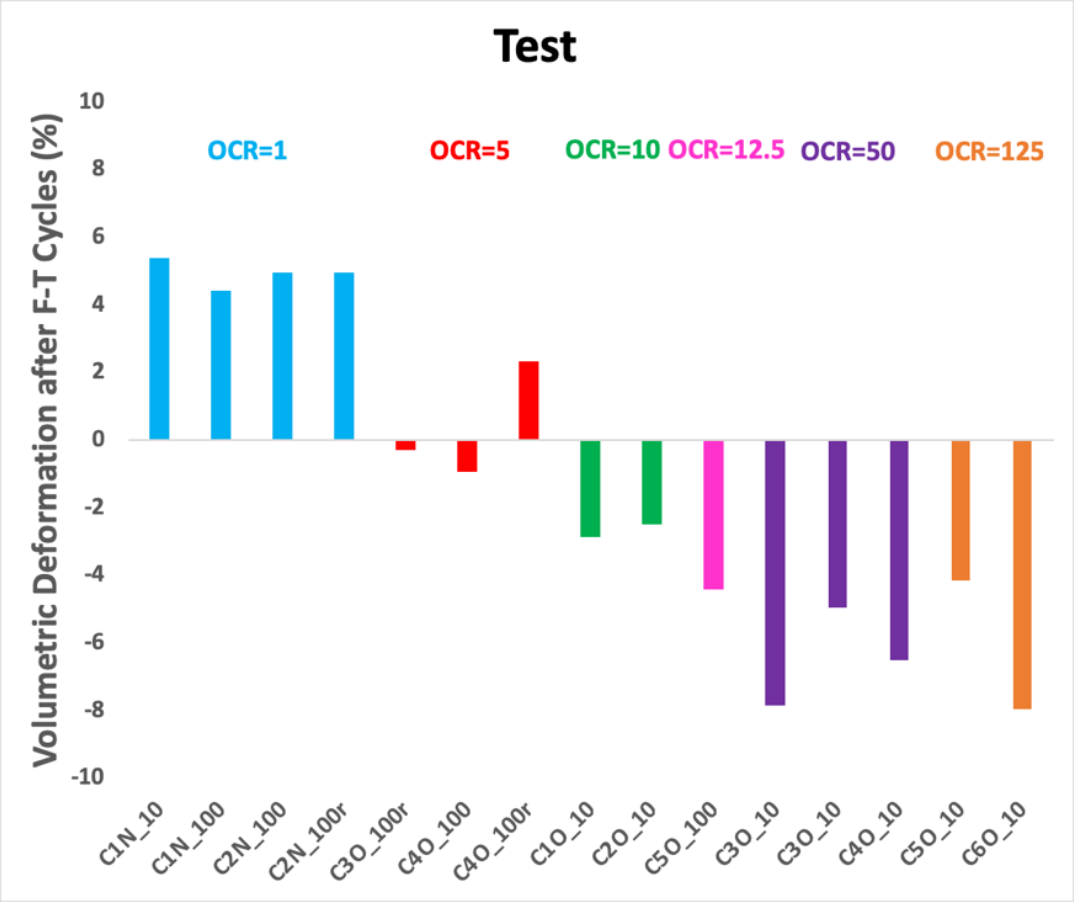

Figure 2.12 Void ratio change vs. OCR for all Cases

Figure 2.12 summarizes the results related to the different cases in terms of the volume changes induced by the *Fr-Th* cycles versus the specimens *OCRs*. The volume change was calculated as $\Delta e/(1+e_b)$x100, where e_b is the void ratio just before the *Fr-Th* cycle, and Δe is the associated *e* variation. *NC* soils subjected to *Fr-Th* cycles tend to accumulate plastic strains with a net contraction of the soil after the cycles, trend that slightly decreases with the stress level. As for

OC soils, all of them showed a tendency to expand, which increases with the soil *OCR*. Based on these tests, it also appears that samples with the same *OCR*, but with a previous history of *Fr-Th* tend to expand less. OCRs higher than 80 has been reported (e.g. Mayne, 2001).

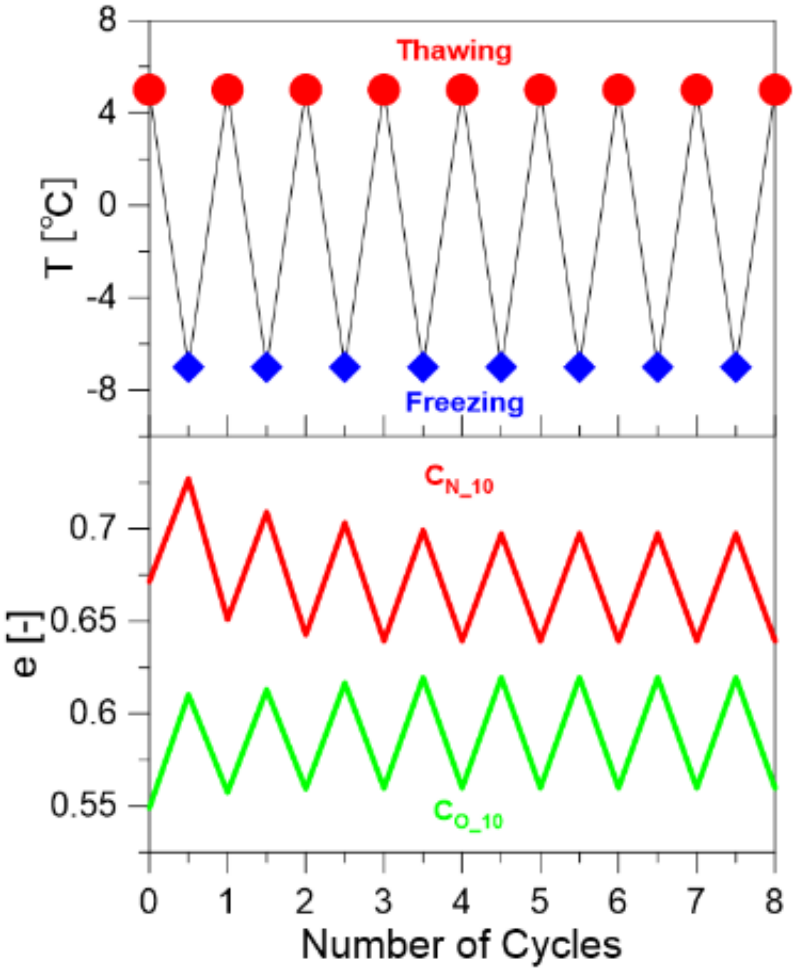

Figure 2.13 Typical responses of NC and OC specimens under Fr-Th cycles

Figure 2.14 and Figure 2.15 illustrate the possible effect of *Fr-Th* cycles on saturated *NC* and *OC* soils, respectively. To support the discussions, typical results from *Fr-Th* cycles conducted on *NC* (i.e. $C1_{N\_10}$) and *OC* (i.e. $C1_{O\_10}$) soils are presented in Figure 2.13. For the case of loose

(*NC*) soils (Figure 2.14), the soil structure after freezing is more open, because the volume expansion associated with the water phase transformation induces a global volume expansion of the material (ΔV_{Fr}), as observed at the end of the $C1_{N\_10}$ first freezing (Figure 2.13). Depending on the subzero temperature, different amounts of unfrozen water (which is mainly located at the contact between grains) can be present in the soil sample. Upon thawing, when ice turns into liquid-water, this very open soil structure collapses leading to a volume reduction (ΔV_{Th}) and a more compact soil. This rearrangement of grains results in a soil that (at the end of the 1st *Fr-Th* cycle) is slightly denser than the one before the initial freezing, as shown in Figure 2.13 ($C1_{N\_10}$), leading to a net volumetric plastic strain (i.e. $\Delta V_{Fr}<\Delta V_{Th}$ in Figure 2.14). Permanent volume deformations (compression) occur during the 2nd *Fr-Th* sequence, but they are less pronounced because the soil is slightly denser at the beginning of this cycle. This behavior repeats in subsequent cycles, with decreasing plastic strains after each cycle, and a trend to achieve equilibrium between ΔV_{Fr} and ΔV_{Th} after a number of *Fr-Th* series.

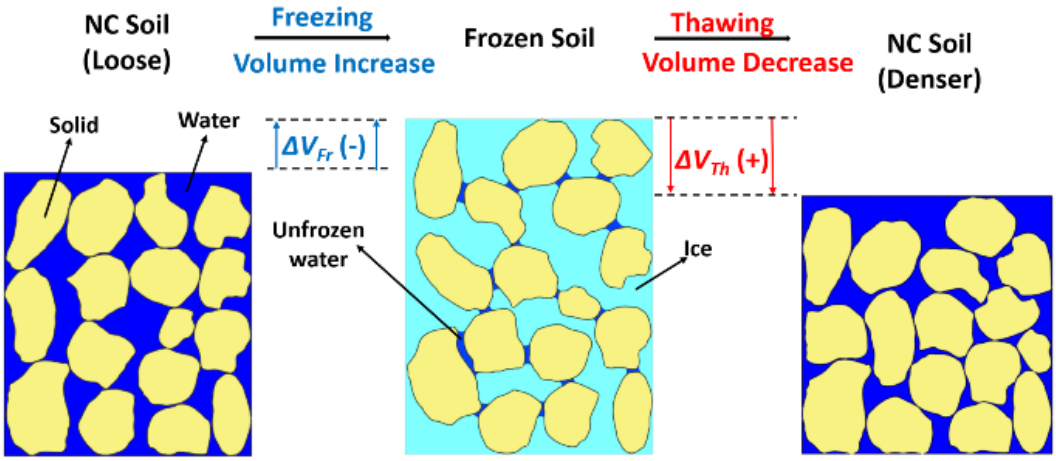

Figure 2.14 Schematic representation of volume changes during Fr-Th cycles for NC soil

As for the case of dense (*OC*) soils (Figure 2.15), they also tend to expand upon the 1st *Fr*. However, the re-arrangement of soil particles during the subsequent *Th* is not effective enough to recover the dense initial structure, leading to a net permanent volumetric expansion, with a soil that is looser than the initial one (i.e. Figure 2.13, $C1_{O\_10}$), exhibiting a net plastic volumetric strain (expansion) at the end of the 1st *Fr-Th* cycle (i.e. $\Delta V_{Fr} > \Delta V_{Th}$, Figure 2.15). In the following *Fr-Th* sequence, additional plastic strains accumulate, but the changes are less pronounced, because the soil in the 2nd cycle is looser than the one before the 1st *Fr*. This soil response repeats in subsequent cycles, with a trend to achieve an equilibrium between ΔV_{Fr} and ΔV_{Th} after a number of *Fr-Th* cycles. In summary, *Fr-Th* cycles on relatively loose saturated soils induce a rearrange of its structure with a final densification of the material, while the disruption induced by the *Fr* in a dense *OC* soils (i.e. soil expansion), is not recovered during *Th*, leading to a net volume increase, and a looser soil.

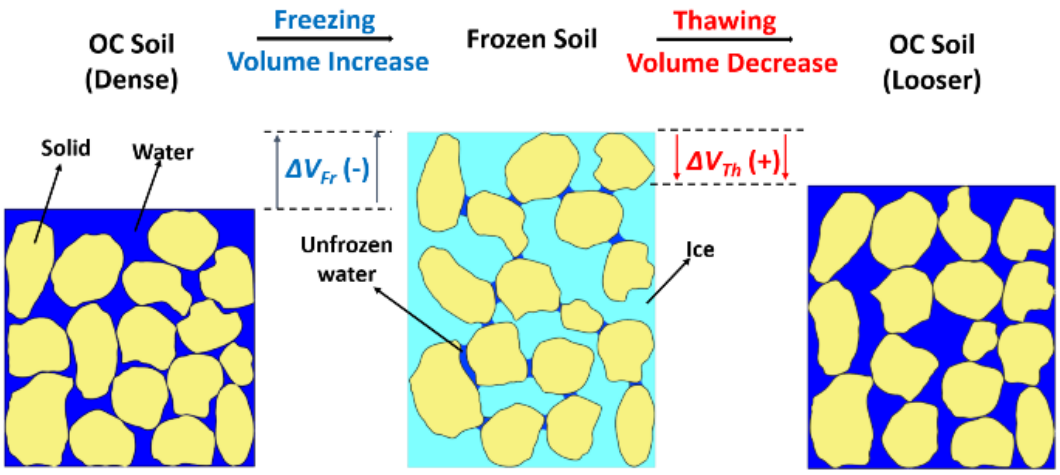

Figure 2.15 Schematic representation of volume changes during Fr-Th cycles for OC soil

2.2.3 Effect of temperature range during Fr-Th cycles on soil behavior

Four additional tests were conducted to investigate the potential effects of the temperature range on soils volume change subjected to *Fr-Th* cycles. Temperature variations between -0.3°C and 5°C where applied to *NC* specimens under σ'_v=10kPa (i.e. like $C1_{N\_100}$) and *OC* samples under the same σ'_v but previously loaded up to σ'_v=500kPa (i.e. like $C3_{O\_10}$). A similar protocol was followed to other two specimens subjected to temperature changes between -20°C and 5°C. In all the cases a maximum of 8 *Fr-Th* cycles were applied. The main results are presented in Figure 2.16. It is observed that for the two states (i.e. *NC* and *OC*) the sequence -0.3°C to 5°C induces less volume changes than the reference one (i.e. -7°C to 5°C), also there are practically no differences between the series -20°C to 5°C and the reference one.

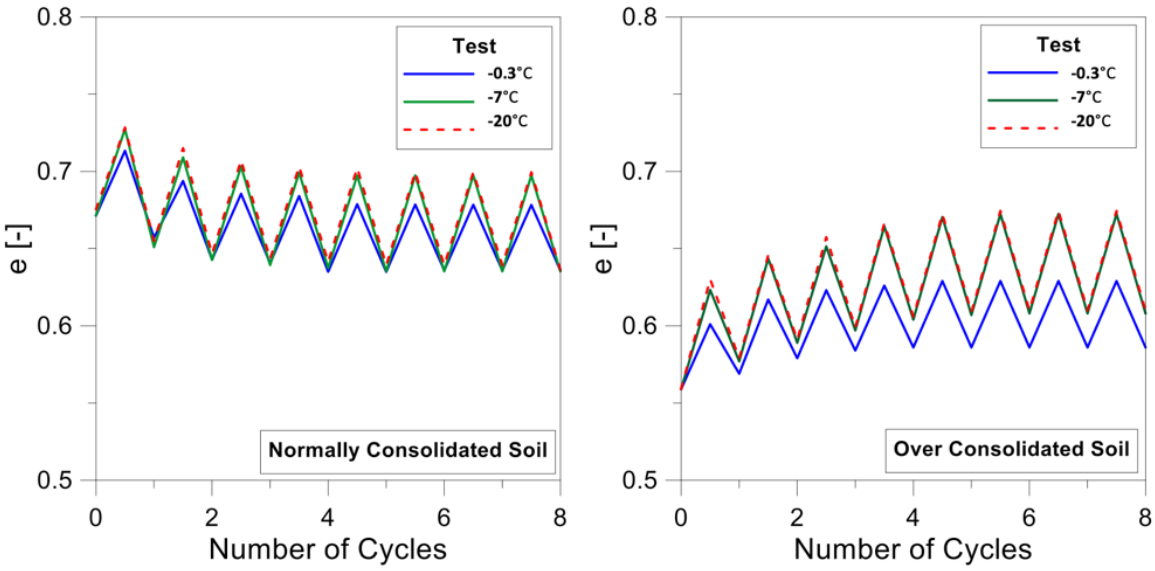

Figure 2.16 Effect of temperature range during Fr-Th cycles on soil behavior

2.2.4 Unfrozen water in frozen soils

The amount of unfrozen-water in frozen soils depends on the freezing temperature. The soil unfrozen-water retention curve (SUWRC) relates cryogenic suction (or subzero temperature) with unfrozen-water content (or with unfrozen-water degree of saturation, S_{luw}). The determination of the unfrozen-water retention curve is very relevant because of the impact of unfrozen water-content on mechanical and hydraulic properties of frozen soils (e.g. Black & Miller 1990; Xu et al., 2016; Watanabe & Osada, 2017). Its determination is also important because it indicates the amount of water involved in the liquid-ice water phase change and its influence on the associated volume change. Mao et al. (2018) investigated electrical conductivity (*EC*) of frozen soils to estimate the amount of unfrozen-water.

Figure 2.17 LandMapper ERM-02

LandMapper ERM-02 was selected in this preliminary research to measure the *EC* of the silty soil. It is a four-electrode portable device, easy to calibrate and use. (Figure 2.17). The *EC* was measured in specimens prepared as the one used in the mechanical tests described above. The

samples were subjected at different subzero temperatures (inside the environmental chamber) under the plunger contact pressure. Figure 2.18a) shows the measured values of *EC* at different temperatures. Based on the Archie's law (1942), the unfrozen-water degree of saturation was estimated by Mao et al. (2018): $S_{luw} = \frac{EC_s \times n^{-p} \times S_r^{-q}}{EC_w}$; where EC_s and EC_w are the electrical conductivities of the frozen soil and interstitial liquid, respectively; n is the porosity; p is an exponent related to soil structure; S_r is the initial liquid degree saturation of the soil (S_r=1 in this case), and q is an exponent associated with S_r. According the Mao et al. (2018), q~2.0 and 1.4<p< 2.0 (q=2.0 and p=1.7 was assumed in Figure 2.18b) for SUWRC). The freezing point of the interstitial liquid is around 0°C and the amount of unfrozen water content decreased sharply as the temperature decreases. For temperature below -2°C, S_{luw} remains almost stable and very low. This behavior explains that no noticeable differences, in terms of volume changes are observed between samples subjected to *Fr-Th* cycles with temperature variations 5°C to -7°C and 5°C to -20°C (i.e. similar S_{luw}); and slight differences are observed with respect to the sample tested in the range 5°C to -0.3°C.

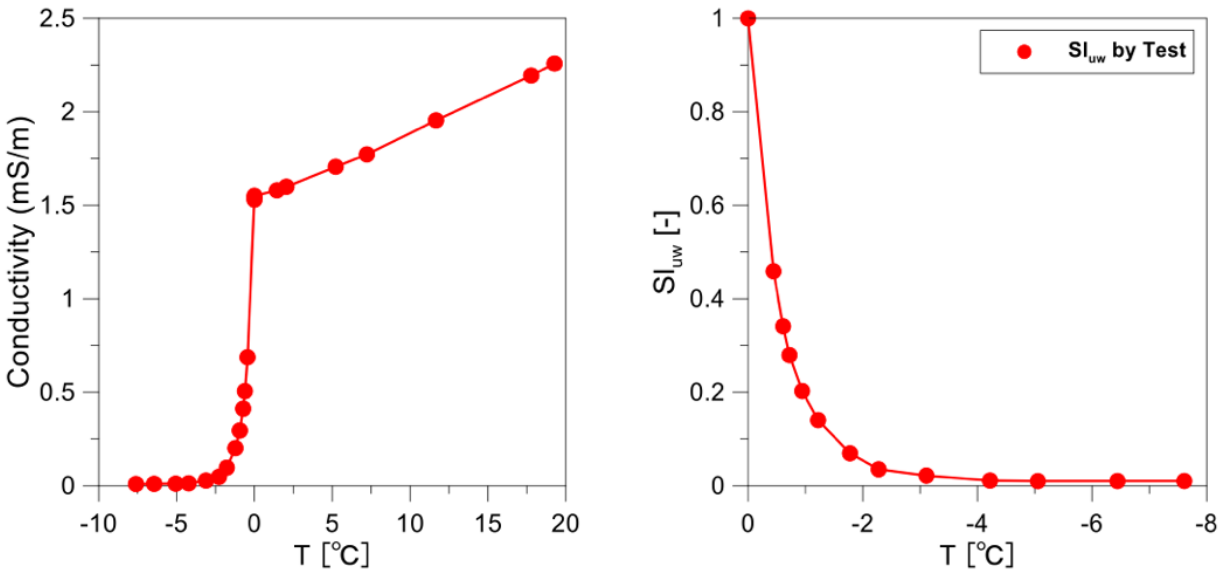

Figure 2.18 a) EC of frozen soil, and b) SUWRC

2.2.5 Collapse tests of frozen soil

Two collapse tests with freezing temperature of -5℃ were performed, the results are shown in Figure 2.19. From the results, firstly, it can be observed that the slope of consolidation curve under subzero temperature (-5℃) and room temperature (20℃) are different. This is because the stiffness of soil sample is changed due to the formation of ice, which has been studied by some former researchers, (e.g. Qi et al., 2010). Also, it can be seen that the void ratio after collapse is a little lower than that got from room temperature consolidation, this may because the soil got contractive rearrangement in the freeze-thaw process like mentioned in the former part, and the more creep due to thawing may give another explanation for this. Besides, From Figure a, the slope of reloading line after collapse has almost the same slope of that from room temperature consolidation, which is consistent with that shown in the loading path figure of cyclic freezing-thawing tests.

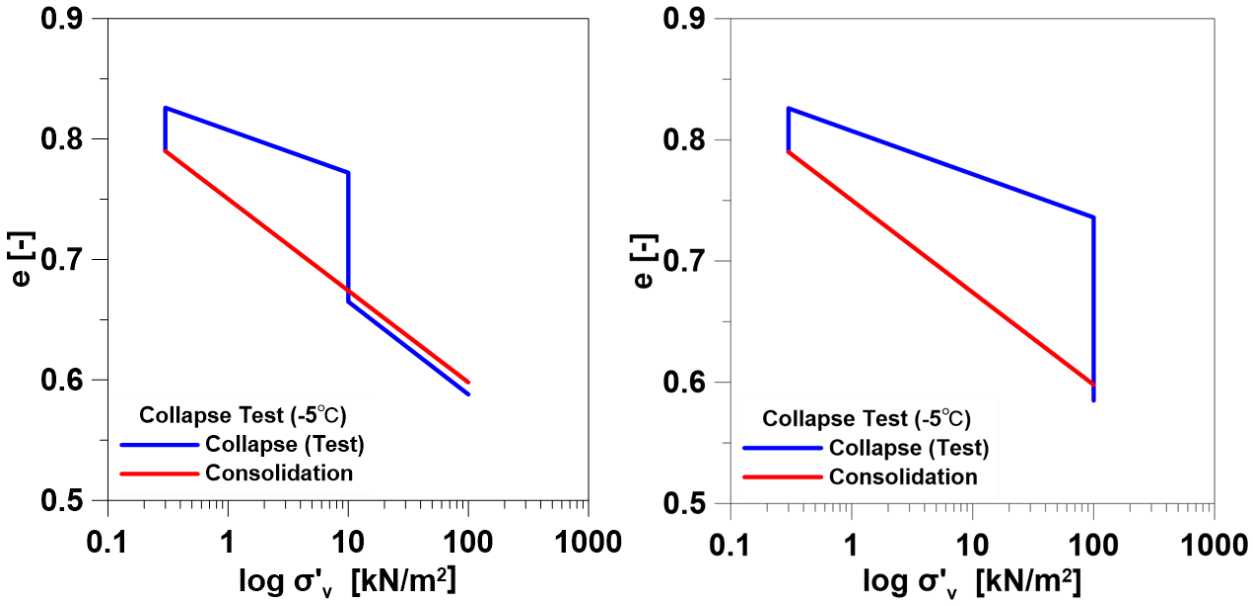

a) b)

Figure 2.19 Collapse tests of frozen soil

2.3 Mechanical model for soil subjected to cyclic freezing-thawing

2.3.1 Model description

The modeling activities have been focused on developing a constitutive model for soils subjected to freezing-thawing cycles and its validation against the experimental data generated in this research. This model incorporated Barcelona Basic Model (BBM) and double structure plasticity model (Sanchez et al., 2005). BBM was stated by Alonso, Gen and Josa in 1990, it was developed from Cam Clay Model to capture unsaturated soil behavior with linking mean stress (p), deviatoric stress (q) and suction (S), elastic domain is changing with a changing in suction value. As shown in Figure 2.20, p_0^* is pre-consolidation pressure and p_0^* is current mean stress. This model is constructed with yield surface, flow rule, hardening law, yield curve (LC) and more detailed explanations can be found in Appendix A.

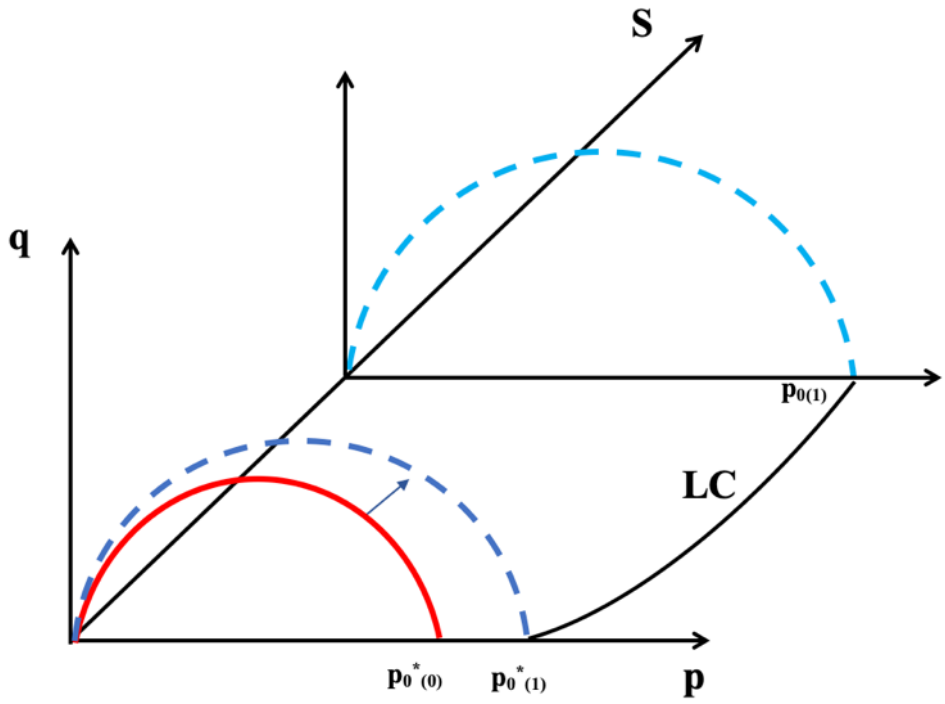

Figure 2.20 Barcelona basic model

BBM was extended from unsaturated soil to frozen soil firstly by Nishimura et al. in 2009. When soil is fully saturated before freezing, air can be totally replaced by ice when frozen. Matric suction (difference between air pressure and liquid pressure, p_a-p_l) in BBM can be replaced by cryogenic suction (difference between ice pressure and liquid pressure, p_i-p_l).

Besides, Gens and Alonso (1992) proposed a general framework to model this type of soil behavior that incorporates the interactions between the expansion of the clay minerals during wetting and the global arrangement of the clay-aggregates, which conforms the 'soil-skeleton' (i.e. the soil 'macrostructure'). This coupling between the expansive clay-minerals and the soil-skeleton is defined through 'interactions functions' (*f)* that allow modeling the interplay between these two phenomena (i.e. clays mineral expansion and global re-arrangement of the soil-skeleton).

The interaction functions depend on the degree of openness of the macrostructure (Sanchez et al., 2005), which can be measured by the ratio between the current stress level and the pre-consolidation pressure (i.e. OCR). This constitutive model has been formulated in the formal framework of plasticity for strain hardening materials, and it has been applied with success to model the cyclic behavior of expansive clays subjected to drying and wetting processes and other solicitations (e.g. Sanchez et al., 2005, Sanchez et al., 2012). Since the response of frozen soils subjected to *Fr-Th* cycles resembles the behavior observed in expansive soils under drying-wetting paths, this frame work (double structure theory) was also adopted in the modeling work accounting for hardening rule in extended BBM model.

In frozen soils, the interaction is between the volume changes associated with the water-phase-transformations and the soil-skeleton. In this preliminary study the model formulated by Sanchez et al. (2005) has been adapted for frozen soils and used to model the tests discussed above. It is assumed that the volumetric strain associated with the water-phase transformations are reversible. However, this phenomenon may induce a rearrangement of the soil-skeleton that could lead to permanent deformations. The ice reversible strains can be calculated as Eq. 2.1.

$$\varepsilon_{vi}^{\dot{e}} = (1 - Sluw) \times n \times \eta \qquad \text{(Eq. 2.1)}$$

where n is the porosity and η is the coefficient associated with the water-volume-change during phase transformation (typically η=0.09). Saturation degree of unfrozen water content is equal to 1-S_i and can be determined based on Tice Model (Tice et al., 1976) displayed in Eq. 2.2 and verified on unfrozen water content measurements tests in this research. The plastic volumetric strains of the soil-skeleton (*ss*) induced by the ice formation/thawing is calculated as Eq. 2.3.

$$S_i = \begin{cases} 1-[1-(T-T_0)]^{\alpha} & T \le T_0 \\ 0 & T > T_0 \end{cases} \quad \text{(Eq. 2.2)}$$

$$\varepsilon_{vSS}^{\dot{p}} = f \times \varepsilon_{vi}^{\dot{e}} \quad \text{(Eq. 2.3)}$$

where *f* depends on the ratio between the current stress level 'p' and the pre-consolidation pressure 'p_0'. The interaction functions for freezing ('1 to 4', Figure 2.21) and thawing ('5 to 8' Figure 2.21) are inferred from experiments (Sanchez et al., 2005). Interaction functions during cyclic freezing-thawing process were calculated separately as Eq. 2.4.

$$f_{freezing} = ff1 + ff2 \times \tanh(ff3 \times (p/p_0) - ff4)$$
$$f_{thawing} = ft1 + ft2 \times \tanh(ft3 \times (p/p_0) - ft4) \quad \text{(Eq. 2.4)}$$

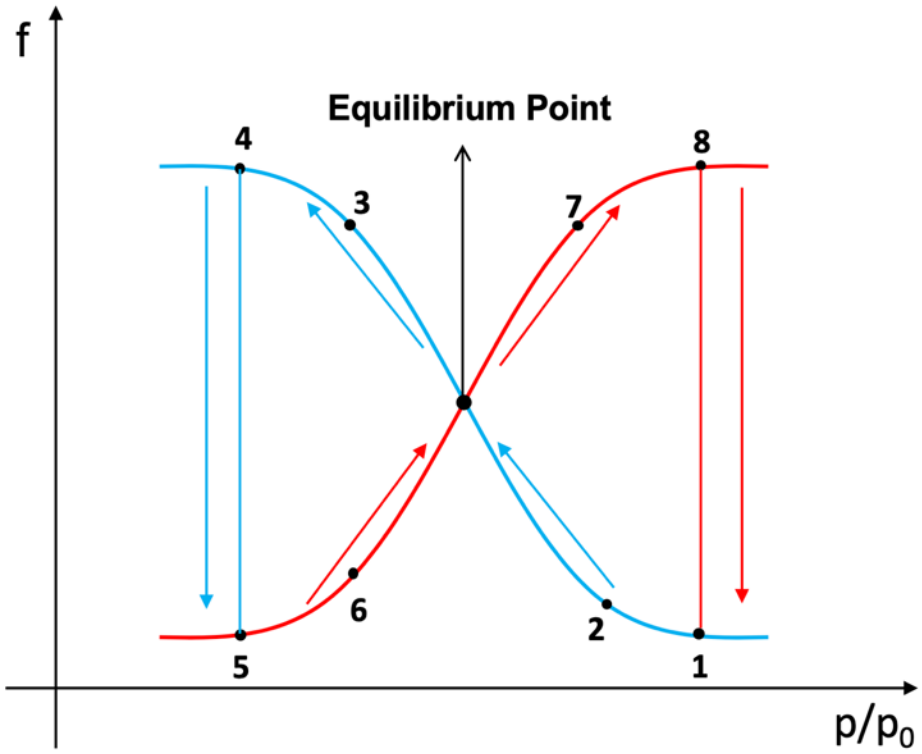

Figure 2.21 Interaction function

In freezing process, p_0 is increasing, which makes the ratio p/p_o of getting smaller, point is moving along the blue freezing curve (i.e. 1 to 4) in arrowed direction, in thawing, the ratio p/p_o is increasing, point is moving along the red curve (i.e. 5 to 8) in arrowed direction. After cycles, the plastic strain accumulated in freezing is equal to that in thawing, then the point will stop moving and converge to the point in the middle (Equilibrium Point (EP)) or moves near the EP, consistently, the volume change in freezing and thawing are the same, achieving the stable state.

It is anticipated that a freezing at high OCR (i.e. low p/p_o, e.g. point 4 in Figure 2.21) will disrupt more the soil-skeleton than a freezing at high stress level (i.e. high p/p_o, e.g. point 1 in Figure 2.21). More details can be demonstrated in Figure 2.22. Therefore, the interaction function for freezing has higher values at high OCR than at low OCR.

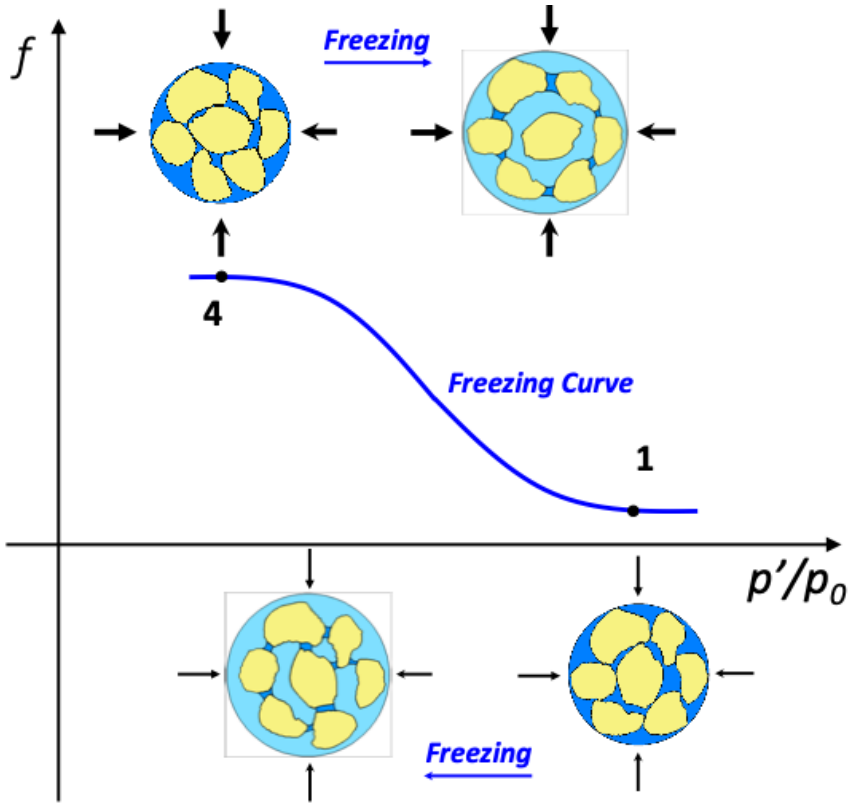

Figure 2.22 Freezing interaction function

An analogous reasoning can be done for a thawing process. A thawing at high OCR (i.e. low p/p_o, e.g. point 5 in Figure 2.21) will close the soil-skeleton less than a thawing at high stress level (i.e. high p/p_o, e.g. point 8 in Figure 2.21). More details can be demonstrated in Figure 2.23. Therefore, the interaction function for thawing has higher values at low OCR than at high OCR. It is assumed that $\varepsilon_{vss}^{\dot{p}}$ will affect the hardening variable of the model adopted for the soil-skeleton, e.g. the modified Cam Clay model (Sanchez et al., 2005).

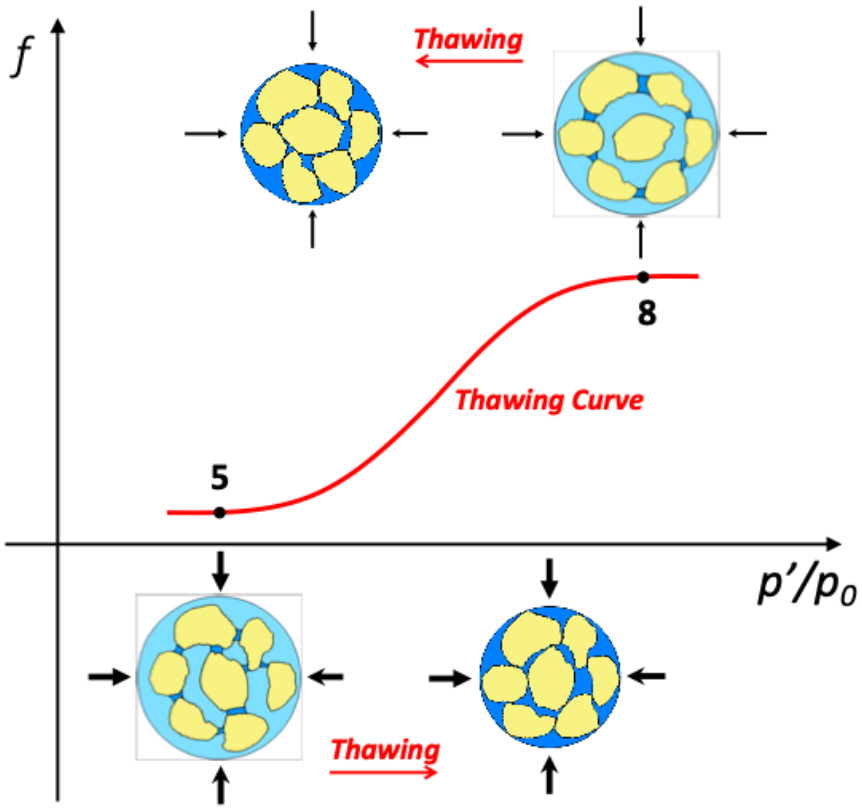

Figure 2.23 Thawing interaction function

In this research, modified BBM (Shastri and Sanchez, 2012) was used with new defined net stress σ_n and cryogenic S_c (Eq.2.5).

$$\sigma_n = \sigma - \max(P_i, P_l, 0)$$

$$S_c = \max(P_i - P_l, 0) \qquad \text{(Eq. 2.5)}$$

Where σ is the mean stress, σ_n is the net stress.

The hardening law is expressed as Eq. 2.6 and the LC curve function is as Eq. 2.7. How the parameter λ_s evolves with suction is obtained in Eq. 2.8.

$$dp_0^* = \frac{1+e}{\lambda_0 - \kappa} \times p_0^* \times d\varepsilon_v^p \quad \text{(Eq. 2.6)}$$

$$p_0 = p^c \left(\frac{p_0^*}{p^c} \right)^{\frac{\lambda_0 - \kappa}{\lambda_s - \kappa}} \quad \text{(Eq. 2.7)}$$

$$\lambda_s = \lambda_0 [r + (1-r)\exp(-\beta s)] \quad \text{(Eq. 2.8)}$$

The volume increment of soil sample during the freezing process will decrease the elastic domain of the soil, and as a result of this, the LC curve will move to the left. Consequently, p_0^* will decrease in freezing process. As for thawing process, elastic domain will increase because of the decreasing of volume, and LC curve will move to right side. Consequently, p_0^* will increase. The movement of LC curve is shown in Figure 2.24.

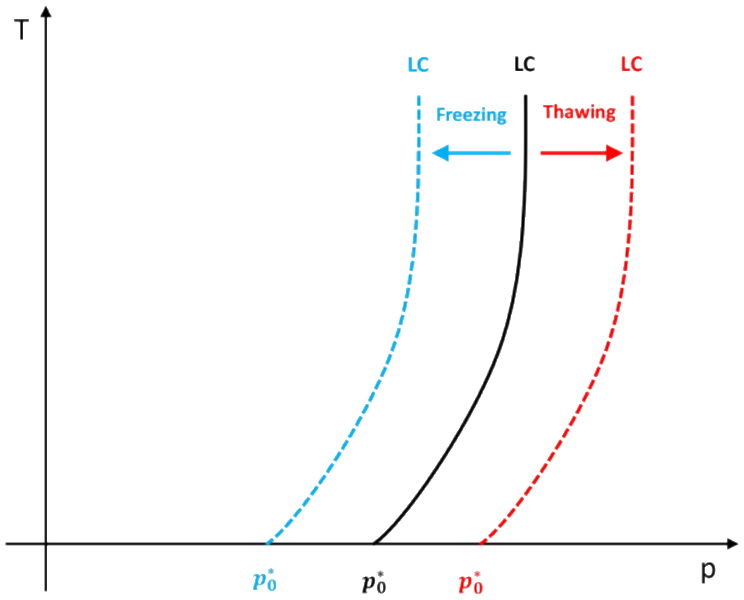

Figure 2.24 Movement of LC curve

If show this in 3D view, as for freezing process (Figure 2.25), elastic domain decreases (red solid arc to red dash arc), make pre-consolidation pressure decrease from $p_0^*{}_{(0)}$ to $p_0^*{}_{(1)}$. Due to suction effects, stress state point moves along the LC to current state $p_{0(1)}$ on blue solid arc. As for thawing (Figure 2.26), elastic domain increases (blue solid arc to blue dash arc), make current stress state point move from $p_{0(1)}$ to $p_{0(2)}$. Due to suction effects, stress state point moves along the LC to $p_0^*{}_{(2)}$ on red solid arc.

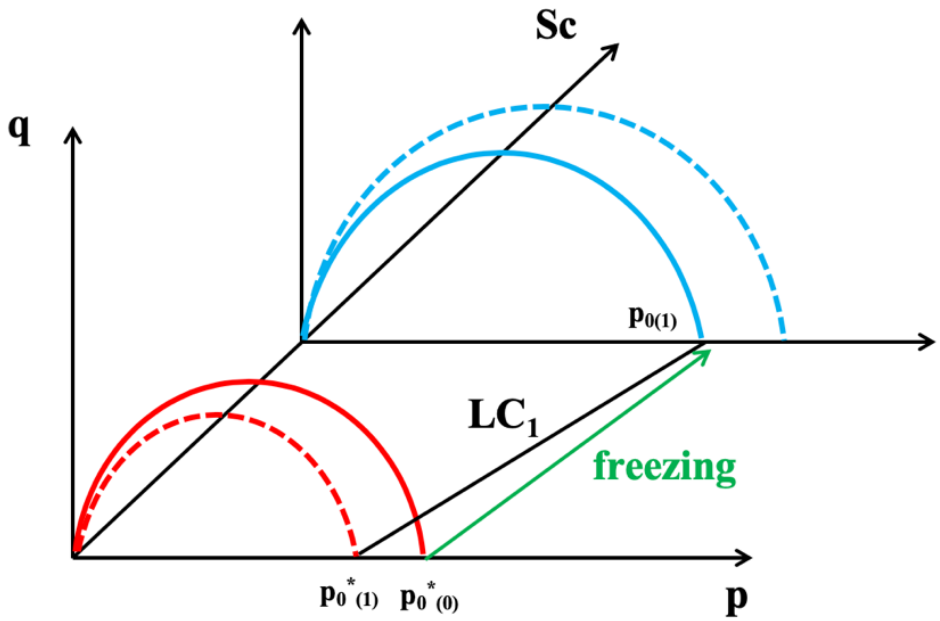

Figure 2.25 3D model demonstration for freezing

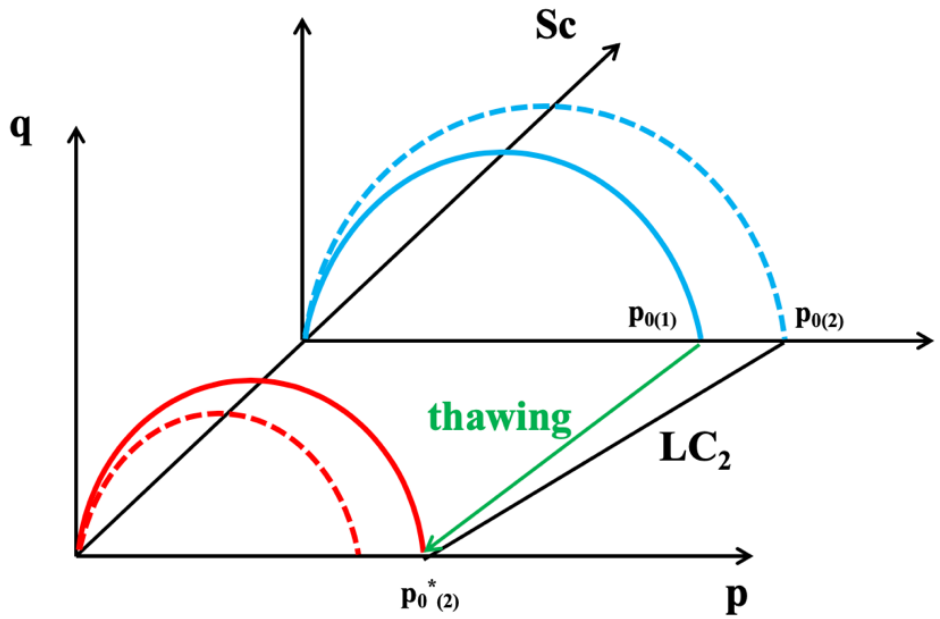

Figure 2.26 3D model demonstration for thawing

In order to clarify the effects of LC curve movement on pre-consolidation pressure under different temperatures, $C1_{N\_10}$ is employed to show that in detail (See Figure 2.27). For this step, the initial LC curve under room temperature (20℃) is shown in red, and the final LC curve after freezing under -7℃ is shown in blue. We can find that the LC moves to the left during freezing as we discussed above.

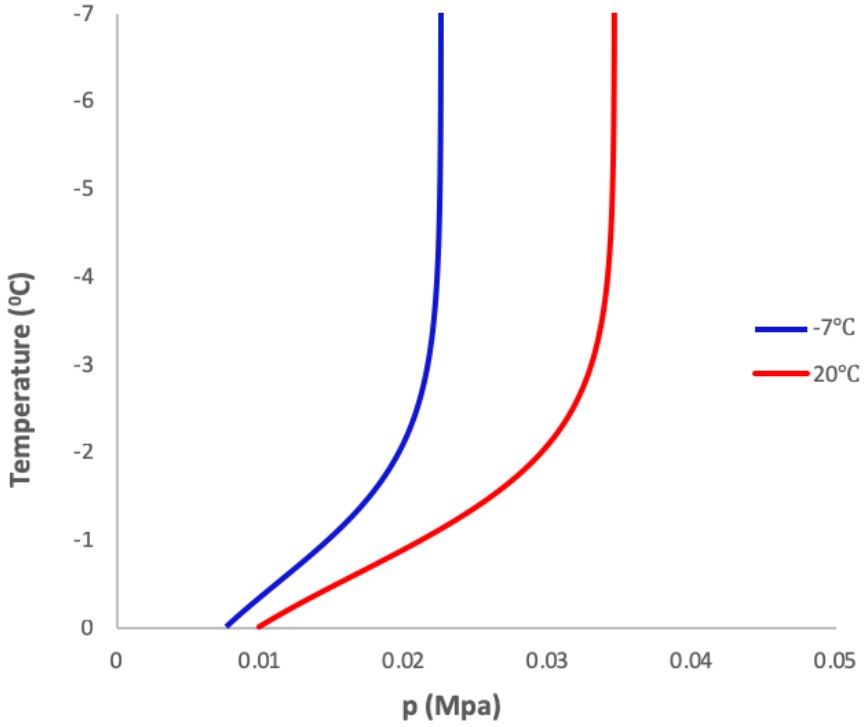

Figure 2.27 LC movement in Case1 freezing

For pre-consolidation pressure changes, five simple tests with pre-consolidation pressure 10kPa under 20℃ was taken to illustrate. Soil samples were frozen to 0℃, -1℃, -4℃, -7℃, -10℃ respectively, then load the sample from 0Mpa to 100Mpa (see Figure 2.28a)). Pre-consolidation pressures by model for different temperatures can also be obtained by the model. Comparison by

tests and model can be shown in Figure 2.28b) below, can we can see that the model can basically capture the change of pre-consolidation pressure with freezing temperature decreasing in a reasonable range. When temperature goes below -4, the change in pre-consolidation is very small this is because the amount of unfrozen water is reaching a stable value.

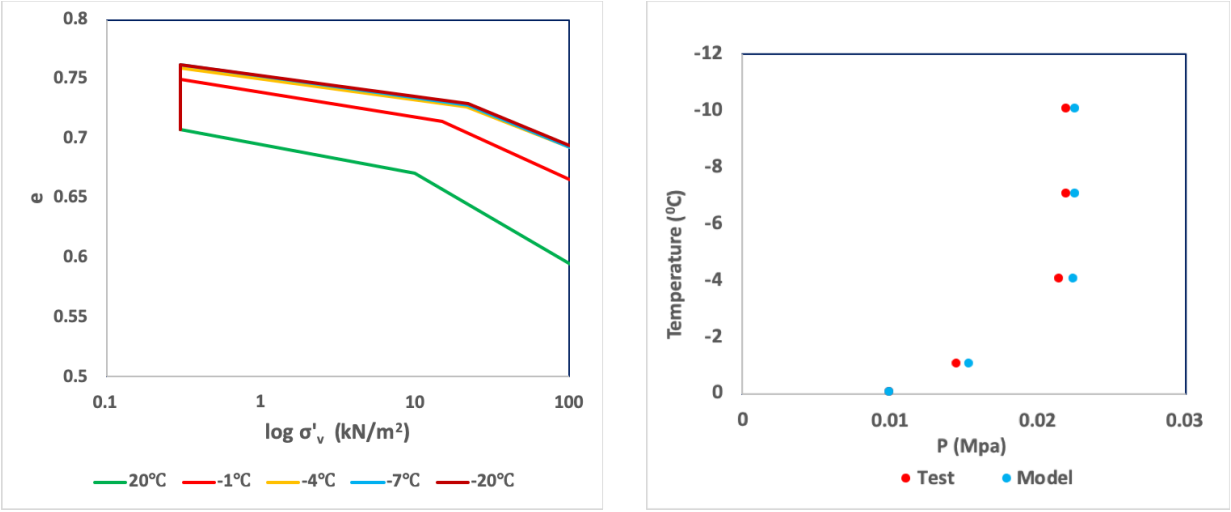

a) b)

Figure 2.28 Pre-consolidation pressure during freezing by test and model for Case1

2.3.2 Model validation and discussion on effect of stress history and Fr-Th cycles

Figure 2.29 to Figure 2.34 are showing the simulation results from Case 1 to Case 6 on volumetric behavior of the tested soil subjected to different stress histories and Fr-Th cycles by the mechanical proposed. Here just adopt Case 1 for introduction and the rest are the same. The left two graphs are the same as shown in the test part and right top one is showing the process of freezing and thawing the right bottom one is the results of model simulation together with the initial test results with all the steps in all the cases.

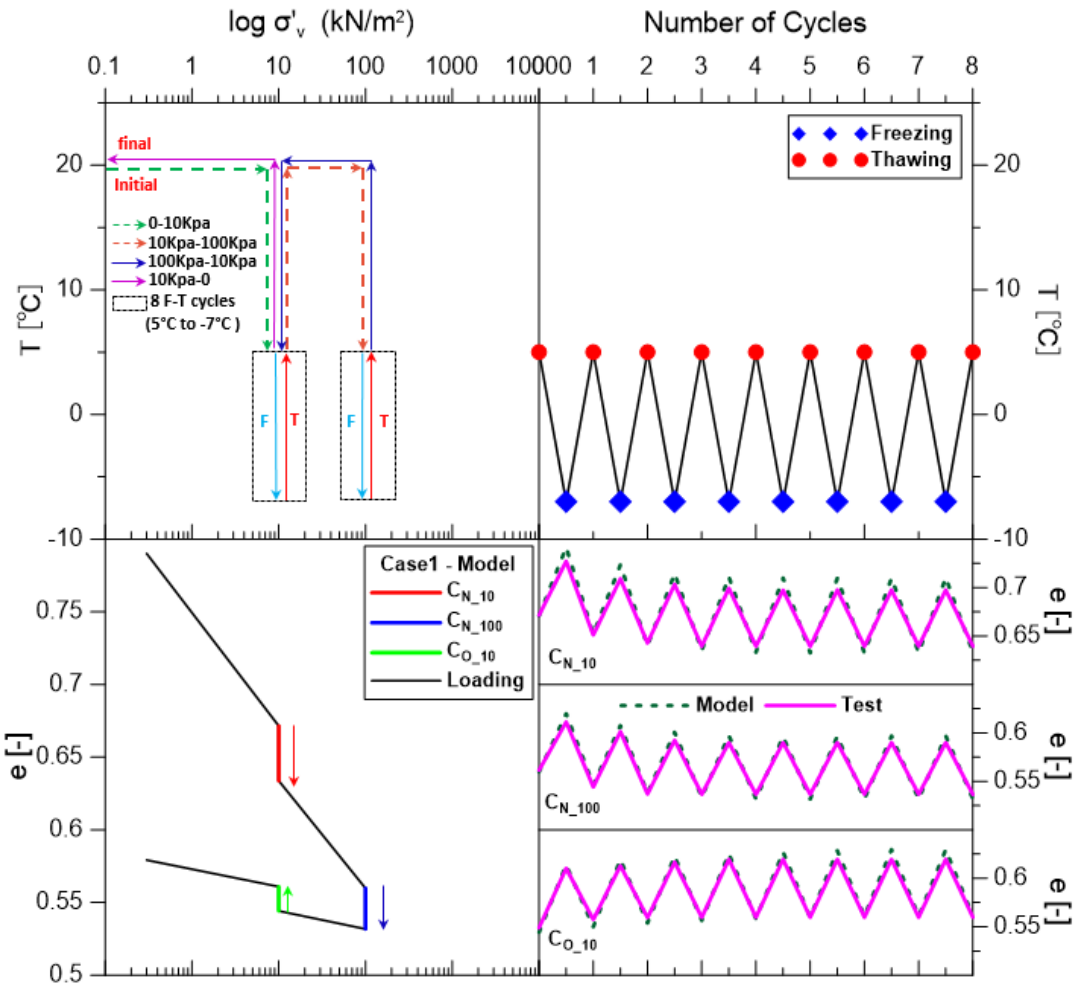

Figure 2.29 Experimental and modeling related to Case 1

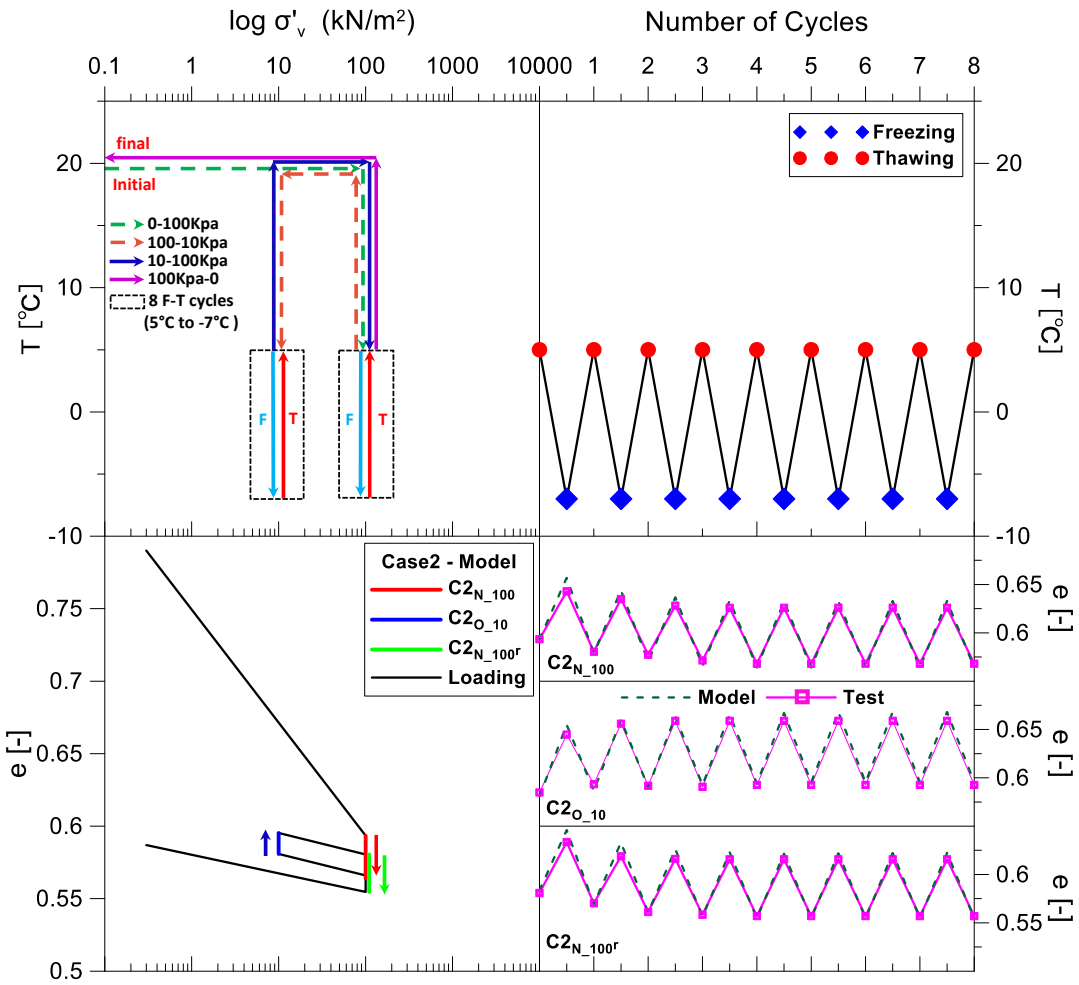

Figure 2.30 Experimental and modeling related to Case 2

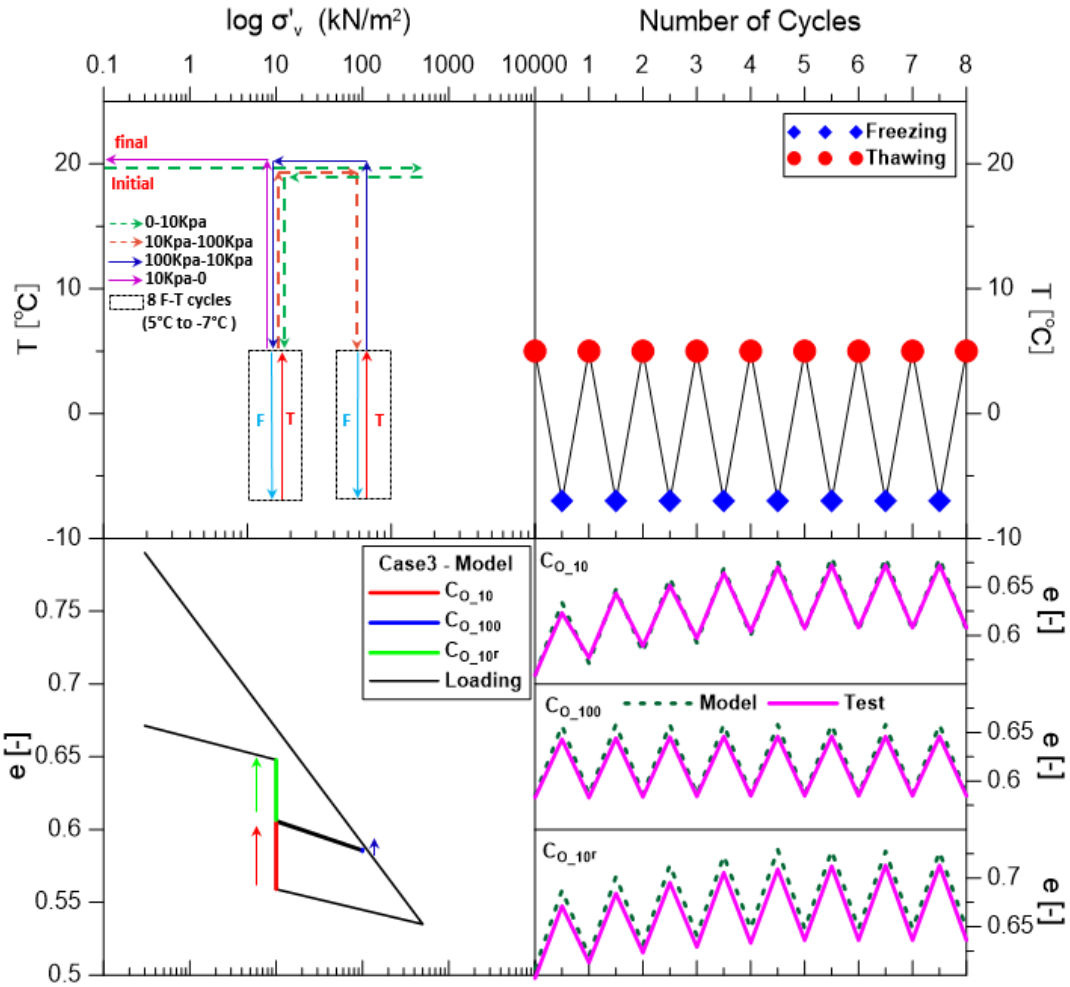

Figure 2.31 Experimental and modeling related to Case 3

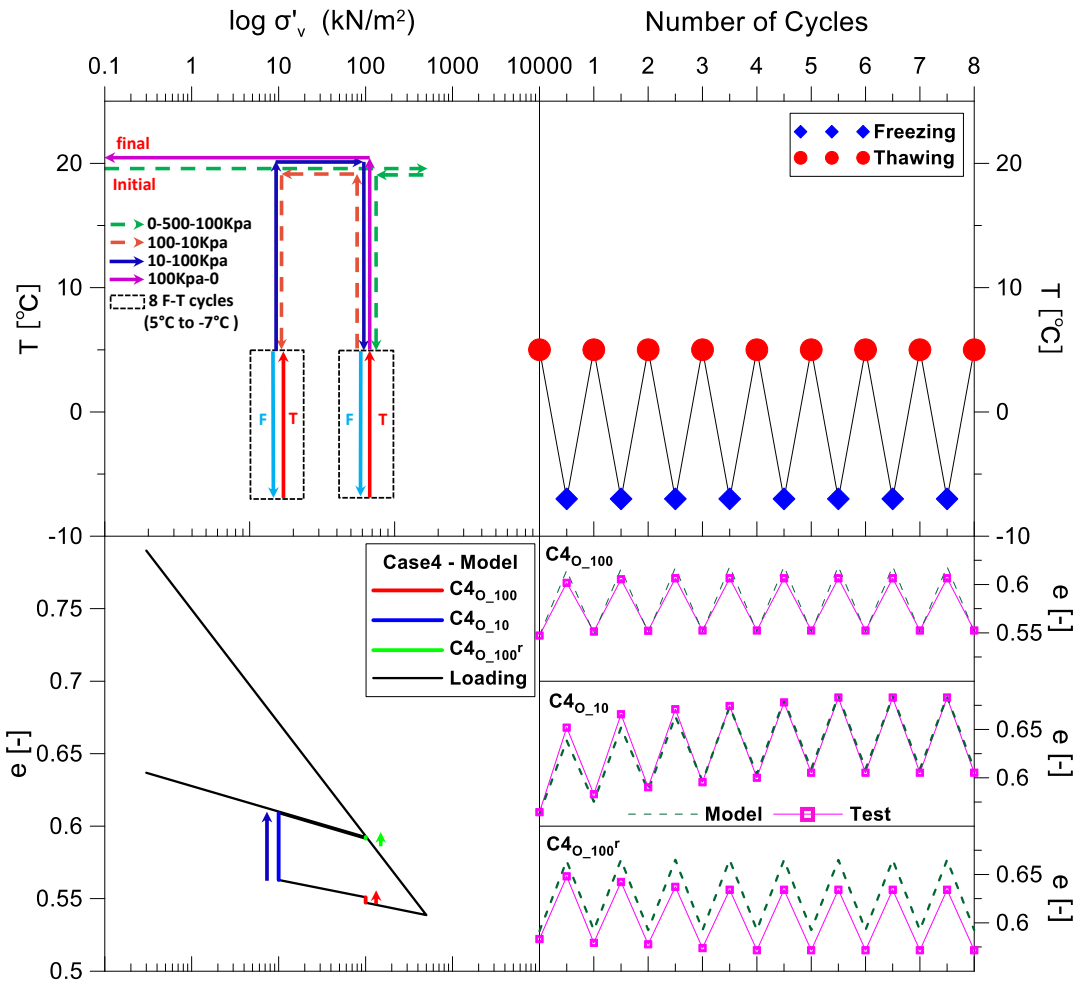

Figure 2.32 Experimental and modeling related to Case 4

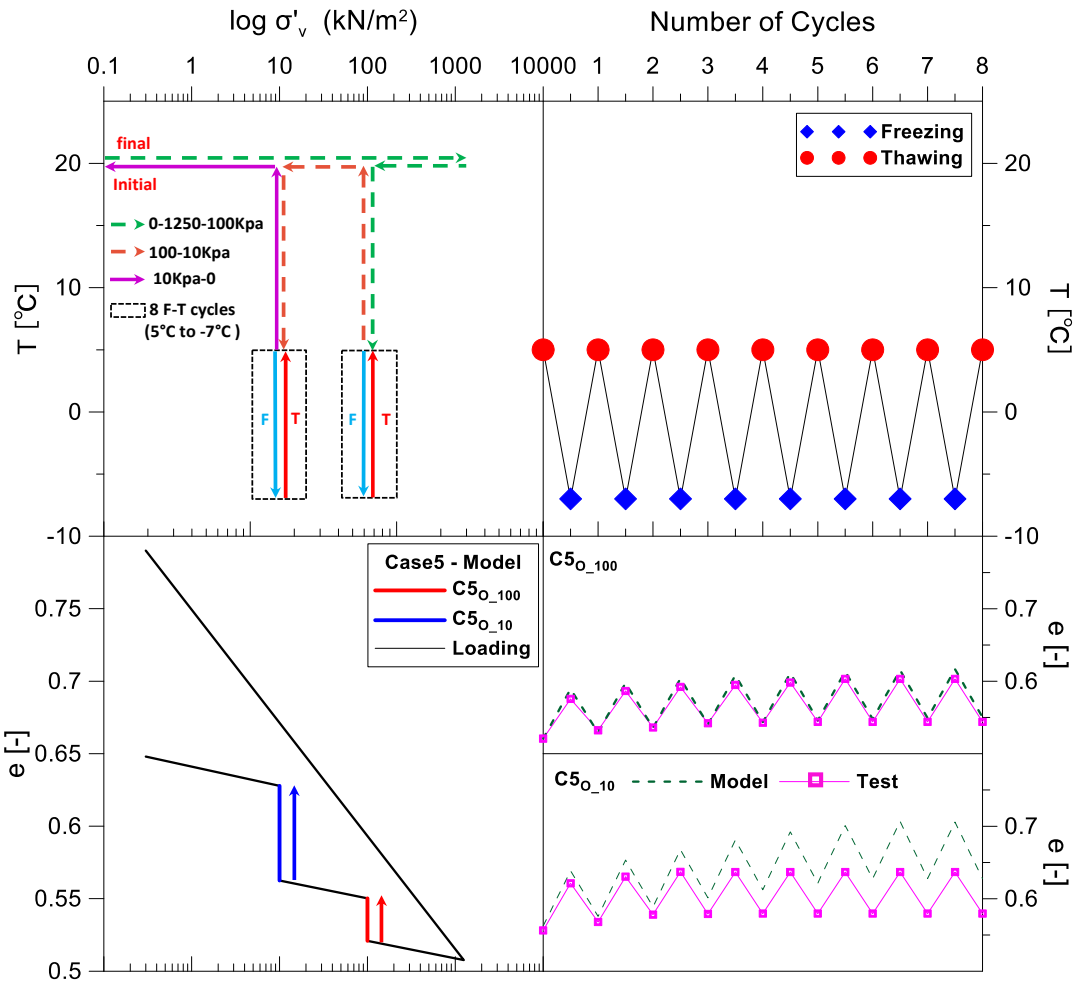

Figure 2.33 Experimental and modeling related to Case 5

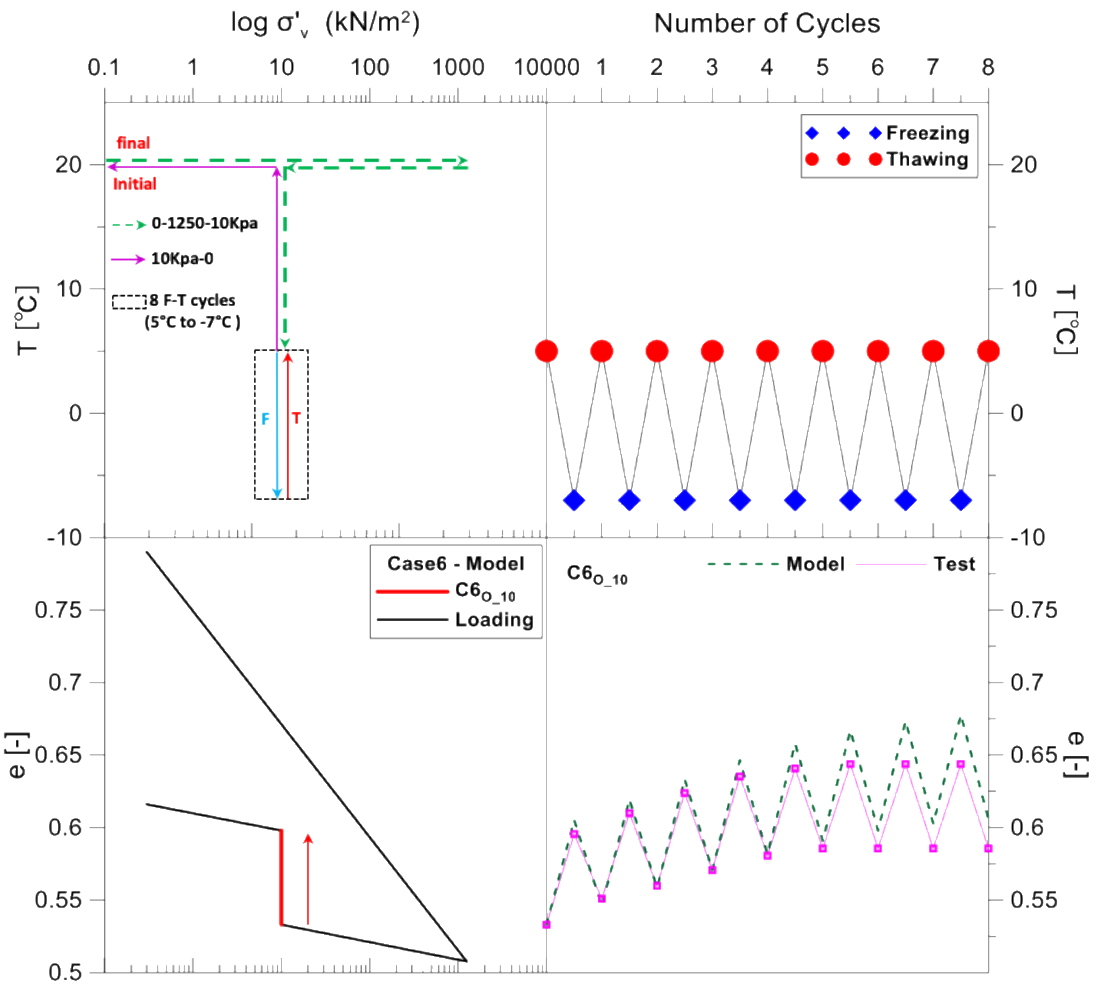

Figure 2.34 Experimental and modeling related to Case 6

The parameters adopted for the model simulation are listed in Table 2.1 and the interaction parameters are listed in Table 2.2.

Table 2.1 Parameters adopted for the model

λ_0	0.028
κ	0.004
β	1.0
r	0.7
I (J/kg)	334000
P_c (MPa)	0.001
α	-3

Table 2.2 Parameters in the interaction functions

ffreezing1	0.3
ffreezing2	-0.2
ffreezing3	5
ffreezing4	0.1
fthawing1	0.25
fthawing2	0.2
fthawing3	5
fthawing4	0.1

From the results shown in Figure 2.29 to Figure 2.34, it can be observed that the mechanical constitutive model developed can capture well of the soil behavior when subjected to cyclic freezing and thawing with different loading histories and freezing-thawing cycles. In the future work, more emphasis will be put on handling with high OCR cyclic tests with a more focus on pre-consolidation pressure change.

In order to show how the freezing and thawing process on the interaction curves and how the volumetric behavior develop according to that, a NC case ($C2_{N\_100}$) and an OC case ($C2_{0\_10}$) are selected for demonstration (see Figure 2.35). In NC case, on the left figure, it starts from 0 to 1 on freezing curve and then 1 to 2 on thawing curve, it is obvious that the plastic strain accumulated from 0 to1 is smaller than that from 1 to 2, as a result, on the right figure, e change from 0 to 1 is smaller than e change from 1 to 2, making point 2 lower that 1. The same reasoning is followed for the rest points. For the last points (i.e. 9-10-11-12-13-14-15-16), the moving path are almost the same around the EP, which is called stable state as discussed about Figure 2.21. As a result, if look at the right figure, e change during freezing and thawing is almost the same, making no more contraction of the sample after each cycle. For the OC case, it is similar, at the last, when the stable state is achieved, on the left figure, points will move along the freezing and thawing curves but around the EP, one the right figure, sample volume change in e also reached stable state.

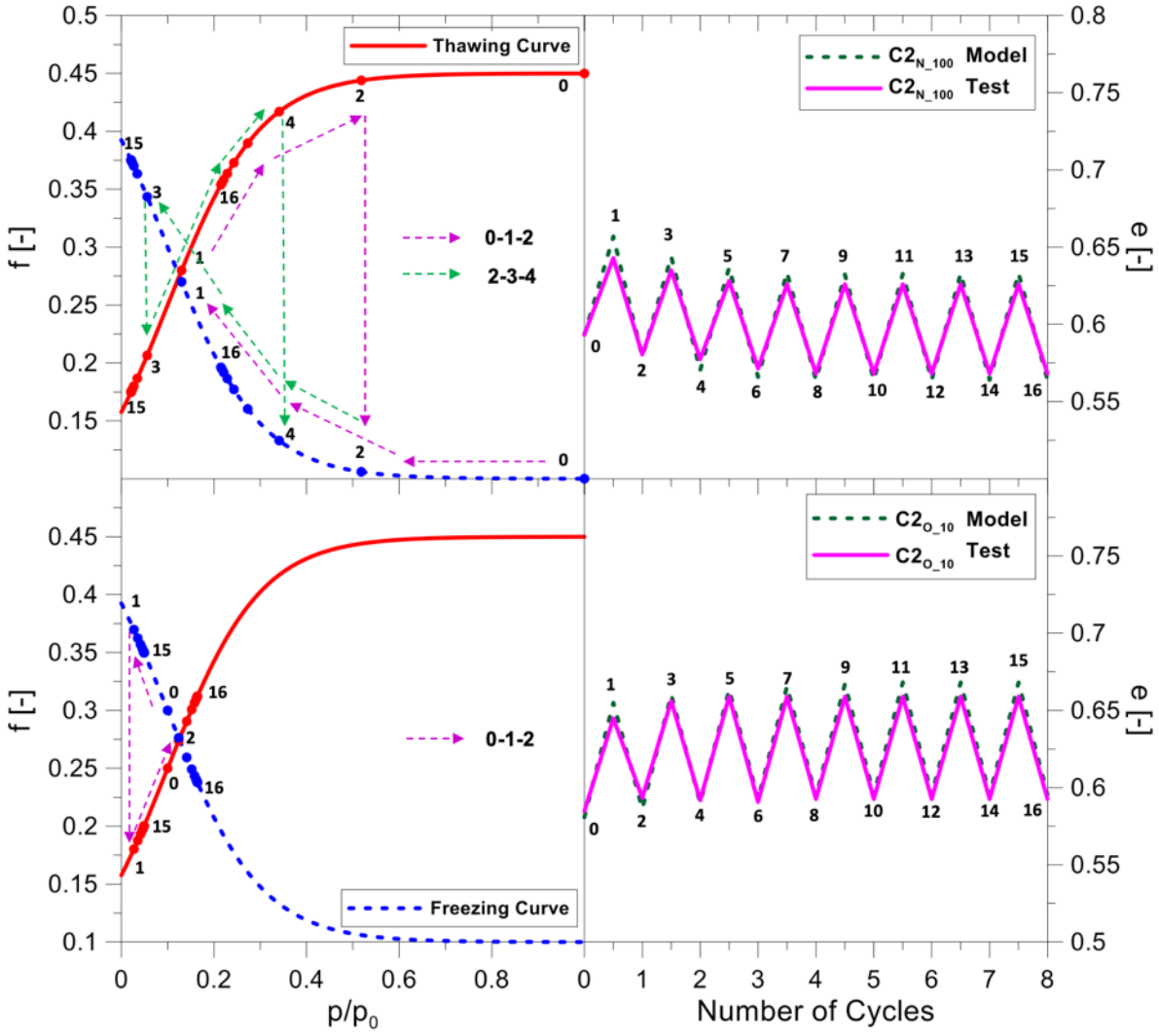

Figure 2.35 Freezing and thawing process on interaction curves

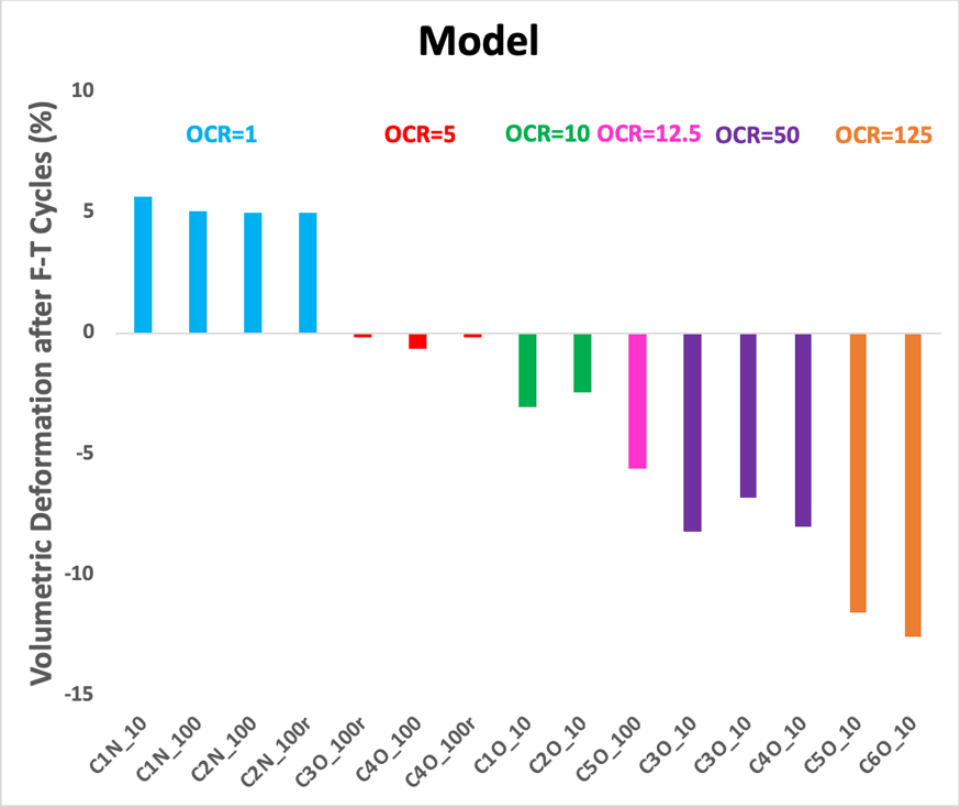

Figure 2.36 Model simulation results about void ratio change vs. OCR for all Cases

Figure 2.36 summarizes the simulation results related to the different cases in terms of the volume changes induced by the *Fr-Th* cycles versus the specimens *OCRs*. The volume change was calculated as $\Delta e/(1+e_b)$ x 100, where e_b is the void ratio just before the *Fr-Th* cycle, and Δe is the associated *e* variation. The results obtained from model share the same tendency with the results obtained from tests that NC soils subjected to *Fr-Th* cycles tend to accumulate plastic strains with a net contraction of the soil after the cycles, trend that slightly decreases with the stress level. As for *OC* soils, all of them showed a tendency to expand, which increases with the soil *OCR*. It also appears that samples with the same *OCR*, but with a previous history of *Fr-Th* tend to expand less based on the results.

2.3.3 Model validation and discussion on effect of temperature range

Simulations on two small cases were also conducted to validate the model on capturing the potential effects of the temperature range on soils volume change subjected to *Fr-Th* cycles. One *NC* case under σ'_v=10kPa (i.e. like $C1_{N\_100}$) and the other one is *OC* case under the same σ'_v but previously loaded up to σ'_v=500kPa (i.e. like $C3_{O\_10}$). For both of these two cases, two temperature ranges will be applied, one is -7°C to 5°C and the other one is -0.3°C to 5°C. The results for NC case are shown in Figure 2.37 and the OC case is shown in Figure 2.38.

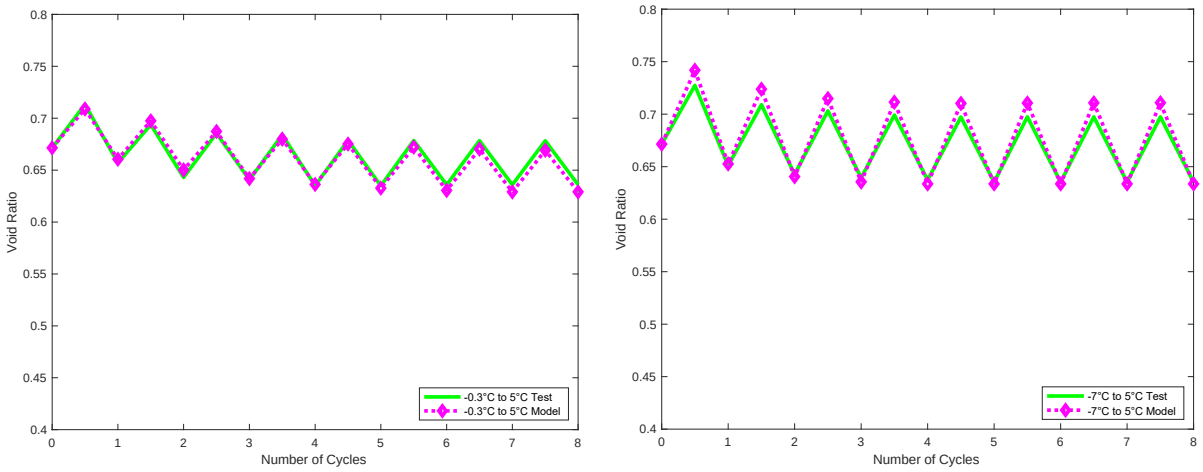

Figure 2.37 Mode validation on temperature range with NC case

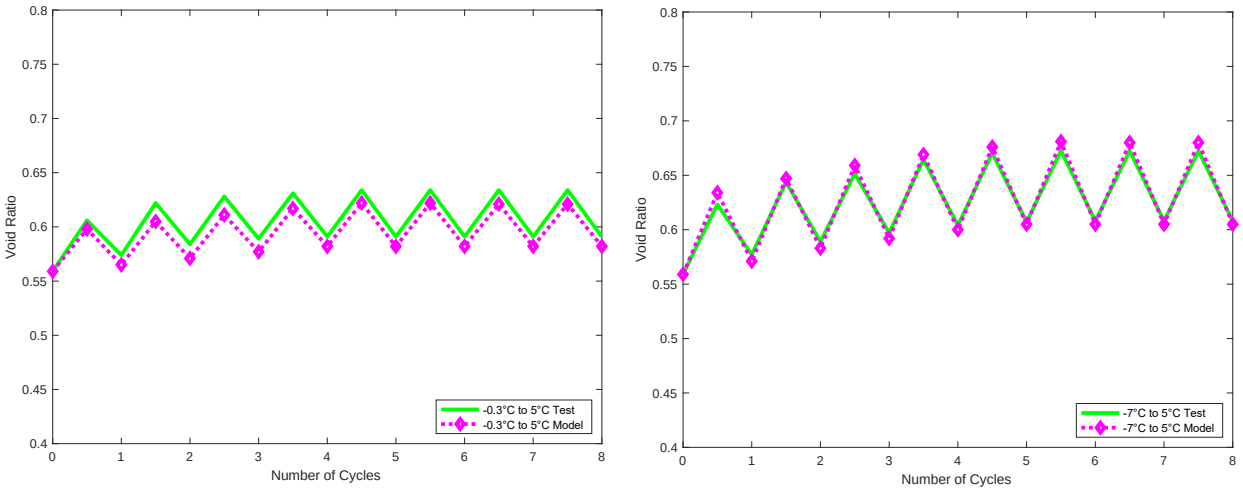

Figure 2.38 Mode validation on temperature range with OC case

From the results we can see that the model can basically capture the volumetric behavior of soil subjected to cyclic F-T with a different temperature range, the difference in volume change amount between different F-T temperature range can also be captured by the mechanical model.

2.3.4 Model validation and discussion on collapse tests

The simulation work in this part will be performed based on two collapse tests as discussed in Section 2.2.4. After consolidation under the load of the plunger only, soil samples were frozen to -5℃. As the volume got stable, soil samples were loaded to 10kPa and 100kPa separately (two tests). When consolidation was done under each load and volume change got stable, temperature was increased to 20℃ (room temperature). Collapse happened during this thawing process and data showing volume change were collected and calculated in terms of void ratio. For the 10kPa test, sample will be load to 100kPa after collapse as a room temperature consolidation. The simulation results are shown in Figure 2.39. From the figure it can be observed that the model can mainly capture the tendency but a little deficient estimation, which is also part the future work.

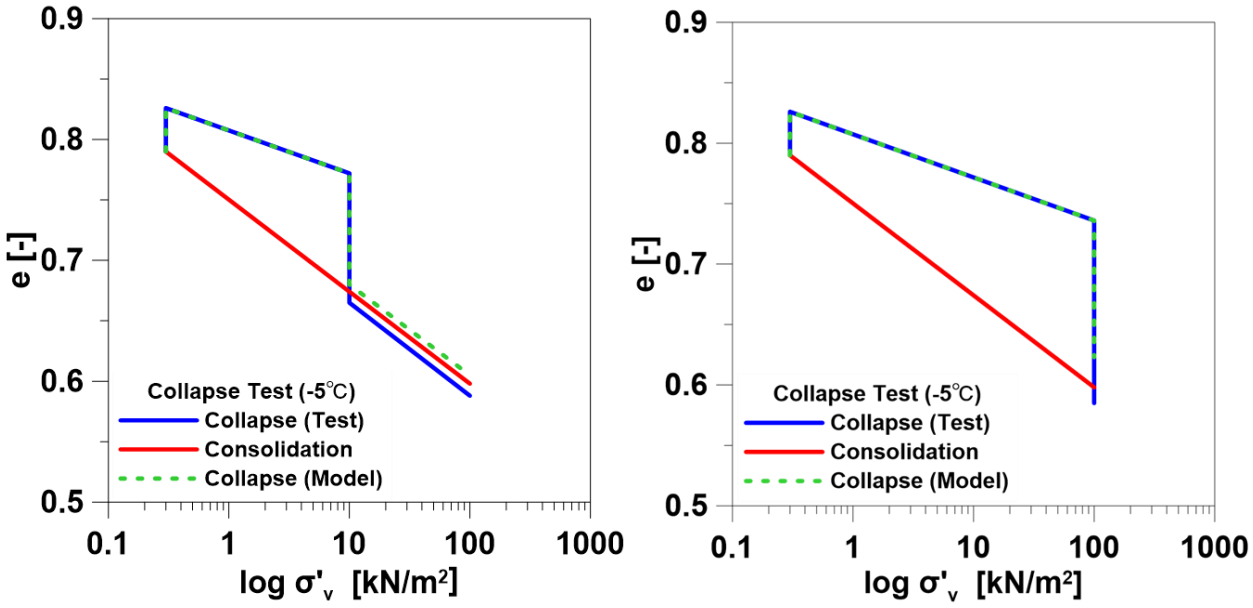

Figure 2.39 Model simulation of collapse tests

2.4 Summary and future works

Through this research topic, in experimental campaign, a better understanding of the behavior of soils subjected to freeze-thaw cycles has been gained. A new set of high-quality experimental data of cyclic freeze-thaw soils with different loading histories and freezing-thawing cycles has been obtained. Normally consolidated *(NC)* soils subjected to freeze-thaw cycles at low stress level tend to accumulate compressive plastic deformations with a net contraction of the sample after the freeze-thaw cycles. for over consolidated *(OC)* tests, samples showed an expansion tendency. *NC* soils subjected to *Fr-Th* cycles tend to accumulate plastic strains with a net contraction of the soil after the cycles, trend that slightly decreases with the stress level. As for *OC* soils, all of them showed a tendency to expand, which increases with the soil *OCR*. Based on these tests, it also appears that samples with the same *OCR*, but with a previous history of *Fr-Th* tend to expand less. Effect from temperature range during *Fr-Th* cycles was also investigated by

several cases, tests with smaller temperature range (e.g. -0.3℃ to 5℃) present smaller volume change when compared with larger range (e.g. -7℃ to 5℃) because of the difference in amount of unfrozen water content when frozen to the lowest temperature. Unfrozen water saturation degree can be measured by measuring electrical conductivity. According to collapse tests, void ratio after thawing collapse is almost the same as that got by room temperature consolidation starting from same initial condition and under same loading path. Knowledge on how OCR and temperature range play the role in cyclic *Fr-Th* process of soil is upgraded one step further, and any effort to reproduce this behavior must therefore include these factors to make an accurate prediction about the volumetric changes in practical problems.

As for modeling campaign, this research presented a mechanical model incorporating both modified BBM and double structure model, extending current modelling work one step further to dealing with frozen soil subjected to cyclic *Fr-Th* process. All the tests in the experimental campaign were adopted for model validation. The simulation results from the model provided good agreement with the test results. The effective simulation workout of the new mechanical model fills the gap existed in mechanical modeling campaign on frozen soil to some extent, and also provide us a good research direction and a better understanding of mechanical behavior of soil subjected to cyclic F-T process.

3 MECHANICAL METHANE HYDRATE BEARING SEDIMENT MODEL

3.1. Introduction

Methane hydrate bearing sediments (MHBS) are typically found in the seabed or permafrost regions where the low temperature and high-pressure conditions favor the formation of a crystalline structure where it is trapped together with water among its pores. Surveys indicate that this a promising energy resource, with very large reserves of methane worldwide that can satisfy the anticipated global energy demand. However, the production of methane from hydrate bearing sediments is very challenging (Dai and Sanchez, 2020), amongst other reasons, because of the complex behavior of this type of material. Methane hydrates are stable under certain low-temperature and high-pressure conditions, however perturbations that bring the methane hydrate out of the stability zone (e.g. depressurization, or heating, or chemical stimulation, or a combination of some of them) will induce the hydrate dissociation with the corresponding uncontrolled production of methane and water.

There are some multinational efforts aimed at identifying safe and profitable strategies for energy production from this type of reservoir but great challenges associated with MHBS still exist. For example, if changes in temperature and/or pressure happen such that the methane hydrate will shift from the 'Pressure-Temperature' stability zone, dissociate problems, which has been investigated a lot (Le et al., 2020, Choi et al., 2020, Zhou et al., 2020), will take place producing methane and water. The huge changes in pore pressure that take place during MH dissociation may trigger several engineering disasters (e.g. large-scale submarine slope failures, borehole instability and platform foundation failures). Furthermore, uncontrolled release of methane to the atmosphere may severely contribute to the exacerbate greenhouse effects.

The geomechanical behavior of hydrate bearing soils is quite complex. A good understanding and modelling of MHBS is a critical component to address the challenges and opportunities associated with this type of sediment. Several constitutive models have been proposed in the last few years to simulate the mechanical behavior of MHBS based on different constitutive theories. Some adopted Mohr–Coulomb based models (Rutqvist and Moridis, 2007, Klar et al., 2010); Some used Modified Cam-Clay Models (Sultan and Garziglia, 2011, Uchida et al., 2016, Gai and Sanchez, 2017); some is based on Strain partition concepts (Sanchez et al., 2017). However, these models have limitations when dealing with MHBS behavior with high dilatancy, temperature effect and viscoplastic phenomenon. In this part, an extended model based on a former research (Gai and Sanchez, 2017), is presented that focus on HBS behaviors with high dilatancy, temperature effect, and time-dependency separately.

Geomechanical strain hardening models generally just incorporate the effect of volumetric strains but the effect of shear strain is not included. An enhanced hardening law for materials exhibiting large dilatancy (Nova, 2004) by incorporating the effect of both shear and volumetric plastic strains will be incorporated in this new model. In order to show the efficient work this model performs, some tests summarized in (Uchida et al. 2016) will in adopted for model validation and the simulation results will be presented and compared with the model simulation results by former model without this component.

Besides, with the increasing interest on temperature effect research, it has been found that during exploration, even if MH has not yet dissociated or decomposed (i.e. in the stability zone), the soil strength may deteriorate after a change in temperature-pressure conditions and this has been verified by triaxial tests performed by some researchers (Hyodo et al., 2005, Li et al., 2011, Hyodo et al., 2013, Hyodo et al., 2013, Liu et al., 2016, Luo et al., 2017), However, this

phenomenon has not been well captured by existing MHBS models. Existing geomechanical models for MHBS generally do not incorporate the potential effect of temperature on sediment behavior. In this new model, a modified evolution law for the pre-consolidation pressure to account for temperature effects is adopted and the model validation on this feature will be conducted based on some already published triaxial tests.

In terms of time-dependent behavior of MHBS, some researchers have performed some triaxial test to capture the visco-plastic behavior. However, the published tests results are very limited (Miyazaki et al., 2009, Miyazaki et al., 2010, Miyazaki et al., 2011, Miyazaki et al., 2012, Miyazaki et al., 2017, Yoneda et al., 2019). As for modeling investigation, some researchers proposed viscoplastic models for geomaterials (Adachi et al., 2005, Qiao et al., 2016, Qiao and Ding, 2017), but almost no validated mechanical model is developed to capture the rate effect of MHBS in coupled multiphase conditions. In this new model, a viscoplastic law based on Perzyna's concept (Perzyna, 1966) is adopted in formulations to simulate time-dependent effects on MHBS and validated against already published triaxial tests.

3.2. Proposed geomechanical model for MHBS

This new model with three new components will be elaborated in section 3.2 continuously with model introductions and formulations for all components. For each new constitutive component on each critical feature, the model will be validated according to already published triaxial tests. Cases for model application on each key feature are presented in Section 3.3. The new model is based on the upgrade of a previous elastoplastic law for HBS, briefly introduced as follows.

3.2.1 Introduction on base model

This new model is developed on a former constitutive model (Gai and Sanchez, 2017), which was proposed to simulate the mechanical behavior of methane hydrate-bearing soils based on the concept of a hierarchical single-surface (Hiss) framework (Desai et al., 1986, Desai, 1989). Some key ingredients proposed by (Uchida et al., 2012) to deal with particular features of HBS are incorporated into the model, namely: sub-loading concepts (Hashiguchi, 1989, Hashiguchi and Chen, 1998); cementing effects associated with the presence of hydrates; and bonding damage.

This model in (Gai and Sanchez, 2017) involves a single and continuous yield surface, which can have different shapes depending on the adopted parameters. An advantage of the HISS is its flexibility to adapt the shape of the yield surface to the particular conditions of the soil under investigation. Besides, this model is able to account for cementing effect and different hydrate morphologies. Sub-loading concept was also introduced to this model to simulate irrecoverable strains that may occur when the stress state is inside the yield surface and to predict a smooth transition between elastic and plastic states, particularly in soils that exhibit dilatancy. The performance of the model was found to be very satisfactory when compared against experimental data from triaxial tests based on natural and synthesized core samples involving different hydrate saturations, hydrate morphology and confinements. However, this model has limitations when simulate HBS behavior with high dilatancy behaviors, temperature effects, and loading rate effects, as a result of which, this research developed on the constitutive model in (Gai and Sanchez, 2017) by incorporating more constitutive components to capture HBS behaviors under more complex multiphases conditions. More details about this base mechanical model can be found in Appendix A.

3.2.2 An enhanced hardening law for MHBS exhibiting high dilatancy

As stated above, the mechanical model introduced in this paper is an extension of the model for MHBS proposed by (Gai and Sanchez, 2017). The yield function of the HISS-MH model incorporating the strength enhancement effects related to the presence of methane hydrate and sub-loading concepts can be written as Eq. 3.1:

$$F = \frac{a}{M^2} q^2 - \gamma 3^2 p'^2 + \gamma 3^2 p'^n [R(p_c + p_d)]^{2-n} \qquad \text{(Eq. 3.1)}$$

where a and r are constants related to the shape of the yield surface; n is the parameter related to the transition from compressive to dilative volume change; p' and q are the mean effective and deviatoric stresses, respectively; M is the slope of critical line in the q-p' space; p_c is the effective pre-consolidation pressure, and p_d controls the increase of the sediment strength associated with the presence of hydrates. The evolution variable R is related to the sub-loading yield surface, which is introduced in the model formulation to account to two main aspects: i) to reproduce irrecoverable strains that may develop when the stress state is inside the yield surface (aspect that cannot be modeled with a standard elasto-plastic model), and ii) to predict a smooth transition between elastic and plastic states, particularly in soils that exhibit dilatancy. Figure 3.1 illustrates the different yield surfaces incorporated in this model.

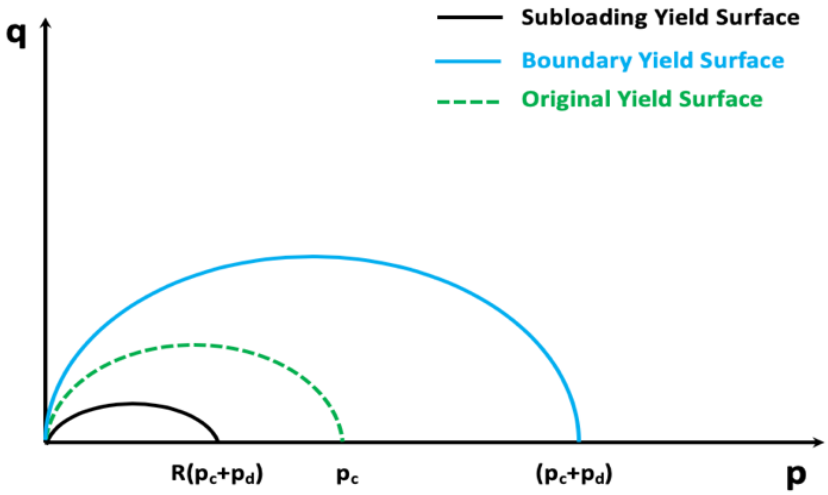

Figure 3.1 Yield surfaces adopted to model the mechanical behavior of MHBS

The developed model adopted an enhanced hardening law for materials exhibiting large dilatancy by incorporating the effect of both shear and volumetric plastic strains. The strain hardening part will combine both volumetric plastic strain and shear plastic strain, and the modified hardening law will be expressed as Eq. 3.2.

$$dp_c = \frac{1+e}{\lambda-\kappa} \cdot p_c \cdot d\epsilon_v^p + D_s \cdot \frac{1+e}{\lambda-\kappa} \cdot p_c \cdot d\epsilon_d^p \qquad \text{(Eq. 3.2)}$$

where e is void ratio; $\lambda \; and \; \kappa$ are slope of isotropic normal compression line and slope of isotropic unload-reload line respectively; D_s is a Nova factor (i.e. with a range from 0 to 1); $d\epsilon_v^p$ and $d\epsilon_d^p$ are volumetric plastic strain and deviatoric plastic strain respectively.

3.2.3 A modified evolution law for accounting for temperature effect on MHBS

In order to introduce temperature effect into the basic mechanical constitutive model (Gai and Sanchez, 2017), the well-established thermoplasticity theory was adopted. The first conceptual

model that considered the heating effect on the behavior of clay was proposed by (Campanella and Mitchell, 1968), It was developed incorporating temperature effects by (Hueckel and Baldi, 1990, Laloui and Cekerevac, 2003). They assumed that the mean effective preconsolidation pressure, which controls the size and evolution of the yield surface, decreases with increasing temperature. Thus, the thermoelastoplastic model proposed in this paper for MHBS is established by combining the mechanical model described above with well-established thermoplasticity theory. The effects of temperature in MHBS behavior was captured by introducing a dependence of p_c on temperature, as in Eq. 3.3:

$$p_c = p_{c0}(1 - r log \frac{T}{T_0}) \quad \text{(Eq. 3.3)}$$

where p_{c0} is the preconsolidation pressure at the reference temperature, T_0 is the reference temperature and r is a model parameter that accounts for the effect of temperature on preconsolidation pressure. A similar approach was followed before to model the effect of temperature on saturated clays (Cekerevac and Laloui, 2004). Figure 3.2 illustrates the effect of temperature on MHBS yield surface movement. With the increment of temperature, the elastic domain shrinks (i.e. from blue to red), which is consistent with tests results.

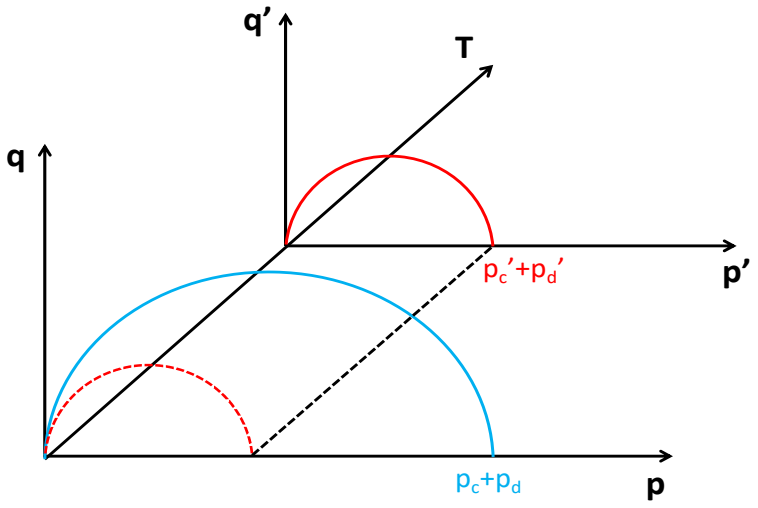

Figure 3.2 Schematic representation of the effect of temperature on MHBS yield surface

3.2.4 A viscoplastic law for time-dependent effect of MHBS

To consider the viscous behavior of soils in the design of geotechnical structures is becoming more important and popular according to many laboratory studies and field observations. A series of general stress–strain–time models have been proposed (Adachi and Oka, 1982, Modaressi and Laloui, 1997, Freitas et al., 2011, Sivasithamparam et al., 2015) and amongst others, models based on Perzyna's overstress theory are most general due to its simplicity. Such models can be differentiated by the definition of over-stress index f and viscosity $< \Phi(F) >$. Hinchberger and Rowe, 2005 proposed a projection method that defines F as the distance between the original stress state and the projection stress state on the static yield surface which was adopted to capture the strain rate influence on the soil strength and preconsolidation pressure. Recently, some authors (Sivasithamparam et al., 2015, Yin et al., 2010) replaced the static yield surface with a reference yield surface and introduced the unique stress-strain-time concept to deduce the overstress function. Some other models are proposed (Naghdi and Murch, 1963, Qiao and Ding, 2017) based on Non-

Stationary Flow Surface (NSFS) theory to describe the time-dependent behavior of materials. However, almost no validated mechanical model is directly developed to capture the rate effect of MHBS in coupled multiphase with sub-loading concept.

In order to capture the time-dependent behavior of MHBS, a viscoplastic law incorporating Perzyna's viscoplasticity theory is constructed in (Gai and Sanchez, 2017). The direction of viscoplasticity is determined by the gradient of a plastic potential function calculated at the current stress point. Associated flow rule is adopted and two yield surfaces (static yield surface and dynamic yield surface, see Figure 3.3) are constructed to represent overstress index f; the static yield surface function is as Eq. 3.4.

$$F_S = \frac{a}{M^2} q_S^2 - 9\gamma\{(p'_S)^2 - (p'_S)^n [R_S(p_{cS} + p_{dS})]^{2-n}\} \quad \text{(Eq. 3.4)}$$

where the meanings of the parameters are the same as introduced in former part about the base mechanical model, but the sub-S means the parameters are for static yield surface (i.e. kind of reference yield surface). The plastic strain is updated by Eq. 3.5, where Λ_S is plastic multiplier and the updated stress state is calculated by Eq. 3.6, where D_S^e is the elastic stiffness matrix.

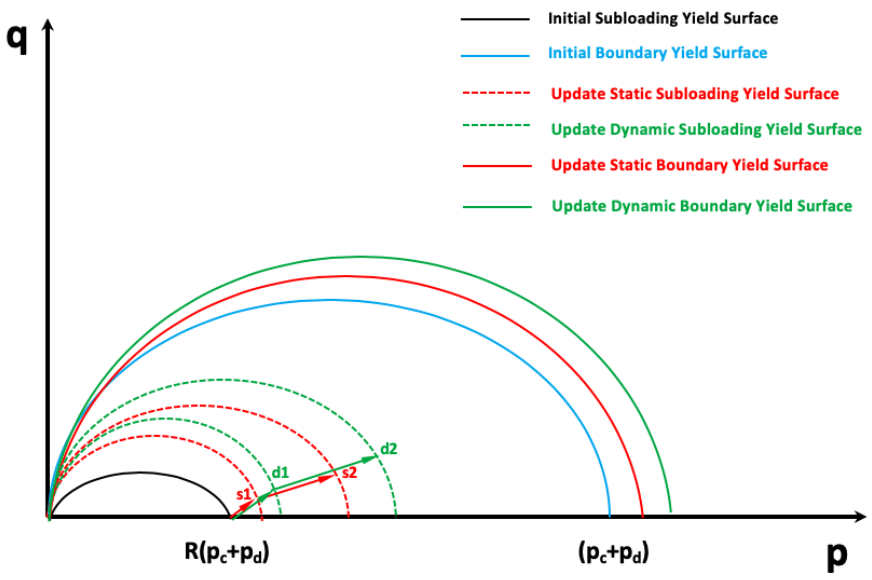

Figure 3.3 Yield surface updating demonstration

$$d\varepsilon_S^p = \Lambda_S \cdot \frac{\partial F_S}{\partial \sigma_S} \tag{Eq. 3.5}$$

$$d\sigma_S = D_S^e \cdot (d\varepsilon_S^{total} - d\varepsilon_S^p) \tag{Eq. 3.6}$$

As for the dynamic yield surface, the yield function is shown in Eq. 3.7, Where the meanings of the parameters are the same as introduced in base mechanical model, but the sub-D means the parameters are for dynamic yield surface.

$$F_D = \frac{a}{M^2} q_D^2 - 9\gamma\{(p_D')^2 - (p_D')^n [R_D(p_{cD} + p_{dD})]^{2-n}\} \tag{Eq. 3.7}$$

The change in plastic strain for dynamic one is shown in Eq. 3.8, where $< \Phi(F) >$ is viscosity and γ is a multiplier. The definition of $< \Phi(F) >$ for this model is shown in Eq. 3.9, where the f is over-stress index and the definition is shown in Eq. 3.10, the value of which is calculated by substituting dynamic stress state into static yield surface. f is adopted to show the relative position of the two yield surfaces. The stress state update of the dynamic yield surface is in Eq. 3.11, which is quite similar as the one for static one.

$$d\varepsilon_D^p = \gamma \cdot < \Phi(F) > \cdot \frac{\partial F_D}{\partial \sigma_D} \cdot \Delta t \qquad \text{(Eq. 3.8)}$$

$$< \Phi(F) > = \begin{cases} f^n & for\ F>0 \\ 0 & for\ F\leq 0 \end{cases} \qquad \text{(Eq. 3.9)}$$

$$f = \frac{a}{M^2} q_D^2 - 9\gamma\{(p_D')^2 - (p_D')^n [R_S(p_{cS} + p_{dS})]^{2-n}\} \qquad \text{(Eq. 3.10)}$$

$$d\sigma_D = D_D^e \cdot (d\varepsilon_D^{total} - d\varepsilon_D^p) \qquad \text{(Eq. 3.11)}$$

Starting from a stress state point on initial sub-loading yield surface, both static yield surface and dynamic yield surface are propagated by small steps of stress state increment with controlled stain. How the static yield surface develop is same as base model. For the dynamic one, the difference formed between the two yield surfaces will generate the overstress index f, which will update fluidity and plastic strain by steps to reach continuously updated stress states.

3.3. Model applications and discussions

For each new constitutive component on each critical feature, the model will be validated according to already published triaxial tests. Cases for model applications on each key feature are presented in Section 3.3.1, 3.3.2 and 3.3.3. Four cases about the model application on MHBS with high dilatancy are presented from 3.3.1.1 to 3.3.1.4; three cases on temperature effect are presented from 3.3.2.1 to 3.3.2.3; three cases on time-dependent behavior are presented from 3.3.3.1 to 3.3.3.3.

3.3.1 Model applications on MHBS behavior with high dilatancy

3.3.1.1 Case 1

Case 1 adopted is a series of triaxial tests performed by former researchers (Miyazaki et al., 2011) using Toyoura sand. The confining pressures were all 1MPa and the hydrate saturations were 0, 34% and 41%. These tests results were adopted and simulated by another modified Cam-Clay based model in (Uchida et al., 2016). However, they did not manage to capture the tests results very well. The results by our model with Nova theory are presented in Figure 3.4 and without Nova theory are presented in Figure 3.5. Model results are shown in blue line and lab tests results are shown in red circle. Test under 1MPa confining pressure and 0 hydrate saturation degree is denoted as "1MPa 0 Test" and similar reasoning can be followed for other tests and model results for section 3.3.1. The parameters adopted in Figure 3.4 and Figure 3.5 are listed in Table 3.1 and Table 3.2 respectively.

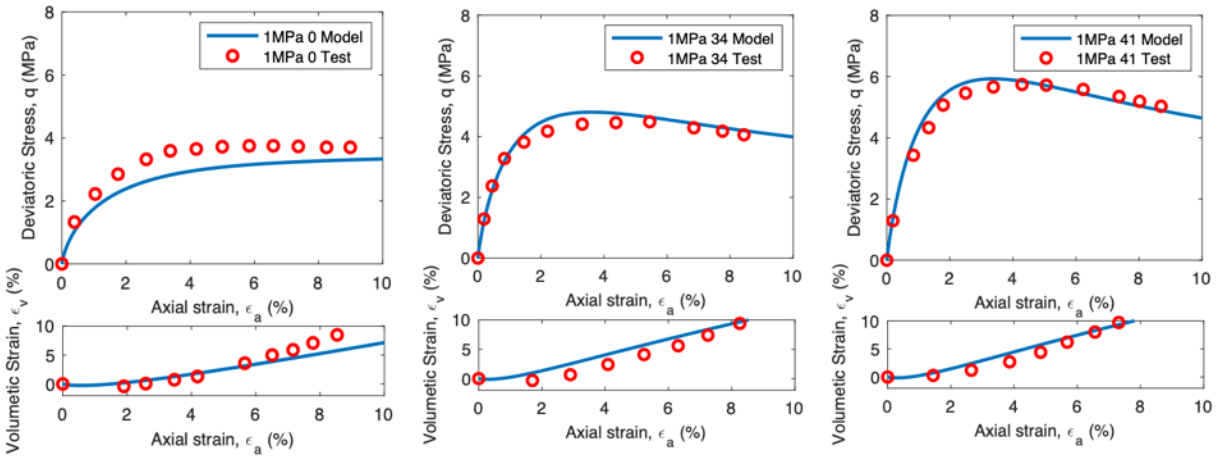

Figure 3.4 Case 1 simulation with shear strain components

Table 3.1 Parameters adopted for model with shear strain components in Case 1

Properties	**S_H=0**	**S_H=0.34**	**S_H=0.41**
M	1.28	1.28	1.28
λ	0.2	0.2	0.2
κ	0.004	0.004	0.004
p_c (MPa)	7.7	7.7	7.7
p_0 (MPa)	1	1	1
n	1.3	1.3	1.3
a	5.5	5.5	5.5
γ	-1/6	-1/6	-1/6
S_H	0	0.34	0.41
α	40	40	40
β	1	1	1
μ	7	7	7
υ	0.1	0.1	0.1
Ds	0.8	0.8	0.8

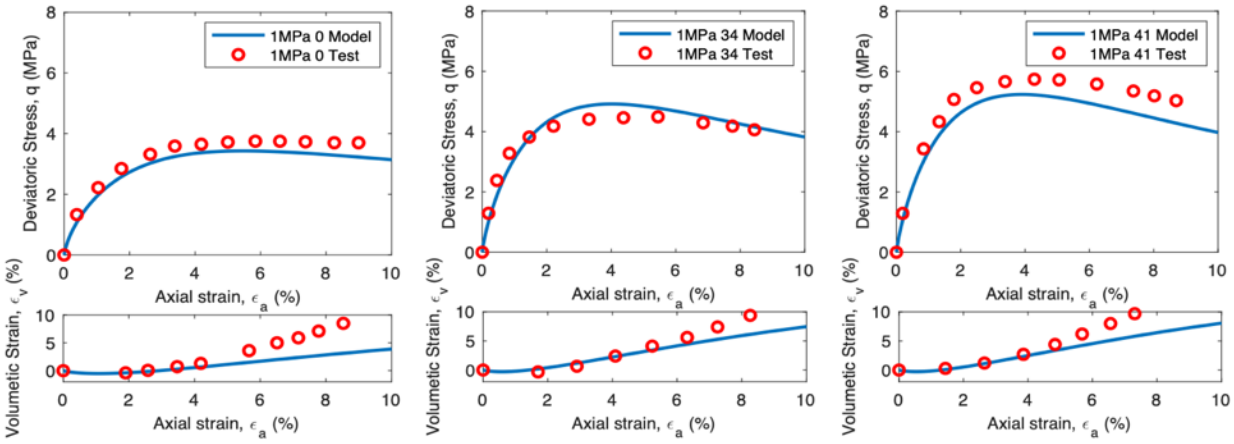

Figure 3.5 Case 1 simulation without shear strain components

Table 3.2 Parameters adopted for model without shear strain components in Case 1

Properties	**S_H=0**	**S_H=0.34**	**S_H=0.41**
M	1.28	1.28	1.28
λ	0.2	0.2	0.2
κ	0.004	0.004	0.004
p_c (MPa)	7.7	7.7	7.7
p_0 (MPa)	1	1	1
n	1.3	1.3	1.3
a	3	3	3
γ	-1/5	-1/5	-1/5
S_H	0	0.34	0.41
α	20	20	20
β	1	1	1
μ	7	7	7
υ	0.1	0.1	0.1
Ds	0.0	0.0	0.0

3.3.1.2 Case 2

Tests adopted in Case 2 are also triaxial tests performed by former researchers (Miyazaki et al., 2011) using Toyoura sand. The confining pressures were all 2MPa and the hydrate saturations were 0, 31% and 43% separately. These tests results were also adopted and simulated by another modified Cam-Clay based model in (Uchida et al., 2016), which can be compared with ours. The results by our model with Nova theory are presented in Figure 3.6 and without Nova theory are shown in Figure 3.7. Parameters adopted for Figure 3.6 and Figure 3.7 are listed in Table 3.3 and Table 3.4 respectively.

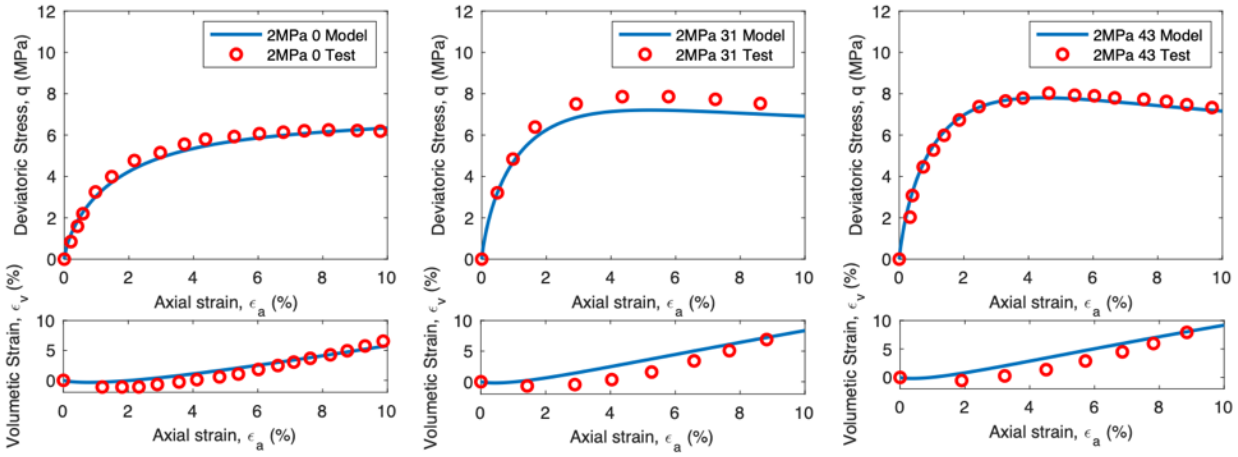

Figure 3.6 Case 2 simulation with shear strain components

Table 3.3 Parameters adopted for model with shear strain components in Case 2

Properties	S_H=0	S_H=0.31	S_H=0.43
M	1.28	1.28	1.28
λ	0.2	0.2	0.2
κ	0.004	0.004	0.004
p_c (MPa)	12.1	12.1	12.1
p_0 (MPa)	2	2	2
n	1.3	1.3	1.3
a	5.5	5.5	5.5
γ	-1/6	-1/6	-1/6
S_H	0	0.31	0.43
α	40	40	40
β	1	1	1
μ	7	7	7
υ	0.1	0.1	0.1
Ds	0.8	0.8	0.8

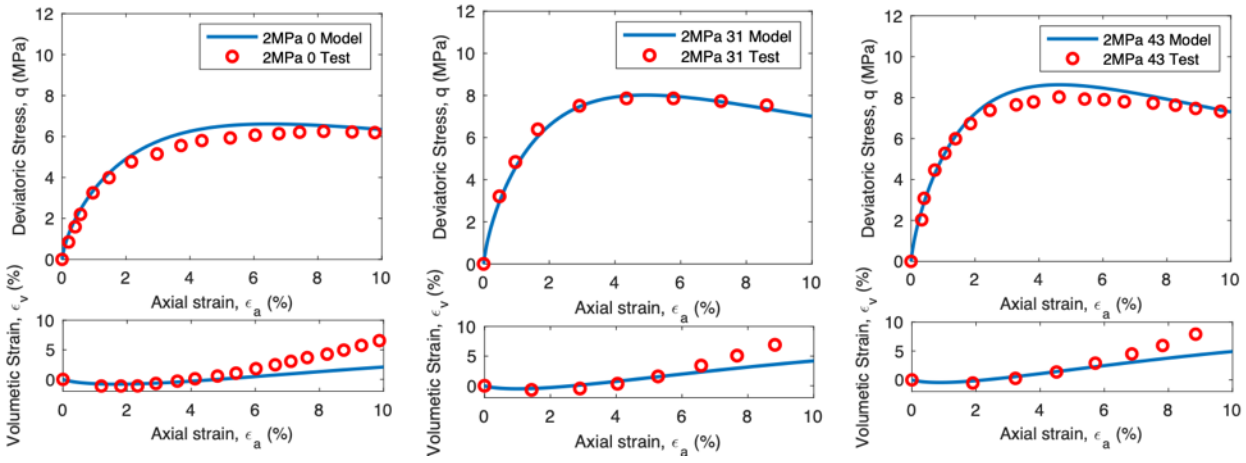

Figure 3.7 Case 2 simulation without shear strain components

Table 3.4 Parameters adopted for model without shear strain components in Case 2

Properties	**S_H=0**	**S_H=0.31**	**S_H=0.43**
M	1.28	1.28	1.28
λ	0.2	0.2	0.2
κ	0.004	0.004	0.004
p_c (MPa)	12.1	12.1	12.1
p_0 (MPa)	2	2	2
n	1.3	1.3	1.3
a	3	3	3
γ	-1/5	-1/5	-1/5
S_H	0	0.31	0.43
α	20	20	20
β	1	1	1
μ	7	7	7
υ	0.1	0.1	0.1
Ds	0.0	0.0	0.0

3.3.1.3 Case 3

A series of triaxial tests performed by same researchers (Miyazaki et al., 2011) using Toyoura sand is adopted for Case 3. These tests shared a higher confining pressure of 3MPa and the hydrate saturations were 0, 27% and 42% respectively. The simulation results by our model with Nova theory are presented in Figure 3.8 and without Nova theory are presented in Figure 3.9. Parameters used for Figure 3.8 and Figure 3.9 are listed in Table 3.5 and Table 3.6 respectively.

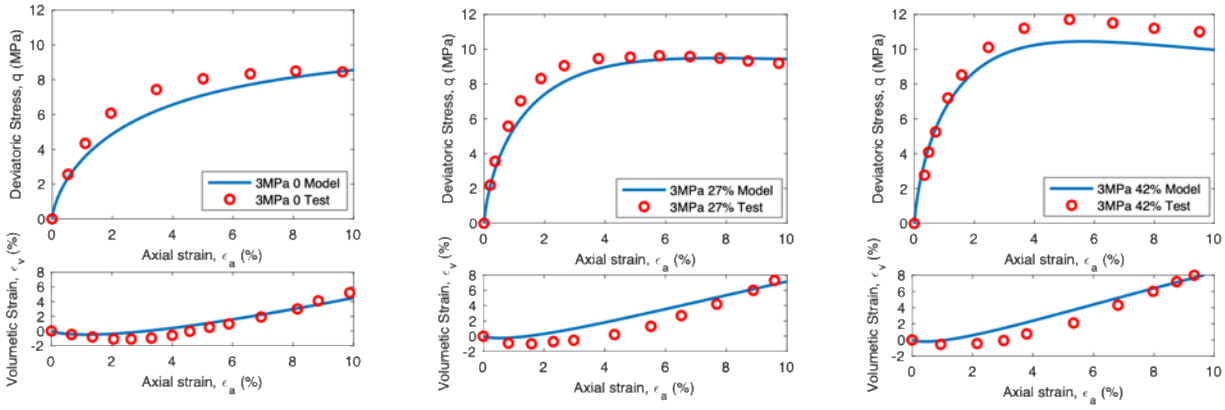

Figure 3.8 Case 3 simulation with shear strain components

Table 3.5 Parameters adopted for model with shear strain components in Case 3

Properties	**S_H=0**	**S_H=0.27**	**S_H=0.42**
M	1.28	1.28	1.28
λ	0.2	0.2	0.2
κ	0.004	0.004	0.004
p_c (MPa)	16.1	16.1	16.1
p_0 (MPa)	3	3	3
n	1.3	1.3	1.3
a	5.5	5.5	5.5
γ	-1/6	-1/6	-1/6
S_H	0	0.27	0.42
α	60	60	60
β	1	1	1
μ	7	7	7
υ	0.1	0.1	0.1
Ds	0.8	0.8	0.8

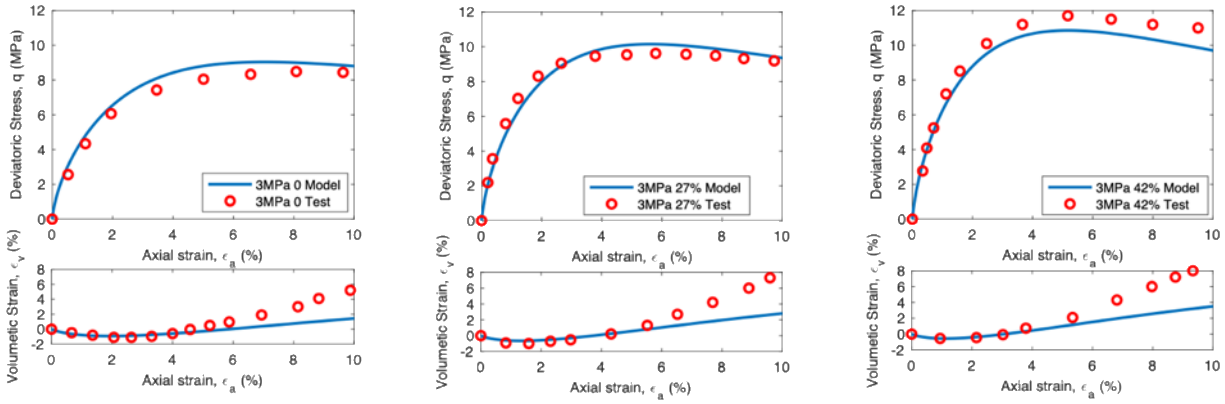

Figure 3.9 Case 3 simulation without shear strain components

Table 3.6 Parameters adopted for model without shear strain components in Case 3

Properties	**S_H=0**	**S_H=0.27**	**S_H=0.42**
M	1.28	1.28	1.28
λ	0.2	0.2	0.2
κ	0.004	0.004	0.004
p_c (MPa)	16.1	16.1	16.1
p_0 (MPa)	3	3	3
n	1.3	1.3	1.3
a	3	3	3
γ	-1/5.2	-1/5.2	-1/5.2
S_H	0	0.27	0.42
α	20	20	20
β	1	1	1
μ	7	7	7
υ	0.1	0.1	0.1
Ds	0.0	0.0	0.0

3.3.1.4 Case 4

Case 4 adopted in this part includes triaxial tests performed by another former researchers (Hyodo et al., 2013) using Toyoura sand. The confining pressures were all 3MPa and the hydrate saturations were 0, 39% and 54%. These tests results were also adopted and simulated by another modified Cam-Clay based model in (Uchida et al., 2016). The results by new model with Nova theory are presented in Figure 3.10 and the parameters adopted are listed in Table 3.7; the results by new model without Nova theory are presented in Figure 3.11 and the parameters adopted are listed in Table 3.8.

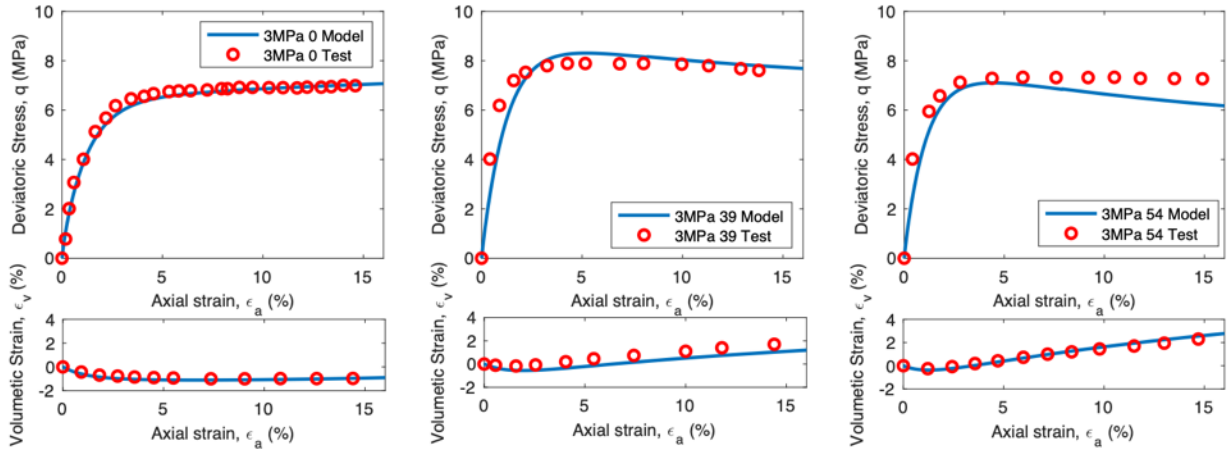

Figure 3.10 Case 4 simulation with shear strain components

Table 3.7 Parameters adopted for model with shear strain components in Case 4

Properties	S_H=0	S_H=0.39	S_H=0.54
M	1.28	1.28	1.28
λ	0.24	0.24	0.24
κ	0.005	0.005	0.005
p_c (MPa)	9.6	9.6	9.6
p_0 (MPa)	3	3	3
n	0.95	0.95	0.95
a	3	3	3
γ	-0.1	-0.1	-0.1
S_H	0	0.39	0.54
α	8	8	8
β	0.7	0.7	0.7
μ	4.5	4.5	4.5
υ	0.35	0.35	0.35
Ds	0.1	0.1	0.1

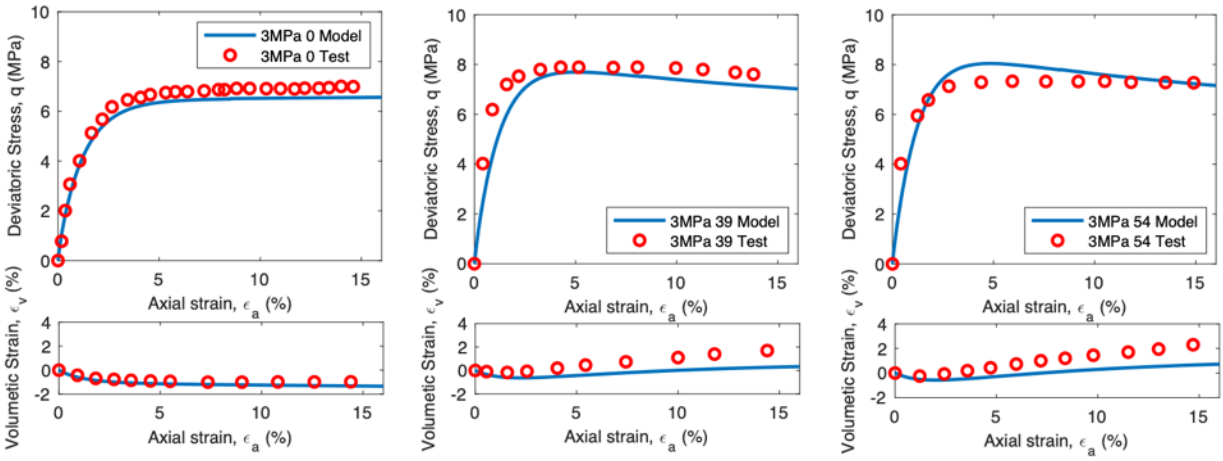

Figure 3.11 Case 4 simulation without shear strain components

Table 3.8 Parameters adopted for model without shear strain components in Case 4

Properties	**S_H=0**	**S_H=0.39**	**S_H=0.54**
M	1.28	1.28	1.28
λ	0.24	0.24	0.24
κ	0.005	0.005	0.005
p_c (MPa)	9.6	9.6	9.6
p_0 (MPa)	3	3	3
n	0.95	0.95	0.95
a	3	3	3
γ	-0.1	-0.1	-0.1
S_H	0	0.39	0.54
α	6	6	6
β	0.7	0.7	0.7
μ	4.5	4.5	4.5
υ	0.35	0.35	0.35
Ds	0.0	0.0	0.0

In Case 1, 2 and 3, tests selected were conducted by same researcher using same Toyoura sand but with different confining pressures and hydrate saturations. In Case 4, tests are from another former researcher using same Toyoura sand. It can be observed that our developed model taking both volumetric strain and shear strain into consideration can better simulate MHBS behavior with high dilatancy under different confining pressures and hydrate saturations when compared with the former base mechanical model (Gai and Sanchez, 2017) as well as the mechanical model presented in (Uchida et al., 2016).

3.3.2 Model applications about temperature effect on MHBS behavior

3.3.2.1 Case 1

The first Case adopted in this part is a series of triaxial tests performed by former researchers (Li et al., 2011) using Kaolin Clay. Triaxial tests were performed under different temperatures (i.e. -5℃, -10℃, -20 ℃) without hydrate dissociation. The confining pressures were all 5MPa and with same loading rate and hydrate saturation. Only relationship between deviatoric

stress and axial strain is evaluated in these tests. The simulation results by our developed model are presented in Figure 3.12 and the parameters adopted are listed in Table 3.9.

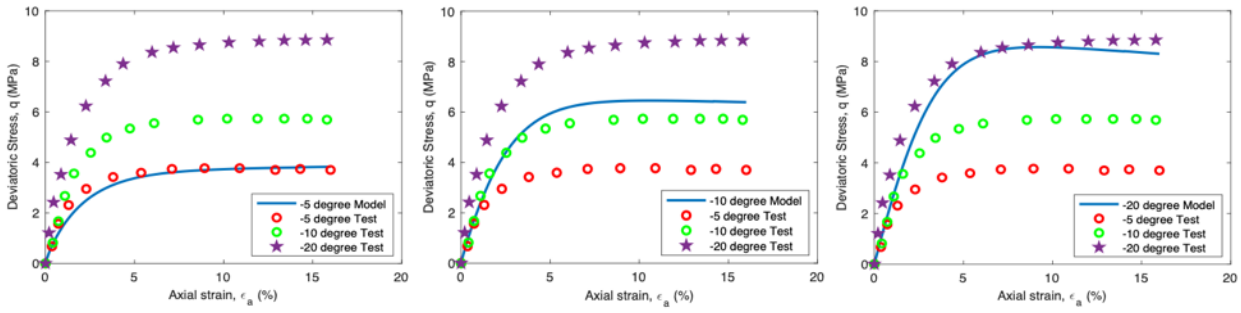

Figure 3.12 Case 1 simulation with thermoplasticity theory

Table 3.9 Parameters adopted for Case 1

Properties	**T=-5℃**	**T=-10℃**	**T=-20℃**
M	1.25	1.25	1.25
λ	0.5	0.5	0.5
κ	0.05	0.05	0.05
p_c (MPa)	5	5	5
p_0 (MPa)	5	5	5
n	1	1	1
a	8	8	8
γ	-1/9	-1/9	-1/9
S_H	0.3	0.3	0.3
α	20	20	20
β	1.2	1.2	1.2
μ	0.1	0.1	0.1
υ	0.15	0.15	0.15

From the results shown above, In Case 1, it can be observed that soil strength based on temperature effect can be mainly captured by the developed model incorporating thermoplasticity theory in a phenomenon logical way.

3.3.2.2 Case 2

The second Case adopted is one set of triaxial tests by (Hyodo et al., 2013) using Toyoura. Two different temperature (i.e. 1°C and 10°C) were adopted for demonstrating the temperature effects on mechanical behavior. Both the pure subloading method (i.e. the starting stress state point is on the subloading yield surface) and partial subloading method (i.e. the starting stress state point is within the subloading yield surface) were employed for the simulation (see Figure 3.13).

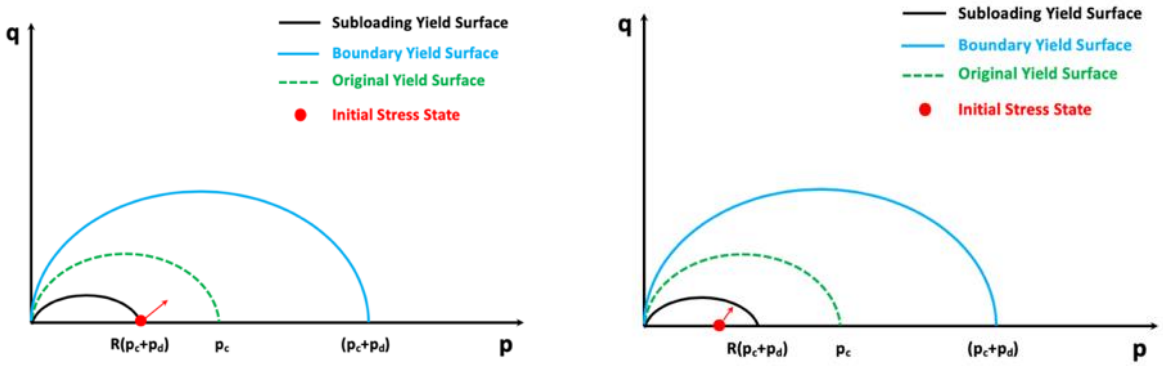

a) b)

Figure 3.13 Schematic representation of a) pure subloading method and b) partial subloading method

The simulation results of pure subloading are shown in Figure 3.14 and the parameters adopted are shown in Table 3.10. As shown in Figure 3.14, the red circle points are tests results under the temperature of 1°C and the green triangle ones are test results under 10°C, the blue line is the model simulation results under 1°C and the purple one is the model simulation results under

10°C. It can be observed that with increasing axial strain, the model can mainly capture the general tendency in both deviatoric stress and volumetric strain. However, the model demonstrates kind of deficiency in stiffness during the beginning part, and as a result, for this case, the partial subloading is tried to progress and compare with this one.

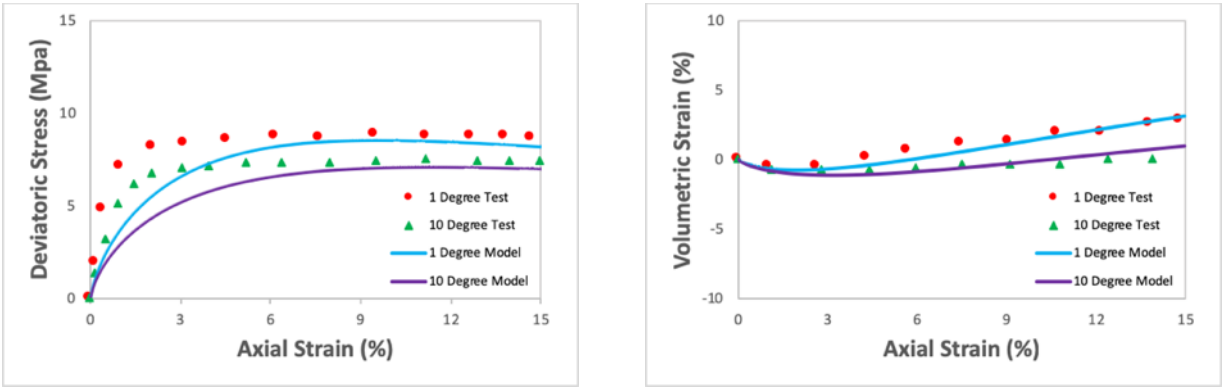

Figure 3.14 Simulation results by model incorporating temperature effect with pure subloading method

Table 3.10 Parameters adopted for simulation with pure subloading method

Properties	**T=1℃**	**T=10℃**
M	1.1	1.1
λ	0.2	0.2
κ	0.005	0.005
p_c (MPa)	3	3
p_0 (MPa)	10	10
n	1	1
a	3	3
γ	-1/9	-1/9
S_H	0.531	0.516
α	20	20
β	1.1	1.1
μ	1	1
υ	0.15	0.15

For partial subloading method, the starting point is inside the subloading yield surface, thus, all the stains taken place during the beginning part are elastic strains; plastic strain will occur when stress state point reaches the yield surface (see Figure 3.13b). The simulation results are shown in Figure 3.15 (i.e. the denotations are the same as the pure subloading one) and the parameters adopted for tests results simulation are shown in Table 3.11.

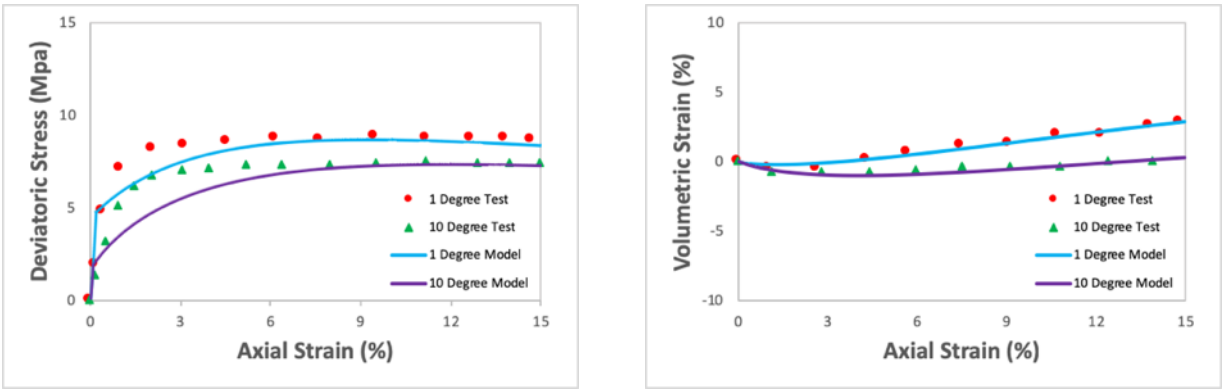

Figure 3.15 Simulation results by model incorporating temperature effect with partial subloading method

Table 3.11 Parameters adopted for simulation with partial subloading method

Properties	**T=1℃**	**T=10℃**
M	1.2	1.2
λ	0.2	0.2
κ	0.005	0.005
p_c (MPa)	3	3
p_0 (MPa)	8	8
n	1	1
a	3	3
γ	-1/9	-1/9
S_H	0.531	0.516
α	20	20
β	1	1
μ	1	1
υ	0.15	0.15

It can be seen that with the partial subloading method, if compare with the pure subloading one, the model can capture the beginning part better by just applying elastic strain, after the stress state reaches the yield surface, plastic strains occur and the different strength tendency due to temperature effect can be mainly captured by the model.

3.3.2.3 Case 3

Case 3 adopted for model validation includes triaxial tests by (Hyodo et al., 2013) using Toyoura sand. Triaxial tests with two different temperatures (i.e. 1 and 5 degree) using gas saturated method were performed. The simulation results by our model using pure subloading method on two different temperatures are shown in Figure 3.16 and the main parameters adopted are listed in Table 3.12.

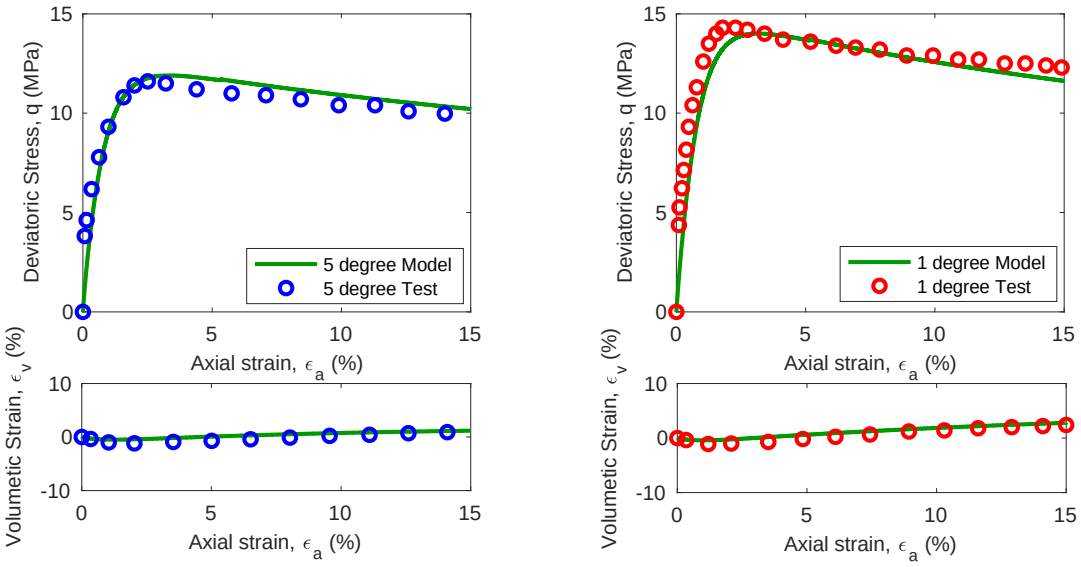

Figure 3.16 Case 3 simulation with thermoplasticity theory

Table 3.12 Parameters adopted for Case 3

Properties	T=1℃	T=5℃
M	1.25	1.25
λ	0.5	0.5
κ	0.05	0.05
p_c (MPa)	3	3
p_0 (MPa)	10	10
n	1	1
a	2	2
γ	-1/9	-1/9
S_H	0.232	0.266
α	20	20
β	0.55	0.55
μ	5	5
υ	0.15	0.15

From the results shown above, it can be observed that in Case 3, soil strength based on temperature effect can be mainly captured by the developed model by incorporatingd thermoplasticity theory in a phenomenon logical way. Both volumetric strain and deviatoric stress can be quite well simulated.

3.3.3 Model applications about time-dependent MHBS behavior

3.3.3.1 Case 1

Case 1 adopted for demonstration includes time-dependent drained compression triaxial tests by (Miyazaki et al., 2010). They performed triaxial tests using artificial methane-bearing-sediment samples (i.e. Toyoura sand) with different loading rates (LR). Three tests with constant but different loading rates are selected here to validate the model. The three tests selected are shown in Figure 3.17 in blue circles. The loading rates are 0.1%/min, 0.05%/min and 0.01%/min in a), b) and c) respectively. For each loading rate, three hydrate-sand specimens and three sand specimens without hydrate were prepared for testing (i.e. all three tests are presented together in blue circles). For model simulation, all the tests shared the same soil parameters; hydrate

saturations of the samples as mentioned in the paper were ranged from 35% to 45%. The model simulation results by our model on loading rate effects are shown in Figure 3.17 in red (i.e. for a), b) and c), top one is test with hydrate and bottom one is test without hydrate) and the parameters adopted are listed in Table 3.13, where the basic parameters share the same meanings with what has been discussed in the former part, while nf and nn are γ and n is Eq. 3.8 and Eq. 3.9 accordingly.

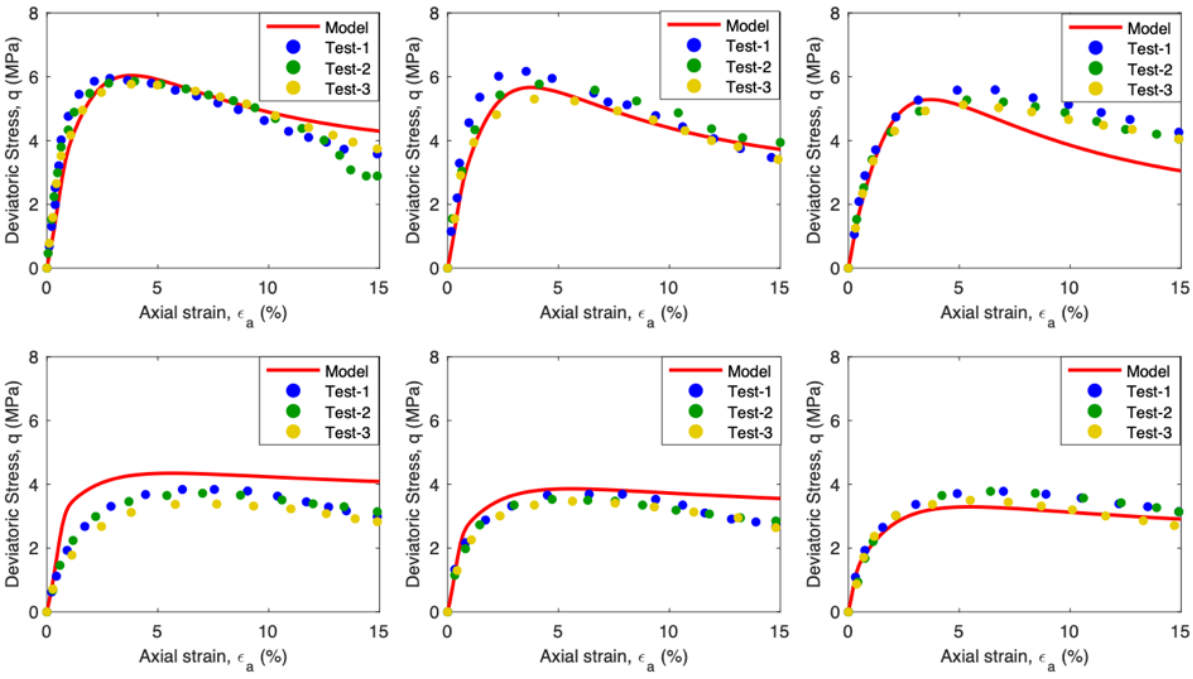

Figure 3.17 Test and model simulation results for Case 1

Table 3.13 Model parameters adopted for Case 1

Properties	Perzyna
M	1
λ	0.15
κ	0.016
p_c (MPa)	9
p_0 (MPa)	2
n	1
a	5
γ	-1/9
α	20
β	1
μ	20
υ	0.2
nf	5e-6
nn	1.0

From the results shown above, it can be observed that higher the loading rate is, higher the soil strength will be. The model can mainly capture this time-dependent behavior when samples are under constant but different loading rates in multiphase conditions. However, the behavior of sample without hydrate as well as the dilatancy behavior of the sample is still not very well captured. This may be because we tried to maintain all the parameter the same when simulate all the three tests but in fact some small changes may take place on parameters due to the loading rate effects (i.e. the paper did not provide the parameters indeed). Also, this may be due to the limitation of Perzyna model which need to be further investigated.

3.3.3.2 Case 2

Case 2 adopted for demonstration is a series of time-dependent drained compression triaxial tests by (Miyazaki et al., 2010). They performed triaxial tests using artificial methane-bearing-sediment samples (i.e. Toyoura sand) with different loading rates (LR). Three tests with changing loading rates and different axial strain intervals (i.e. Δe) were selected here to validate the model. The three tests selected are shown in Figure 3.18 in blue. In test a), curve 1 is with LR=0.01%/min

and curve 2 with LR =0.1%/min, Δe=0.25%; in test b), curve 1 is with LR=0.05%/min and curve 2 with LR=0.1%/min, Δe=0.25%; in test c), curve 1 is with LR=0.05%/min and curve 2 with LR=0.1%/min, Δe=0.5%. All the three tests shared the same soil parameters for simulation; hydrate saturation for a) is 35% and hydrate saturation for b) and c) is 48%. The model simulation results by our model on loading rate effects are shown in Figure 3.18 in red and the parameters adopted are listed in Table 3.14, where the basic parameters share the same meanings with what has been discussed in the former part, while nf and nn are γ and n is Eq. 3.8 and Eq. 3.9 accordingly.

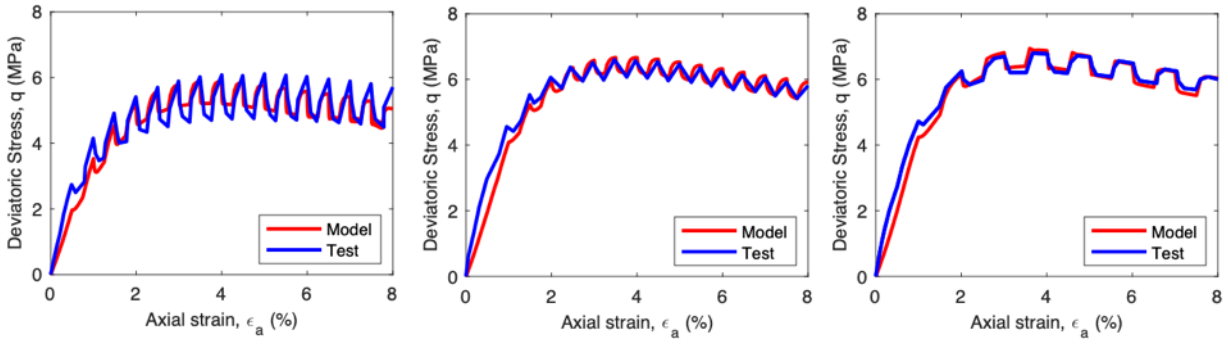

a) b) c)

Figure 3.18 Tests and model simulation results for Case 2

Table 3.14 Model parameters adopted for Case 2

Properties	Perzyna
M	1.03
λ	0.15
κ	0.016
p_c (MPa)	9
p_0 (MPa)	2
n	1
a	3.3
γ	-1/9
α	20
β	1
μ	20
υ	0.2
nf	5e-6
nn	1.0

From the results shown above, it can be observed that the model simulation results and tests can well agree with each other, which providing a good proof for the validation of the developed model incorporating viscoplasticity theory. It can mainly capture the time-dependent behavior of the methane hydrate sediment artificial samples in Case 2 that have different loading rate and strain intervals in multiphase conditions.

3.3.3.3 Case 3

Case 3 adopted for demonstration is a series of time-dependent drained compression triaxial tests by (Yoneda et al., 2019). They performed triaxial tests using artificial methane-bearing-sediment samples (i.e. Toyoura sand) with different loading rates (LR). Two tests with changing loading rates and same axial strain interval (i.e. Δe=1%) and were selected here to validate the model. The two tests selected are shown in Figure 3.19. In a), the test shown in red was with a lower LR=0.01%/min and a higher LR =0.05%/min; in b), the test shown in red was with a lower LR=0.001%/min and a higher LR=0.01%/min. The model simulation results by our model on loading rates effects are shown in Figure 3.19 (i.e. model simulation results were marked

in dark green); the model parameters adopted for a) are listed in Table 3.15 and for b) are listed in Table 3.16, where the parameters share the same meanings with what has been discussed in the former part and Case 1. These two soil samples were collected from different depths and places, the soil parameters (i.e. not provided by Yoneda et al., 2019) are not exactly the same but should be very similar, so we try to keep most of the soil parameters the same (i.e. Table 3.15 and Table 3.16) when simulate the two tests with the developed model.

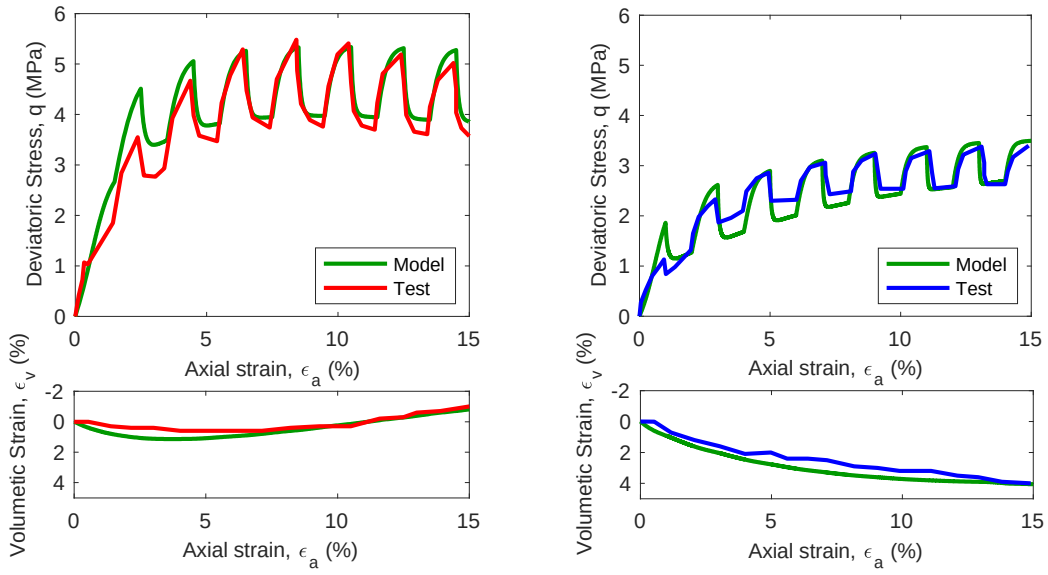

a) b)

Figure 3.19 Tests and model simulation results for Case 3

Table 3.15 Model parameters adopted for Case 3 a)

Properties	Red Test
M	1.2
λ	0.28
κ	0.025
p_c (MPa)	10
p_0 (MPa)	1.6
n	1
a	5
γ	-1/12
S_H	0.799
e	0.6
α	10
β	10
μ	5
υ	0.2
nf	2e-6
nn	1.0

Table 3.16 Model parameters adopted for Case 3 b)

Properties	Blue Test
M	1.2
λ	0.28
κ	0.025
p_c (MPa)	6.8
p_0 (MPa)	1.6
n	1
a	4.3
γ	-1/12
S_H	0.655
e	0.6
α	10
β	10
μ	5
υ	0.2
nf	2e-6
nn	1.0

From the results shown above, it can be concluded that the model simulation results and tests can well agree with each other in both stress-strain relationship and volume strain-axial strain relationship, which providing another good proof for the validation of the developed model incorporating viscoplasticity theory. It can mainly capture the time-dependent behavior of the methane hydrate sediment samples from field in Case 3 that have different loading rate in multiphase conditions.

3.4 Summary and future work

Constructed on a former Modified Cam-Clay mechanical model, this paper proposed an extended mechanical model that incorporating an enhanced hardening law to capture MHBS exhibiting large dilatancy behavior; adopting a modified evolution law based on thermos-elastoplastic theory for the pre-consolidation pressure to account for temperature effects; accepting a visco-plastic law based on Perzyna's concept to capture load rate effects on MHBS behavior. All these three model components are introduced in details separately with comparing to the basic model and validated against already published triaxial tests. The tests results show good agreement with the model simulation results. The developed models proposed in this paper can mostly capture the critical features of MHBS behaviors when dealing with high dilatancy behavior, temperature effects and time-dependent behavior, which are not well capture by former mechanical models. This paper presented some good directions when modeling complex MHBS behavior and more comprehensive models that can combine these laws and theories will be researched on in the future works.

4 EXPERIMENTAL STUDY ON GAS MIGRATION AND BREAKTHROUGH PRESSURE FOR HIGH-LEVEL NUCLEAR WASTE DISPOSAL BARRIER SYSTEM

4.1 Introduction

The safe isolation of high-level radioactive waste (HLW) is an unavoidable requisite for the use of nuclear power as a resource to meet present and future social energy need. The main safety function of a geological repository for the disposal of HLW is to confine pollute waste, prevent or delay the radionuclides to the host rock. Usually an Engineered Barrier System (EBS) may be composed of a variety of sub-components, such as the waste form, the canisters, buffer materials, backfill, and plugs, to prevent and delay the release of radionuclides from the waste to the repository host rock (see Figure 4.1).

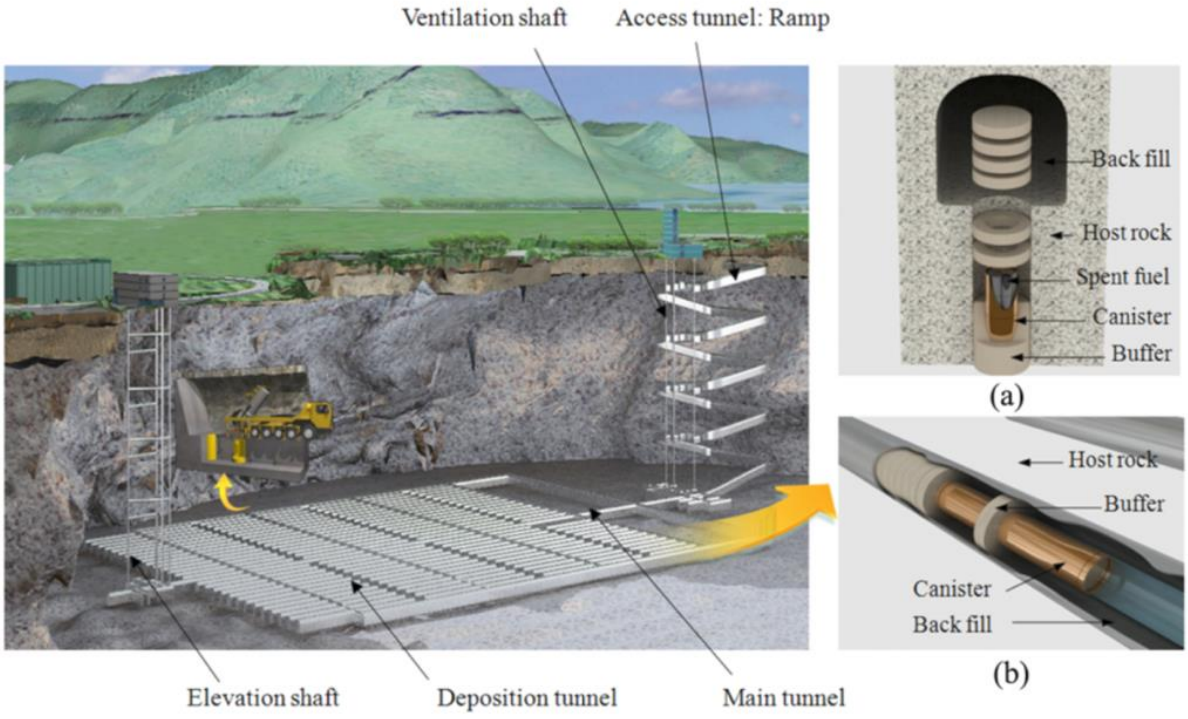

Figure 4.1 High-level radioactive waste disposal barrier system (reprinted from Kim et al., 2011)

Complex Thermo-Hydro-Mechanical and Chemical (THMC) phenomenon will take place in the repository due to heating and hydration under highly confined conditions. Several physical and chemical phenomena (e.g. metal corrosion, water radiolysis, biodegradation) will take place during the lifetime of a waste repository that can will give rise to the generation of gas (e.g. metal corrosion, water radiolysis, biodegradation). This process of gas generation under confined conditions could induce the increase of the gas pressure in the repository, which may negatively affect key properties of the bentonite and geological barriers and may lead to the releasing of radionuclides to the human environment. Therefore, investigating the influence of the gas migration process on the sealing ability of bentonite, host rock and other barriers materials is extremely important for the safe isolation of high-level radioactive waste.

How the accumulated gas migrates through the barrier system and its potential impact on the host sedimentary rocks has been a key point for all major international waste disposal programs (e.g., NDA in UK, ANDRA in France, SKB in Sweden, NAGRA in Switzerland, SCK-CEN in Belgium, NWMO in Canada). A lot of research worldwide were performed to deal with how gas migrates through barrier material in both experimental studies (Pusch and Forsberg, 1983, Horseman et al., 2004, Davy et al., 2009, Villar et al., 2008, Cuss et al., 2011, Graham et al., 2016) and numerical works (Alonso et al., 2006, Arnedo et al., 2008, Xu et al., 2013, Fall et al., 2014, Xu et al., 2017).

The movement of gas induced by pressure gradients (i.e. advective gas flux) can take place either through: i) the interconnected porous space and pre-existing discontinuities, or ii) through evolving discontinuities triggered by the gas pressure. The former is generally termed ‘visco-capillary flow’, which is controlled by pore structure (e.g. pore size distribution and throat radii) and the amount of water in the porous media (i.e. given e.g. by the average degree of saturation),

which must progressively be displaced in order for the gas to migrate (Graham et al., 2016). The second mechanism is termed ‘pathway dilatancy’ (Marschall et al., 2005). Since this process essentially involves the separation of two parts of the barrier under the action of an applied stress, it might be also possible to describe it as a type of microfracture formation.

The gas permeability in saturated Mx-80 bentonite via gas breakthrough tests was examined in Pusch and Forsberg, 1983. Eight tests were carried out on saturated Mx80 specimens with a dry density ranging between 1.1 to 1.8 $Mg.m^{-3}$ (Pusch and Forsberg, 1983). The gas pressure was incrementally increased from one to five days intervals, until advective gas outflow was observed at the downstream end of the sample at some critical value of pressure, which was in same order of magnitude than the swelling pressure. This critical threshold is generally known as the ‘gas breakthrough pressure’. Data and test details about gas breakthrough pressures in saturated Mx-80 is reported by Pusch et al., 1987.

Sand/bentonite mixtures are being considered as potential barrier and seal materials. Gas migration experiments on compacted sand/ Kunigel VI-bentonite mixtures are reported by Hokari et al., 1997. Some used a volumetrically confined cell to examine gas-migration through the mixture of sand and bentonite (Arnedo et al., 2008). The authors suggested that the interfaces between compaction layers within the bentonite could have a significant role in the gas transportation process. The same mechanism was suggested by Harrington et al., 1997 to explain their observations from gas flow tests through Boom Clay. Liu et al., 2015 performed experiments to find the coupled effects of water content, dry density and confining pressure on gas permeability through bentonite-sand mixtures. Wang et al., (2012) performed tests to study on the relationship between suction and swelling pressure by using vapor transfer technique.

In terms of gas permeability measurements, previous studies were mainly focused on samples with different saturation degrees, dry densities, confinements as well as soil types (Tanai et al., 1997, Galle and Tanai, 1998, Villar et al., 2013, Liu et al., 2015). However, these researches are mainly focused on intact samples without systematical considerations of how induced cracks due to heating and drying will impact on the barrier material permeability values, which is naturally happening on site. It is known that the heat generated by the HLW will induce a drying of the engineered barrier surrounding the canister and this dry-out may lead to the formation of desiccation cracks (Graham, 1997, Garcia-Sineriz et al., 2015). Drying cracks have been observed in large scale heating experiments aimed at studying the feasibility of engineered barrier systems (EBS) for HLW (Graham, 1997, Garcia-Sineriz et al., 2015). This type of crack will increase the barrier permeability and how these cracks will propagate (i.e. cracking and self-healing) with heating and drying strongly influent the gas transfer process discussed above as well as the safety of nuclear waste disposal system.

Cracking of soil is not new topic and it can develop due to several processes comprising; desiccation and shrinkage, freezing and thawing, differential settlement, syneresis, and penetrated plant roots (Yesiller et al., 2000). The propagation of cracks will impact on soil compressibility and permeability, also, a reduction in the overall strength and stability. Amongst others, desiccation cracks are what mainly happened to nuclear waste disposal barrier and their effects on gas permeability of barrier material are the focus study of this paper. Cracking behaviors of clay material due to desiccation have been investigated by many former researchers (Morris et al., 1992, Albercht and Benson, 2001, Atique et al., 2009). Besides, hydraulic permeability due to cyclic drying-wetting has also been researched (Atique et al., 2009, Louati, 2018, Wan et al., 2018). However, gas permeability due to such cracks on clay, particularly on barrier material is not well

studied yet. As for healing behavior of clay materials, phenomenon and its impact on soil properties were investigated by former researchers (Eigenbrod, 2003, Sporer et al., 2001, Bastiaens et al., 2007, Wang et al., 2013, Mohammadi and Choobbasti, 2018), among which, hydraulic permeability due to healing were investigated (Sporer et al., 2001, Wang et al., 2013). Gas permeability due to self-healing of barrier material is still blank.

However, all the self-healing discussed above are due to wetting, thawing, sealing, etc. Healing due to continuous heating and drying for clay material is still a very new topic that has never been investigated before, particularly for nuclear disposal barriers, where such cracking-healing behaviors due to continuous heating and drying are potentially happening and calling for more attention. Therefore, how such cracking-healing combined with effects from saturation degrees, dry densities and confinements will affect gas flow in terms of gas permeability for barrier material is in great need to be further investigated. This is also an aim of this research, i.e. to better understand how clay barrier materials behave upon heating and drying processes, and also to investigate how gas permeability will change as the moisture decrease and drying cracks evolve. This information will be instrumental to achieve a safe and optimal design of repositories for nuclear waste.

In Section 4, the experimental campaign with comprehensive gas migration tests, including gas permeability tests and gas breakthrough tests, will be introduced in detail. For gas permeability tests, samples with different test devices, different dry densities, different conditions, different cracking-healing patterns will be elaborated in detail separately.

4.2 Characterization tests

4.2.1 Test material MX-80 bentonite

The MX-80 bentonite from Wyoming (USA) is the material adopted in the whole experimental campaign. This clay has been adopted by some former researchers in several research projects aimed at investigating the performance of EBS for HLW. Several key properties of this clay make it a very appropriate barrier material, namely, extremely low permeability, self-healing ability, low ion transport capacity, high chemical stability, and high swelling potential.

This sodium bentonite is from American Colloid Company in Wyoming, in a state of grey powder (Figure 4.2). The average particle size is ranging between #40 and #200 sieve mesh. Water content in lab condition is around 11% and specific gravity (Gs) is 2.8. Some basic properties, including Atterberg limits, compaction curves, water retention curves have been investigated by some basic geo-tests and will be introduced in the following parts.

Figure 4.2 MX-80 bentonite

4.2.2 Atterberg limit tests

4.2.2.1 Liquid Limit (LL) tests

The liquid limit, plastic limit, and the plasticity index of soils are used extensively to correlate with engineering behavior such as compressibility, hydraulic conductivity, shrink-swell, and shear strength. The water content of this MX-80 under laboratory conditions is around 11%. Higher water content was achieved by mixing the bentonite and the required amount of distilled water.

In this part, liquid limit was measure by Casagrande liquid limit device based on ASTM D4318 with no deviations. We repeated tests twice to minimize the error and the average value of them is around 300%.

4.2.2.2 Plastic Limit (PL) tests

In this part, plastic limit tests were performed using rolling thread method based on ASTM D4318 with no deviations. This test was also conducted for three times, and the average result is 55%. Then the Plastic Index (PI) of this MX-80 bentonite will be 245%. These results are within common LL and PL values for this material.

4.2.3 Compaction tests

4.2.3.1 Standard compaction tests

For the compaction tests, standard compaction tests were performed firstly with stand compaction mold and hammer following ASTM D698. Soil materials were fully dried by the oven, and the samples with different target water content (0-70%) were prepared by adding distilled water. The results are shown in Figure 4.3. From the plot, it is obviously that the compaction curve is double peaks, and dry density with standard compaction effort is very low (maximum value around 1.25g/cm^3). At the beginning, due to the very sticky property of the soil, high friction force

exists between soil particles and the standard compaction effort cannot break it, so the dry density decreases with increment of water content, then with more water added working as lubricant, soil get denser and dry density goes up; finally, more voids will be occupied by water with continuing adding water, soil dry density decreases again in a same way as the tradition compaction curve.

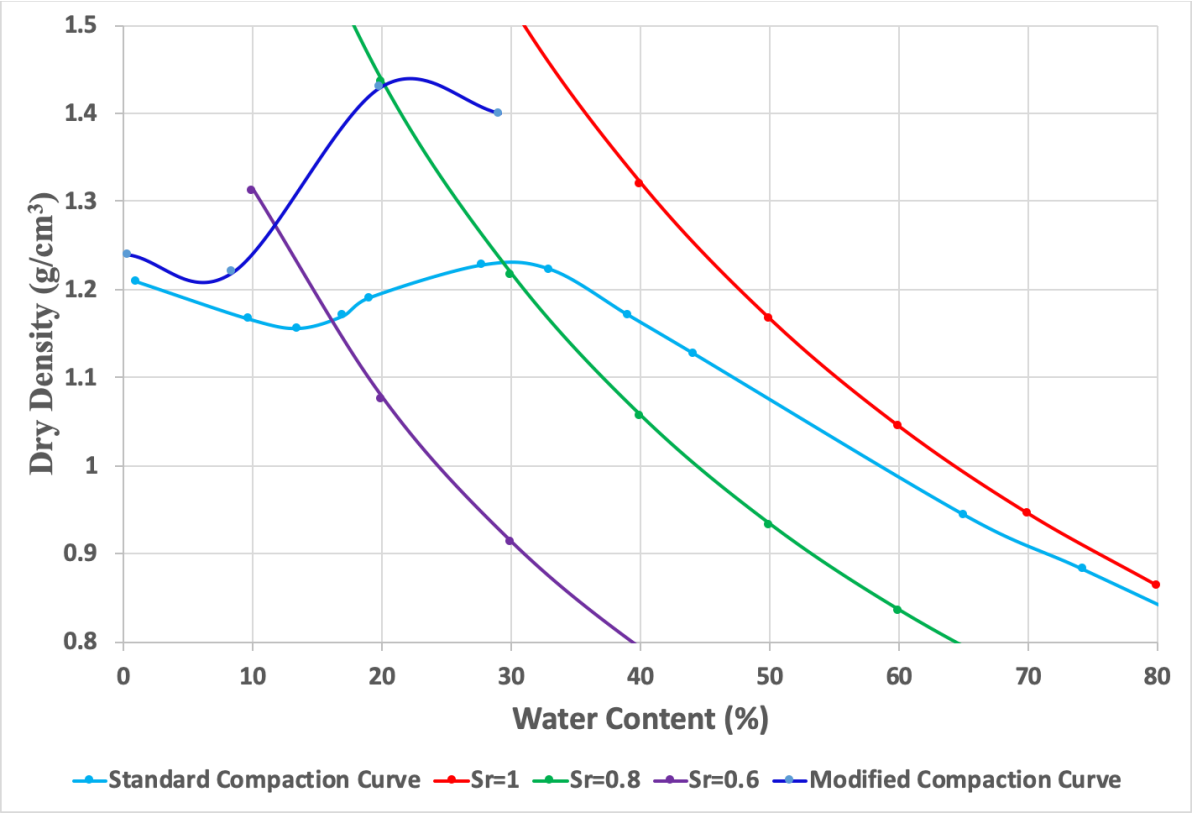

Figure 4.3 Compaction curve of MX-80

4.2.3.2 Modified compaction tests

In order to know how the curve develops with more compaction energy, we continued the modified compaction tests with larger mold and heavier hammer. Samples with target water content of 0, 10%, 20% and 30% were prepared as described in the former part. Then we

compacted the soil in 5 layers and 100 drops for each layer (usually 25 drops for modified compaction tests). Then another compaction curve is generated and the comparison of both (standard and modified) is shown in Figure 4.3 also. It makes sense that with higher energy compaction, the soil has higher maximum dry density, but the double peak phenomenon still exists there. This compaction tests results informed us that the dry density we targeted cannot be achieved by compaction, so we adopted static compaction equipment to prepare our sample.

4.2.4 Water retention measurement

Water retention curve, which relates the saturation degree with suction, is a critical unsaturated soil property. It can provide basic information for the future modeling and simulation work. In order to know the water retention behavior of MX-80 bentonite under different dry density, two dry density values, 1.3g/cm^3 and 1.6g/cm^3 were adopted and these two dry density values are what we used for the gas migration investigation. Both WP4 method and filter paper method were used.

4.2.4.1 WP4 method

WP4 (see Figure 4.4a)) is dew point potential meter, which can measure suction values by humidity equalizing in a small chamber. Suction values can be taken directly from the screen after equilibrium. In this part, soil samples were compacted using numerical load frame into small cylinders with similar dimension of the WP4 cup. Different dry densities were selected (i.e. 1.3g/cm^3, 1.6g/cm^3). For each dry density, samples with different water content were prepared and each water content will have three samples for obtaining average value. All the samples will be sealed in plastic bag for one-night equilibrium (see Figure 4.4b)).

a)

b)

Figure 4.4 WP4 and samples

4.2.4.2 Filter paper method

Filter paper test is a basic approach to measure the suction value of unsaturated soil samples. This method was adopted to compensate the WP4 results at high saturation degrees. The procedure of the test was followed ASTM D5298 with no deviations. All the glass containers were stored in a cooler with constant temperature for moisture equilibrium for two weeks. The optimized retention curve after combination and compensation is shown in Figure 4.5.

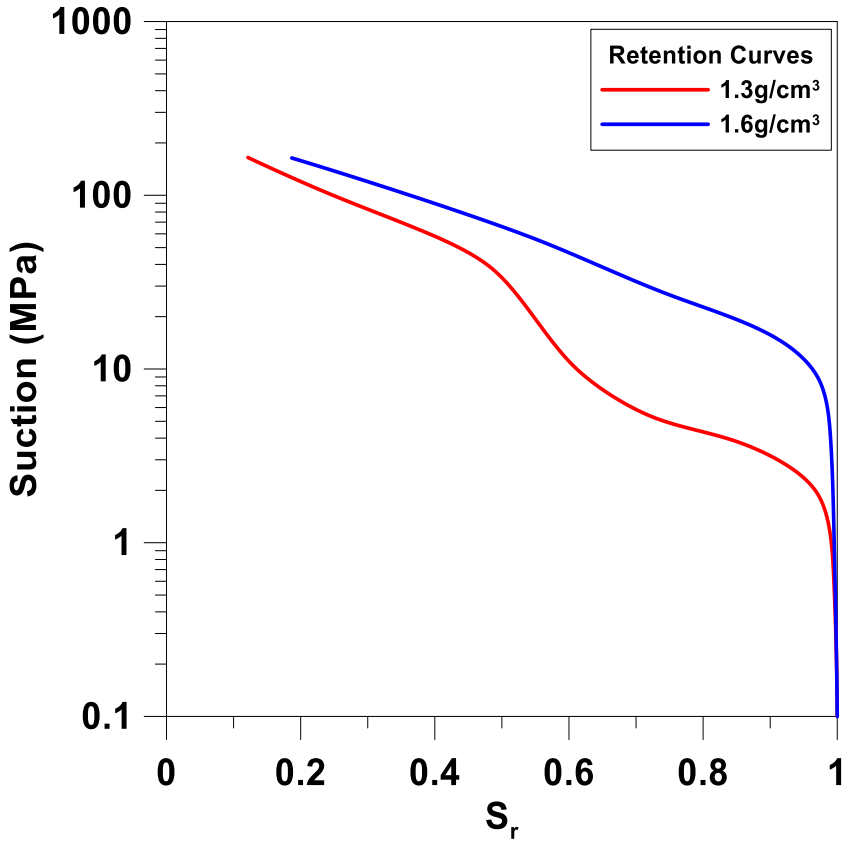

Figure 4.5 Water retention curves for samples with two different dry density values

4.2.5 Swelling tests

As a sealing material, nuclear waste barrier clay should show high swelling potential and as a result of that, high swelling pressure will be accumulated very high to hinder the migration of gas and prevent the release of nuclide to the environment. In this part, some swelling property related tests, including free swelling tests, swelling under loading tests, swelling pressure measurement tests will be introduced.

For swelling tests, we firstly performed the free swelling tests (i.e. sample with almost zero loading). Sample was prepared in a dimension of 2.5inches in diameter (i.e. same size of the oedometer ring) and 5mm in height (i.e. around 1/4 of the height of the oedometer ring). Samples

were compacted to target dry density values (i.e. 1.3g/cm^3 and 1.5g/cm^3). The tests were performed in oedometers with a thin porous stone on top of each sample to contact with the LSCT sensors. The whole setup is shown in Figure 4.6a. The hydration is from the bottom the sample.

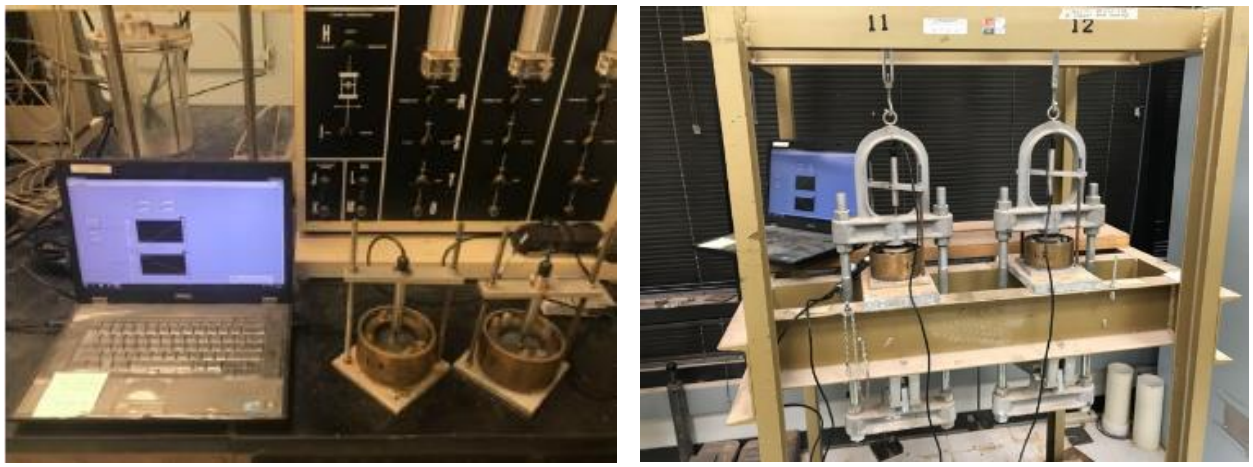

a) b)

Figure 4.6 Setups for swelling tests

From the results shown in Figure 4.7, it can be seen the higher dry density, the high expansion extent. The 1.3 g/cm^3 sample has an expansion around 350% while 1.5 g/cm^3 sample has an expansion of around 550%.

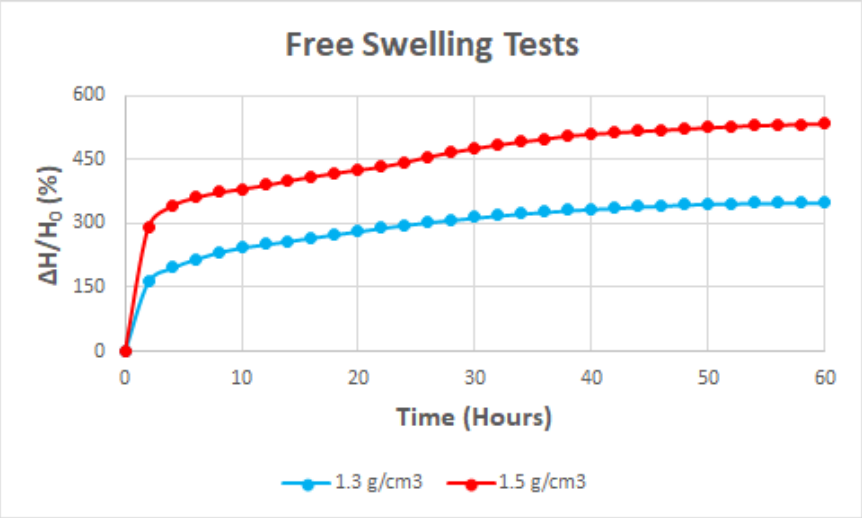

Figure 4.7 Free Swelling tests results

Swelling tests under loading were also conducted on sample with a dry density of 1.3g/cm^3. Samples were firstly compacted to target dry density and then were fixed to oedometers the same as the free swelling tests; mechanical load frames were adopted for providing loadings; different loading 0kPa, 50kPa, 100kPa, 200kPa, 300kPa, 400kPa were applied to the samples separately. Hydration is from the bottom of these samples. The setup is shown in Figure 4.6b.

We observed that expansion of samples decreases with the increment of applied loadings (see Figure 4.8). For higher loadings (i.e. 300kPa and 400kPa), collapse was observed and that can be explained by the movement of LC curve during wetting, the higher the loading, the nearer the stress state will be with the LC curve, wetting will force the LC curve to the right direction, which results in collapse. Also, the unexpected collapse pattern of higher loading aroused our interest in this topic and some cyclic wetting-drying tests with samples of different dry densities, under different loadings as well as different bentonite/sand mixtures are being performed for more research on these now and in the future.

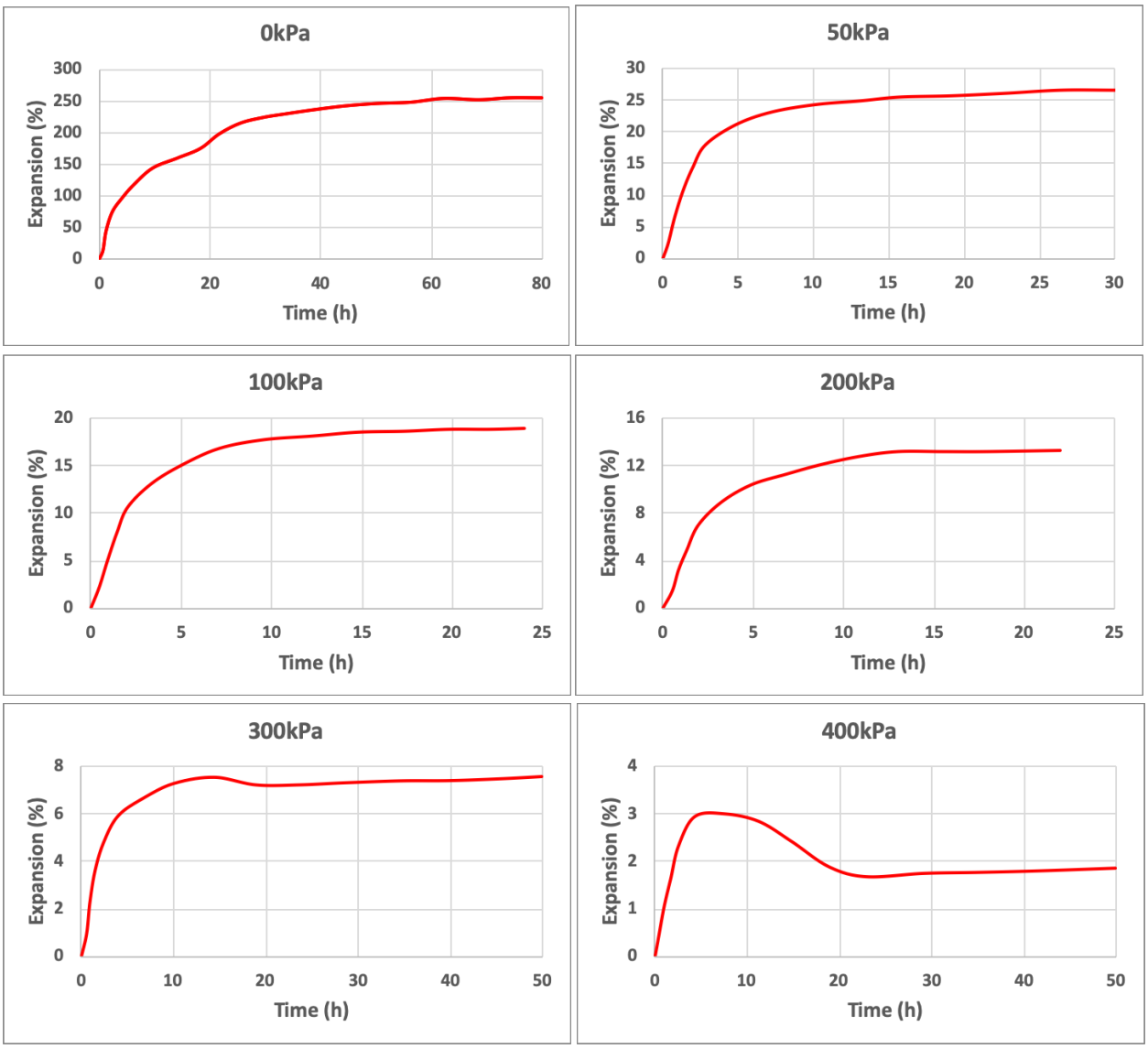

Figure 4.8 Swelling under loadings tests

Besides, tests with a swell-consolidation path was also conducted for sample with 1.3g/cm^3 dry density (see Figure 4.9). Sample was wetted and expanded under low loading first and then increase the loading to next load step when the expansion is finished. Then the cross point between the swell-consolidation curve and x axial when sample collapse under high loadings (i.e. return to initial sample height) is considered as the swelling pressure. In our tests, the 1.3 g/cm^3 dry density

sample has a swelling pressure of 0.45MPa, which is quite similar to the results we obtained by UPC oedometer that will be introduced in detail in the following.

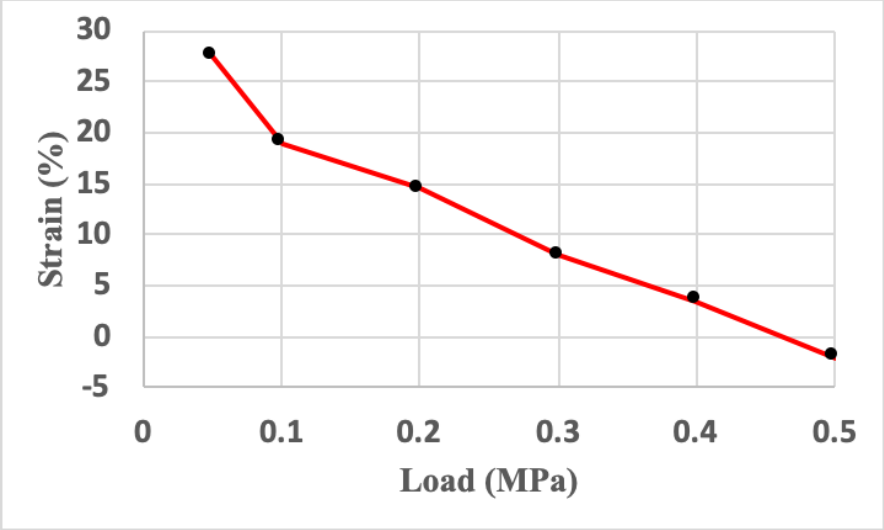

Figure 4.9 Swell-consolidation tests

Besides, swelling pressure of samples with different dry densities were measured by UPC oedometer, volume is maintained constant by load frame and hydration is from bottom of the sample by connected water pump. Swelling pressure was measure by calibrated high capacity load cell (i.e. 10000lbs) contact with the top of the UPC oedometer (Figure 4.10), LabView was adopted for showing and collecting data. The detailed introduction of UPC oedometer will be presented in Section 4.3.2. When the saturation is finished, the stress state shown on LabView will show stable and also water will show up in the pipe connected to the upper outlet which is on top of the sample.

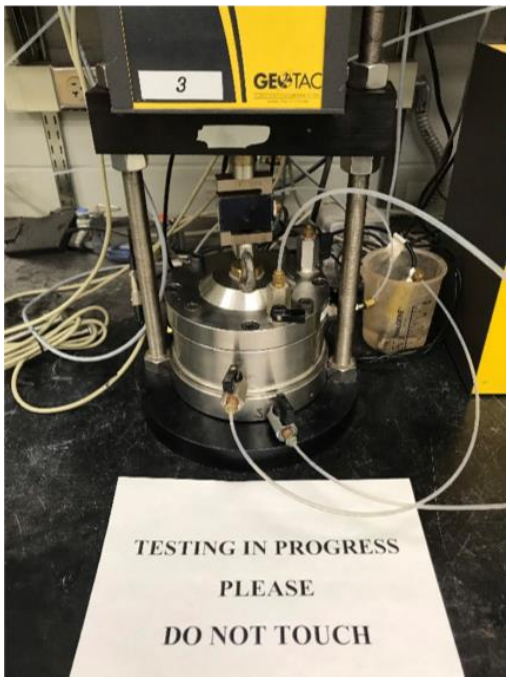

Figure 4.10 Setup for swelling pressure measurements

It can be obtained that higher the dry density is, the larger swelling pressure will be. The swelling pressure of 1.3g/cm^3 is measured with a swelling pressure of around 0.45MPa while the sample with 1.6g/cm^3 showed a swelling pressure of 2.7MPa (see Figure 4.11). Another obvious behavior of the constant volume tests is the double peak pattern, which is also found by some former researchers, which can be explained by double structure theory (Sanchez et al., 2005). With the wetting going on, at the beginning, macrostructure dominate and the elastic domain is enlarged due to wetting, resulting in collapse of the sample, However, with more wetting happening, microstructure swelling dominates in the sample, the swelling due to microstructure expansion is larger than collapse in the macrostructure, as a result of which, sample shows increasing swelling pressure again.

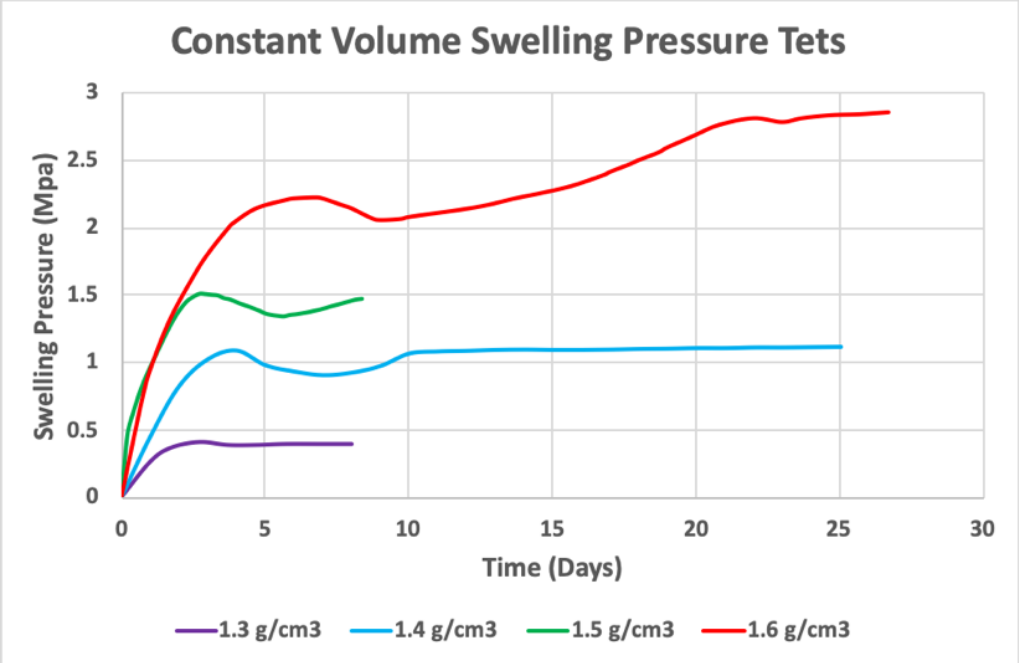

Figure 4.11 Swelling pressure tests

4.2.6 Test summary

In this part, some characterization tests were conducted to help us get better knowledge on this powder barrier material. Atterberg limits, compaction curves, retention curves were obtained. Besides, basic swelling properties of this nuclear waste barrier material were also investigated, including free swelling tests, tests under loadings, swell-consolidation as well as swelling pressure measurements tests, which can provide us a better understanding of swelling property of this barrier material. Larger dry density sample shows larger swelling tendency in both free swelling and swelling under loadings; for swelling pressure under constant volume, larger dry density sample has larger swelling pressure, double peak pattern is observed during swelling pressure measurements.

4.3 Gas migration tests in UPC oedometer

4.3.1 Introduction

This part mainly introduced how to adopt UPC oedometer to run gas permeability tests with constant volume during different hydration steps by vapor transfer technique. Two different dry densities are 1.3g/cm^3 and 1.6g/cm^3. For 1.3g/cm^3 sample, after vapor transfer, it was saturated to fully saturated and hydraulic permeability was also conducted with the UPC oedometer and pressure/volume controllers. Besides, gas break through tests were also tried but no breakthrough happened within the capacity of UPC oedometer. The main goal in this part is to establish relationships among gas permeability, swelling pressure and suction under different steps of the hydration process for the barrier material with different initial dry densities, which needs to be more investigated. Some former researchers were focus on relationship between swelling pressure and suction (Wang et al., 2012), some focused on the relationship between gas permeability and saturation degrees (Tanai et al., 1997, Liu et al., 2015). Therefore, this research can help to widen current research and provide a better and more systematically understanding of barrier material.

4.3.2 UPC oedometer

The UPC oedometer cell is designed for pneumatic loading with a diaphragm pressure. There is one upper chamber (for vertical loading), and one lower chamber (for suction controlled specimen) in this cell. A 1mm membrane is used to separate the upper chamber from the lower. A piston attached to the membrane is sitting on the top of the specimen in the lower chamber, thus transferring the upper chamber pressure to the specimen. Figure 4.12 shows the schematic of the UPC oedometer cell and Figure 4.13 shows the components of the oedometer.

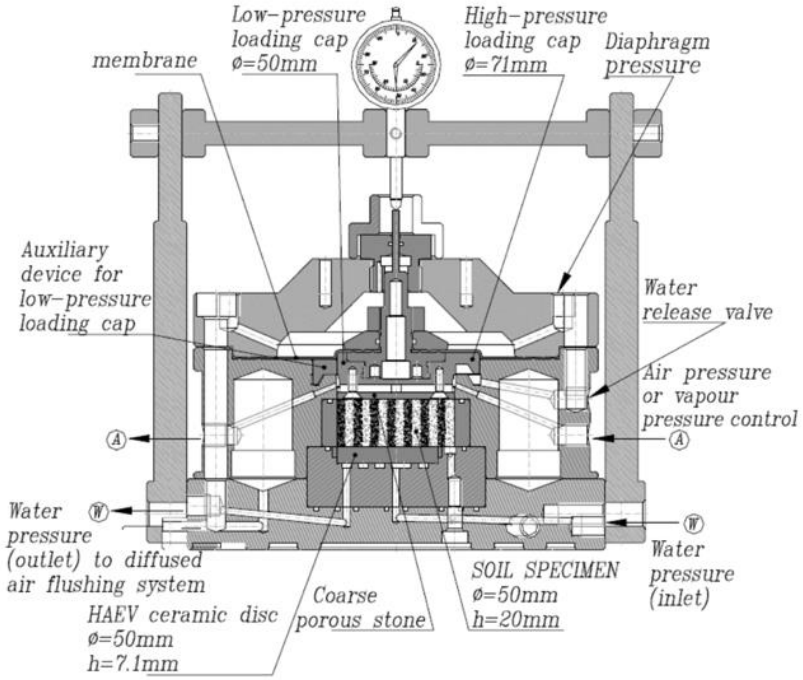

Figure 4.12 Schematic diagrams of UPC oedometer

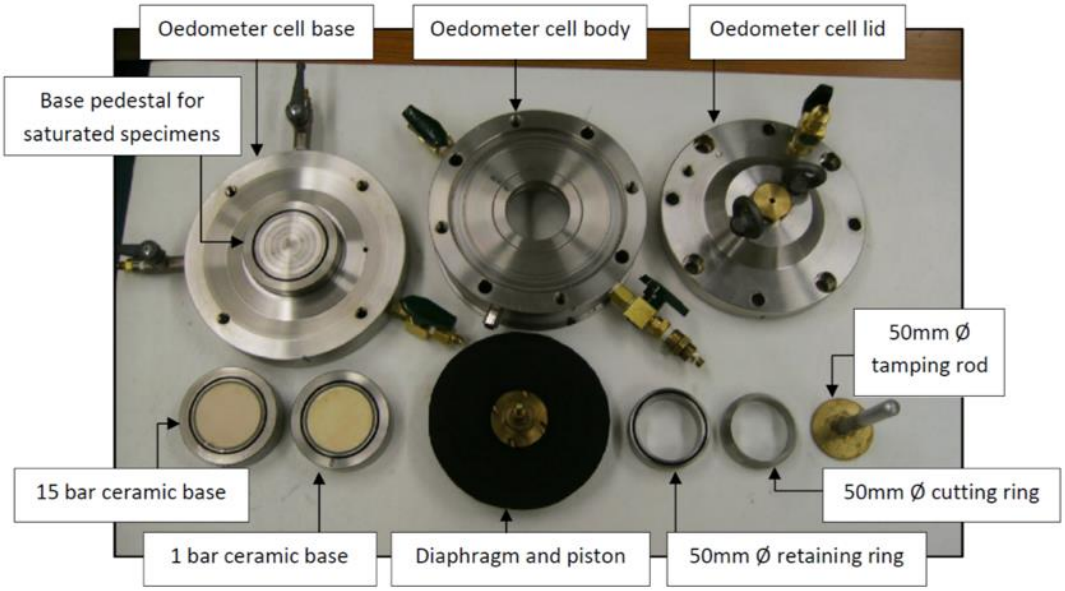

Figure 4.13 Components of UPC oedometer

Two different specimen bases are used for UPC oedometer cell, aiming for different purposes. One is concentric metallic ring; this base has a high permeability and is suitable for saturated specimens as well as for suction control using vapor transfer technique. The other kind is a high air entry value ceramic plate. The high air entry value ceramic plate is an essential component for unsaturated soil test using axis translation technique. This plate separates the air pressure and water pressure, so that the difference between water and air pressure can be maintained as the matric suction. Two ranges of air entry value are available for this cell, namely, 1 Bar (100kPa), and 15 Bar (1.5MPa). Air is not able to pass the saturated ceramic plate if the suction value is less than the air entry value.

4.3.3 Tests outlines

The outlines of gas migration tests are listed as follows:

- MX-80 bentonite in powder was tested in different dry densities (i.e. 1.3g/cm^3, 1.6g/cm^3), and the corresponding retention curves were already obtained by both WP4 and filter paper methods;
- Preference pathway through the soil-metallic ring contact is minimized by a thin glued sand-bentonite mixture layer;
- Different larger suction values (i.e. larger than 4MPa) were planned to be controlled by vapor transfer technique in a hydration path (i.e. wetting sample using a series of salt solutions);
- Axis translation technique with high air entry value (HAEV) disk can also be a choice to be adopted for controlling smaller suctions (i.e. smaller than 1.5MPa);
- Nitrogen in gas is injected from the bottom of the soil specimen;

- Gas permeability under different stable suction (i.e. saturation degree) of soil specimen are measured using mass flowmeter;
- Relationships between suction, stress and gas permeability during swelling are obtained.

4.3.4 Test procedures

Before run the tests, sample preparation is critical and need to be pay much attention. In order to minimize the problem of preference pathway through the soil-metallic ring contact, we 3D printed a same size ring and super-glued a thin layer of sand-bentonite mixture to make the inner wall coarser.

Table 4.1 Hydration steps by vapor transfer technique

Step #	Salt Type	Controlled Suction (MPa)
1	$Ca(NO_3)_2 \bullet 10H_2O$	92
2	$NaNO_2$	57
3	NaCl	39
4	KCl	24
5	KNO_3	11
6	K_2SO_4	4

Vapor transfer technique was adopted to change the relative humidity of the sample in a hydration way, the hydration steps by different salts were divided into six (Table 4.1). For $1.3 g/cm^3$ sample, we used the salt solution for vapor transfer at the beginning then distill water for lower suction control. There will be a small checking cell (i.e. much smaller size sample with same dry density as well as filter paper is place inside) in the pipeline to help check and control suction

values. After some checking tests, using the small sample in the checking cell to predict the suction in the large sample is reliable. Sample was compacted under measured room humidity (i.e. around 120MPa) to target dry density 1.3 g/cm^3 and after the sample is ready, the whole system is set up as shown in Figure 4.14. A pump is driving air into the salt solution and then to a filter bottle (i.e. to avoid congealed liquid contact with sample); then the air goes into a small sealed cell that includes both a same dry density small size sample and filter paper for checking the suction value inside the oedometer in a simple and feasible way. A pipe is connected the sealed small cell to the bottom inlet of the oedometer (i.e. bottom if the sample). After the vapor goes through the sample, the outlet on top of the sample will be connected to the pump to make up the whole circuit. Swelling pressure was measured by calibrated high capacity load cell (i.e. 10000lbs) contact with the top of the oedometer; gas permeability will be measure using steady state method with volume/pressure controller, pressure gauges, 0-1000ml/min flowmeter. Steady state method has been successfully adopted in previous investigations (Liu et al., 2015, Wei et al., 2019, Joseph et al., 2019, Xu et al., 2020). Temperature and relative humidity of the lab environment is monitored all the day by temperature-humidity recorder; stress state is shown and recorded by LabView software. Relationships between suction, stress and permeability during swelling can be obtained. Test results are shown in 4.3.5. the relationship between swelling pressure and suction can be obtained well, but gas permeability seems changed a little during this wetting (Figure 4.17), which is a little weird. We guess that may due to the interface problem exist because the dry density is low and the sample is still with a S_r smaller than 60%. So, we tried a denser sample, 1.6g/cm^3. In order to shorten the wetting time, with the help of the checking cell, we adopted distill water for vapor transfer technique directly at the beginning. For this sample, suction was measured many times during the wetting, together with swelling pressure and gas permeability. Since the gas

permeability change is more obvious than 1.3g/cm^3 sample (Figure 4.17), After the last wetting step by vapor we did not fully saturate the sample but started a cyclic wetting and drying tests to study on the effect from wetting-drying cycles. The results of 1.6g/cm^3 are introduced in 4.3.5. Moreover, in order to check whether the interface problem is avoided in these tests, gas permeability tests using triaxial cell with a membrane holding the sample were also performed for both 1.3g/cm^3 and 1.6g/cm^3 samples. This will be introduced in 4.4.

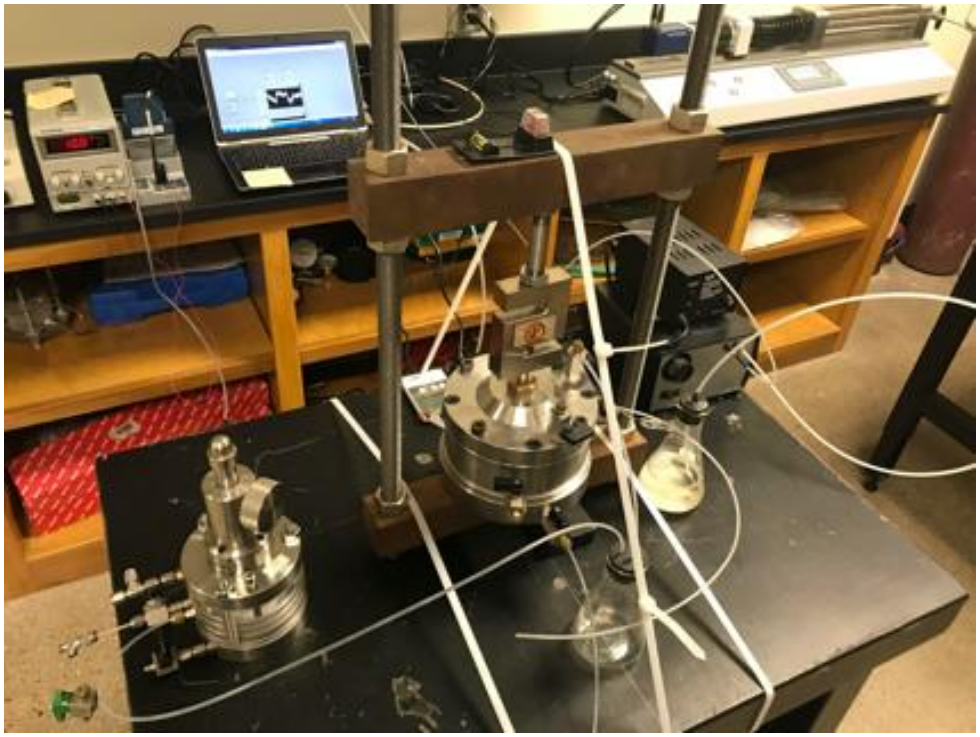

Figure 4.14 Whole setup of the tests

4.3.5 Tests results

For 1.3g/cm^3 dry density sample, after six salt solutions and distill water, the swelling pressure vs. time curve is shown in Figure 4.15 below, suction values during the hydration were measure and is denoted as red points in Figure 4.15, also some gas apparent permeability values

during hydration were also obtained and denoted as green points on the same figure. For gas permeability tests, on each selected point, two different tests of different constant flow rate were performed (i.e. 100ml/min and 200ml/min) and we calculate the average value to consider as gas permeability.

From Figure 4.15, it can be observed that swelling pressures decreased during the 6th step and shows the double peak pattern as former swelling pressure tests we performed. The swelling pressure is around 0.55MPa which is also quite similar as our former tests before.

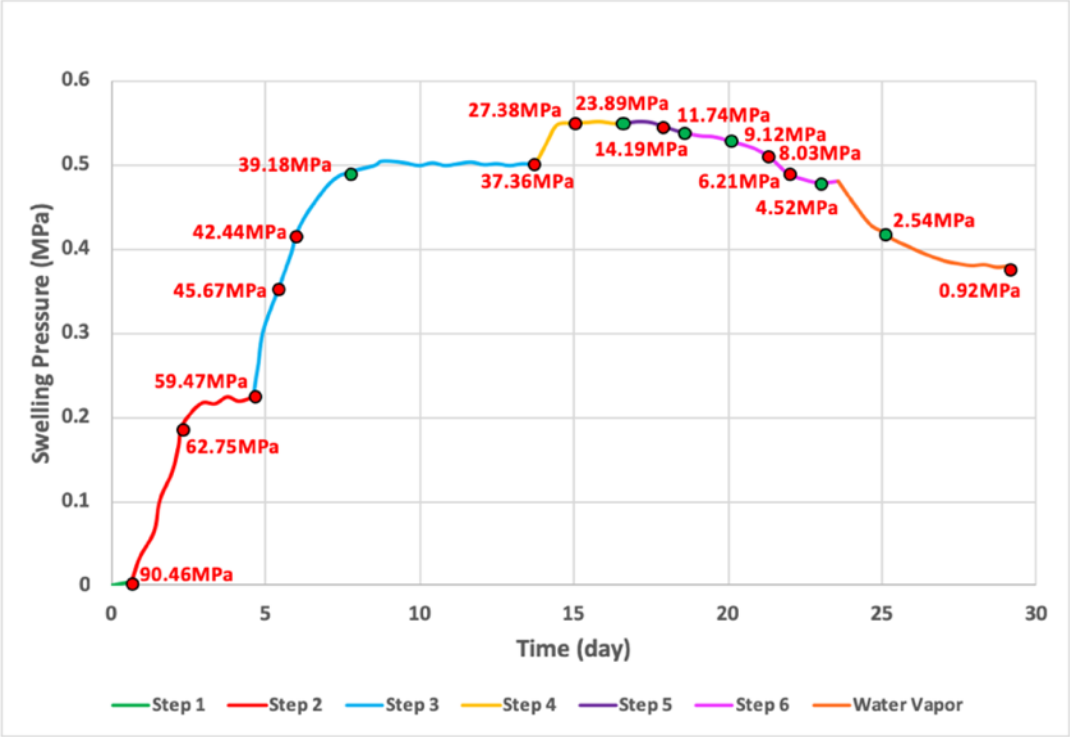

Figure 4.15 Gas migration tests at different hydration steps using vapor transfer technique

Also, the suction-stress relationship curve is also obtained and is shown in Figure 4.16 below, it is obvious that swelling pressure decreased at high saturation with the decrease of suction,

which shows consistency with our former tests. The gas permeability values of the green points are shown in Figure 4.17. Only results of 200ml/min flow rate is shown here because the sample is lose and 100ml/min injection flow rate cannot result in large enough pressure changes. We can also find that the gas permeability decreased a little with the hydration proceeding and swelling pressure increasing. This is a little strange and it arose our plan to check whether the interface problem is avoided with the glued layer, gas permeability tests using triaxial cell with a membrane holding the sample were also performed and will be introduced in 4.4.

After vapor transfer technique, the sample is hydrated with distill water directly to reach fully saturated, the upstream pressure liquid injection pressure was 3MPa and the downstream liquid back pressure was 0.5MPa, after around 50 days hydration, when flow-in more or less is equal to flow-out, we performed a waster permeability test for 1.3g/cm^3 sample also, obtaining a value of 0.2×10^{-12}m/s, which is in a reasonable range.

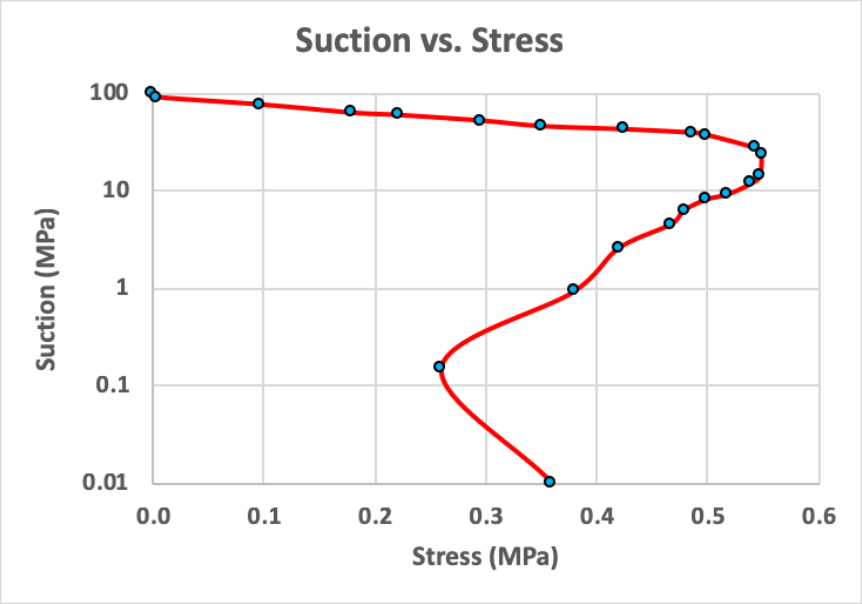

Figure 4.16 Evolution of swelling pressure with suction

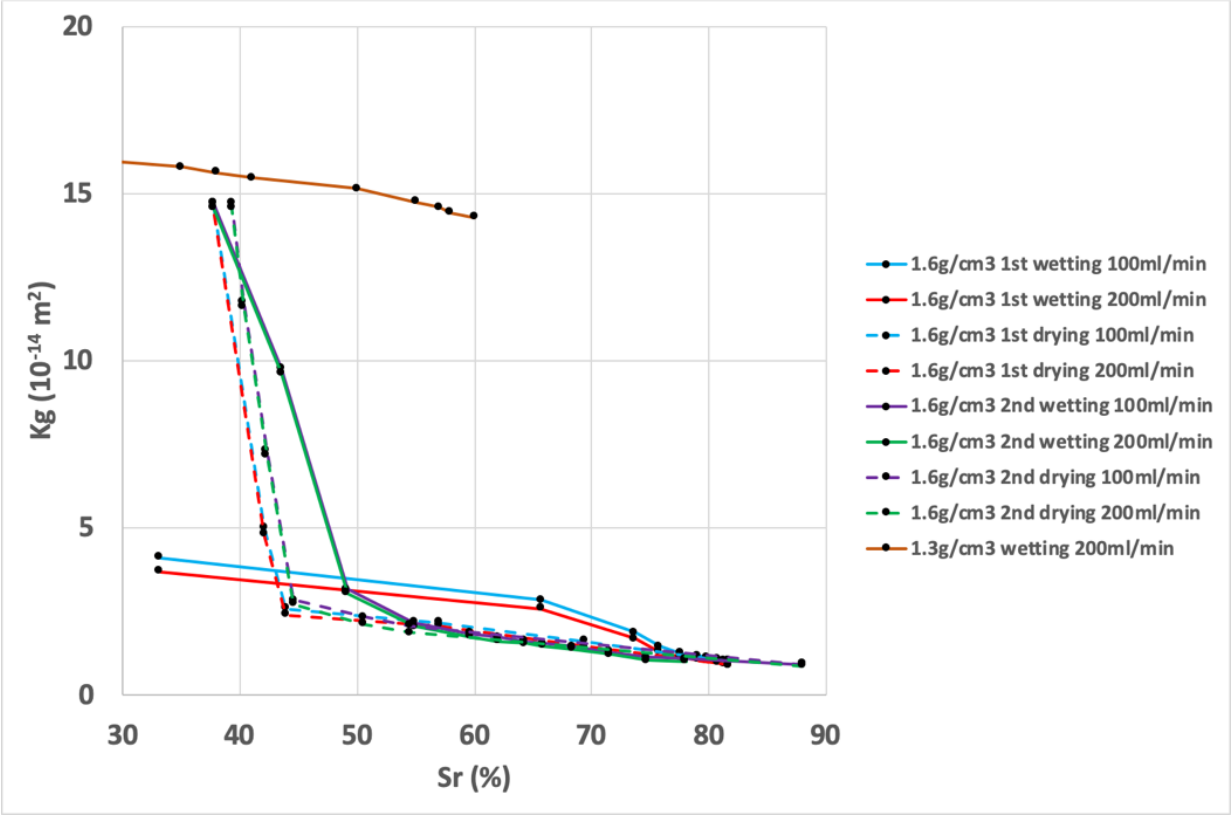

Figure 4.17 Gas permeability of samples with two different initial dry densities

For 1.6g/cm^3 dry density sample, we conducted a similar test as 1.3g/cm^3, the only difference is that we used distill water vapor all the time. For this sample, we conducted cyclic test with 2 wetting-drying cycles. The gas permeability curve with selected points are shown in Figure 4.17. We noticed that the gas permeability evolutions are quite different between wetting-1 and the successive drying-1, wetting-2 and drying-2 although the values are quite similar for drying-1, wetting-2 and drying-2 under high saturation degrees (S_r > 50%). At higher saturation degree (S_r > 50%), gas permeability values are larger in wetting-1 than the rest wetting and drying processes, this is because macro soil structure vanished during first wetting, resulting in lower gas permeability, and this change is not recoverable. At saturation degree lower than 50%, the sudden

change of gas permeability values in drying-1, wetting-2 and drying-2 is because the sample is more easily got detached from the ring as a result of cyclic wetting and drying processes. From 2nd drying-wetting, the evolution of gas permeability according to saturation degree is becoming stable; this is similar to volume change of expansive soil under cyclic wetting-drying, which is already well known. Under low saturation degrees (S_r<50%), gas permeability evolution is following two different lines for wetting and drying. Detailed information for wetting-1, drying-1, wetting-2 and drying-2 are shown in Figure 4.18 to Figure 4.21. If compare with 1.3g/cm^3 sample, the change in gas permeability during wetting was much larger.

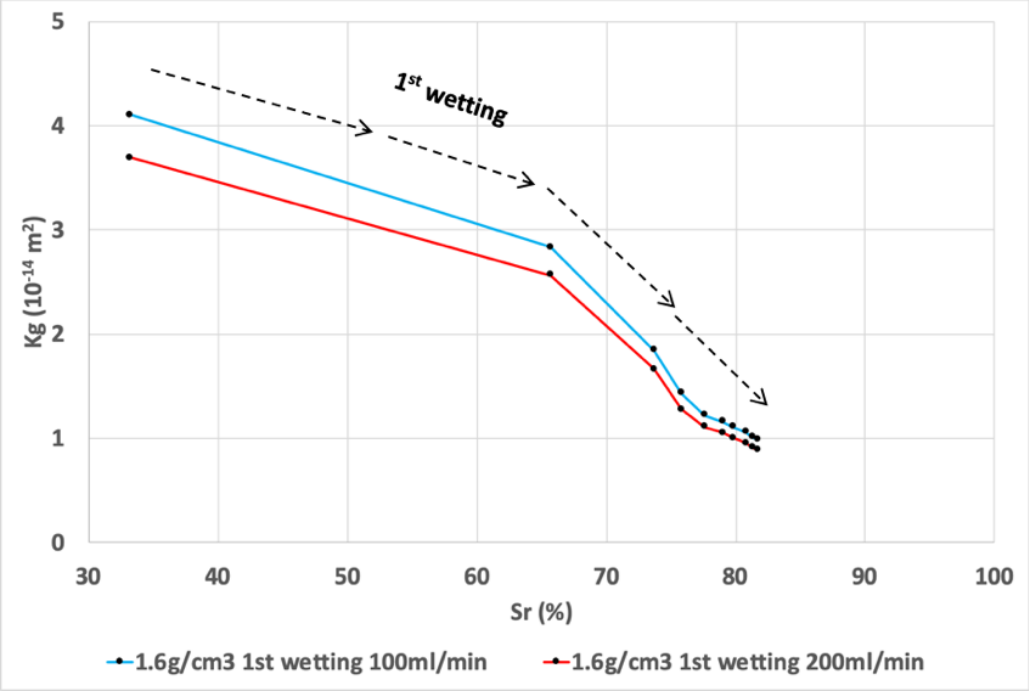

Figure 4.18 1st wetting for 1.6g/cm^3 sample

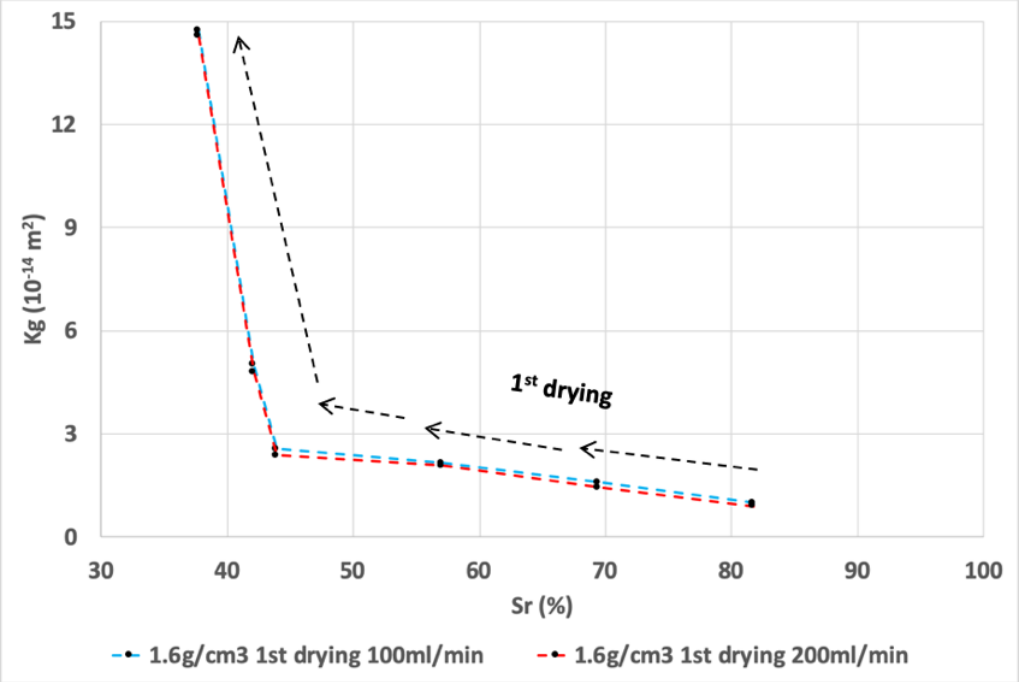

Figure 4.19 1st drying for 1.6g/cm3 sample

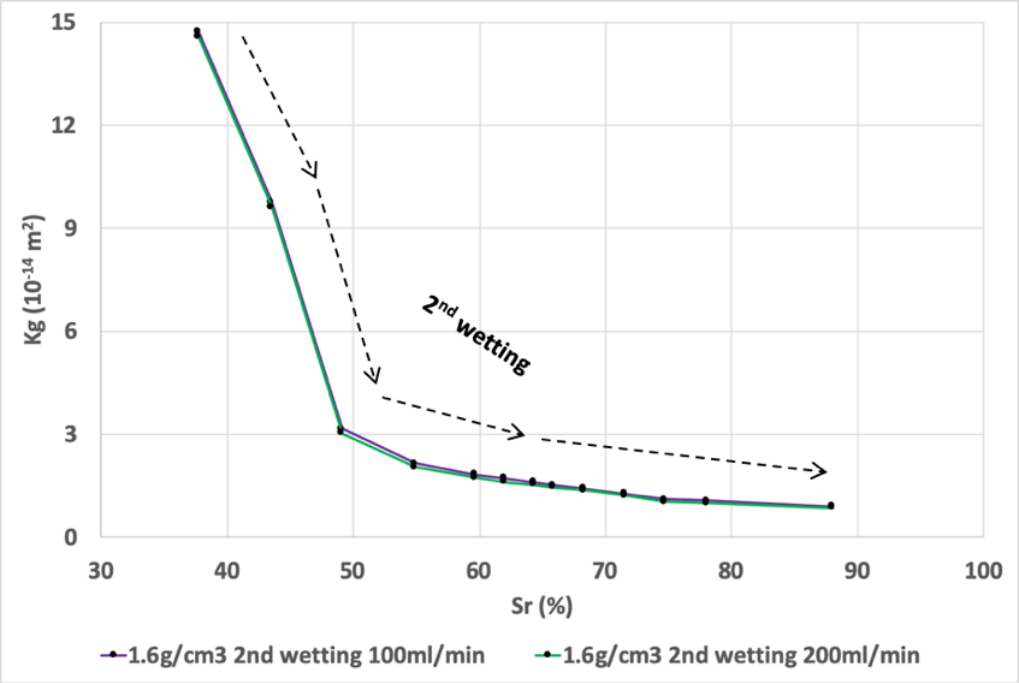

Figure 4.20 2nd wetting for 1.6g/cm3 sample

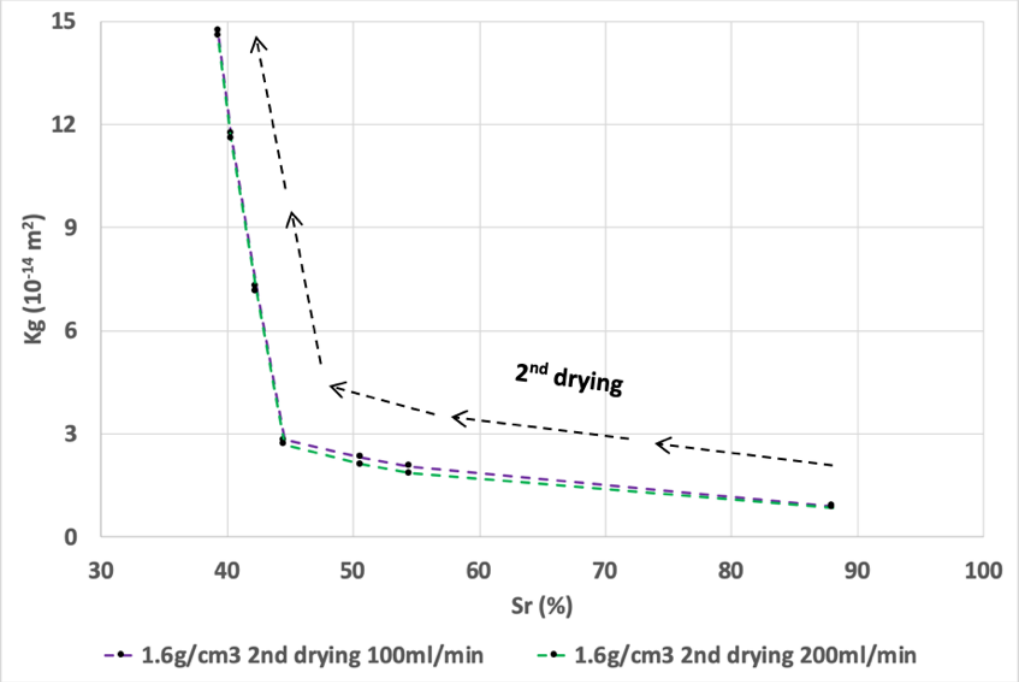

Figure 4.21 2nd drying for 1.6g/cm^3 sample

The swelling pressure and S_r evolutions with time for 1.6g/cm^3 are shown in Figure 4.22 and Figure 4.23. Another interesting phenomenon observed is that the swelling pressure in wetting-2 is less than that in wetting-1, this can also give credit to soil structure change due to cyclic wetting-drying. Besides, at the end of each drying process, the swelling pressure cannot return to 0; the residual swelling pressure is due to some historic effects.

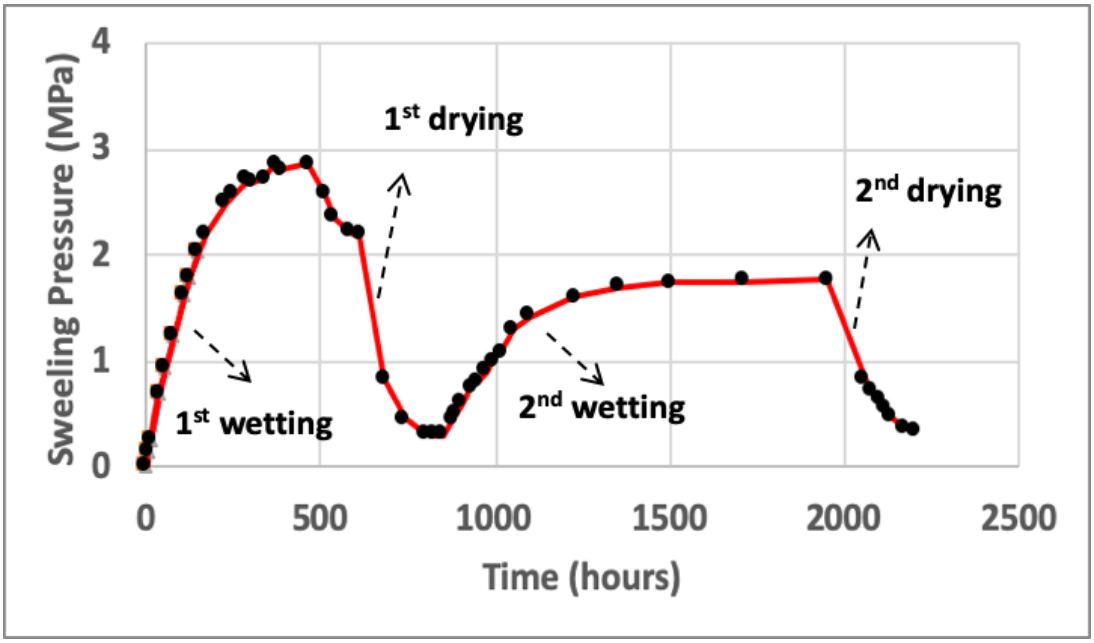

Figure 4.22 Evolution of swelling pressure with time

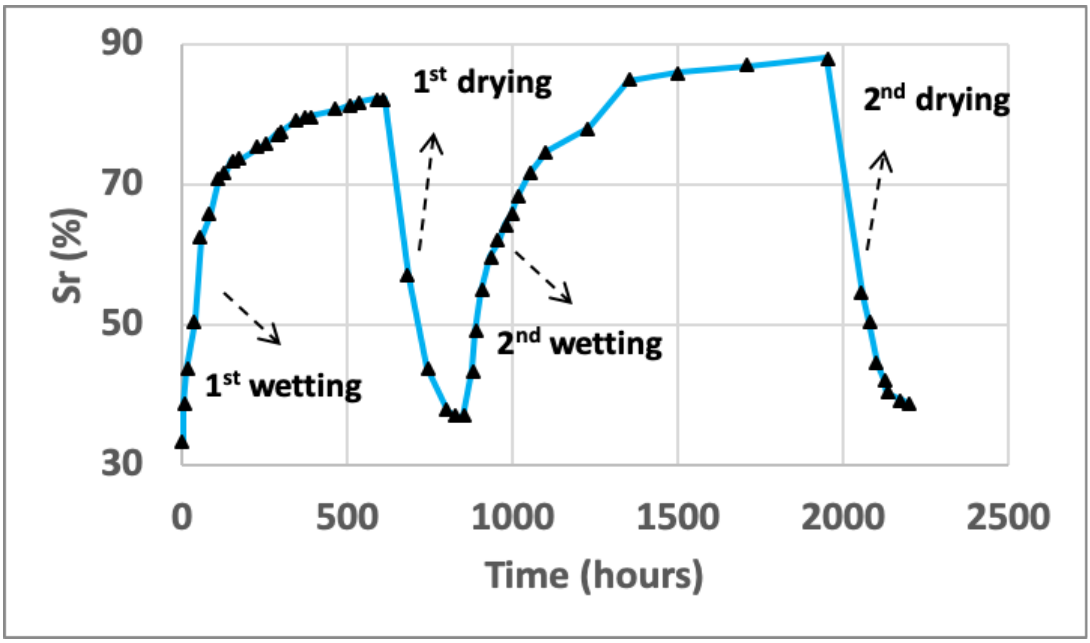

Figure 4.23 Evolution of Sr with time

4.4 Gas migration tests in triaxial cell

4.4.1 Introduction

In section 4.3, we planned to link suction, swelling pressure and gas permeability, all the gas permeability tests were performed with constant volume in the UPC oedometer cell. We tried to minimize the interface problem by a glued layer of bentonite on the inner wall of the ring, but we are not sure whether the interface problem is solved or not. So, some gas permeability tests were also performed by triaxial cell as a backup (i.e. triaxial cell can solve the interface problem and has been adopted by former researchers). The same dry density values as section 4.3 were used here and the confinement for maintaining constant volume is applied by cell pressure (i.e. always larger than injection pressure to solve interface problem). Since the triaxial cell cannot hold high pressure, just gas permeability values were obtained here, working as a backup for the relationships created in section 4.3. Two group of samples with different dry densities (i.e. 1.3g/cm^3 and 1.6g/cm^3) were measured here, under a series of saturation degrees from 0% to 97%. Steady state method was also adopted in this part for measuring and calculating gas permeability values.

4.4.2 GEOTAC triaxial cell

All the tests performed in this part were by the triaxial cell from GEOTAC. This is an automated stress path system consisting of a Sigma-1 load frame, two Digi-Flow pressure volume actuators (i.e. flow pumps), and a high-resolution analog data acquisition system. These components are connected to a computer through TestNet. Cell pressure can be applied under the control of TruePath software installed on the computer. Liquid water was used for applying cell pressure and it can reach as high as 125psi. A high-precision mass flowmeter was adopted to measure the gas outflow and a liquid filter from Swagelok was connected before the flowmeter to

eliminate the moisture. Figure 4.24 shows the adopted setup to conduct the gas permeability test. Nitrogen gas was adopted for the tests.

Two valves were adopted to control gas-in and gas-out. Gas was injected from upstream, through the sample then out at downstream. Then after the filter, gas will go through the mass flowmeter and the gas flow rate will be obtained. Samples were prepared in the same way as in section 4.3 but the size for the triaxial cell is 3.5cm in diameter and 1.4cm in height. The reason for this is that the base for sample in the triaxial cell is just 1.4 inches, besides, we want to keep the ratio between diameter and height the same as the sample in UPC oedometer.

Figure 4.24 Setup for gas permeability tests with triaxial cell

4.4.3 Test outlines and procedures

In this part, all the gas permeability tests were conducted based on the following procedures:

(1) Prepare the sample with target saturation degrees and initial dry densities;

(2) Setup the sample in the cell and then fill the cell with distill water;

(3) Connect the cell pressure pipe, gas injection pipe and out-flow pipe together with a liquid filter and mass flowmeter;

(4) Set the cell pressure, open the flow-in valve and flow-out valve, then inject the gas;

(5) When upstream gas pressure (i.e. obtained from pressure gauge on regulator) and gas outflow (i.e. obtained from mass flow meter) are getting stable, record the upstream pressure as well as the gas out flow rate;

(6) Dismantle the cell and performed the next test with another saturation degree, then sample with another dry density and with different saturation degrees.

4.4.4 Test results and discussions

The gas permeability (K_g) results for samples with these two dry densities under different confinements are shown in Figure 4.25 below. It can be observed that higher dry density sample ($1.6g/cm^3$) is less permeable for gas when compared with lower dry density sample ($1.3g/cm^3$), this is because the porous space is smaller in denser samples. Besides, with the increment of water saturation degree, gas permeability decreased a lot until impermeable at S_r larger than 90%. In terms of confinements (i.e. cell pressure in CP), higher confinements tent to result in lower gas permeability in both of these two samples, this makes sense because higher cell pressure will compress the sample a little bit more to make the penetration path narrower. For $1.3g/cm^3$ sample, S_r under 30% was not shown because sample will be very easily broken up when after compaction under low saturation degrees.

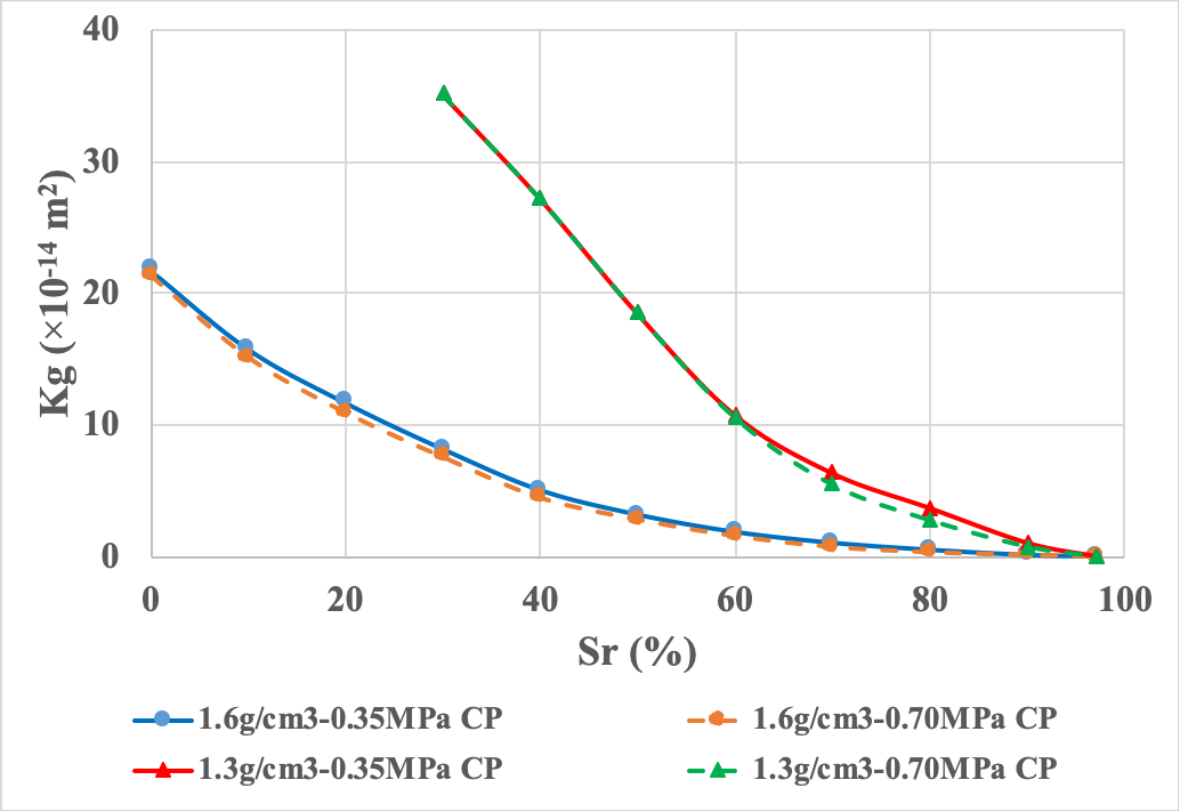

Figure 4.25 Gas permeability for compacted samples with different Sr

4.4.5 Test summary

Gas permeability tests by triaxial cell can work as a backup for the relationship between S_r and K_g, this can also be a good reference for tests conducted with cracking-healing behavior introduced in Section 4.7. Samples with higher saturation degrees and larger dry densities tend to be less permeable to gas. Confinements have a little influence to the gas permeability of compacted barrier material that larger confinements result in smaller gas permeability values. When compare with results from UPC oedometer, differences due to test methods can be found and the reliable S_r range of UPC oedometer to predict gas permeability for 1.6g/cm^3 dry density sample was also evaluated.

4.5 Gas breakthrough test

4.5.1 Introduction

As discussed above, in samples with low water saturation degree, gas permeability is mainly adopted to evaluate how easy it is for the gas to penetrate the HLW barrier material. However, when under high saturation degree, gas may not be easy to penetrate the sample due to high pore pressure and continuous liquid phase with high saturation inside the sample, gas pressure may be accumulated to tens of MPa and finally a preferential pathway through the sample is generated and gas will break through the barrier system, as a result of which, nuclear waste will be brought to and jeopardize the environment. Therefore, how much gas pressure the barrier system can hold is key for this potential problem.

The earliest papers on gas migration in clay relating to radioactive waste disposal were published by Pusch and co-workers in Sweden. Saturated Mx-80 bentonite was used in the experiments. Pusch and Forsberg, 1983 examined the gas permeability of this clay after gas breakthrough. They found that the breakthrough pressure was of the same order of magnitude as the swelling pressure. Hokari et al, 1997 undertook gas migration experiments on compacted mixtures of sand and bentonite. They measured water permeability first and then gas permeability after outflow was observed in the downstream. The threshold pressure of breakthrough is very low when compare with pure bentonite. Galle and Tanai, 1998 described a program of gas migration experiments on Fo-Ca clay and he defined two different thresholds for gas breaking through. Increments of 0.1 to 0.05 MPa gas pressure were applied for periods of 12 to 24 hours. Tanai et al, 1997 also examined the relationship between the dry density, the swelling pressure and the breakthrough pressure of saturated Kunigel VI and French Fo-Ca clay. Gas pressure was raised in increments of 0.5 MPa, applied at time intervals of 120 hours. They found that breakthrough pressures were close to the measured swelling pressures for both clay-types. **Hume, 1999** reported

a detailed laboratory study on compacted Avonlea (or Saskatchewan) bentonite. They used a faster injection rate (increment of gas pressure was 1MPa every 5minutes until the capacity of the cell, 50MPa) and found that consistent breakthrough cannot be obtained for sample with dry density larger than 0.6g/cm^3 when they rehydrate the sample in 2 days with a liquid pressure of 5MPa. They also maintained constant pressure to obtain the breakthrough time and the time to breakthrough was likely to be determined by the time required for water to flow from the specimen so as to create a passage for gas. Horseman et al., 1999 reported a series of controlled flow rate gas injection experiments on pre-compacted Mx-80 buffer bentonite under isotropic stress condition. Harrington and Horseman, 2003 extended this research by adopting new device capable of monitoring stress and pressure changes. Villar et al., 2013 performed gas breakthrough of barrier material FEBEX with interface between different materials (bentonite and bentonite, granite and bentonite). In terms of methods to measure gas passage through a liquid saturated sample, many different methods were adopted by former researchers (Thomas et al., 1968; Egermann et al., 2006, Hildenbrand et al., 2002; Horseman et al., 1999), e.g. step-by-step, dynamic, residual etc.

In our current research according to the topic of gas breakthrough in barrier material, we planned to find out under constant volume, what will be the gas breakthrough pressure of a target dry density sample under given gas injection flow rate with evaluations of interface problems between the steel cell inner wall and sample by trying different gas inlet and outlet connections. A 1.05g/cm^3 dry density sample is presented in this part and tests were performed with a self-manufactured high-capacity steel TAMU gas breakthrough cell, the details of the cell are also introduced in the following parts.

4.5.2 TAMU gas breakthrough cell

This cell is mainly made up of three parts (i.e. one steel tube in the middle and two steel caps on both end). The two same caps are consisted of a plate and a base (see Figure 4.26). The whole cell is sealed with O-rings and constrained with 6 high capacity threaded steel rods around the edges as shown in Figure 4.26. The overview and schematics of the cell can be found in Figure 4.26 below. The dimensions (i.e. all units on figures showing dimensions of this cell are in inches) of the steel tube are shown in Figure 4.27 and the inner diameter of it is 5cm, which is also the diameter of the sample. The thickness of the tube is 2cm (i.e. high capacity) and there are two grooves on both sides of the tube to position the O-ring that used for sealing.

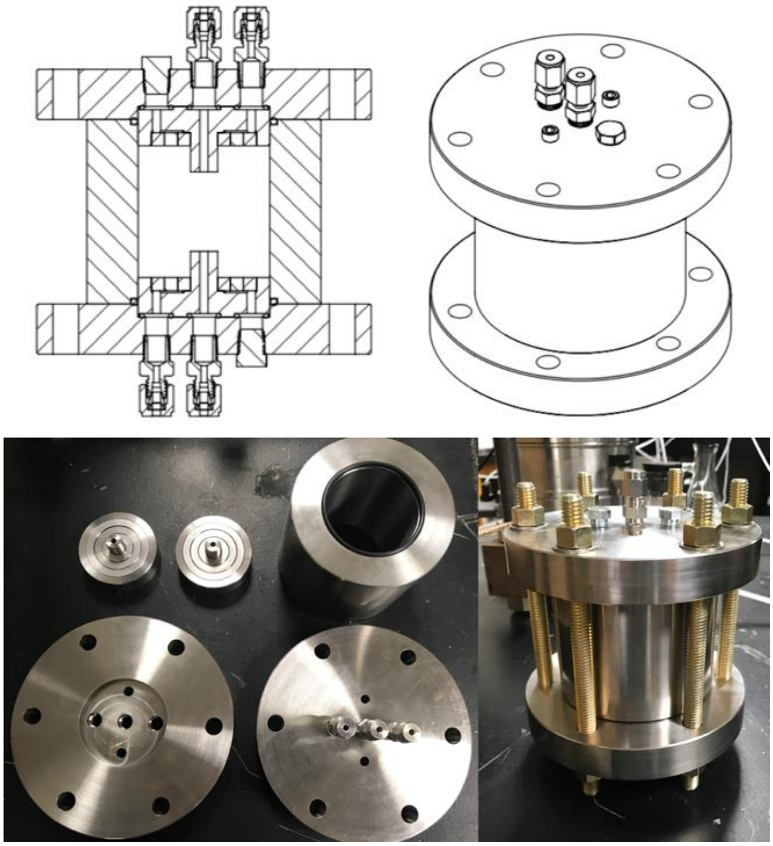

Figure 4.26 Overview of gas breakthrough cell

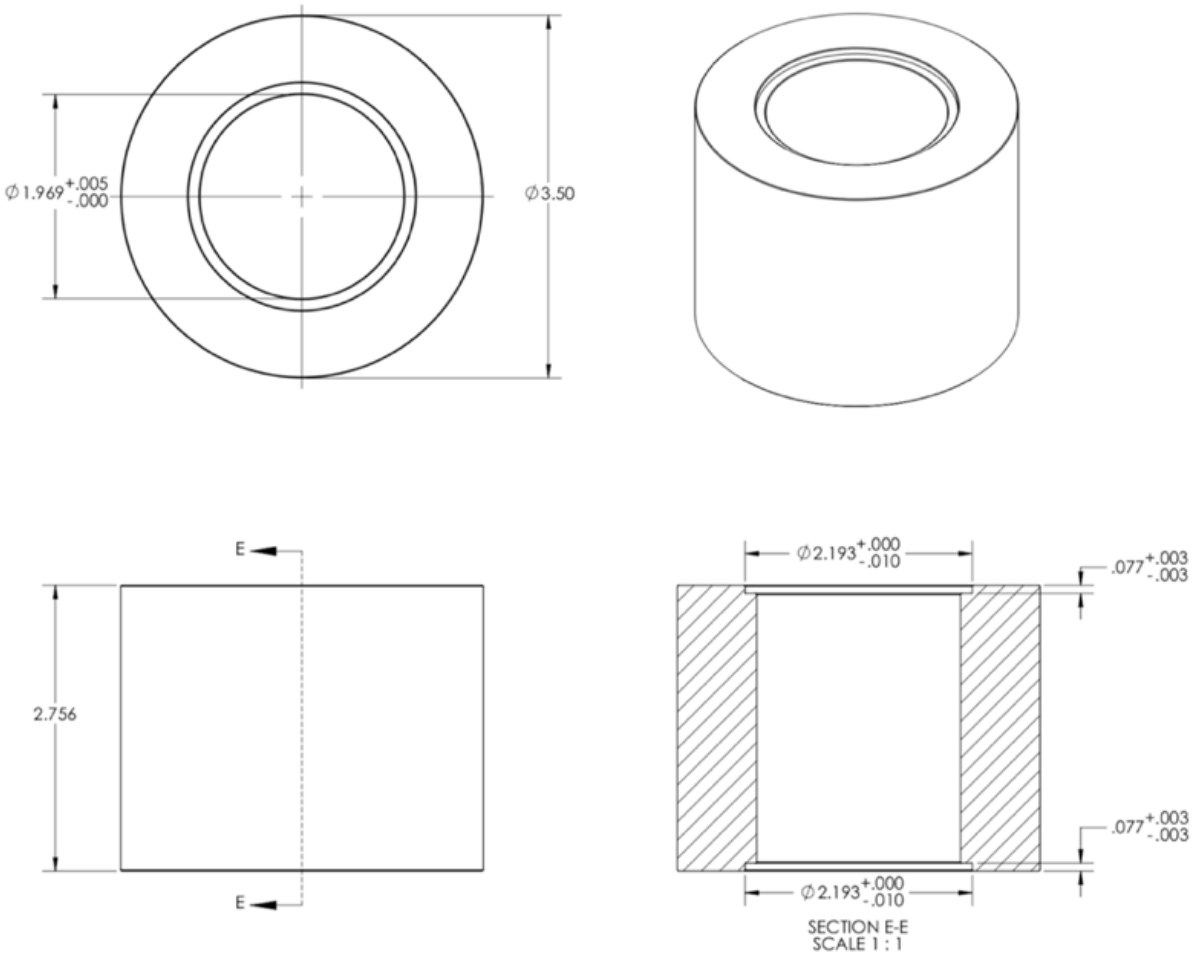

Figure 4.27 Dimensions of the middle tube

For the two caps, more comprehensive design is performed, just take one cap for example and the other one is totally the same. As shown in Figure 4.26, there are three Swagelok pipe connections go through the plate, which are used for liquid (i.e. two at the outside) and gas (i.e. in the middle) flowing in and flowing out. The other small holes are used for fix the plate to the base with water distribution and threaded (i.e. in case the tip need to be increased) gas injection bulge together. This kind of bulge structure can make sure the gas is through the soil sample instead of the interface. On the base, two grooves on each side is constructed for better water penetration and

on top of the groove are three rings with different sizes and nested with each other for better water distribution; the whole setup of the plate together with the base is shown in Figure 4.28.

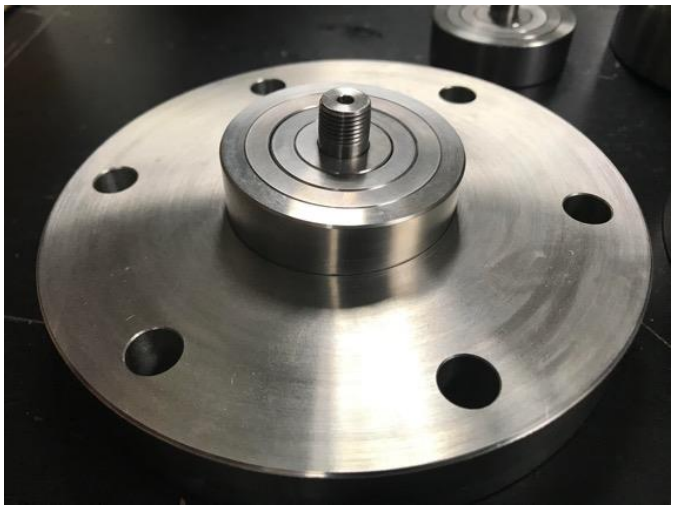

Figure 4.28 Combination of plate and base

A more detailed look at the base (Figure 4.29) shows that in the top side there are groove, threaded bulge (that inserts into the clay sample), and the nested rings. As for the bottom base, there are also three small grooves around the three flow connection holes that hold small size O-rings for a better sealing and isolation between gas flow line and liquid flow lines and there is also threaded bulge that inserts in the clay sample. Besides, the other two small threaded holes on base bottom side in a vertical direction with the flow connection holes are used for fixing together with the cap plate.

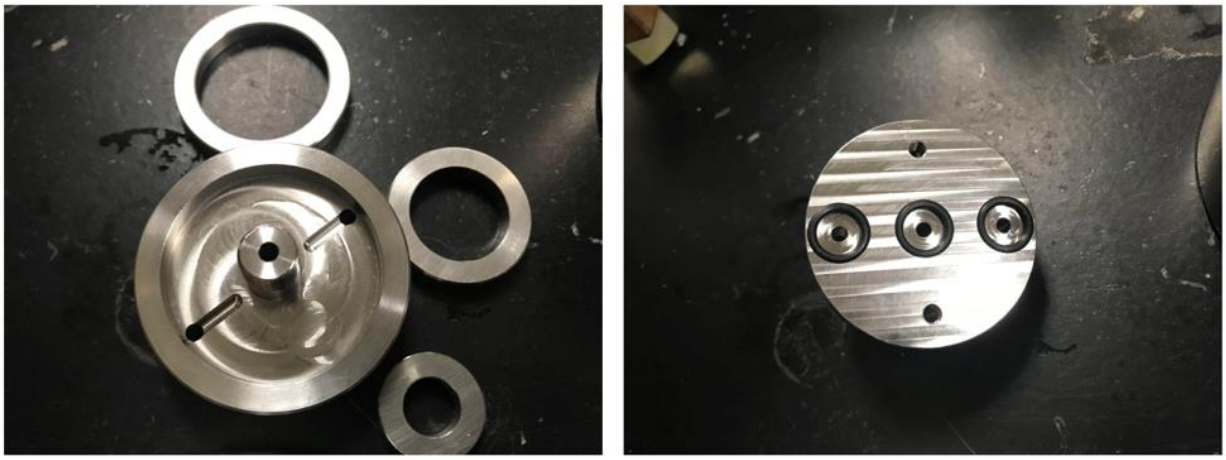

Figure 4.29 Base overview

4.5.3 Test outlines and procedures

Samples with dry densities of 1.05g/cm^3 was firstly investigated in this part. Constant flow rate 20ml/min was applied until breakthrough before the capacity of Wille volume/pressure controller (20MPa) or maintain high pressure (around 15MPa) if no breakthrough happened till the capacity of the controller. Gas nitrogen was the gas adopted for injection.

In this part, the test setup is shown in Figure 4.30. The basic procedures are as follows:

(1) Prepare compacted sample with target initial dry density in the cell;

(2) Hydrate the sample with upstream liquid pressure of 3MPa and downstream backpressure of 0.5Mpa;

(3) When flow-in rate and flow-our rate are more or less the same, sample is considered to be fully saturated;

(4) Setup the whole devices for gas breakthrough;

(5) For continuous injection test, fix the injection flow rate, inject the gas form upstream, record the pressure increment by volume and pressure controller as well as the gas flow rate at downstream by flowmeter until breakthrough happens.

(6) If no breakthrough happens till the capacity of the controller (around 20MPa), maintain the pressure at around 15MPa (for controller safety consideration) for days to see breakthrough happens or not.

Figure 4.30 Setup for gas breakthrough tests

4.5.4 Test results and discussions

For 1.05g/cm^3 dry density sample, first test was using connection 1 (upstream) to connection 1 (downstream) and the flow rate was 20ml/min (see Figure 4.31), we started from around 5 MPa. Until injection pressure accumulated to 18.5MPa, no breakthrough happened. Pressure of around 15MPa was maintained for 4 days, still no breakthrough happened. No gas flow rate at downstream was detected by mass flowmeter. The results are shown in Figure 4.32.

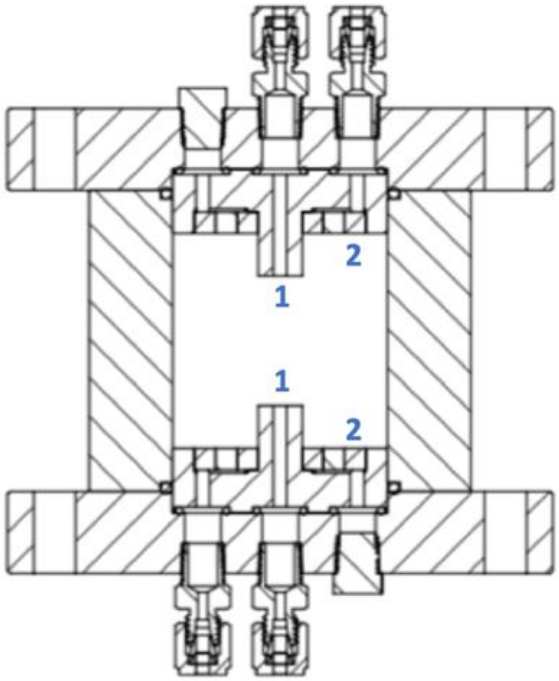

Figure 4.31 Gas upstream and downstream connections

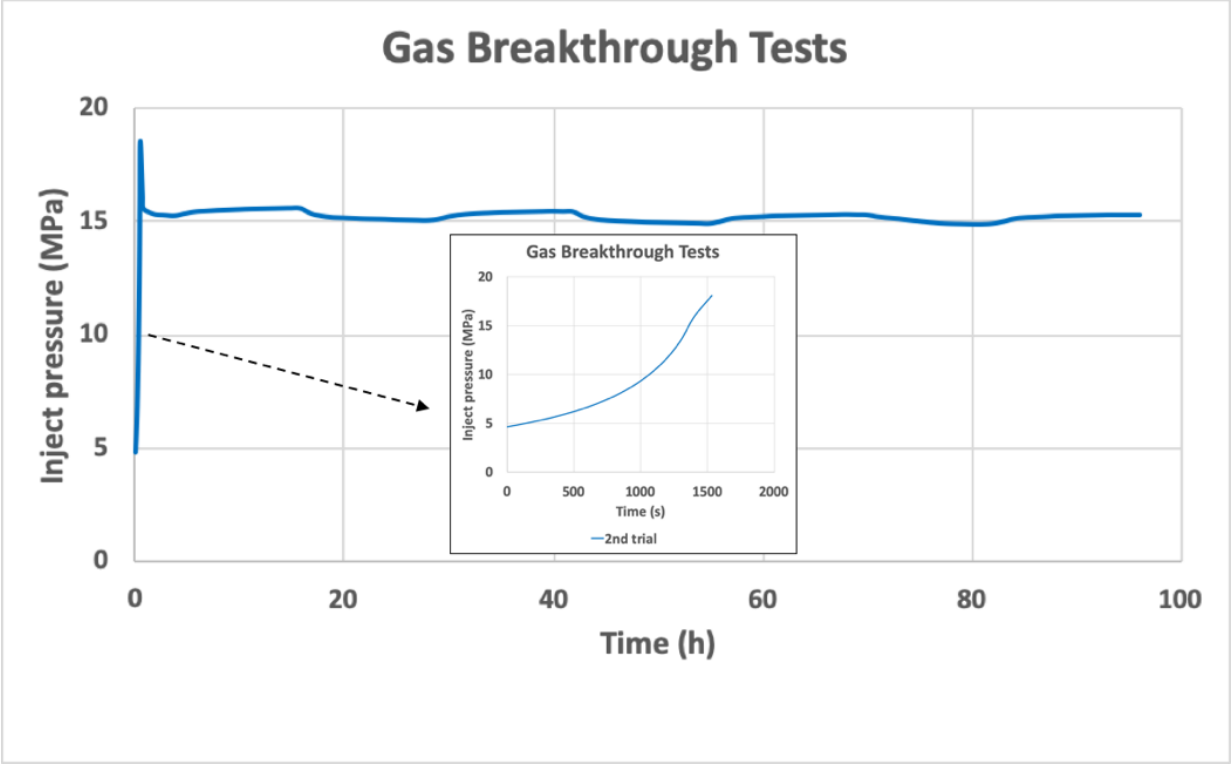

Figure 4.32 Results of test 1 with constant injection flow rate of 20ml/min

Test 2 was performed with flow rate of 20ml/min, but the connection is from 2 to 2, which is same as most of the former gas breakthrough tests. However, this method may have the interface problem and we will discuss about that as follows. We started from an injection pressure around 5 MPa, until injection pressure accumulated to around 18.5MPa, no breakthrough happened. Pressure of around 14MPa was maintained for 2 days, breakthrough happened at around 40h. Gas flow rate at downstream was also detected by mass flowmeter. The pressure results are shown in Figure 4.33 and pressure and outflow evolution are shown in Figure 4.34. After we dismantled the cell, it can be observed that there formed a small gap between the sample and the steel wall at the upstream side, at the downstream side, gap was not visible but if inject gas from bottom again and

pour water on top of the sample, gas bubbles can be observed from the edge of the sample, which confirmed the interface problem.

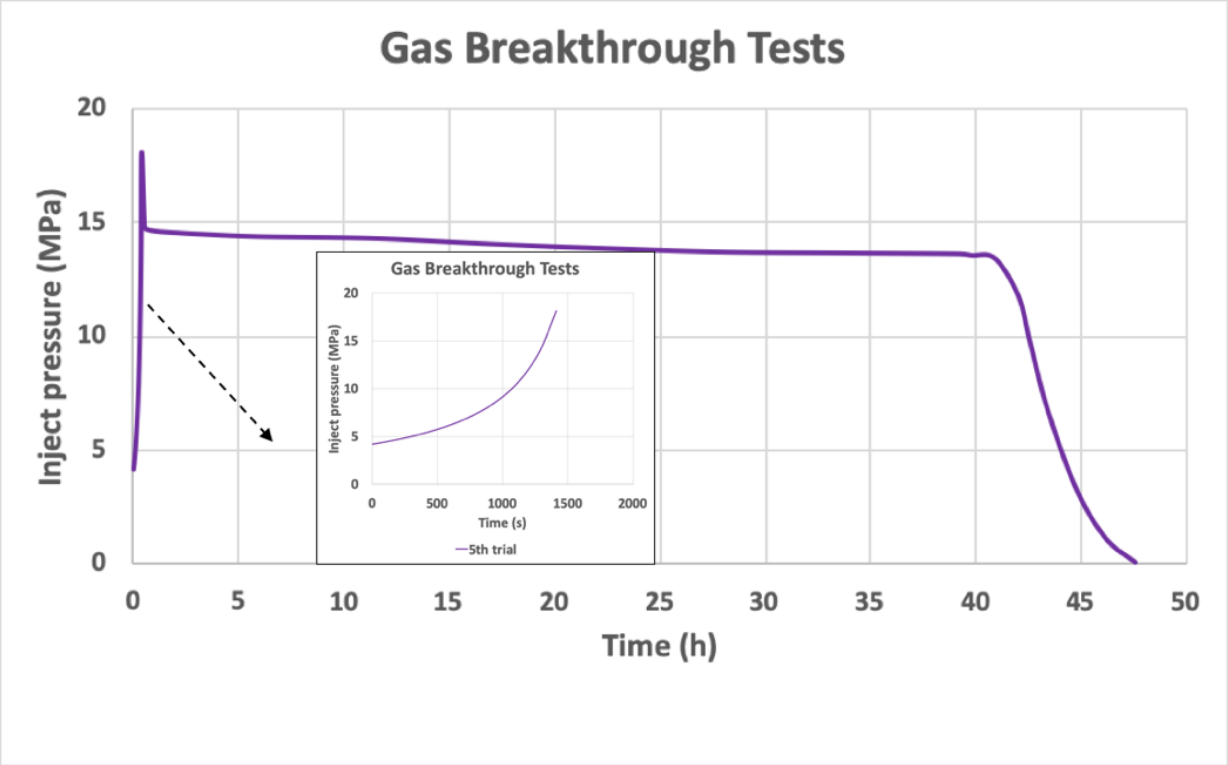

Figure 4.33 Results of test 2 with constant injection flow rate of 20ml/min

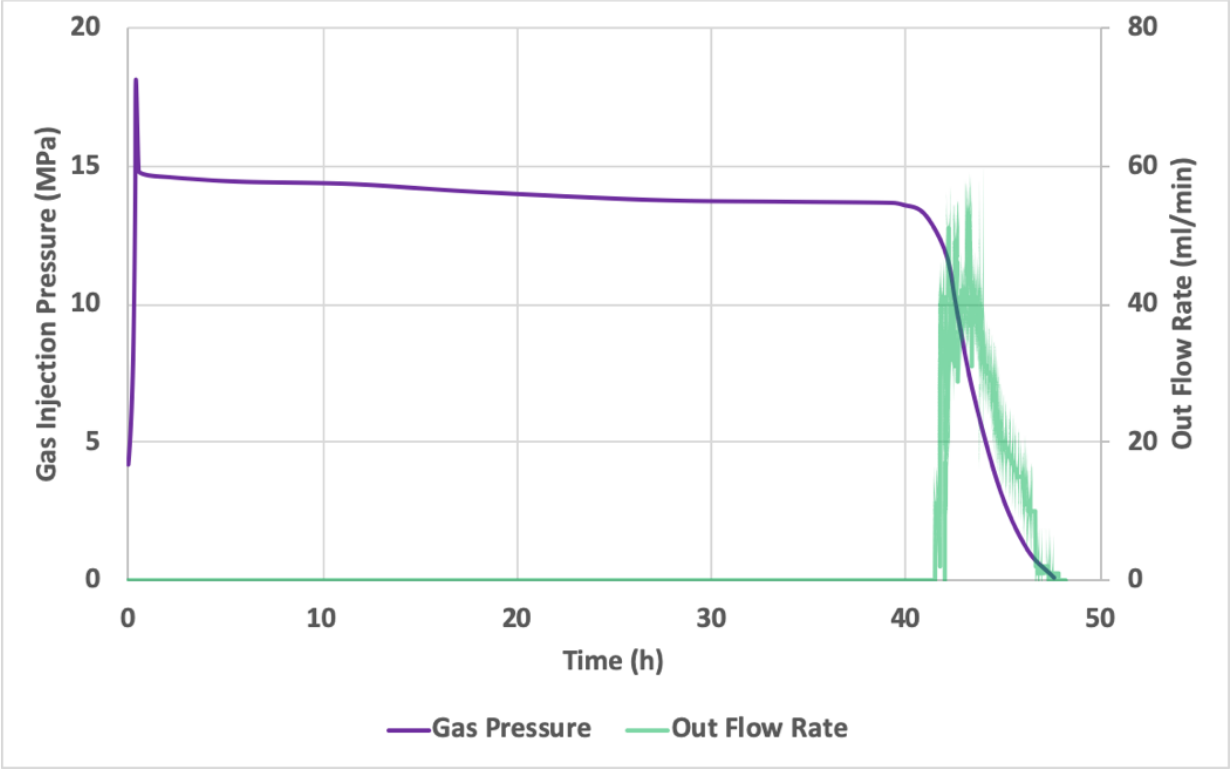

Figure 4.34 Gas pressure and outflow evolution in test 2

How the gas breakthrough happens is a complex process, to our understanding, it's mainly due to pore water gets replaced by gas and then a preference path is formed to let the gas penetrate the sample.

When gas is injected in the constant volume cell, pore water pressure for a fully saturated sample increases immediately, this process is very similar to the consolidation, pore water pressure dissipate with time and water is driven out (observed in the tests), making gas penetrate the sample slowly. This is a very slow process, if the gas injection rate is very high, pore water pressure cannot dissipate in time, as a result, sample can hold a much higher injection pressure when compare with a very small injection rate. Since gas breakthrough pressure of this kind of barrier material has been investigated with a much smaller rate (i.e. months of test period) by former researchers. For

example, Harrington and Horseman, 1999 adopted constant injection rate of 375μl/h and obtain gas breakthrough pressure of 16.3MPa for a much larger dry density sample, 1.67g/cm^3. Gas breakthrough pressures tend to have injection rate dependency if compare former slow tests with our tests under faster rates (20ml/min); larger gas injection rate makes it more difficult to breakthrough because it will take more time for liquid pressure dissipation and gas breakthrough.

To compare test 1 and test 2, they showed breakthrough due to interface problem. For test 2, since the water is drained from top connection 2 and interface is easier to be penetrate, so water along the edge line (between sample and steel wall) can be easily drained out first, forming the interface path and breakthrough. However, if top connection is 1, the same path for interface breakthrough is difficult to form, because outlet along top line (connection 2) was closed and under high saturation, continuous liquid phase and pore water pressure along the top lines make it hard to penetrate. Gas will tend to penetrate the sample for breakthrough without interface problem. This can explain why breakthrough did not happened in test 1 but happened in test 2.

4.5.5 Test summary

According to the gas breakthrough tests results obtained in this part, we can draw a conclusion that, the self-designed cell can be used for sample saturation and gas breakthrough tests with interface problem avoided under high pressure very well. Moreover, it can be concluded that gas breakthrough pressures tend to have gas injection rate dependence, higher rate makes it more difficult to breakthrough. By trying different connections, interface problem may exist for traditional gas breakthrough device and method. Fast rates as adopted in the tests cannot breakthrough fully saturated sample with dry density of 1.05g/cm^3 within 18.5MPa. In the future work, we will try much smaller gas injection rate to have a more detailed investigation on that. Heterogeneous samples with pre-exist fractures or material interfaces inside the sample will also

be investigated. We also plan to study on breakthrough time when different dry density samples are under constant injection pressures. Besides, we are updating the cell in order to obtain stress values (e.g. swelling pressure) as well as pore water pressure during the whole process in both axial and lateral directions in our future tests to help us better understand the gas breakthrough mechanism in barrier materials.

4.6 Study on cracking and self-healing behavior of barrier material

4.6.1 Introduction

As discussed above, the final and safe disposal of high-level nuclear waste (HLW) is a problem that still needs to be addressed. Current efforts in this area focus on the design of repositories for HLW in deep geological media. This type of disposal envisages a system of galleries excavated in good qualities rocks (e.g. granite, limestones, or salt rocks) around 500m below the ground level (or deeper). The HLW will be encapsulated in a metallic container and the empty space between the canister and the host rock will be filled by an engineered barrier (generally made up of compacted bentonite). The main safety functions of such type of repository is to confine the highly pollutant waste for hundred thousand of years, provide mechanical stability to the canister containing the HLW, delay the water flow from the host rock to the canister, serve as a buffer around the canister, and prevent the transport of radionuclides to the host rock.

Complex Thermo-Hydro-Mechanical and Chemical phenomena will take place in the repository near field because of the simultaneous heating (from HLW) and natural hydration (from the host-rock) under highly confined conditions. It can be anticipated that gas will form during the repository lifetime triggered by several physical and chemical processes (e.g. metal corrosion, water radiolysis, biodegradation). Gas generation under confined conditions will increase the gas

pressure inside the repository inducing gas flow through the barrier, process that may jeopardize the repository safety functions discussed above.

How the accumulated gas migrates through the barrier system and its potential impact on the host sedimentary rocks has been a key point for all major international waste disposal programs (e.g., NDA in UK, ANDRA in France, SKB in Sweden, NAGRA in Switzerland, SCK-CEN in Belgium, NWMO in Canada). A lot of research worldwide were performed to deal with how gas migrates through barrier material in both experimental studies (Pusch and Forsberg, 1983, Horseman et al., 2004, Davy et al., 2009, Cuss et al., 2011, Graham et al., 2016) and numerical works (Alonso et al., 2006, Arnedo et al., 2008, Xu et al., 2013, Fall et al., 2014, Xu et al., 2017). In terms of gas permeability measurements, previous studies were mainly focused on samples with different saturation degrees, dry densities, confinements as well as soil types (Tanai et al., 1997, Galle and Tanai, 1998, Villar et al., 2013, Liu et al., 2015). However, these researches are mainly focused on intact samples without systematical considerations of how induced cracks due to heating and drying will impact on the barrier material permeability values, which is naturally happening on site. It is known that the heat generated by the HLW will induce a drying of the engineered barrier surrounding the canister and this dry-out may lead to the formation of desiccation cracks (Graham, 1997, Garcia-Sineriz et al., 2015). Drying cracks have been observed in large scale heating experiments aimed at studying the feasibility of engineered barrier systems (EBS) for HLW (Graham, 1997, Garcia-Sineriz et al., 2015). For example, Figure 4.35 shows the final state of a clay barrier during the dismantling of a heating and hydration field tests (Garcia-Sineriz et al., 2015). This type of crack will increase the barrier permeability and how these cracks will propagate (i.e. cracking and self-healing) with heating and drying strongly influent the gas transfer process discussed above as well as the safety of nuclear waste disposal system.

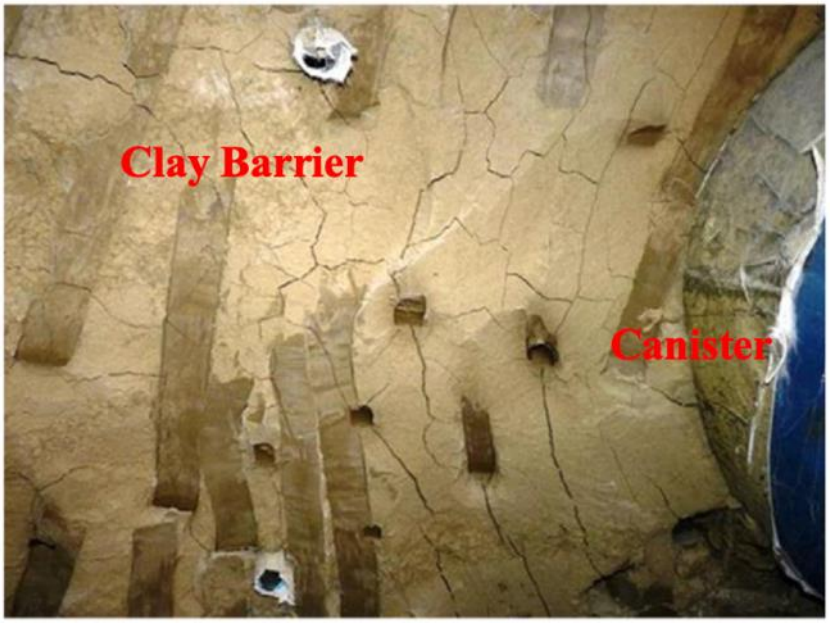

Figure 4.35 Drying cracks observed in a high-level nuclear waste disposal barrier experiment (reprinted from Garcia-Sineriz et al., 2015).

Cracking of soil is not new topic and it can develop due to several processes comprising; desiccation and shrinkage, freezing and thawing, differential settlement, syneresis, and penetrated plant roots (Yesiller et al., 2000). The propagation of cracks will impact on soil compressibility and permeability, also, a reduction in the overall strength and stability. Amongst others, desiccation cracks are what mainly happened to nuclear waste disposal barrier and their effects on gas permeability of barrier material are the focus study of this paper. Cracking behaviors of clay material due to desiccation have been investigated by many former researchers (Morris et al., 1992, Albercht and Benson, 2001, Atique et al., 2009). Besides, hydraulic permeability due to cyclic drying-wetting has also been researched (Atique et al., 2009, Louati, 2018, Wan et al., 2018). However, gas permeability due to such cracks on clay, particularly on barrier material is not well studied yet. As for healing behavior of clay materials, phenomenon and its impact on soil

properties were investigated by former researchers (Eigenbrod, 2003, Sporer et al., 2001, Bastiaens et al., 2007, Wang et al., 2013, Mohammadi and Choobbasti, 2018), among which, hydraulic permeability due to healing were investigated (Sporer et al., 2001, Wang et al., 2013). Gas permeability due to self-healing of barrier material is still blank.

However, all the self-healing discussed above are due to wetting, thawing, sealing, etc. Healing due to continuous heating and drying for clay material is still a very new topic that has never been investigated before, particularly for nuclear disposal barriers, where such cracking-healing behaviors due to continuous heating and drying are potentially happening and calling for more attention. Therefore, how such cracking-healing combined with effects from saturation degrees, dry densities and confinements will affect gas flow in terms of gas permeability for barrier material is in great need to be further investigated. This is also the main research work in section 4.6 and section 4.7, i.e. to better understand how clay barrier materials behave upon heating and drying processes, and also to investigate how gas permeability will change as the moisture decrease and drying cracks evolve. This information will be instrumental to achieve a safe and optimal design of repositories for nuclear waste.

In section 4.7, in order to better study cracking behavior for barrier material, a series of heating and drying tests under different conditions were performed. Effects from initial conditions, including initial dry densities (i.e. ρ_d = 1.3g/cm3 and ρ_d = 1.6g/cm3), initial saturation degrees (i.e. Sr=97% and Sr=60%), as well as drying condition, including lab condition (T=20℃) and oven condition (T=90℃) were all investigated in this research.

4.6.2 Test outlines and procedures

Same material MX-80 bentonite was adopted for the tests. Soil samples were prepared to target water content and then sealed in a plastic zip bag for better homogenization for 24h. After

that, samples were compacted in a metallic ring or 3D printed ring using ABS material (i.e. strong enough) with the help of high capacity load frame (see Figure 4.36 a)). The dimension of the cylindrical samples was 5cm in diameter and 2 cm in height (see Figure 4.36 b)).

a) b)

Figure 4.36 Load frame for compaction and mold

In order to better understand how the barrier material cracks and self-healed during drying process. Different static compacted samples with different initial dry densities, different initial saturation degree and different heating and drying conditions will be investigated. The two dry densities adopted for this investigation are ρ_d = 1.3g/cm^3 and ρ_d = 1.6g/cm^3; two initial saturation degrees adopted are S_r=97% and S_r=60%; one drying condition is under lab environment (i.e. 20℃) and the other one is under oven with a temperature of 90℃. All the S_r values in this section 4.6

and 4.7 are from initial calculations without taking sample shrinkage and crack patterns into consideration, because it hard to estimate the true saturation at a given water content, but these pre-calculated S_r values can help us quantify how much moisture we lost during drying in a systematical way. Test results with different initial conditions and different drying and heating methods are introduced in the following part. In order to provide more accurate results, in section 4.7, the evolution of gas permeability will be shown according to water content in the plots.

For lab condition, four different samples are chosen for demonstration below with different initial conditions. Two with high initial saturation degree (S_r=97%) but different initial dry densities are recorded by Nikon digital camera while the other two with low initial saturation degree (S_r=60%) are recorded by stereo microscope from AmScope company. This is because for low saturation degree sample, cracking and healing are not obvious enough to be captured by digital cameras. The two setups for digital cameras and microscope are shown in Figure 4.37 below.

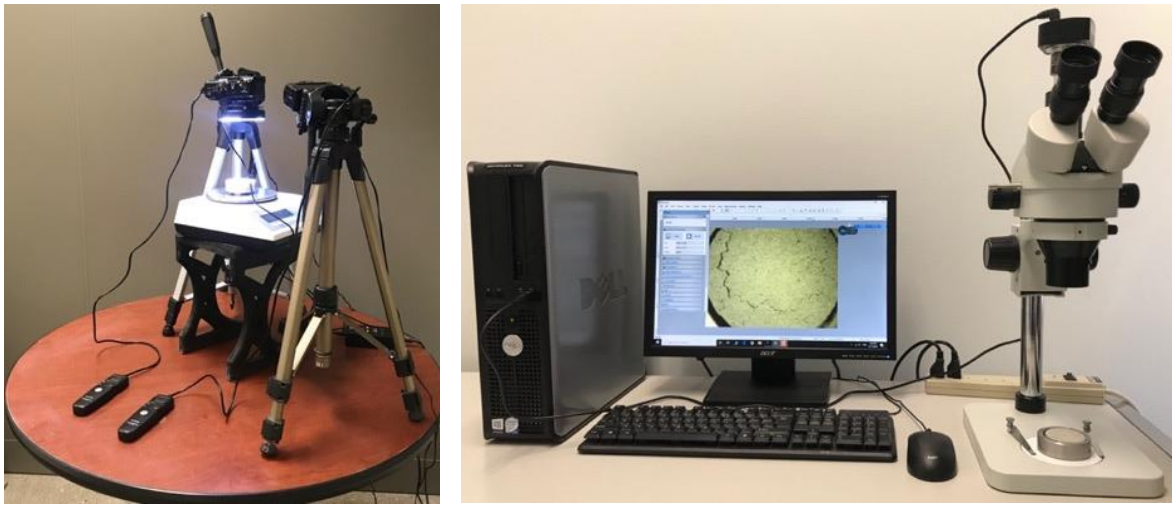

a) b)

Figure 4.37 a) Digital camera setup; b) microscope setup

Two digital cameras are used at the same time, one is to capture the cracks pattern at different times of the sample (i.e. sample is placed on a scale) and the other one is used to capture the water content changes of the sample at different corresponding times. Both of the two cameras are taking photos under control of separate remote time controller (i.e. type AP-TR1C). For the microscope, which can be connected to a laptop, photos can be taken with fixed time period automatically by the matched software installed on the laptop.

For heating and drying under oven condition (T=90℃), also four different samples are chosen for cracking-healing demonstration. For each saturation degree, two samples are with different dry densities (i.e. 1.3g/cm^3 and 1.6g/cm^3) are selected for demonstration. All the photos were taken by Nikon digital camera.

4.6.3 Test results and discussions

4.6.3.1 Lab condition (T=20℃), S_r=97%, ρ_d = 1.3g/cm^3

Sample was compacted to the target initial saturation degree and dry density, then was placed on the scale under the digital camera. Photos were taken every 30mins and the change of crack patterns under selected Sr values are shown in Figure 4.38 below.

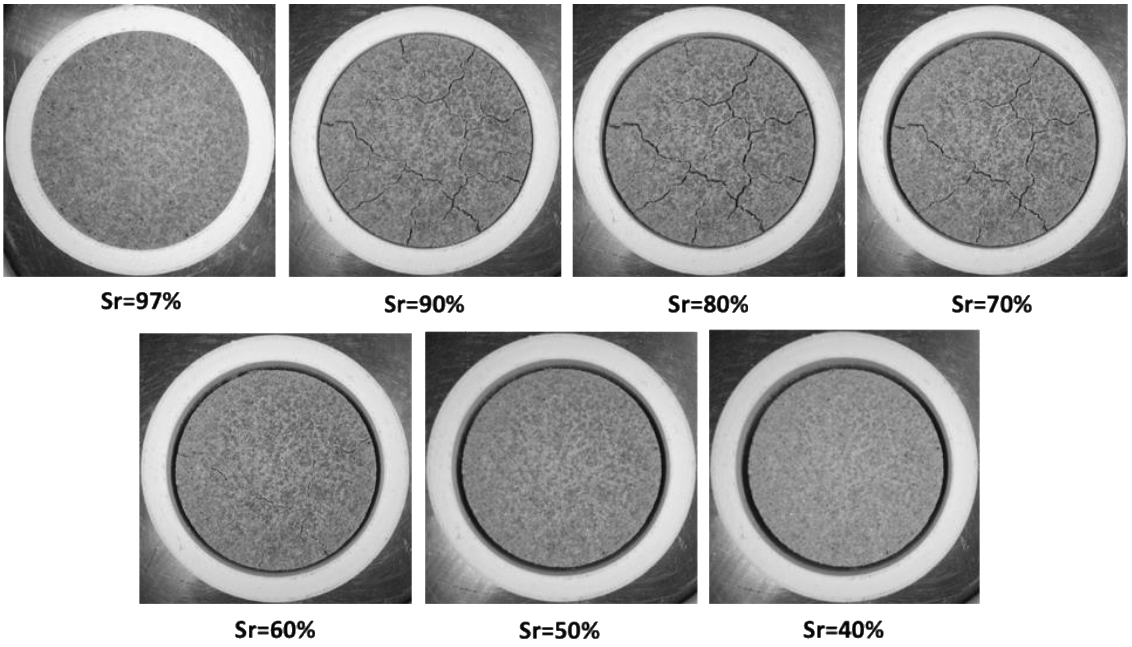

Figure 4.38 Cracking patterns development for lab test 1 under lab condition

4.6.3.2 Lab condition (T=20℃), S_r=97%, ρ_d = 1.6g/cm^3

This test was performed following the same procedure as last test 1 just the dry density is different. The propagation and healing of cracks during drying under selected S_r values are recorded and shown in Figure 4.39 below.

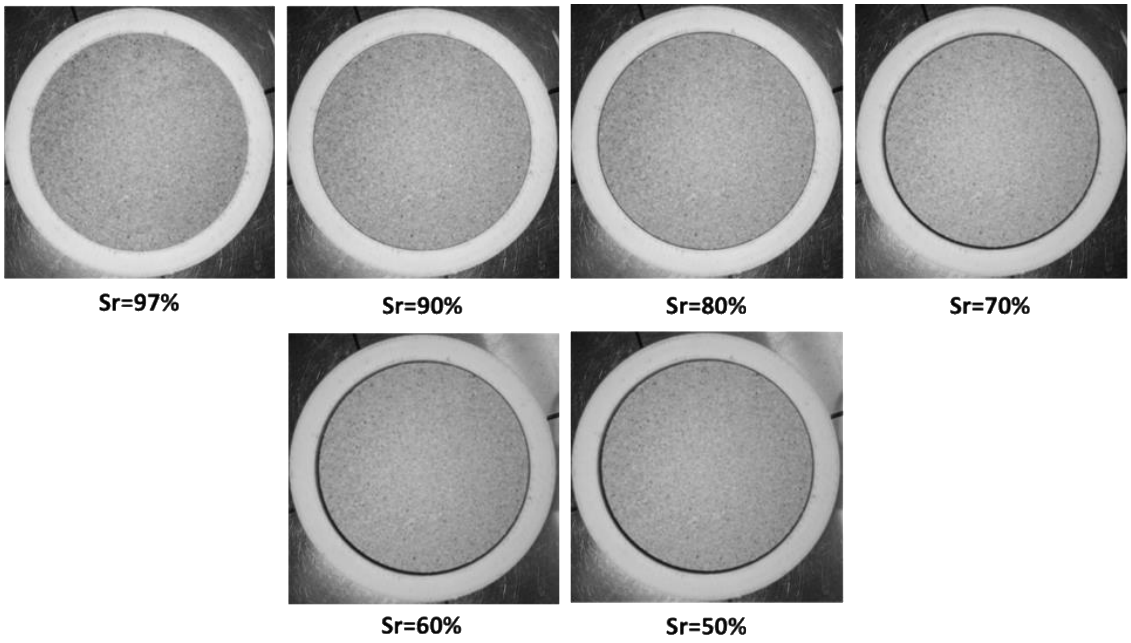

Figure 4.39 Cracking patterns development for lab test 2 under lab condition

4.6.3.3 Lab condition (T=20℃), S_r=60%, ρ_d = 1.3g/cm^3

For this lower initial saturation degree sample, microscope was adopted to record the crack behavior. The part enlarge was almost the center of the sample for all photos with the same position. Photos (i.e. 20X magnification) were taken and recorded every 10mins under the control of the matched software. A series of photos (see Figure 4.40) at different times were selected to show how the cracks developed and self-healed during this drying process.

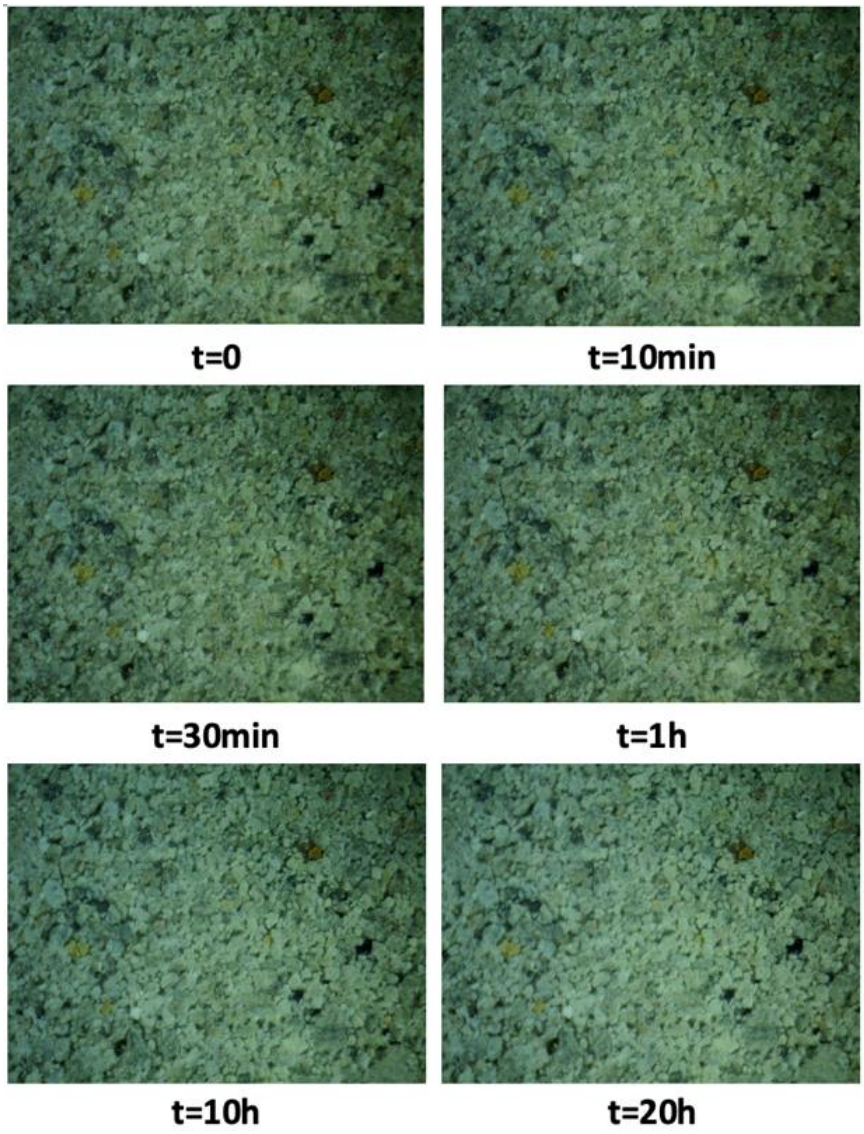

Figure 4.40 Cracking patterns development for lab test 3 under lab condition

4.6.3.4 Lab condition (T=20℃), S_r=60%, ρ_d = 1.6g/cm^3

This test was following same procedure as last test 3 just the dry density is higher. The propagation and healing of cracks during drying at selected times is shown in Figure 4.41 below.

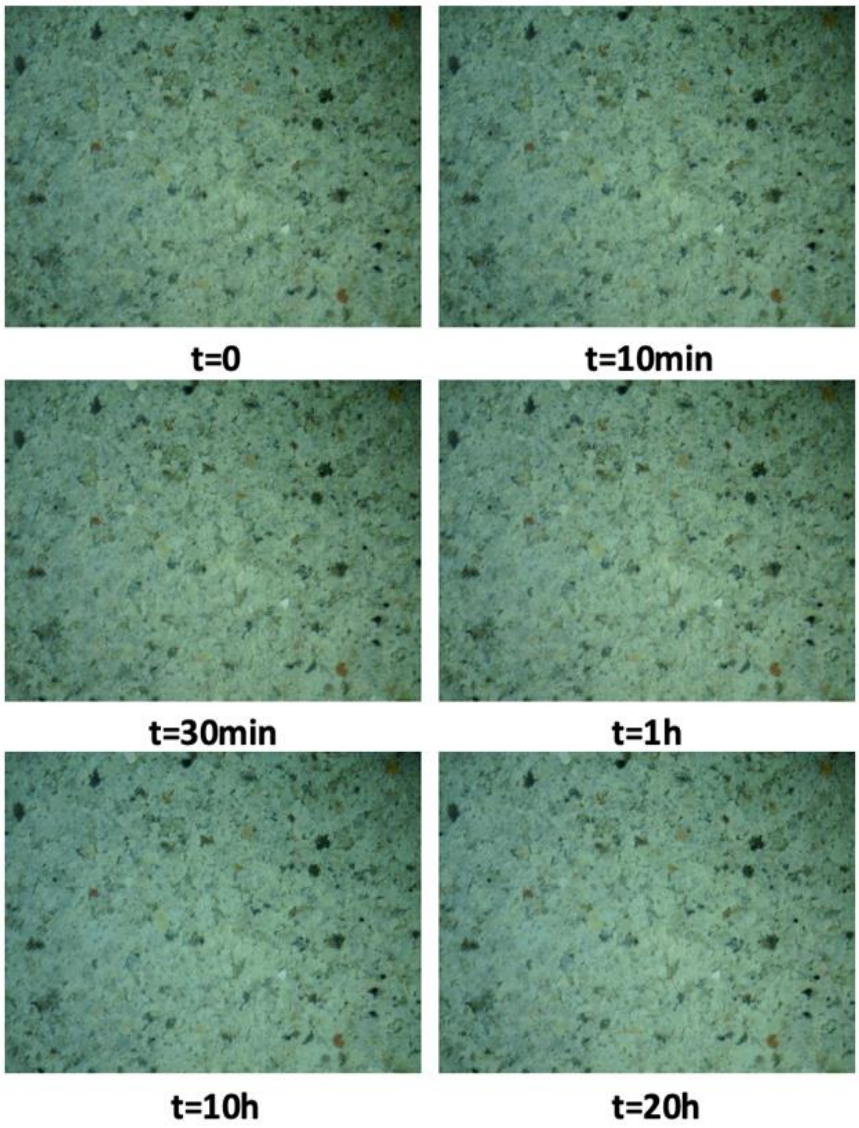

Figure 4.41 Cracking patterns development for lab test 4 under lab condition

From the test 1 and 3 conducted under lab condition, it can be discovered that cracks developed first and then got healed with continuous drying process. Sample keep shrinking until got stable in final stages. For test 2 and 4, sample contracted but cracks were not observed. Crack patterns are quite different with different initial saturation degrees and initial dry densities. When comparing 1 with 2, 3 with 4, it can be concluded that with same initial saturation degree, the lower

initial dry density shows much more obvious cracking and self-healing patterns. For 1.3g/cm^3 dry density sample, we can observe a small crack developed on the left-middle part of the photo (i.e. 1h), so if comparing 1with 3, it can be concluded that, with same initial dry density, the higher initial saturation degree it is, the more obvious cracking and self-healing it will show.

For heating and drying under oven condition (T=90℃), also four different samples are chosen for cracking-healing demonstration. For each saturation degree, two samples are with different dry densities (i.e. 1.3g/cm^3 and 1.6g/cm^3) are selected for demonstration. All the photos were taken by Nikon digital camera.

4.6.3.5 Oven condition (T=90℃), S_r=60%, ρ_d = 1.3g/cm^3

Sample was compacted to the target initial saturation degree and dry density as discussed above. Then the sample is placed in the oven heating and drying. Keep measuring and recording the moisture loss all the time (i.e. around every 10mins). Photos were taken every time before measuring the weight of the sample using digital camera. The change of crack patterns under selected S_r values are shown in Figure 4.42 below.

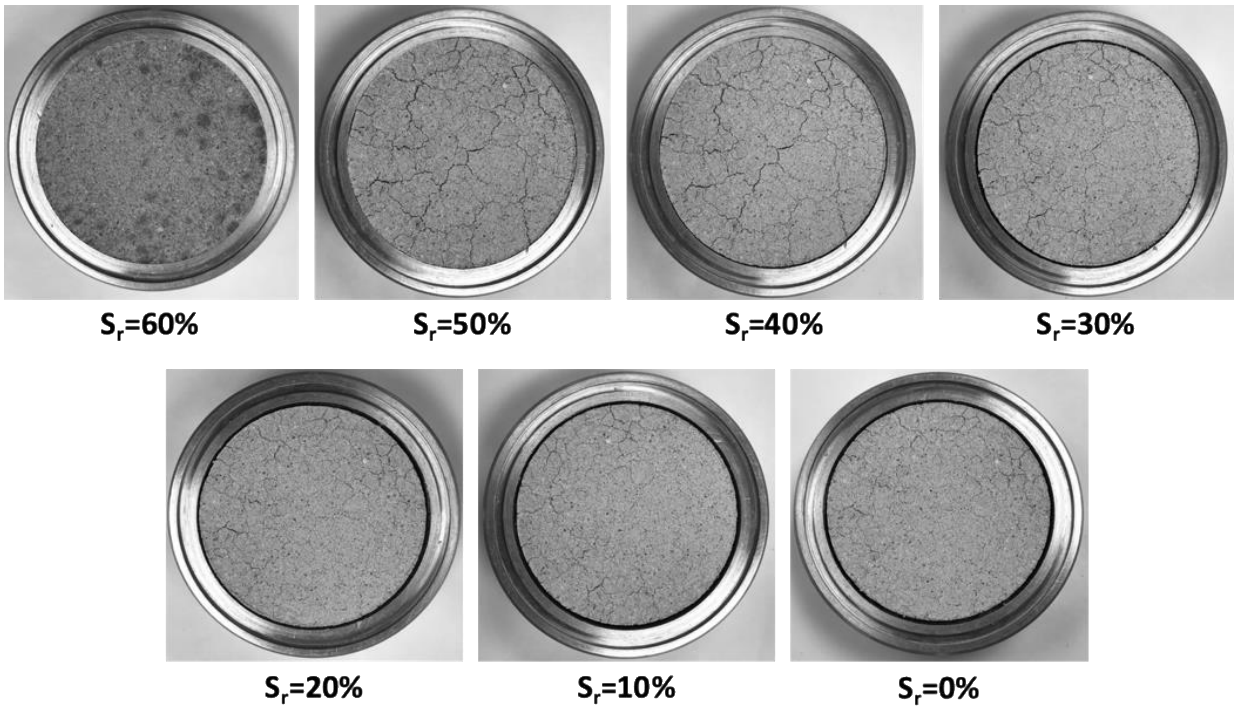

Figure 4.42 Cracking patterns development for lab test 5 under oven condition

4.6.3.6 Oven condition (T=90℃), S_r=60%, ρ_d = 1.6g/cm^3

Sample was prepared and tests was conducted as test 5 above. The change of crack patterns under selected S_r values are shown in Figure 4.43 below.

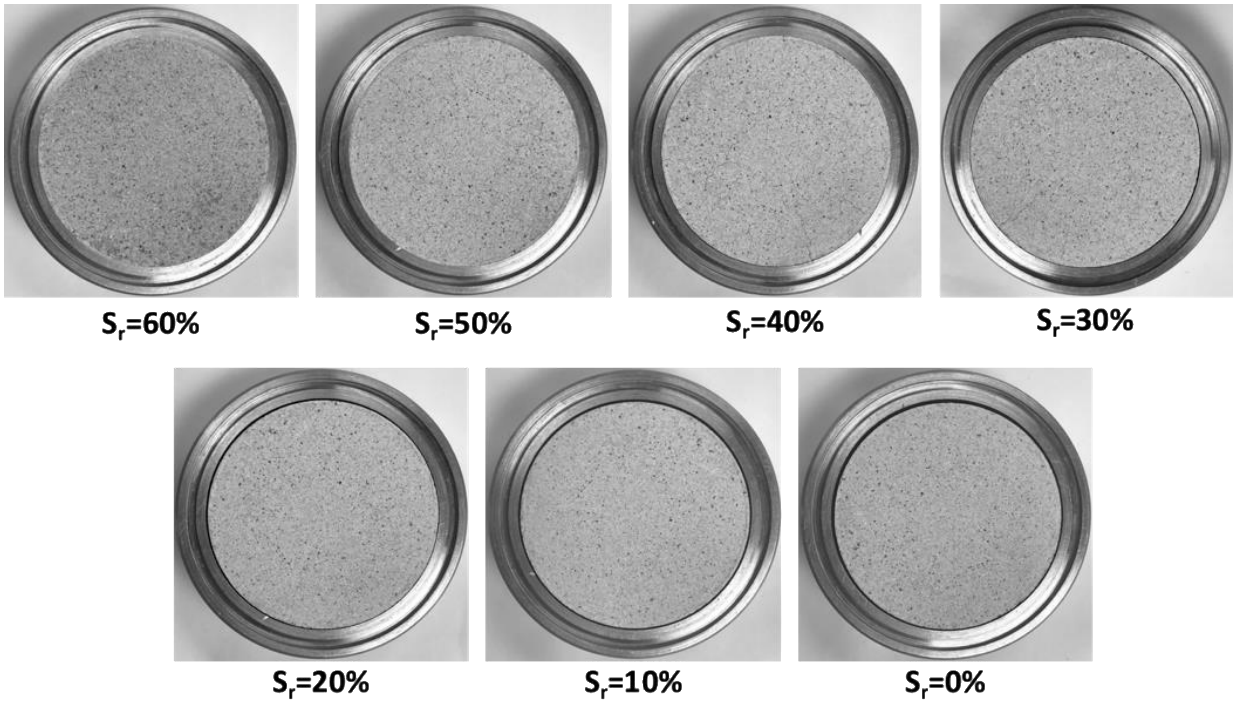

Figure 4.43 Cracking patterns development for lab test 6 under oven condition

4.6.3.7 Oven condition (T=90℃), S_r=97%, ρ_d = 1.3g/cm^3

Sample was prepared and tests was conducted as test 1 above. The change of crack patterns under selected S_r values are shown in Figure 4.44 below.

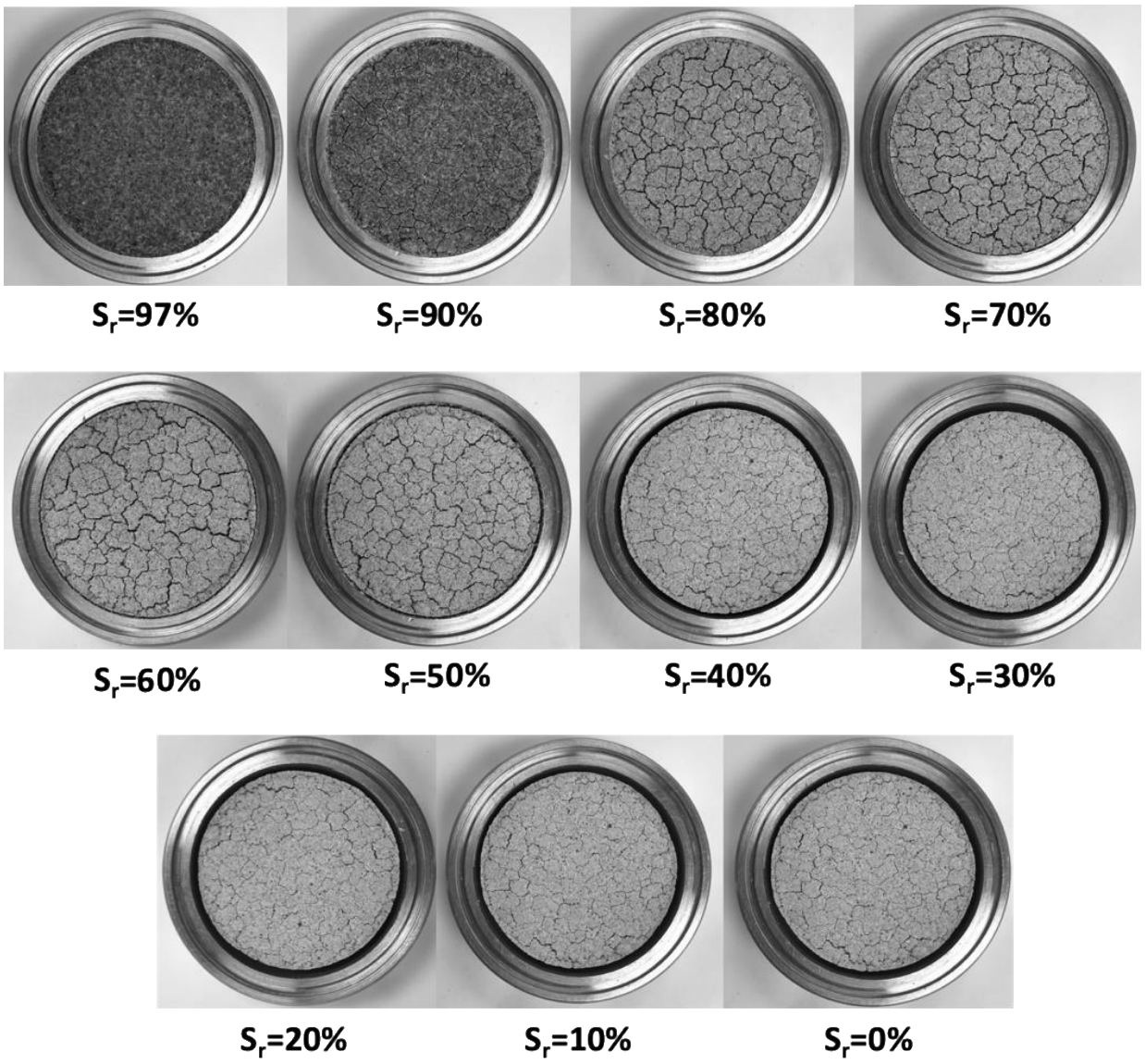

Figure 4.44 Cracking patterns development for lab test 7 under oven condition

4.6.3.8 Oven condition (T=90℃), S_r=97%, ρ_d = 1.6g/cm^3

Sample was prepared and tests was conducted as test 1and 2 above. The change of crack patterns under selected S_r values are shown in Figure 4.45 below.

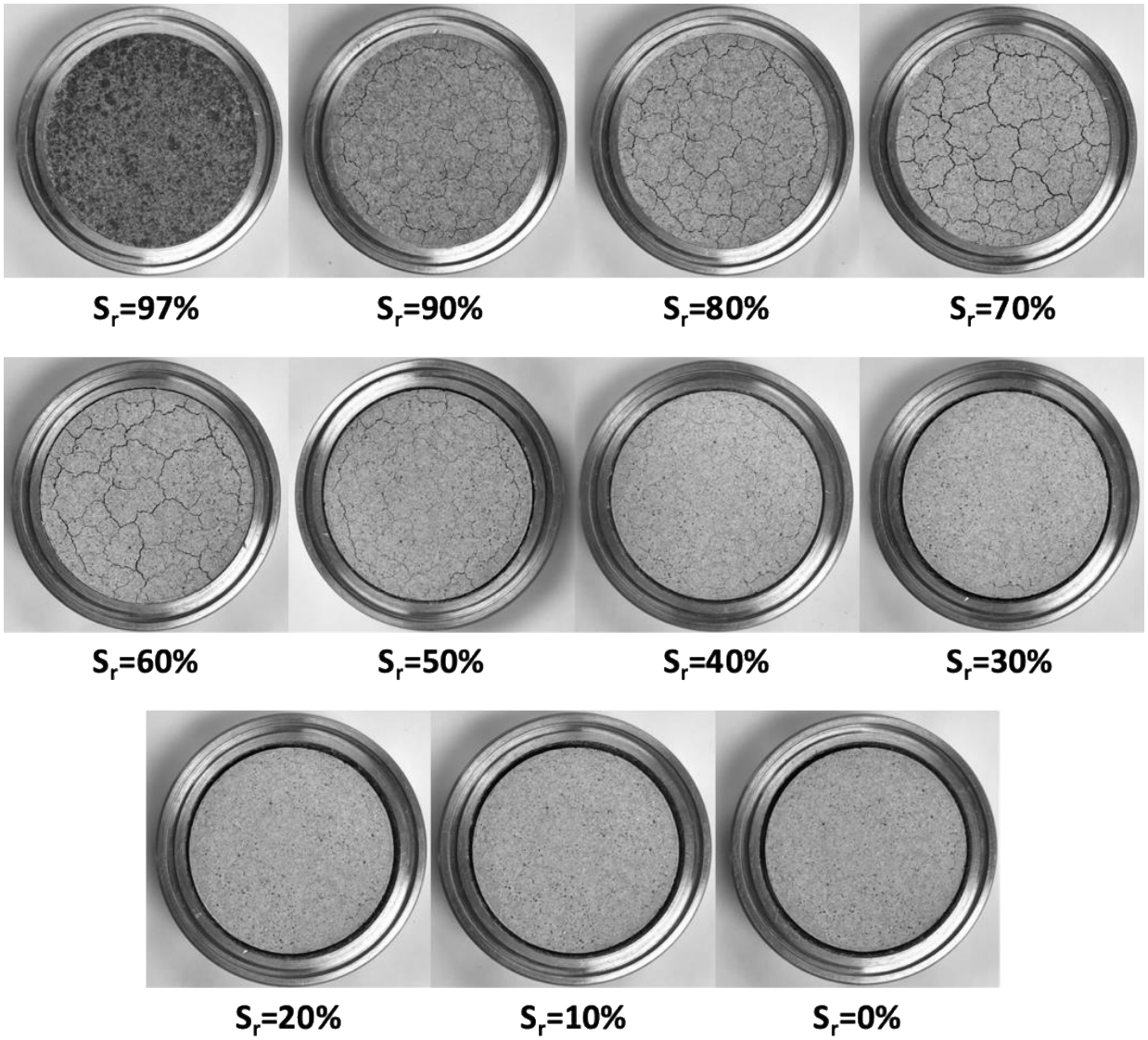

Figure 4.45 Cracking patterns development for lab test 8 under oven condition

From the four groups of tests conducted under oven condition, it can be discovered that samples under same initial dry density and saturation degree, higher heating and fast drying conditions can result in more prominent cracking and self-healing patterns. Similar conclusions can be drawn as in room condition: When comparing 5 with 6, 7 with 8, it can be concluded that with same initial saturation degree, the lower initial dry density shows much more obvious

cracking and self-healing patterns; if comparing 5with 7 and 6 with 8, it can be concluded that, with same initial dry density, the higher initial saturation degree it is, the more obvious cracking and self-healing it will display. Another interesting thing discovery is that when comparing 7 and 8, the cracks developed both start to heal when around S_r=70%, when around 27% of initial total moisture is dried out.

Besides, if we compare test 1 under lab condition and test 7 under oven condition, the peak of cracking was with a smaller S_r in oven condition (S_r=70%, w=29%) than in lab condition (S_r=80%, w=33%).

Tests above are about how cracking and healing develop when samples are under continuous heating and drying under oven condition till fully dried. How sample will behave if stopping such heating and drying process suddenly by sealing the sample inside a zip-bag was also investigated with three cases (i.e. S_r=70%, S_r=50%, S_r=30%) below.

Three separate samples were prepared with initial saturation degree of 97%, dry density of 1.6g/cm^3. They were heating and dried in the oven to different S_r separately (70%, 50%, 30%), then they were moved out of the oven and sealed in a plastic zip-bag to investigate how self-healing due to moisture redistribution and homogenization will be. During this process, crack patterns were recorded at different time points. Figure 4.46 is a comprehensive demonstration of how cracking and self-healing develop with continuous heating and drying as well as paused at different saturation degrees.

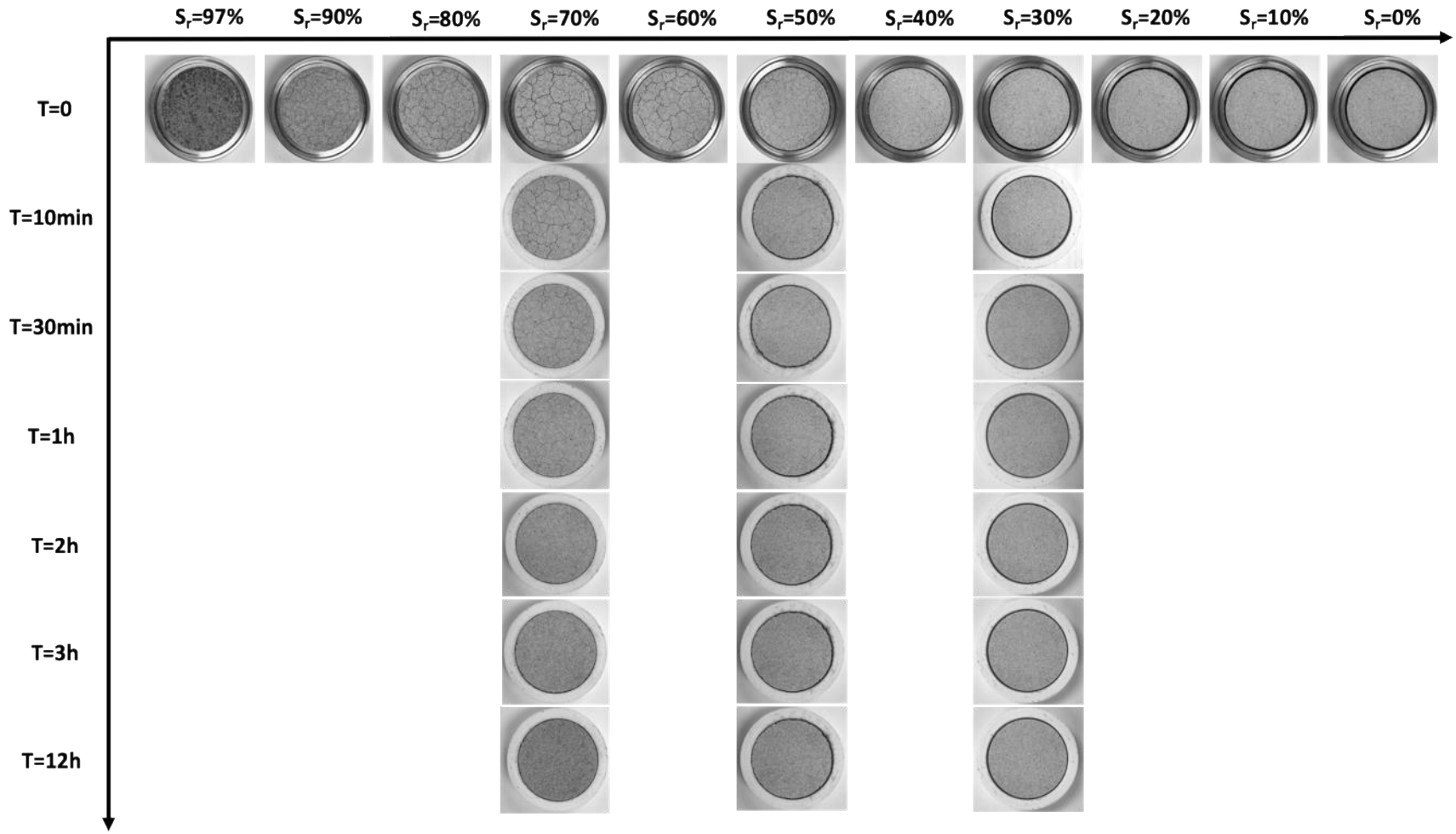

Figure 4.46 Cracking and healing with continuous and paused method

From Figure 4.46 above, it can be observed that when stop the heating and drying process at a given saturation degree, and seal the sample in an environment without moisture loss, samples will also show self-healing due to redistribution and homogenization of moisture. At high saturation degree (e.g. S_r=70%), this behavior is more obvious while at low saturation degree (e.g. S_r=30%), it is almost no obvious change.

4.6.4 Digital Imagine Correlation (DIC) analysis

The Digital Image Correlation (DIC) which is also known as Particle Image Velocimetry (PIV) is an image-based deformation measurement technique in progressively widespread use in multidisciplinary fields, such as, fluid, solid and soil mechanics. This method can provide full and continuous measurements of displacements/strains fields that would be equivalent to numerous of sensors, which makes it easy-use, low-priced and more competitive than other techniques in the research area.

In this part, the DIC method was employed to capture the displacement fields of the deformed soil during cracking and self-healing. Samples were prepared following the same procedures as discussed above (i.e. lab condition (T=20℃), S_r=97%, ρ_d = 1.3g/cm^3). Photos were taken with the same set up as shown in Figure 4.47. The only difference is the surfaces of these samples were marked by small black points (see Figure 4.47 a)), which can help capture the particles' movements by DIC. A Matlab code (Mori and Chang, 2003) was adopted for this DIC analysis. Sample will be drying under lab condition and a series of high-quality photos (i.e. highest resolution of 3648-pixel x 2736-pixel) were taken every 30mins until the samples were dried under lab condition.

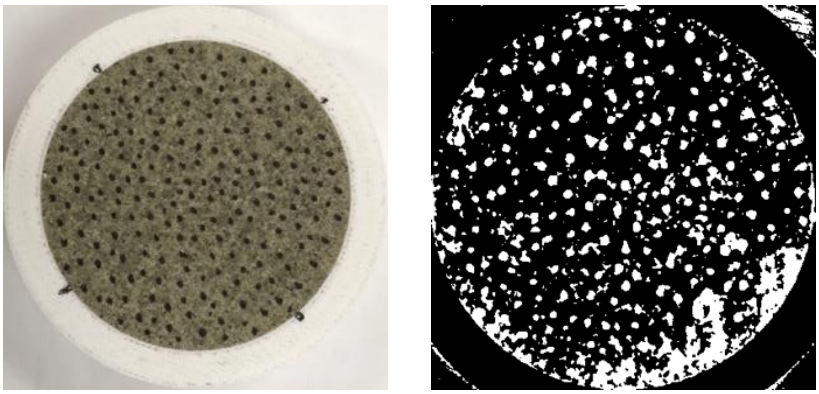

a) b)

Figure 4.47 Samples for DIC analysis

Before performing DIC analysis, all the true color/RGB photos should be processed to binary ones by ImageJ software. Firstly, the digital image (TrueColor/RGB) of soil sample was converted to a grayscale image. The grayscale image was obtained by converting the image to the type of 8-bit. Afterward, the background of the image had been subtracted from the image. Then, the grayscale image was converted to a binary black-and- white (B & W) image (see Figure 4.47 b)). For better demonstrating how the particles move during the drying process with cracking first and then self-healing, two photos taken continuously were always selected and compared in pair. Totally, six processed pictures in 3 pairs (i.e. initial sate vs. 30mins later; cracking state vs. 30mins later; healing state vs. 30mins later) are selected to conduct DIC analysis. From Figure 4.48 to Figure 4.50, on the left side, the top two are the pair of two photos to compare in TrueColor while the bottom is the DIC analysis results with movement vectors shown, on the right side, movement vectors after smooth process as well as vorticity plot are also shown.

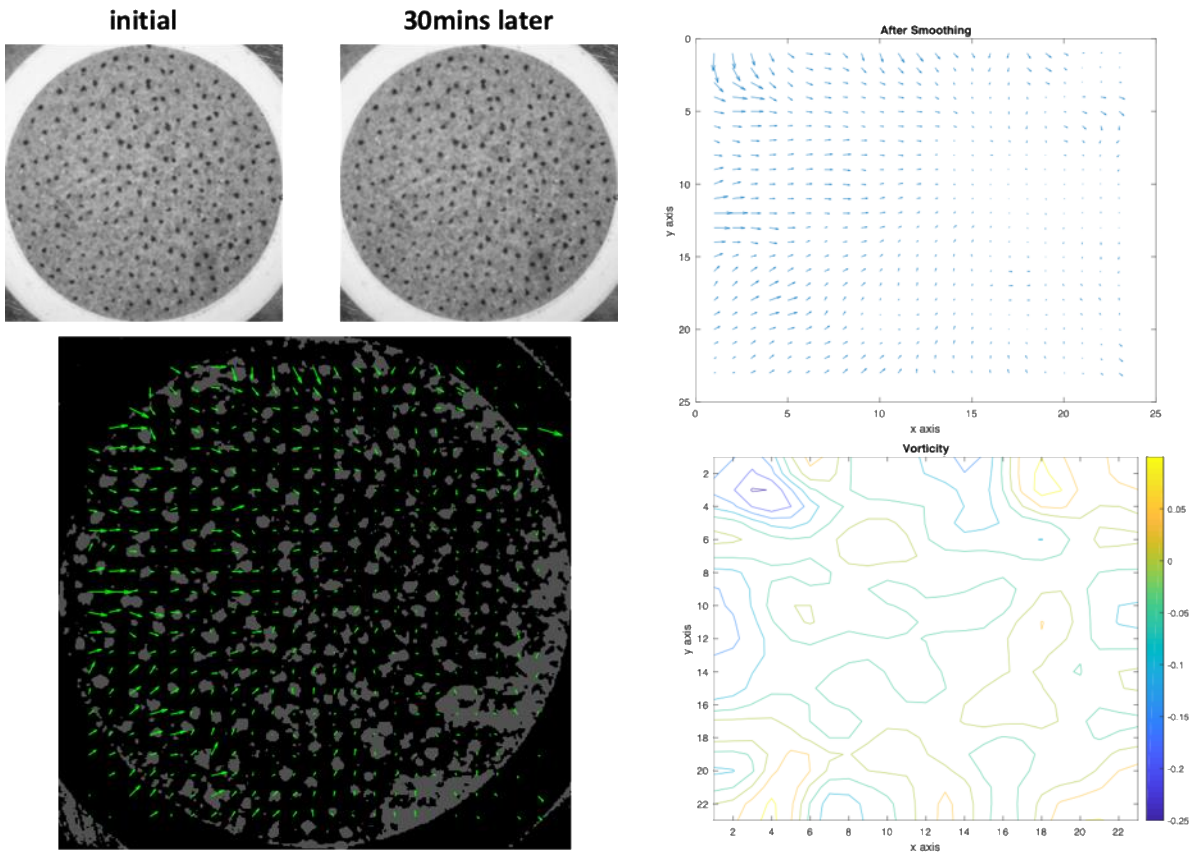

Figure 4.48 DIC analysis of case 1

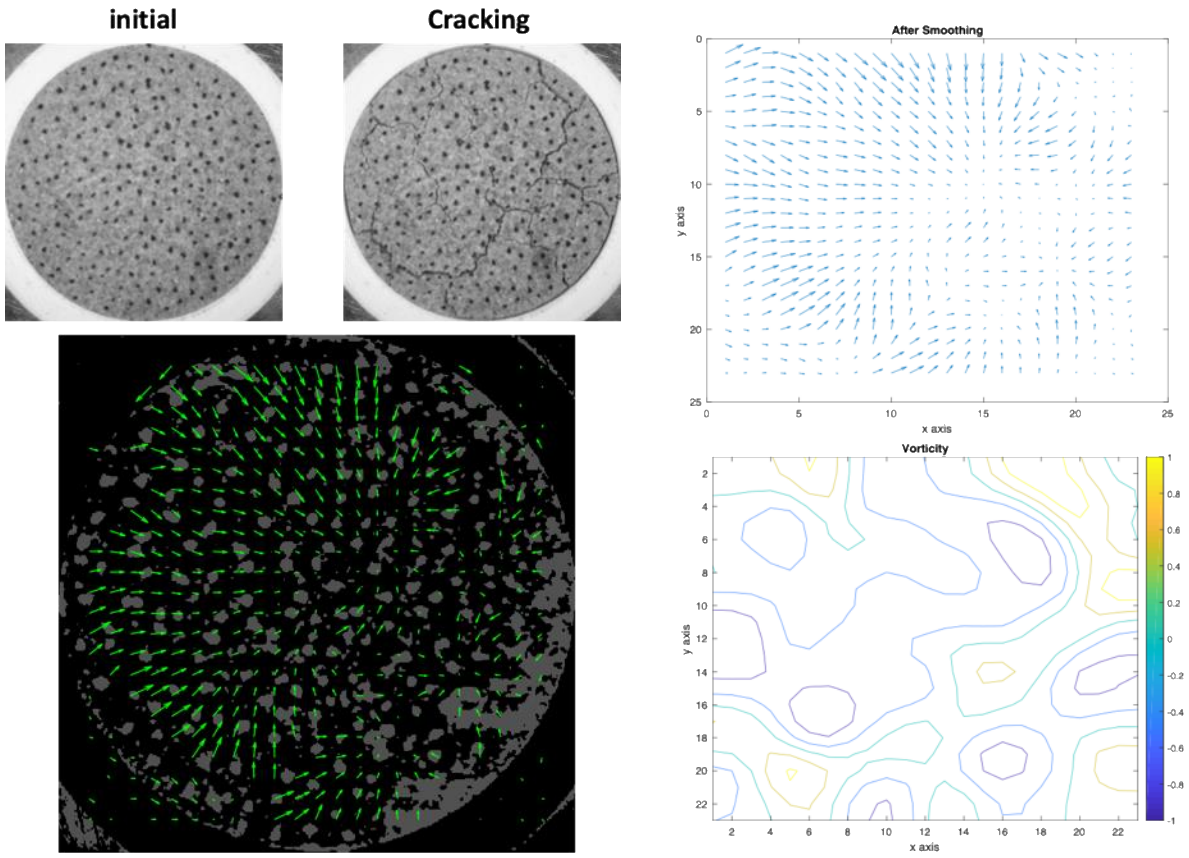

Figure 4.49 DIC analysis of case 2

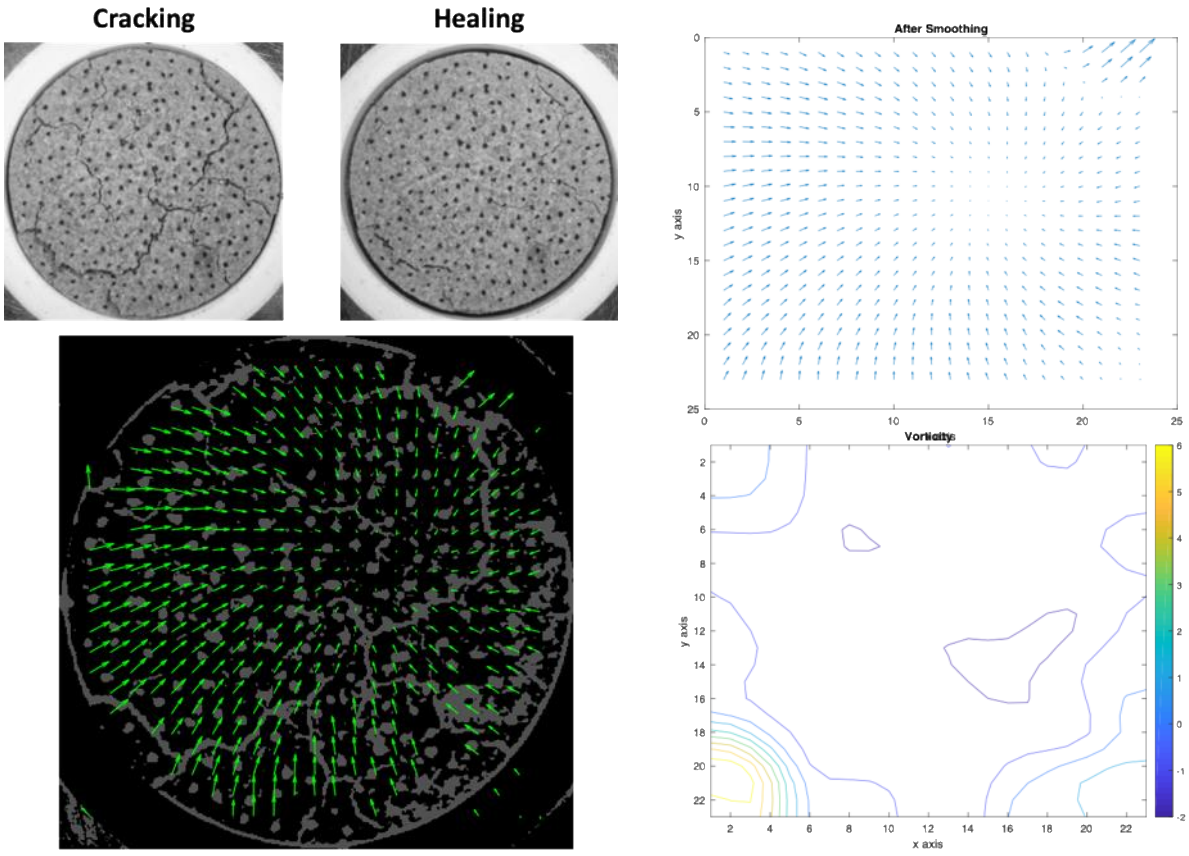

Figure 4.50 DIC analysis of case 3

Figure 4.48 is comparing two states between initial and 30 mins after that (no obvious cracking happen), very small movement (i.e. green arrows) can be seen on the sample surface; if compare the initial state with a cracking state (Figure 4.49) by DIC analysis, it can be observed that the soil particles, from initial state, are moving apart from each other along the cracks positions; However, when healing happens, the whole sample is shrinking much more than during cracking, which make the dominate pattern as particles converged to the center (i.e. due to the shrinking of the sample) instead of particles just moving towards each other along positions of the developed cracks (Figure 4.50).

4.6.5 Test summary

A detailed study on cracking and self-healing behavior was performed in this section, one is self-healing subjected to continuous heating and drying, which is new and not discovered before while the other one is self-healing due to moisture redistribution without water loss if heating and drying is stopped after cracks formed. For self-healing subjected to continuous heating and drying, pattern differences due to different initial sample saturation degree, initial dry density, different heating and drying conditions were all investigated and analyzed. For the other self-healing, three tests under three different S_r values for 1.6g/cm^3 sample were conducted, healing behavior with time was recorded and for different start S_r values, patterns were also quite different. How this different cracking and self-healing behaviors will impact the gas permeability of this barrier material is to be presented in Section 4.7.

4.7 Gas migration in samples with cracking and self-healing

4.7.1 Introduction

As a series of cracking and self-healing tests under different conditions performed and introduced above, it is obvious this nuclear waste barrier material, when under continuous heating and drying condition, showed cracking behavior first and then followed with self-healing when dried to lower saturation degrees. Besides, another style of self-healing also happens when samples were dried to a given saturation degree and then isolated from the environment without any moisture loss. Since gas permeability is one of the most considered properties of barrier material, how these two kinds of self-healing behavior affect the gas permeability of samples with different dry densities (i.e. ρ_d = 1.3g/cm^3 and ρ_d = 1.6g/cm^3) were also investigated in this research.

4.7.2 Test outlines and procedures

For both of these two kinds of self-healing, samples with dry density of 1.3g/cm^3 and 1.6g/cm^3 were tested with GEOTAC triaxial cell system as shown in section 4.4.2. Sample size was same as section 4.5, 3.5cm in diameter and 1.4cm in height; all the samples were tested under pre-calculated saturation degrees. For continuous heating, S_r started from 97%, then 80%, 70%, …… 0%. For isolated self-healing, S_r started from 97%, then dried to 80%, 70%, when reached 70%, sample was sealed in a plastic bag for self-healing, and gas permeability values were measured at different time steps, from 30min to 48h. Sample preparation and gas permeability tests procedures are the same as introduced in section 4.4.

4.7.3 Test results and discussions

4.7.3.1 Cracks self-healing due to continuous heating and drying

For sample with 1.3g/cm^3 initial dry density, gas permeabilities were firstly measured for different heating and drying stages with different crack patterns. Crack patterns for drying stages

selected in S_r are shown in Figure 4.51. Gas permeability results with water contents corresponding to each pre-calculated saturation degrees are shown in Figure 4.52 below.

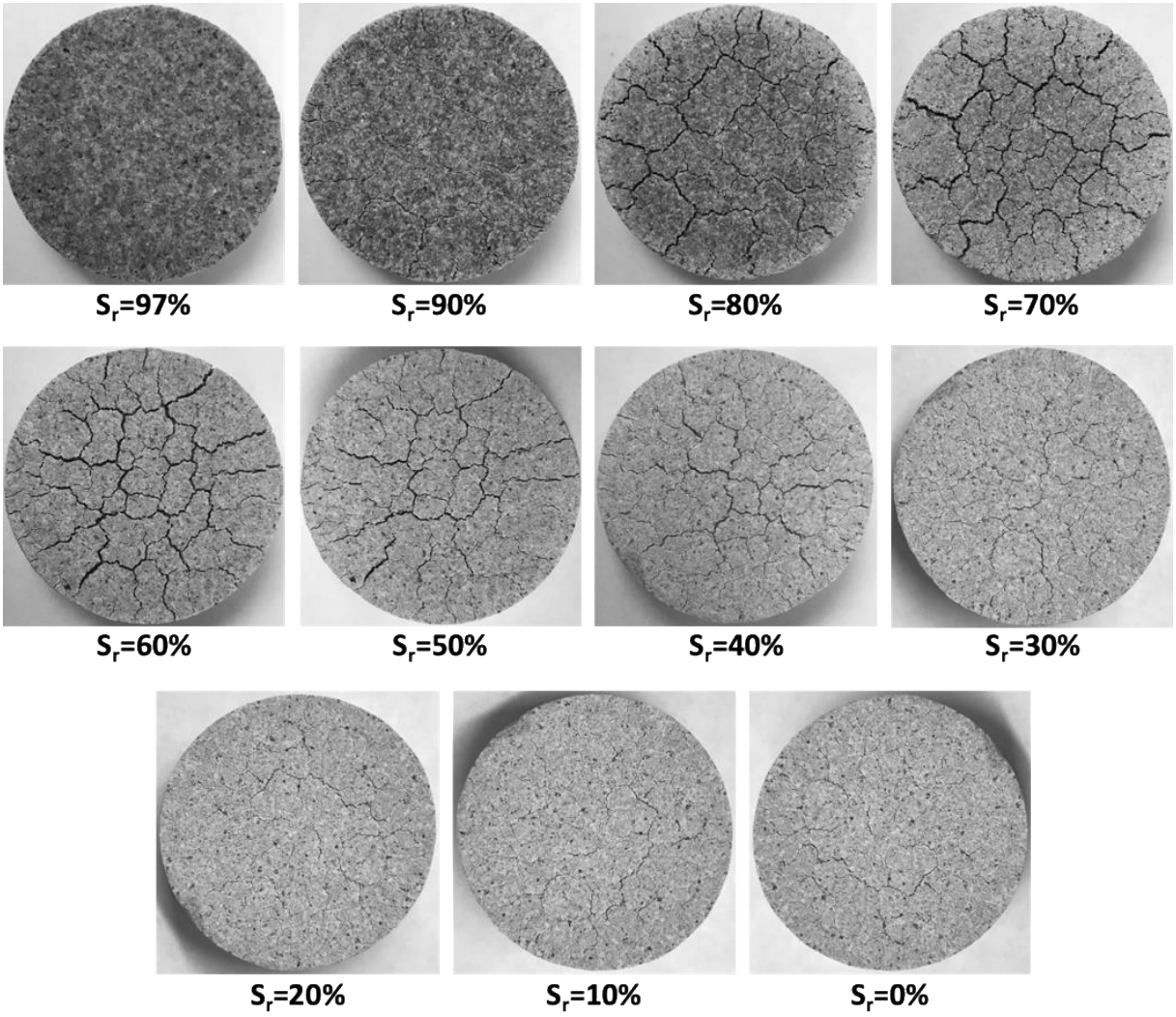

Figure 4.51 Cracking-healing patterns under different stages for sample with 1.3g/cm^3 sample

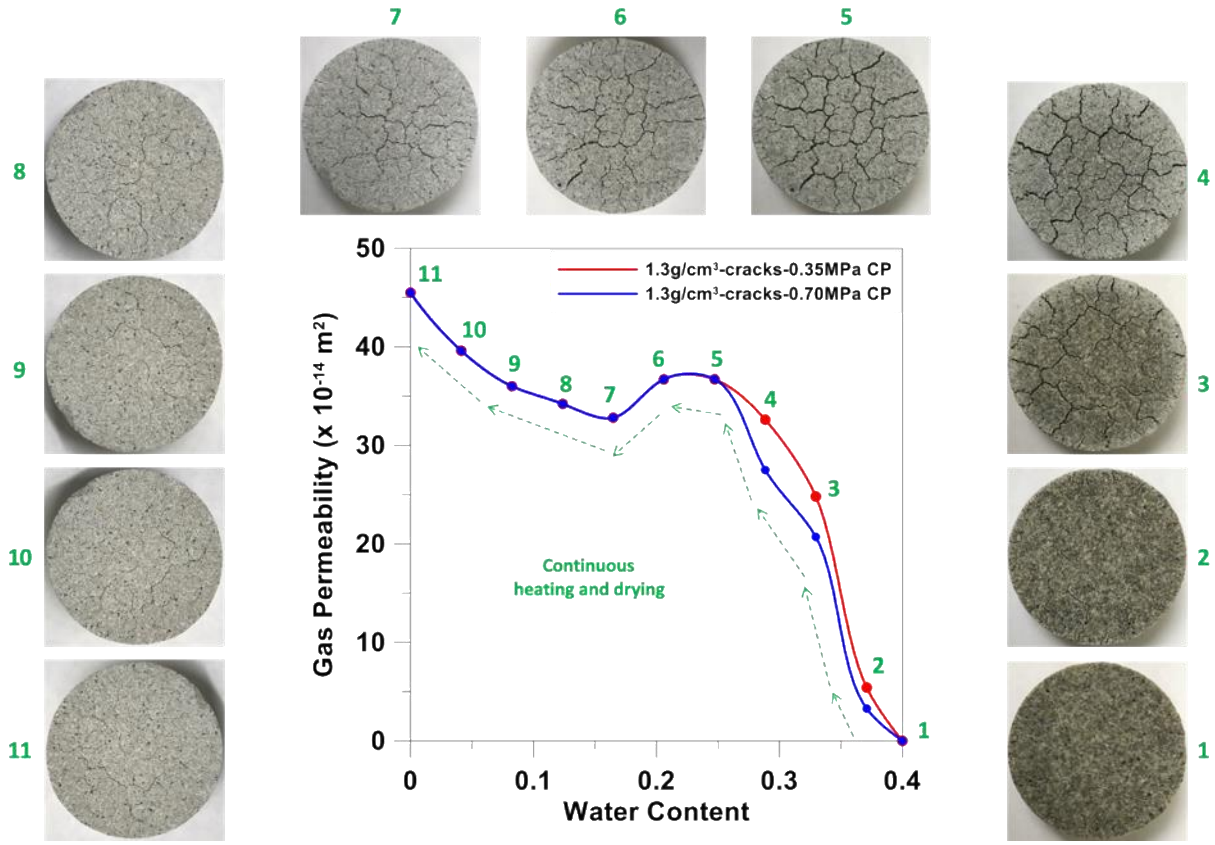

Figure 4.52 Gas permeability variations with cracking and healing for 1.3g/cm^3 dry sample

In terms of cracking sample, with continuous heating and drying (following green arrows), it can be observed from Figure 4.51 that cracks kept developing from initial state to a saturation degree around 70%, and on Figure 4.52, consistently, gas permeability keeps increasing (i.e. more permeable) due to cracks development. Then gas permeability decreased a little bit due to crack healing (S_r=70% to S_r=60%). This can also be proved on Figure 4.51 that from saturation degree around 70%, cracks developed started to heal which makes the material less permeable, and as a result, gas permeability decreased. From initial state to around a S_r value of 60%, gas permeability is mainly dominated by cracks patterns (cracking and healing). However, after the turning point

(S_r=60%), gas permeability started to increase again, in this part, particularly when volume and crack patterns were getting stable, gas permeability became mainly dominated by the saturation degree of the sample, with less moisture in the sample, gas permeability is getting larger. Confinements effects on gas permeability are getting larger for both samples at the beginning heating. With continuous heating and drying, this effect is getting much less and stable, this is due to larger cracks even penetrate cracks developed.

For sample with 1.6g/cm^3 initial dry density, gas permeabilities were measured in a similar way as 1.3g/cm^3 sample. Crack patterns for drying stages selected in pre-calculated Sr are shown in Figure 4.53. Gas permeability results with water contents corresponding to each pre-calculated saturation degrees are shown in Figure 4.54 below.

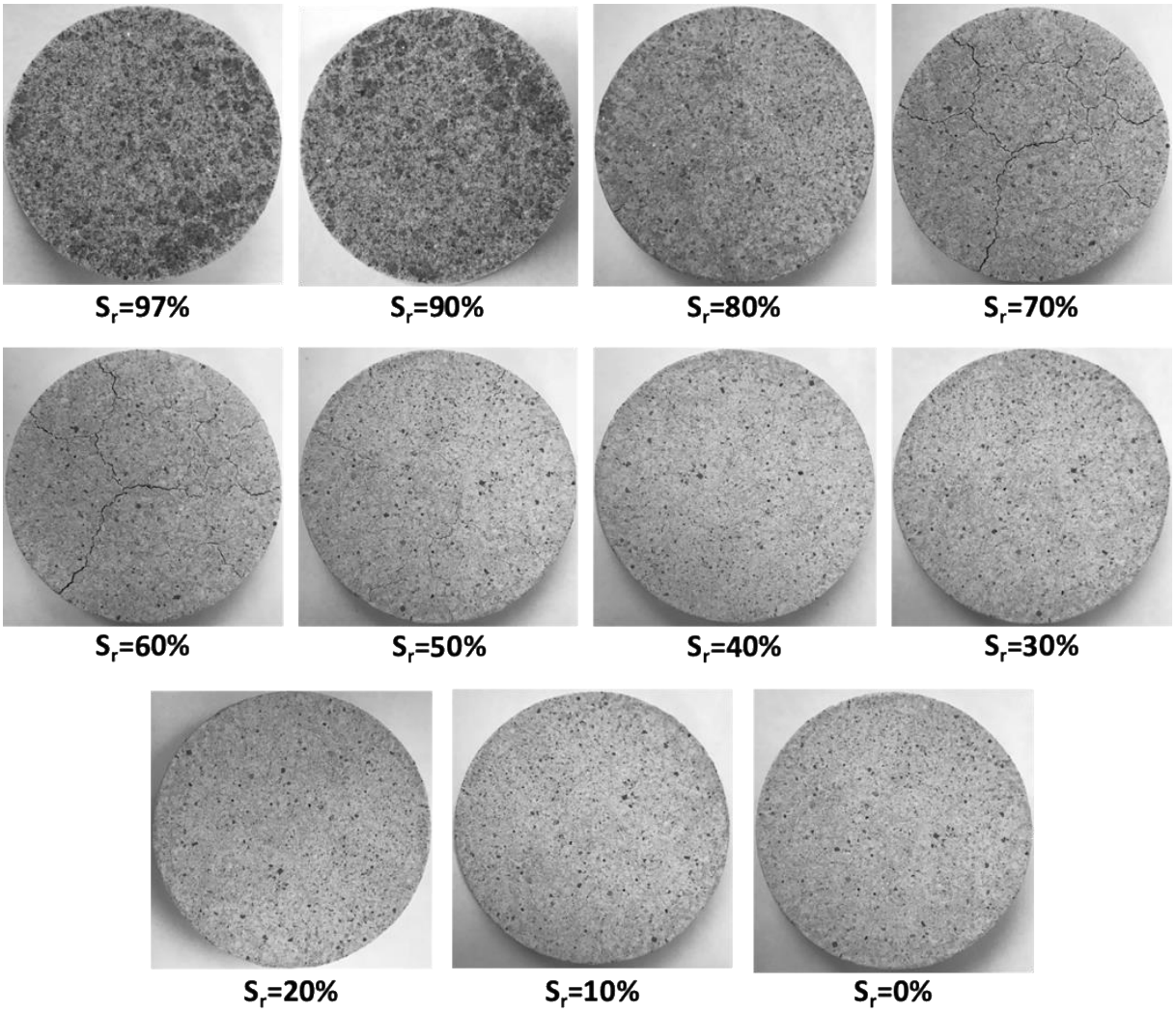

Figure 4.53 Cracking-healing patterns under different stages for sample with 1.6g/cm^3 sample

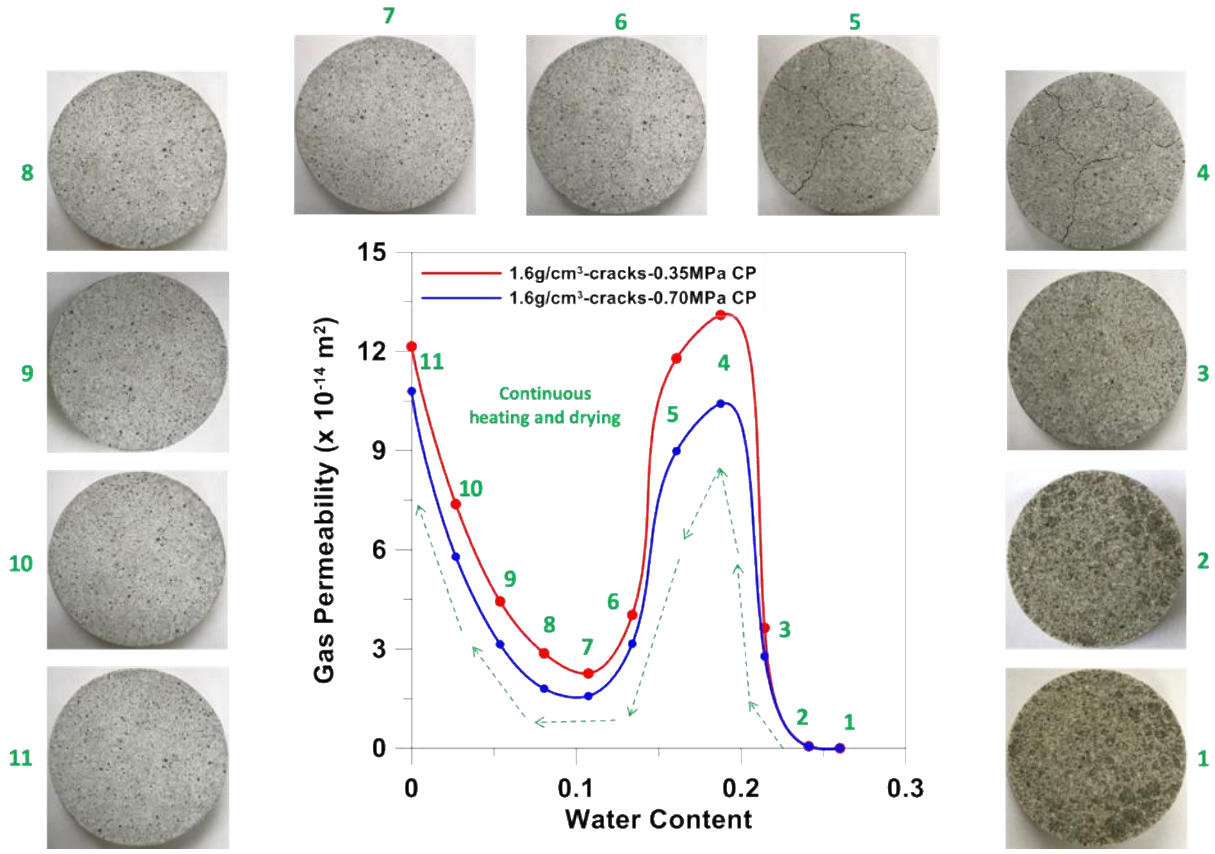

Figure 4.54 Gas permeability variations with cracking and healing for 1.6g/cm^3 sample

From Figure 4.53, with continuous heating and drying (following green arrows), it can be observed that cracks kept developing from initial state to a saturation degree also around 70%, and on Figure 4.54, consistently, gas permeability keeps increasing (i.e. more permeable) due to cracks development. Then gas permeability started to decrease from a saturation degree around 70%. Similar as 1.3g/cm^3 sample, this is due to crack healing. This can also be proved on Figure 4.53 that from saturation degree around 70%, cracks developed started to heal which makes the material less permeable, and as a result, gas permeability decreased. From initial state to around S_r=60%, gas permeability is mainly dominated by cracks patterns (cracking and healing). However, after

the turning point (S_r=60%), gas permeability also started to increase again, in this part, particularly when volume and crack patterns were getting stable, gas permeability became mainly dominated by the saturation degree of the sample, with less moisture in the sample, gas permeability is getting larger, which is similar as we discussed for 1.3g/cm^3 dry density sample. If compare the results of 1.3g/cm^3 and 1.6g/cm^3 in terms of gas permeability, it can be discovered that increment of gas permeability due to cracking is more for 1.3g/cm^3 than 1.6g/cm^3. This is because cracks, which make sample more permeable, is more developed for 1.3g/cm^3 sample than 1.6g/cm^3 sample. However, the influence from healing is more obvious for 1.6g/cm^3 sample because cracks developed are much better healed. Smaller and less cracks with better healing, makes the self-healing influences on gas permeability more remarkable. Confinements effects on gas permeability are getting larger for both samples at the beginning heating. With continuous heating and drying, this effect is getting much less and stable, this is due to larger cracks even penetrate cracks developed.

4.7.3.2 Cracks self-healing due to stopped heating and drying

For sample with 1.3g/cm^3 initial dry density, gas permeabilities were measured for different heating and drying stages (Sr=97%, 90%, 80% and 70%) with different crack patterns. Then the sample was sealed in a plastic bag for self-healing. Self-healing patterns (Figure 4.55) at different time periods (i.e. 30min, 1h, 2h, 3h, 24h, 48h) were recorded by digital camera and gas permeability tests with water contents for sample under each stage were conducted and the results are shown in Figure 4.56.

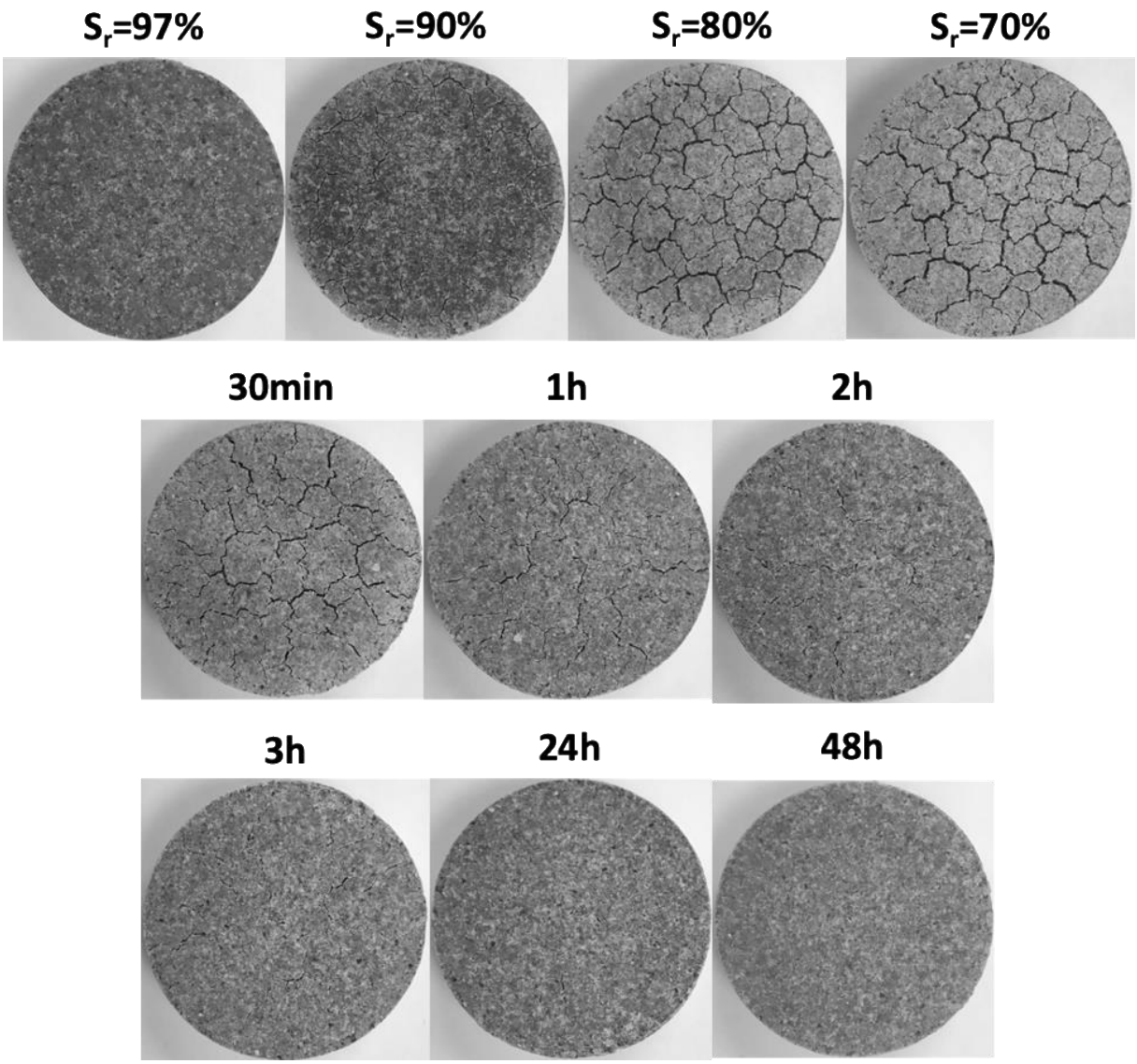

Figure 4.55 Cracking-healing patterns under different stages for sample with 1.3g/cm^3 sample

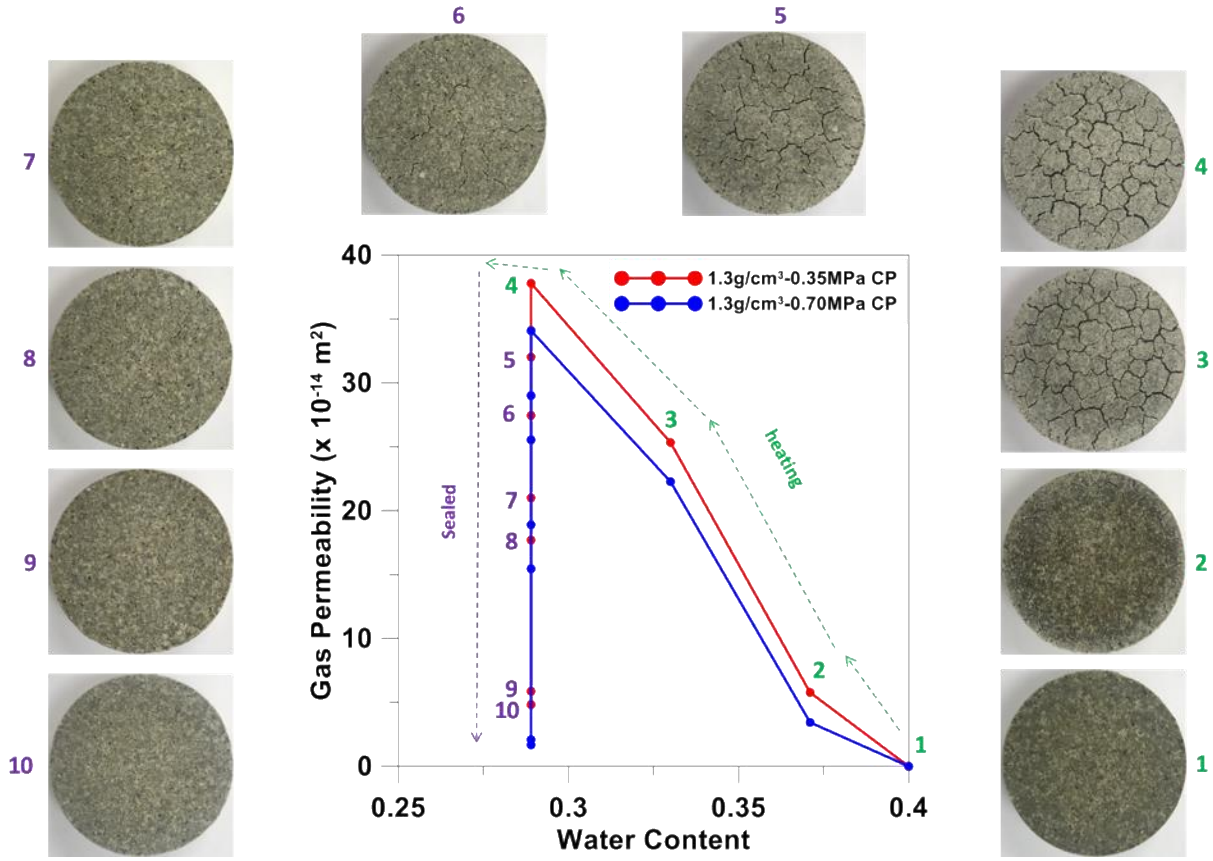

Figure 4.56 Gas permeability variations with cracking and self-healing due to isolation for 1.3g/cm^3 sample

It can be observed from Figure 4.55 that, following the arrows, during heating and drying process, cracks are propagating in similar cracking patterns as the continuous heating and drying test with 1.3g/cm^3 sample and this can be proved by gas permeability values also from Figure 4.56, which kept increasing with heating and drying mainly due to the formation of cracks. When sample was sealed in a plastic bag, self-healing with time (i.e. 30min, 1h, 2h, 3h, 24h, 48h) due to moisture redistribution happened (see Figure 4.55), as a result of which, gas permeability decreased consistently with the self-healing patterns. During this self-healing process, sample was shrinking and cracks were also changing in dimensions. Water content was also adopted to show evolution

of gas permeability. Cracks developed during heating and drying at the beginning, gas permeability keeps increasing due to cracks development. Smaller cell pressure results in larger gas permeability as the beginning of continuous heating tests. After sealed in a plastic bag, cracks developed started to heal as well as continuous sample shrinking, which makes the material less permeable, and as a result, gas permeability decreased. Confinements effects on gas permeability are getting more obvious at the beginning of heating. Cracking pattern and gas permeability got stable after 24h. However, for 1.3g/cm^3 sample, the differences in gas permeability due to confinements after 48h were still large, which means that cracks were not well healed when crack pattern and gas permeability got stable, this is also true if take a look at the sample after 48h, visible cracks are be found on the surface of 1.3g/cm^3 sample.

For sample with 1.6g/cm^3 initial dry density, gas permeabilities were measured in a similar way as 1.3g/cm^3 sample. Crack patterns for drying stages selected are shown in Figure 4.57. Gas permeability results with water contents are shown in Figure 4.58.

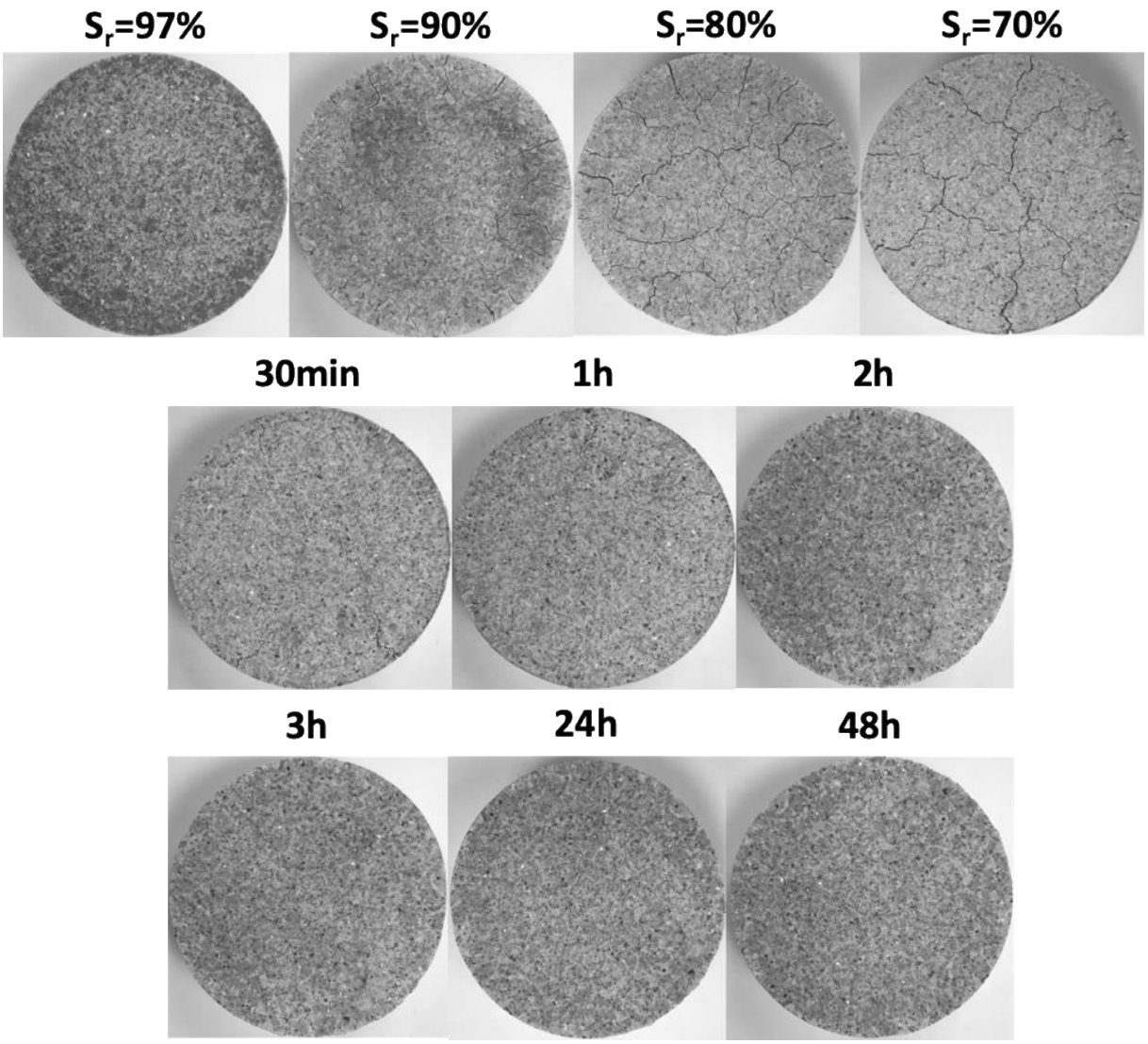

Figure 4.57 Cracking-healing patterns under different stages for sample with 1.6g/cm^3 sample

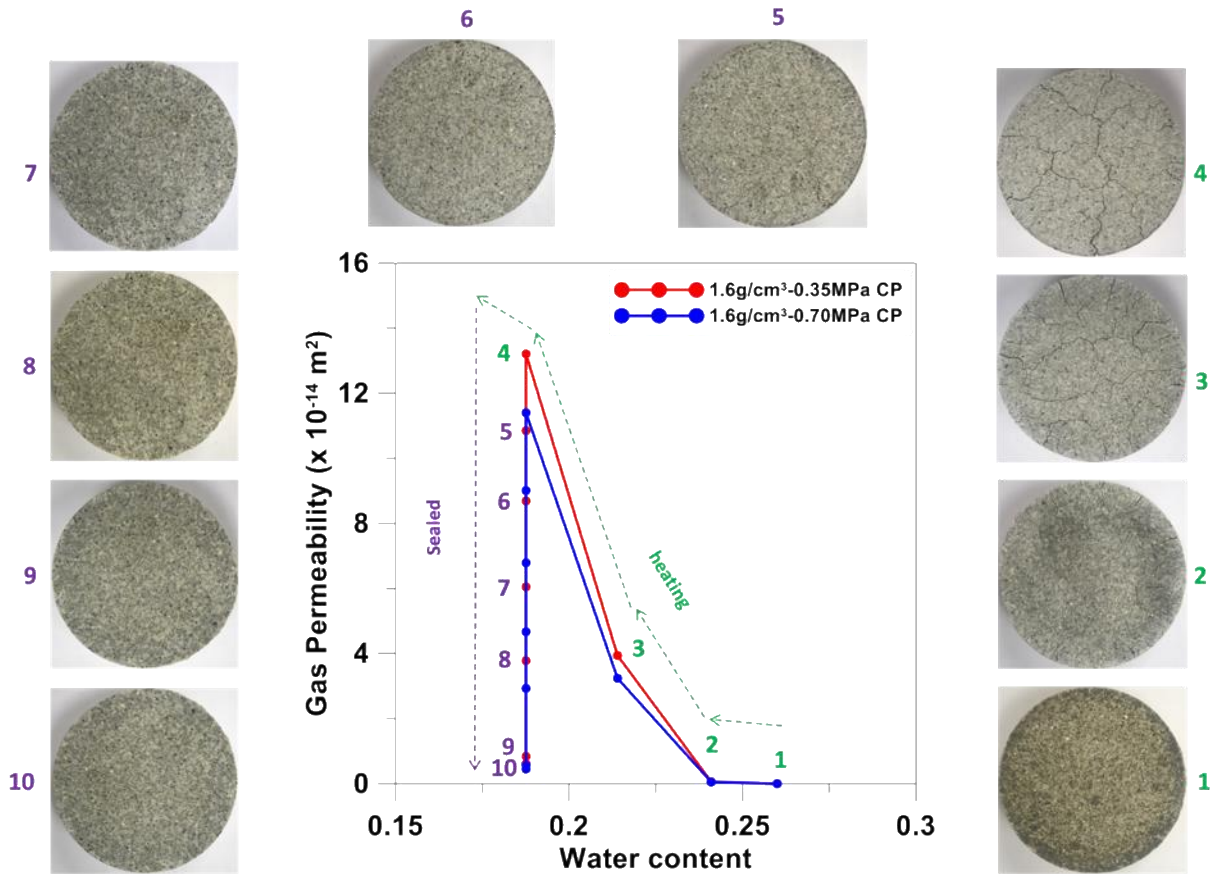

Figure 4.58 Gas permeability variations with cracking and self-healing due to isolation for 1.6g/cm^3 sample

It can be observed from Figure 4.57 that, following the arrows, during heating and drying process, cracks are propagating in similar cracking patterns as the continuous heating and drying test with 1.6g/cm^3 sample and this can be proved by gas permeability values also from Figure 4.58, which kept increasing with heating and drying mainly due to the formation of cracks. When sample was sealed in a plastic bag, self-healing with time (i.e. 30min, 1h, 2h, 3h, 24h, 48h) due to moisture redistribution happened (see Figure 4.57), as a result of which, gas permeability decreased consistently with the self-healing patterns. Similar gas permeability evolution patterns were observed similar to 1.3g/cm^3 sample. During this self-healing process, sample was shrinking and

cracks were also changing in dimensions. Water content was also adopted to show evolution of gas permeability. Cracks developed during heating and drying at the beginning, gas permeability keeps increasing due to cracks development. Smaller cell pressure results in larger gas permeability as the beginning of continuous heating tests. After sealed in a plastic bag, cracks developed started to heal as well as continuous sample shrinking, which makes the material less permeable, and as a result, gas permeability decreased. Confinements effects on gas permeability are getting more obvious at the beginning of heating. Cracking pattern and gas permeability got stable after 24h. However, for 1.6g/cm^3 sample, the differences in gas permeability due to confinements after 48h were very small (similar as the beginning of heating and drying process), which means cracks are well healed and returned to a high saturation degree, this is also true if take a look at the sample after 48h, no visible cracks are be found on the surface of 1.6g/cm^3 sample.

4.7.4 Test summary

In this part, gas permeability variations due to cracking and self-healing were investigated. A lot of gas permeability tests were conducted using triaxial cell with steady state method. For self-healing subjected to continuous heating and drying, samples with different initial dry densities and different confinements were tested, all the samples show gas permeability increase due to cracking and decreasing saturation degree and decrease due to healing, larger dry density sample shows more obvious gas permeability change in this process. For self-healing after isolating with outside environment with constant moisture content, also different dry densities and confinements were taken into consideration, K_g change according to time steps were recorded and healing extent for different dry density samples were evaluated.

4.8 Summary

In this research topic, a lot of preliminary tests on investigating the geo-properties and swelling properties of the barrier material adopted for this research were conducted. Sample with two different dry densities were investigated. Gas permeabilities with different test devices under different conditions were performed. Relationships between swelling pressure, suction and gas permeability was established.

A self-designed gas breakthrough cell was manufactured and gas breakthrough trials were made. It is verified that the self-designed cell can be used for sample saturation and gas breakthrough tests with interface problem avoided under high pressure very well. Gas breakthrough pressures tend to have gas injection rate dependence, higher rate makes it more difficult to breakthrough. By trying different connections, interface problem was evaluated and it may exist for traditional gas breakthrough device and method.

A series of cracking and self-healing tests with samples of different initial conditions and different heating and drying conditions were conducted. It is discovered that for this nuclear waste barrier material, cracking patterns are quite different under different initial conditions and different heating and drying methods, but cracking and self-healing behaviors are always happened successively. There is a peak for cracking behavior, after which, cracks on sample started to be self-healed. During this heating and drying process, particularly at higher saturation degrees, volume of sample is decreasing while dry density keeps increasing, while at low saturation degrees, volume and dry density become quite stable.

Besides, it can be observed that the soil particles, from initial state to largely cracked, are moving apart from each other along the positions of the cracks. However, when healing happens, the whole sample is shrinking much more than during cracking, which make the dominate pattern

as particles converged to the center instead of particles just moving towards each other along positions of the former developed cracks.

Moreover, gas permeability is affected by cracking and self-healing behavior. For continuous heating and drying, at high saturation degrees, cracking and self-healing dominate on controlling gas permeability, resulting in gas permeability decreasing firstly when cracking propagates and then decreasing when cracks start to heal. However, at low saturation degrees, volume and dry density become quite stable, gas permeability is mainly affected by saturation degree, showing an increasing tendency with losing of moisture. Under same conditions, sample with lower dry density will develop larger and more cracks, which increase sample gas permeability more distinct. However, the influence from healing is more obvious for denser sample because cracks developed are smaller and less but better healed, making the self-healing influences on gas permeability more remarkable. Confinements effects on gas permeability are getting larger for both samples at the beginning heating. With continuous heating and drying, this effect is getting much less and stable, this is due to larger cracks even penetrate cracks developed. For self-healing after isolating with outside environment with constant moisture content, also different dry densities and confinements were taken into investigation, K_g change according to time steps were recorded and healing extent for different dry density samples were evaluated based on tests results.

5 SUMMARY AND FUTURE WORKS

In this dissertation, three topics dealing with multiphase problems are investigated in detail and the main achievements and conclusions will be listed in this section. Some future work plans on each topic will also be discussed separately in this part.

5.1 Frozen soil subjected to cyclic freezing-thawing

From the experimental campaign the following points can be highlighted:

- A better understanding of the behavior of soils subjected to freeze-thaw cycles has been gained.
- A new set of high-quality experimental data of cyclic freeze-thaw soils with different loading histories and freezing-thawing cycles has been obtained.
- Normally consolidated *(NC)* soils subjected to freeze-thaw cycles at low stress level tend to accumulate compressive plastic deformations with a net contraction of the sample after the freeze-thaw cycles. for over consolidated *(OC)* tests, samples showed an expansion tendency.
- *NC* soils subjected to *Fr-Th* cycles tend to accumulate plastic strains with a net contraction of the soil after the cycles, trend that slightly decreases with the stress level. As for *OC* soils, all of them showed a tendency to expand, which increases with the soil *OCR*. Based on these tests, it also appears that samples with the same *OCR*, but with a previous history of *Fr-Th* tend to expand less.
- Effect from temperature range during *Fr-Th* cycles was also investigated by several cases, tests with smaller temperature range (e.g. -0.3℃ to 5℃) present smaller volume change when compared with larger range (e.g. -7℃ to 5℃) because of the difference in amount of unfrozen water content when frozen to the lowest temperature.
- Unfrozen water saturation degree can be measured by measuring electrical conductivity.

- According to collapse tests, void ratio after thawing collapse is almost the same as that got by room temperature consolidation starting from same initial condition and under same loading path.
- Knowledge on how OCR and temperature range play the role in cyclic *Fr-Th* process of soil is upgraded one step further, and any effort to reproduce this behavior must therefore include these factors to make an accurate prediction about the volumetric changes in practical problems.

As for modeling campaign, this research show that:

- A mechanical model that incorporates both the modified BBM and double structure model, is able to properly capture the observed behavior of soils subjected to cyclic *Fr-Th* process.
- The proposed model was able to reproduce very satisfactorily all the tests conducted in the experimental campaign.
- The proposed and validated model represents a clear step forward in this area, where mechanical models able to properly describe the behavior of frozen soils subjected to F-T cycles were lacking.

As future work, triaxial tests should be conducted to validate and extension of the model to 3D stress conditions. Besides, this model should be implemented into a finite element software and it should be used to simulate real application cases involving frozen grounds.

5.2 Mechanical modeling on methane hydrate bearing sediment

The elasto-visco-plastic model for MHBS developed in this research has shown:

- The proposed enhanced hardening law is capable of capturing the response of MHBS exhibiting large dilatancy behavior.
- The simple upgrade of the evolution law for the pre-consolidation pressure based on thermo-plasticity that is adopted in this research has been able to account for the thermal effects observed in the experiments.

- The traditional Perzyna's concept to deal with visco-plastic effects in solids has been able to capture load rate effects observed in MHBS.
- The models proposed in this research can capture the critical features of MHBS behaviors when dealing with high dilatancy, temperature effects, and time-dependent behavior, which are not well capture by previous mechanical models.

5.3 Gas migration through engineered barrier systems intended for HLW disposal

In this research topic:

- Gas permeabilities with different test devices and techniques under different conditions were performed and mutually complemented.
- More comprehensive relationships among swelling pressure, suction and gas permeability was established at the same time.
- A self-designed high-capacity steel cell was manufactured and successfully used for sample saturation and gas breakthrough tests with interface problem avoided under high pressure.
- Gas breakthrough pressure has gas injection rate dependence, higher gas injection rate makes it more difficult to breakthrough. After interface problem evaluations, it is concluded that such kind of problem may exist for traditional gas breakthrough device and method.
- A series of cracking and self-healing tests with samples of different initial conditions and different continuous heating and drying conditions were conducted. It is discovered that for this nuclear waste barrier material, cracking patterns are quite different under different conditions, but cracking and self-healing behaviors are always happened successively during continuous heating and drying, which broaden current knowledge on this barrier material.

- Gas permeability is affected by cracking and self-healing behavior during continuous heating and drying. At high saturation degrees, cracking and self-healing dominate on controlling gas permeability, resulting in gas permeability decreasing firstly when cracking propagates and then decreasing when cracks start to heal. However, at low saturation degrees, volume and dry density become quite stable, gas permeability is mainly affected by saturation degree, showing an increasing tendency with losing of moisture.
- Under same conditions, sample with lower dry density will develop larger and more cracks, which increase sample gas permeability more distinct. However, the influence from healing is more obvious for denser sample because cracks developed are smaller and less but better healed, making the self-healing influences on gas permeability more remarkable.
- Confinements effects on gas permeability are getting larger for both samples at the beginning heating. With continuous heating and drying, this effect is getting much less and stable due to larger cracks even penetrate cracks developed.
- For self-healing after isolating from outside environment with constant moisture content, also different dry densities and confinements were taken into investigation, gas permeability changes according to time steps were recorded and healing extent for different dry density samples were evaluated based on tests results, which was not well investigated before.

In the future work, for gas breakthrough tests, much smaller gas injection rate will be adopted to have a more detailed investigation on injection rate effects. Heterogeneous samples with pre-exist fractures or material interfaces inside the sample will also be investigated. Breakthrough time can also be studied when different dry density samples are under constant injection pressures. Moreover, cracking and healing behavior is planned to be further investigated. Healing due to wetting the sample back to initial state will be studied. Also, some cyclic wetting-

drying tests will be performed to study the effect from cracking and wetting-drying cycles on gas permeability of barrier material. Another task in the future is to find an accurate way to measure the volume change of the sample to have a clearer understanding on saturation degree change during these complex processes.

REFERENCES

Adachi, T., Oka, F. (1982). “Constitutive equations for normally consolidated clay based on elasto-viscoplasticity.” *Soils Found*, *22*(4), 57–70.

Adachi, T., Oka, F., Koike, M. (2005). “An elasto-viscoplastic constitutive model with strain-softening for soft sedimentary rocks.” *Soil and Foundations, 45*(2), 125-133.

Albercht, B.A., Benson, C.H. (2001). “Effect of desiccation on compacted natural clay.” *Journal of Geotechnical and Geoenvironmental Engineering*, *67*(1), 67-75.

Alonso, E.E., Gens, A., Josa, A. (1990). “A constitutive model for partially saturated soils.” *Géotechnique*, *40*(3), 405-430.

Alonso, E.E., Olivella, S., Arnedo, D. (2006). “Mechanisms of gas transport in clay barriers.” *Journal of Iberian Geology*, *32*(2), 175–196.

Amiri, S.A.G., Grimstad, G., Kadivar, M., Nordal, S. (2016). “Constitutive model for rate-independent behavior of saturated frozen soils.” *Canadian Geotechnical Journal, 53*(10), 1646-1657.

Andersland, O. B., Akili, W. (1967). “Stress effect on creep rates of a frozen clay soil.” *Géotechnique, 17*(1), 27-39.

Arnedo, D., Alonso, E.E., Olivella, S. and Romero, E. (2008). “Gas injection tests on sand/bentonite mixtures in the laboratory, experimental results and numerical modelling.” *Physics and Chemistry of the Earth*, *33*(1), S237-S247.

Atique, A., Sánchez, M., & Romero, E. (2009). “Investigation of crack desiccation in soil from a flood protection embankment.” *CRC Press*, 413-418.

Bastiaens, W., Bernier, F., Xiang, L.L. (2007). “SELFRAC: Experiments and conclusions on fracturing, self-healing and self-sealing processes in clays.” *Physics and Chemistry of the Earth, 32*(8-14), 600–615.

Black, P.B., Miller, R.D. (1990). “Hydraulic conductivity and unfrozen water content of air-free frozen silt.” *Water Resource Research, 26*(2), 323-329.

Campanella, R.G., Mitchell, J.K. (1968). “Influence of temperature variations on soil behavior.” *Journal of Soil Mechanics and Foundations Division, 94*(3), 709–734.

Cekerevac, C., Laloui, L. (2004). “Experimental study of thermal effects on the mechanical behavior of a clay.” *International Journal for Numerical and Analytical Methods in Geomechanics, 28*(3), 209–228.

Chamberlain, E., Groves, C., Perham, R. (1972). “The mechanical behaviour of frozen earth materials under high pressure triaxial test conditions.” *Géotechnique*, *22*(3), 469-483.

Choi, J.H., Lin, J.S., Dai, S., Lei, L., Seol, Y. (2020). “Triaxial compression of hydrate-bearing sediments undergoing hydrate dissociation by depressurization.” *Geomechanics for Energy and the Environment, 23*, 100187.

Clausius, R. (1850). “Ueber die bewegende kraft der wärme und die gesetze, welche sich daraus für die wärmelehre selbst ableiten lassen.” *Annalen der Physik (in German)*, *155*(4), 500–524.

Clayperon, B.P.M. (1834). “Mémoire sur la puissance motrice de la chaleur.” *Journal de l’Ecole Polytechnique, 14*(23), 153-190.

Cui, Z.D., He, P., Yang, W. H. (2014). “Mechanical properties of a silty clay subjected to freezing-thawing.” *Cold Region Science and Technology, 98*, 26-34.

Cuss, R.J., Harrington, J.F., Noy, D.J., Wikman, A., Sellin, P. (2011). “Large scale gas injection test (Lasgit): results from two gas injection tests.” *Physics and Chemistry of the Earth, 36,* 1729-1742.

Dai, S., Sanchez, M. (2020). “Geomechanics for energy and the environment [GETE]—special issue: ‘Challenges of gas production from hydrate-bearing sediments.’” *Geomechanics for Energy and the Environment, 23,* 100189.

Davy, C.A., Skoczylas, F., Lebon, P., Dubois, T. (2009). “Gas migration properties through a bentonite/argillite interface.” *Applied Clay Science, 42,* 639-648.

Desai, C.S., Somasundaram S., Frantziskonis, G. (1986). “A hierarchical approach for constitutive modelling of geologic materials.” *International Journal for Numerical and Analytical Methods in Geomechanics, 10*(3), 225-257.

Desai, C.S. (1989). “Letter to editor single surface yield and potential function plasticity models: A review.” *Computers and Geotechnics, 7*(4), 319-333.

Egermann, P., Lombard, J. M., & Bretonnier, P. (2006 September). “A fast and accurate method to measure threshold capillary pressure of caprocks under representative conditions.” In International Symposium of the Society of Core Analysts held in Trondheim, Norway.

Eigenbrod, K.D. (2003). “Self-healing in fractured fine-grained soils.” *Canadian Geotechnical Journal, 40*(2), 435–449.

Fall, M., Nasir, O., Nguyen, T.S. (2014). “A coupled hydro-mechanical model for simulation of gas migration in host sedimentary rocks for nuclear waste repositories.” *Engineering Geology, 176,* 24–44.

Feldler-Feldegg, J. (1969). “The measurement of dielectrics in the time domain.” *The Journal of Physical Chemistry,* 73, 616–623.

Freitas, T.M.B., Potts, D.M., Zdravkovic, L. (2011). “A time dependent constitutive model for soils with isotach viscosity.” *Computers and Geotechnics, 38*(6), 809–820.

Gai, X., and Sánchez, M. (2017). “A geomechanical model for gas hydrate bearing sediments.” *Environmental Geotechnics*, *4*(2), 143–156.

Galle, C., Tanai, K. (1998). “Evaluation of gas transport properties of backfill materials for waste disposal: H2 migration experiments in compacted Fo-Ca clay.” *Clay Miner*, *46*(5), 498-508.

Garcia-Sineriz, L., Villar, M., Rey, M., Palacios, B. (2015). “Engineered barrier of bentonite pellets and compacted blocks: State after saturation.”, *Engineering Geology, 192,* 33-45.

Gens, A., Alonso, E.E. (1992). “A framework for the behaviour of unsaturated expansive clays.” *Canadian Geotechnical Journal*, *29*(6), 1013-1032.

Graham, (1997). “The buffer/container experiments: results, synthesis.”, AECL Report 11746. Retrieved from https://inis.iaea.org/collection/NCLCollectionStore/_Public/31/030/31030401.pdf?r=1.

Graham, J., Au, V. C. S. (1985). “Effects of freeze-thaw and softening on a natural clay at low stresses.” *Canada Geotechnical Journal, 22*(1), 69-78.

Graham, C.C., Harrington, J.F., and Sellin, P. (2016) “Gas migration in pre-compacted bentonite under elevated pore-water pressure conditions.” *Applied Clay Science, 132–133,* 353–365.

Han, Y., Wang, Q., Wang, N., Wang, J., Zhang, X., Cheng, S. (2018). “Effect of freeze-thaw cycles on shear strength of saline soil.” *Cold Region Science and Technology, 154,* 42-53.

Harrington, J.F., Horseman, S.T. (1997). “Gas transport properties of clays and mudrocks.” Muds and Mudstones: Physical and Fluid Flow Properties, Geological Society of London, Special Publication, 158, 107-124.

Harrington, J. F., Horseman, S. T. (1999). “Gas transport properties of clays and mudrocks.” In: Muds and Mudstones: Physical and Fluid Flow Properties, Geological Society of London, Special Publication No. 158, 107–124.

Harrington, J. F., Horseman, S. T. (2003). “Gas migration in KBS-3 buffer bentonite.” Technical report TR-03-02. Retrieved from https://inis.iaea.org/search/search.aspx?orig_q=RN:34035698.

Hashiguchi, K. (1989). “Subloading surface model in unconventional plasticity.” *International Journal of Solids and Structures, 25*(8), 917-945.

Hashiguchi, K., Chen, Z.P. (1998). “Elastoplastic constitutive equation of soils with the subloading surface and the rotational hardening.” *International Journal for Numerical and Analytical Methods in Geomechanics*, *22*(3), 197-227.

Hazirbaba (2019). “Effects of freeze-thaw on settlement of fine-grained soil subjected to cyclic loading.” *Cold Regions Science and Technology*, *160*, 222-229.

Hildenbrand, A., S. Schlömer, & B. Krooss. (2002). “Gas breakthrough experiments on fine-grained sedimentary rocks.” *Geofluids, 2*, 3-23.

Hinchberger, S.D., Rowe, R.K. (2005). “Evaluation of the predictive ability of two elastic–viscoplastic constitutive models.” *Canada Geotechnical Journal*, *42*(6), 1675–1694.

Hokari, T., Okihara, M., Ishii, T., Ikuse, H. (1997). “Experimental study on scale effects of bentonite/sand mixtures on gas migration.” In: Proceeding Scientific Basis for Nuclear Waste Management, Boston. Materials Research Society, 465, 1019–1026.

Horseman, S.T., Harrington, J.F, Sellin, P. (1999). “Gas migration in clay barriers.” *Engineering Geology, 54*(1-2), 139-149.

Horseman, S.T., Harrington, J.F., Sellin, P. (2004). “Water and gas flow in Mx80 bentonite buffer clay.” *Materials Research Society*, *807*, 715-720.

Hueckel, T., Baldi, G. (1990). “Thermoplasticity of saturated clays: experimental constitutive study.” *Journal of Geotechnical Engineering, 116*(12), 1778–96.

Hyodo, M., Nakata, Y., Yoshimotoa, N., Ebinuma, T. (2005). “Basic research on the mechanical behavior methane hydrate-sediment mixture.” *Soils and Foundations, 45*(1), 75-85.

Hyodo, M., Yonedab, J., Yoshimotoa, N., Nakata, Y. (2013). “Mechanical and dissociation properties of methane hydrate-bearing sand in deep seabed.” *Soils and Foundations, 53*(2), 299–314.

Hyodo, M., Li, Y., Yoneda, J., Nakata, Y., Yoshimoto, N., Nishimura, A., Song, Y. (2013). “Mechanical behavior of gas-saturated methane hydrate-bearing sediment.” *Journal of Geophysical Research: Solid Earth, 118*(10), 5185–5194.

Joseph, J., Kuntikana G., Singh, D.N. (2019). “Investigations on gas permeability in porous media.” *Journal of Natural Gas Science and Engineering*, *64*, 81-92.

Kanitha, T., Reid, D.S. (2004). “DSC and NMR relaxation studies of starch water interactions during gelatinization.” *Carbohydrate Polymers, 58*(3), 345–358.

Kärnbränslehantering, S. (2011). “Long-term safety for the final repository of spent nuclear fuel at Forsmark.” SKB Report TR-11-01. Retrieved from https://skb.se/upload/publications/pdf/TR-11-01_vol1.pdf.

Kim, J.S., Kwon, S.K., Sanchez, M., Cho, G.C. (2011). “Geological storage of high-level nuclear waste.” *KSCE Journal of Civil Engineering*, *15*(4), 721-737.

Klar, A., Soga, K., Ng, M.Y.A. (2010). “Coupled deformation–flow analysis for methane hydrate extraction.” *Géotechnique, 60*(10), 765-776.

Lai, Y., Liao, M., Hu, K. (2016). “A constitutive model of frozen saline sandy soil based on energy dissipation theory.” *International Journal of Plasticity, 78,* 84–113.

Laloui, L., Cekerevac, C. (2003). “Thermo-plasticity of clays: an isotropic yield mechanism.” *Computers and Geotechnics, 30*(8), 649–60.

Le, T.X., Rodts, S., Hautemayou, D., Aimedieu, P., Bornert, M., Chabot, B., Tang, A.M. (2020). “Kinetics of methane hydrate formation and dissociation in sand sediment.” *Geomechanics for Energy and the Environment, 23,* 100103.

Lee, W., Bohra, N., Altschaeffl, A. and White, T. (1995). “Resilient modulus of cohesive soils and the effect of freeze-thaw.” *Canadian Geotechnical Journal*, *32*(4), 559-568.

Li, Y., Song, Y., Yu, F., Liu, W., Zhao, J. (2011). “Experimental study on mechanical properties of gas hydrate-bearing sediments using kaolin clay.” *China Ocean Engineering*, *25*(1), 113-122.

Lin, B., Zhang, F., Feng, D., Tang, K., Feng, X. (2017). “Accumulative plastic strain of thawed saturated clay under long-term cyclic loading.” *Engineering Geology*, *231*, 230-237.

Ling, X. Z., Zhang, F., Li, Q. L., An, L. S., Wang, J. H. (2015). “Dynamic shear modulus and damping ratio of frozen compacted sand subjected to freeze–thaw cycle under multi-stage cyclic loading.” *Soil Dynamics and Earthquake Engineering*, *76*, 111-121.

Liu, J.F., Skoczylas, F., Talandier, J. (2015). “Gas permeability of a compacted bentonite–sand mixture: coupled effects of water content, dry density, and confining pressure.” *Canadian Geotechnical Journal, 52*(8), 1159.

Liu, W., Luo, T., Li, Y., Song, Y., Zhu, Y., Liu, Y., Zhao, J., Wu, Z., Xu, X. (2016). "Experimental study on the mechanical properties of sediments containing CH4 and CO2 hydrate mixtures." *Journal of Natural Gas Science and Engineering*, *32,* 20-27.

Louati, F., Trabelsi, H., Jamei, M., Taibi, S. (2018). "Impact of wetting-drying cycles and cracks on the permeability of compacted clayey soil." *European Journal of Civil and Environmental Engineering*. https://doi.org/10.1080/19648189.2018.1541144.

Lu, Y., Liu, S., Alonso, E., Wang, L., Xu, L., Li, Z. (2019). "Volume changes and mechanical degradation of a compacted expansive soil under freeze-thaw cycles." *Cold Regions Science and Technology*, *157,* 206-214.

Luo, T., Li, Y., Liu, W., Sun, X., Shen, S. (2017). "Experimental study on the mechanical properties of CH4 and CO2 hydrate remodeling cores in Qilian Mountain." *Energies 10*(12), 2078.

Ma, W., Wu, Z., Pu, Y., Chang, X. (1997). "Monitoring the change of structures in frozen soil during the triaxial creep process by computer tomography." *The 7th International Permafrost Conference, Yellowknife,* Canada. Collection Nordicana NO 55.

Mao, Y., Romero, E., Gens, A. (2018). "Ice formation in unsaturated frozen soils." *7th International Conference on Unsaturated Soils,* Hong Kong, China. Retrieved from https://upcommons.upc.edu/handle/2117/129404?show=full.

Marschall, P., Horseman, S., Gimmi, T. (2005) "Characterization of gas transport properties of the Opalinus Clay, a potential host rock formation for radioactive waste disposal." *Oil and Gas Science and Technology-Revue IFP, 60*(1), 121–139.

Mathew, T.B. (2012). "The influence of cryostructure on the creep behavior of ice-rich permafrost." *Cold Regions Science and Technology*, *79-80,* 43-52.

Mayne, P.W. (2001). “Stress-strain-strength-flow parameters from enhanced in-situ tests.” *Proceedings, International Conference on In-Situ Measurement of Soil Properties & Case Histories,* Bali, Indonesia, 27-48.

Miyazaki, K., Masui, A., Yamaguchi, T., Sakamoto, Y., Haneda, H. et al. (2009). “Strain-rate dependency of peak and residual strength of sediment containing synthetic methane hydrate in triaxial compression test.” *The Nineteenth International Offshore and Polar Engineering Conference*, ISOPE-I-09-344.

Miyazaki, K., Masui, A., Aoki, K., Sakamoto, Y., Yamaguchi, T. et al. (2010). “Strain-rate dependence of triaxial compressive strength of artificial methane-hydrate-bearing sediment.” *International Journal of Offshore and Polar Engineering*, 20(4).

Miyazaki, K., Yamaguchi, T., Sakamoto, Y., Aoki, K. (2011). “Time-dependent behaviors of methane-hydrate bearing sediments in triaxial compression test.” *Japanese Committee for Rock Mechanics, 7*(1), 43-48.

Miyazaki, K., Tenma, N., Sakamoto, Y., Yamaguchi, T., Okubo, S. (2012). “Effects of methane hydrate saturation and confining pressure on strain-rate dependence of artificial methane-hydrate-bearing sediment in triaxial compression test.” *International Journal of Offshore and Polar Engineering*, 22(1).

Miyazaki, K., Tenma, N., Yamaguchi, T. (2017). “Relationship between creep property and loading-rate dependence of strength of artificial methane-hydrate-bearing toyoura sand under triaxial compression.” *Energies, 10*(10), 1466.

Modaressi, H., Laloui, L. (1997). “A thermo-viscoplastic constitutive model for clays.” *International Journal for Numerical and Analytical Methods in Geomechanics, 21*(5), 313–335.

Mohammadi, M., Choobbasti, A.J. (2018). “The effect of self-healing process on the strength increase in clay.” *Journal of Adhesion Science and Technology, 32*(16), 1750-1772.

Mori, N., & Chang, K. (2003). Introduction to MPIV, user reference manual. Retrieved from http:// www.oceanwave.jp/softwares/mpiv".

Morris, P.H., Graham, J., Williams, D.J. (1992). “Cracking in drying soils.” *Canadian Geotechnical Journal, 29*(2), 263-277.

Naghdi, P.M., Murch, S.A. (1963). “On the mechanical behavior of viscoelastic/plastic solids.” *Journal of Applied Mechanics, 30*(3), 321–328.

Nassr, A., Esmaeili-Falak, M., Katebi, H., Javadi, A. (2018). “A new approach to modeling the behavior of frozen soils.” *Engineering Geology, 246,* 82-90.

Nishimura, S., Gens, A., Olivella, S. & Jardine, R. J. (2009). “THM-coupled finite element analysis of frozen soil: formulation and application.” *Géotechnique, 59*(3), 159–171.

Nova, R. (2004). “Development of elastoplastic strain hardening models of soil behavior.” *Degradations and Instabilities in Geomaterials*, 35-76.

Parameswaran, V., & Jones, S. (1981). “Triaxial testing of frozen sand.” *Journal of Glaciology, 27*(95), 147-155.

Perzyna, P. (1966). “Fundamental problems in viscoplasticity.” *Advances in Applied Mech*anics, 9, 243–377.

Pusch, R. (1979). “Unfrozen water as a function of clay microstructure.” *Engineering Geology, 13*(1), 157-162.

Pusch, R., Forsberg, T. (1983). “Gas migration through bentonite clay.” SKB Technical Report 83-71, Stockholm, Sweden.

Pusch, R., Hökmark, H., Börgesson, L. (1987). “Outline of models of water and gas flow through smectite clay buffers.” SKB Technical Report 87-10, Stockholm, Sweden.

Qi, J., Hu, W., and Ma, W. (2010). “Experimental study of a pseudo-preconsolidation pressure in frozen soils.” *Cold Regions Science and Technology, 60*(3), 230-233.

Qi, J., Ma, W., Song, C. X. (2008). “Influence of freeze-thaw on engineering properties of a silty soil.” *Cold Regions Science and Technology, 53*(3), 397-404.

Qiao, Y., Ferrari, A., Laloui, L., Ding, W. (2016). “Nonstationary flow surface theory for modeling the viscoplastic behaviors of soils.” *Computers and Geotechnics, 76,* 105–119.

Qiao, Y., Ding, W. (2017). “ACMEG-TVP: A thermoviscoplastic constitutive model for geomaterials.” *Computers and Geotechnics, 81,* 98–111.

Rekacewicz, P. (2005). Permafrost distribution in the Arctic. Retrieved 2020, from https://www.grida.no/resources/7000.

Romanovsky, V. Photo retrieved 2020, from https://www.helsinki.fi/en/news/science-news/the-thaw-of-permafrost-is-a-threat-for-arctic-cities-and-industries?utm_source=facebook&utm_medium=cpc&utm_campaign=kv_tiedeuutiset_rahoittajat_permafrost.

Rotta Loria, A.F., Frigo, B., Chiaia, B. (2017). “A non-linear constitutive model for describing the mechanical behaviour of frozen ground and permafrost.” *Cold Regions Science and Technology*, *133*, 63-69.

Rutqvist J., Moridis, G. (2007). “Numerical studies on the geomechanical stability of hydrate-bearing sediments.” *Society of Petroleum Engineers Journal,* 14(2).

Saarenketo, T., Aho, S. (2005). “Managing spring thaw weakening on low volume roads.” Final report of Phase II subproject of Roadex II Project. Retrieved from https://www.roadex.org/wp-content/uploads/elearning/publications/docs-RII-EN/2_3%20Spring_Thaw_Weakening_l.pdf.

Sanchez, M., Gai, X., and Santamarina, J.C. (2017). “A constitutive mechanical model for gas hydrate bearing sediments incorporating inelastic mechanisms.” *Computers and Geotechnics, 84,* 28–46.

Sanchez, M., Gens, A. Guimarães, L. (2012). “Thermal–hydraulic–mechanical (THM) behaviour of a large-scale in situ heating experiment during cooling and dismantling.” *Canadian Geotechnical Journal, 49,* 1169–1195.

Sanchez, M., Gens, A., Guimarães, L. and Olivella, S. (2005). “A double structure generalized plasticity model for expansive materials.” *International Journal for Numerical and Analytical Methods in Geomechanics*, *29*(8), 751–787.

Shastri, A., Sanchez, M. (2012). “Mechanical modeling of frozen soils incorporating the effect of cryogenic suction and temperature.” *GeoCongress conference (GeoCongress 2012),* Oakland, California, US.

Sivasithamparam, N., Karstunen, M., Bonnier, P. (2015). “Modelling creep behaviour of anisotropic soft soils.” *Computers and Geotechnics, 69,* 46–57.

Sporer, H., Zanzinger, H. Gartung, E. (2001). “Self-healing properties of geosynthetic clay liners.” *Geosynthetics International, 8*(5), 461–470.

Sultan, N., Garziglia, S. (2011). “Geomechanical constitutive modelling of gas-hydrate-bearing sediments.” *Proceedings of the 7th International Conference on Gas Hydrates,* Edinburgh, Scotland, United Kingdom.

Sunjay, S., Jain, N., Banerjee, M. (2014). “Geophysical Study of Gas Hydrate Stability.” *Environmental Management and Current Practices in Mining and Allied Industries conference,* Varanasi, India. Retrieved from https://www.researchgate.net/publication/280623586_Geophysical_Study_of_Gas_Hydrate_Stability.

Taber, S. (1930). “The mechanics of frost heaving.” *The Journal of Geology, 38*(4), 303-317.

Tanai, K., Kanno, T., Gallé, C. (1997). “Experimental study of gas permeabilities and breakthrough pressures in clays.” *In: Scientific Basis for Nuclear Waste Management,* Boston, Materials Research Society, *45,* 1003–1010.

Tang, Y., Li, J. (2018). “Experimental study on dynamic cumulative axial-strain performance of freezing–thawing saturated sandy silt.” *Cold Regions Science and Technology, 155,* 100-107.

Tian, S., Tang, L., Ling, X., Li, S., Kong, X., Zhou, G. (2019). “Experimental and analytical investigation of the dynamic behavior of granular base course materials used for China's high-speed railways subjected to freeze-thaw cycles.” *Cold Regions Science and Technology, 157,* 139-148.

Tice, A., Anderson, D.M., Banin, A. (1976). “The prediction of unfrozen water contents in frozen soils from liquid limit determinations.” *Symp. Frost Action Roads, Paris*.

Tice, A.R., Oliphant, J.L., Nakano, Y., Jenkins, T.F. (1982). “Relationship between the ice and unfrozen water phases in frozen soil as determined by pulsed nuclear magnetic resonance and physical desorption data.” *Cold Regions Research and Engineering Lab Report,* 82-15.

Tice, A., Black, P., and Berg, R. (1988). “Unfrozen water contents of undisturbed and remolded Alaskan silt.” *Cold Regions Science and Technology*, *17*(2), 103-111.

Thomas, L. K., Katz, D. L., Tek, M. R. (1968). “Threshold pressure phenomena in porous media.” *Old SPE Journal*, *8*(2), 174-184.

Thomas, H. R., Cleall, P., Li, Y. C., Harris, C., Kern-Luetschg, M. (2009). “Modelling of cryogenic processes in permafrost and seasonally frozen soils.” *Géotechnique, 59*(3), 173–184.

Turchetta, D. (2010). “Taking stock: climate change and transportation.” *Federal Highway Publication 73*(5), 112-125.

Uchida, S., Soga, K., Yamamoto, K. (2012). “Critical state soil constitutive model for methane hydrate soil.” *Journal of Geophysical Research: Solid Earth*, *117*(B3), 1-13.

Uchida, S., Xie, X.G., Leung, Y.F. (2016). “Role of critical state framework in understanding geomechanical behavior of methane hydrate-bearing sediments.” *Journal of Geophysical Research: Solid Earth, 121*(8), 5580-5595.

Viklander, P. (1998). “Permeability and volume changes in till due to cyclic freeze-thaw.” *Canada Geotechnical Journal, 35*(3), 471-477.

Villar, M.V., Gutierrez-Rodrigo, V., Martin, P.L., Romero, F.J., Barcala, J.M. (2013). “Gas transport in bentonite.” Ciemat Report 1301.

Villar, M.V., Sánchez, M., Gens, A. (2008). “Behaviour of a bentonite barrier in the laboratory: experimental results up to 8 years and numerical simulation”. *Physics and Chemistry of the Earth*, *33*(1), S476-S485.

Wan, Y., Xue, Q., Liu, L., Wang, S. (2018). “Crack characteristic and permeability change of compacted clay liners with different liquid limits under dry-wet cycles.” *Advances in Civil Engineering*. https://doi.org/10.1155/2018/5796086.

Wang, D., Ma, W., Niu, Y., Chang, X., Wen, Z. (2007). “Effects of cyclic freezing and thawing on mechanical properties of Qinghai-Tibet clay.” *Cold Regions Science and Technology*, *48*(1), 34-43.

Wang, J., Satoshi Nishimura, S., Okajima, S., Joshi, B. R. (2019). “Small-strain deformation characteristics of frozen clay from static testing.” *Géotechnique*, *69*(9), 816-827.

Wang, J., Zhang, H., Zhang, L., Liang Y. (2013). “Experimental study on self-healing of crack in clay seepage barrier.” *Engineering Geology*, *159*, 31-35.

Wang, Q., Tang, A.M., Cui, Y.J., Delage, P., Gatmiri. B. (2012). “Experimental study on the swelling behavior of bentonite/claystone mixture.” *Engineering Geology*, Elsevier, *124*, 59-66.

Watanabe, K., Osada, Y. (2017). “Simultaneous measurement of unfrozen water content and hydraulic conductivity of partially frozen soil near 0°C.” *Cold Regions Science and Technology*, *142*, 79-84.

Wei, T., Hu, D., Zhou, H., Lu, J., Lü, T. (2019). “Influences of degree of saturation and stress cycle on gas permeability of T unsaturated compacted Gaomiaozi bentonite.” *Engineering Geology*, *254*(6), 54-62.

White, T.L., Coutard, J-P. (1999). “Modification of silt microstructure by hydrocarbon contamination in freezing ground.” *Polar Record (Gr Brit)*, *35*(192), 41–50.

Williams, P. J. (1964). “Unfrozen water content of frozen soils and soil moisture suction.” *Géotechnique*, *14*(3), 231-246.

Xu, L., Ye, W.M., Chen, Y.G., Chen, B., Cui, Y.J. (2020). “Investigation on gas permeability of compacted GMZ bentonite with consideration of variations in liquid saturation, dry density and confining pressure.” *Journal of Contaminant Hydrology, 230,* 103622.

Xu, L., Ye, W.M., Ye, B. (2017). “Gas breakthrough in saturated compacted GMZ bentonite under rigid boundary conditions.” *Canada Geotechnical Journal, 54*(8), 1139–1149.

Xu, W.J., Shao, H., Hesser, J., Wang, W., Schuster, K., Kolditz, O. (2013). “Coupled multiphase flow and elasto-plastic modelling of in-situ gas injection experiments in saturated claystone (Mont Terri rock laboratory).” *Engineering Geology, 157,* 55–68.

Xu, X., Wang, Y., Yin, Z., Zhang, H. (2017). “Effect of temperature and strain rate on mechanical characteristics and constitutive model of frozen Helin loess.” *Cold Regions Science and Technology, 136*(c), 44–51.

Yang, Y., Lai, Y., Dong, Y., Li, S. (2010). “The strength criterion and elastoplastic constitutive model of frozen soil under high confining pressures.” *Cold Regions Science and Technology, 60*(2), 154–160.

Yao, X., Xu, G., Zhang, M. Yu, F. (2019). “A frozen soil rate dependent model with time related parabolic strength envelope.” *Cold Regions Science and Technology, 159,* 40–46.

Yesiller, N., Miller, C., Inci, G., Yaldo, K. (2000). “Desiccation and cracking behavior of three compacted landfill liner soils.” *Engineering Geology, 57*(1-2), 105-121.

Yin, Z.Y., Chang, C.S., Karstunen, M., Hicher, P.Y. (2010). “An anisotropic elastic–viscoplastic model for soft clays.” *International Journal of Solids and Structures, 47*(5), 665–677.

Yoneda, J., Oshima, M., Kida, M., Kato, A., Konno, Y., Jin, Y., Jang, J., Waite, W., Kumar, P., Tenma, N. (2019). “Pressure core based onshore laboratory analysis on mechanical properties of hydrate-bearing sediments recovered during India's National Gas Hydrate Program Expedition (NGHP) 02.” *Marine and Petroleum Geology, 108*, 482-501.

Zhang, Y., Michalowski, R. L. (2015). “Thermal-hydro-mechanical analysis of frost heave and thaw settlement.” *Journal of Geotechnical and Geoenvironmental Engineering*, *141*(7), 04015027.

Zhang, Z. L., Cui, Z. D. (2018). “Effect of freezing-thawing on dynamic characteristics of the silty clay under K0-consolidated condition.” *Cold Regions Science and Technology*, *146*, 32-42.

Zhang, D., Li, Q., Liu, E., Liu, X., Zhang, G., Song, B. (2019). “Dynamic properties of frozen silty soils with different coarse-grained contents subjected to cyclic triaxial loading.” *Cold Regions Science and Technology*, *157*, 64-85.

Zhou, M., Soga, K., Yamamoto, K., Huang, H. (2020). “Geomechanical responses during depressurization of hydrate-bearing sediment formation over a long methane gas production period.” *Geomechanics for Energy and the Environment*, *23*, 100111.

Zhou, Z., Ma, W., Zhang, S., Mu, Y., Li, G. (2018). “Effect of freeze-thaw cycles in mechanical behaviors of frozen loess.” *Cold Regions Science and Technology*, *146*, 9-18.

APPENDIX A

The appendix lists equations of all the basic models incorporated in this dissertation.

A.1 Tice model

Tice model (Tice et al., 1976) is referred to in this dissertation for the calculation of saturation degree of ice. The function relates saturation degree of ice with temperature as well as an experimental factor α.

$$S_i = \begin{cases} 1-[1-(T-T_0)]^{\alpha} & T \le T_0 \\ 0 & T > T_0 \end{cases} \tag{A1}$$

Where T is temperature in Celsius temperature; T_0 is freezing temperature of pore water in Celsius temperature; α is an experimental factor.

A.2 Clausius–Clapeyron equation

The equilibrium between liquid water and ice phases is described by the Clausius–Clapeyron equation. This equation represents a thermodynamic requirement for equilibrium that needs to be satisfied by P_i, P_l and T.

$$P_i = \frac{\rho_i}{\rho_l} P_l - \rho_i l \ln\left(\frac{T}{273{\cdot}15}\right) \tag{A2}$$

Where P_i and P_l are pressure of ice and pressure of unfrozen water; ρ_i and ρ_l are density of ice and water; l is the latent heat of fusion; T is temperature in Celsius temperature.

In this dissertation, this equation will be used to calculate the pressure of ice together with Cryogenic Suction formulation as well as equation by Thomas et al., (2009).

$$S_c = \rho_l \times l \times \ln(\frac{T}{T_0}) \tag{A3}$$

Where S_c is Cryogenic Suction; l is the latent heat of fusion; ρ_l is the density of water.

A.3 Mechanical constitutive model

The mechanical constitutive model used in the mechanical modeling part is modified Barcelona Basic Model (BBM). As elaborated in Section 4, BBM is a constitutive for unsaturated soils. When it is extended to frozen soils, the two variables, net stress and cryogenic suction, are defined as follows.

$$\begin{aligned} \sigma_n &= \sigma - \max(P_i, P_l, 0) \\ S_c &= \max(P_i - P_l, 0) \end{aligned} \tag{A4}$$

Where σ is the mean stress; σ_n is the net stress.

The Load-Collapse (LC) curve (shown in Figure A1), which causes the yielding of the soil. The yield mean stress on LC curve is calculated by:

$$p_0 = p^c \left(\frac{p_0^*}{p^c} \right)^{\frac{\lambda_0 - \kappa}{\lambda_s - \kappa}} \tag{A5}$$

Where,

$$\lambda_s = \lambda_0 [r + (1-r)\exp(-\beta s)] \tag{A6}$$

p_0 is mean yield stress; r and β are model parameters; λ_s is slope of consolidation under cryogenic suction s; λ_0 is slope of consolidation curve when cryogenic suction value is 0.

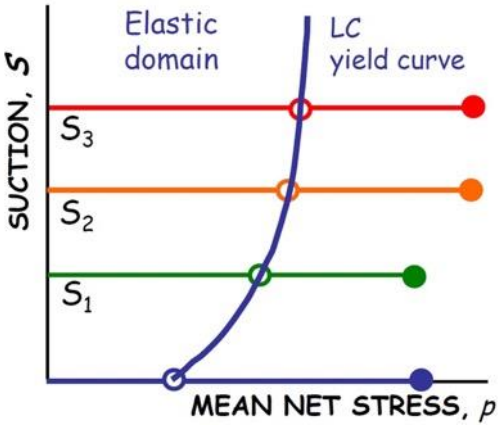

Figure A1 LC curve of BBM

As for hardening law in BBM, the change of pre-consolidation pressure is calculated by:

$$dp_0^* = \frac{1+e}{\lambda_0 - \kappa} \times p_0^* \times d\varepsilon_v^p \tag{A7}$$

Where λ_0 is slope of virgin consolidation curve when cryogenic suction is 0; κ is slope unloading or reloading curve; e is void ratio; the plastic volume strain because of ice can be calculated by interaction function multiplied by elastic volume strain as introduced in Section 4.

A.4 Interaction functions for double structure model

In this dissertation, interaction function derived from double structure plasticity model (Sanchez et al., 2005) will be incorporated to help make clear the relationship of elastic volume strain and plastic volume strain due to ice formation. Freezing interaction function and thawing interaction function will be used separately in freezing and thawing process.

$$f_{freezing} = ff1 + ff2 \times \tanh(ff3 \times (p / p_0) - ff4) \quad \text{(A8)}$$

Where ff1, ff2, ff3, and ff4 are parameters for freezing function; p/p0 is the ratio describing the openness of soil structure as introduced in Section 4.

$$f_{thawing} = ft1 + ft2 \times \tanh(ft3 \times (p / p_0) - ft4) \quad \text{(A9)}$$

Where ft1, ft2, ft3, and ft4 are parameters for freezing function; p/p0 is the ratio describing the openness of soil structure as introduced in Section 4.